Universidad
Carlos III de Madrid

TESIS DOCTORAL

SUPERCONDUCTING NON-CONTACT LINEAR SLIDER FOR PRECISION POSITIONING IN CRYOGENIC ENVIRONMENTS

Autor Ignacio Valiente-Blanco

Director: José Luis Perez-Diaz

DEPARTAMENTO DE INGENIERÍA MECÁNICA

Leganés, Abril de 2013

TESIS DOCTORAL

SUPERCONDUCTING NON-CONTACT LINEAR SLIDER FOR PRECISION POSITIONING IN CRYOGENIC ENVIRONMENTS

Autor: Ignacio Valiente Blanco

Director: José Luis Pérez Díaz

Firma del tribunal calificador:

Presidente: Dra. Mª Carmen Muñoz de Pablo

Vocal: Dr. Johannes Franciscus Zevenbergen

Secretario: Dr. Carlos Luis Molpeceres Álvarez

Calificación:

Leganés, 16 de Abril de 2013

A mis padres y a mi abuelo

Agradecimientos

Llegado este momento, he de decir que redactar esta sección de agradecimientos ha sido, para mí, uno de los momentos más satisfactorios durante el desarrollo de esta investigación. Tan duro trabajo jamás hubiera llegado a buen puerto sin la ayuda de las siguientes personas, a las cuales estoy y estaré siempre agradecido:

Me siento en la obligación de agradecer, en primer lugar, a mi tutor **José Luis Pérez Díaz** por las innumerables oportunidades y consejos que me ha dado, así como el tiempo, el interés y los recursos que me ha dedicado a lo largo del desarrollo de mi carrera en la Universidad Carlos III de Madrid.

En segundo lugar, agradezco al resto de profesores del Departamento de Ingeniería Mecánica de la Universidad Carlos III la oportunidad que me brindaron en su día de forma parte de este equipo. También me gustaría agradecer al profesor **Yi Qin,** de la Universidad de Strathclyde su contribución a mi formación como investigador.

En un ámbito más personal, pero igualmente indispensable, se encuentra la amistad ganada en estos años con **Cristian, Marco, Chus, Edu, Álvaro, Mauricio, Javi, Marlem,** y otros muchos compañeros del departamento y de fuera de él. Siempre estaré en deuda con **Efrén Díez Jiménez**, que ha sido un gran compañero, consejero y amigo. En el contexto de esta tesis he de

agradecerle a él y a **Juan Sánchez** sus absolutamente imprescindibles aportaciones.

Igualmente he de reconocer y agradecer al equipo de LIDAX ingeniería S.L., con el cual tuve el placer de colaborar, su irremplazable aportación a esta tesis. A todos ellos, a **Javier Serrano, David González, Mikel Lamensans, Violeta Sanz** y especialmente a **Heribert Argelaguet** y **Fernando Romera**, muchas gracias.

No obstante, mis mayores agradecimientos he de dirigirlos a toda mi familia, y muy especialmente **a mis padres**. Ellos me han apoyado y aguantado de manera incondicional siempre, muchas veces en detrimento de sus propios intereses y siempre velando por los míos. Gracias a ellos, soy hoy la persona que soy. También a mi hermana **Sara**, porque la quiero y la necesito a mi lado. Ellos, **mis tíos y mis abuelos** siempre tendrán un lugar reservado en mi corazón.

Son también parte de mi familia muchos de **mis amigos**. A ellos y a mis antiguos compañeros de universidad, quiero agradecerles los buenos momentos que hemos pasado juntos. Y por último, pero con total seguridad no menos importante, gracias a **Silvia.** Ella es en gran parte la responsable de la consecución de esta tesis y ha disfrutado y sufrido conmigo los buenos y los malos momentos de ésta. Sin ti jamás hubiese encontrado el camino. Gracias por estar siempre ahí para todo.

Acknowledgments

This moment is a very sweet moment for me. This thesis is the contribution of many people around me and I own them my most sincerely gratitude:

First of all, I have to extend my infinite thankfulness to my supervisor, Professor **Jose Luis Perez-Diaz**. He has offered me plenty of opportunities and useful advice during my career in Carlos III University of Madrid

I would like to say thank you to the rest of professors in the Mechanical Department of that university, for bringing me the opportunity to work with them. In addition, I would like to extend my gratitude to Professor **Yi Qin** from The University of Strathclyde for his hospitality, support and contribution to my background as a researcher.

It has been extremely important to me the friendship I have earned with **Cristian, Marco, Chus, Edu, Álvaro, Mauricio, Javi, Marlem** and so many others. I will always be in debt with **Efren Diez-Jimenez** who has been a very good friend and colleague all over these years. In the context of this thesis, I really must show him and **Juan Sanchez García Casarrubios** my gratitude for their precious contributions to this thesis.

Furthermore, the contribution from my colleagues at LIDAX ingeniería S.L. cannot be overemphasized. To **Javier Serrano, David Gonzalez, Mikel**

Lamesans, and especially to **Heribert Argelaguert** and **Fernando Romera**, thank you.

I cannot thank enough the effort and support that my families gives me. Specially **my parents**, who have unconditionally supported and love me no matter what. I will be everlastingly in debt with them, because they are my role models. I want to say thank you to my treasure sister **Sara**, for showing preference for me, without care of the circumstances. All of them, together with **my uncle**, **my aunt** and my **grandparents**, will always have a place deep in my heart.

Thank you to **my friends**, who are in fact, an extension of my family. To them and my classmates, thank you for the precious moments we have shared. And last, but definitely no least, thank you very much to **Silvia**. She has always been there during the ups and downs of this thesis. I wouldn't have found the strength to persevere without you. Thank you for always supporting me.

Resumen

En esta tesis doctoral se propone, diseña, construye y demuestra un dispositivo de alta resolución para posicionado en una carrera larga para entornos criogénicos. Este dispositivo está basado en levitación magnética superconductora de manera que, un conjunto de superconductores de alta temperatura (superconductores de tipo II) permiten a un imán permanente levitar de manera estable sobre ellos y, al mismo tiempo, ser guiado. De hecho, se establece un par cinemático de deslizamiento entre el imán y los superconductores gracias a la alta simetría traslacional del campo magnético aplicado en estos últimos. Además, la posición de la deslizadera puede ser controlada mediante una estrategia de control en bucle abierto de la corriente circulante en un par de bobinas diseñadas específicamente para esta tarea, obteniéndose una excelente resolución y un consumo de energía muy reducido.

Así mismo, se proponen una serie de reglas de diseño que fueron verificadas a una temperatura de operación de 77 K. Estas reglas demuestran que hay una serie de parámetros característicos del desempeño del mecanismo como la sensibilidad, la rigidez, la frecuencia natural, las desviaciones o el consumo energético que pueden ser modificados mediante un diseño apropiado.

Tras obtener estas reglas de diseño, un par de prototipos de un nanoposicionador de larga carrera han sido diseñados en consecuencia, construidos y probados en un ambiente relevante (T $\sim$ 15 K, alto vacío $< 10^{-6}$ Pa). Una resolución nanométrica en el posicionamiento de una masa de 170 gramos ha sido demostrada en una carrera de hasta 18 mm.

Abstract

In this thesis, a novel device for precision positioning in a long stroke suitable for cryogenics environments has been proposed, designed, built and tested.

The device is based on superconducting magnetic levitation. A set of high temperature superconductors allows a long permanent magnet to levitate stably over them. Furthermore, due to the high translational symmetry of the magnetic field applied on the superconductors for any position of the slider in its path, the superconductors not only provide stable levitation to the slider, but also guide it. Therefore, a sliding kinematic pair is established between the permanent magnet and the superconductors. Finally, using a pair of coils, the position of the slider can be controlled with an open-loop control strategy of the current in the coils with nanometre resolution and reduced power consumption.

Besides, a set of design rules has been proposed and experimentally verified at 77 K. Parameters of the performance of the mechanism such as the stroke, sensitivity, stiffness, natural frequency, run outs or the power consumption can be modified and optimized by an appropriate design.

After this, two prototypes of a long stroke nanopositioner based on these design rules have been built and tested in a relevant environment (T~15 K, in a high vacuum $< 10^{-6}$ Pa). Nanometre resolution in the positioning of a mass of about 170 g has been demonstrated in a stroke up to 18 mm.

CONTENTS

LIST OF FIGURES

LIST OF TABLES

Chapter I

Introduction and objectives

In this chapter the interest and motivation to start this research are briefly conveyed. Although a general overview of the techniques and applications available are discussed, it should be noticed that a detailed description of the state-of-the-art is presented in chapter II of this document. The objectives and goals of this thesis and a summary of the general structure of this document are also introduced.

1.1 Introduction and motivation

It is usually accepted that nanotechnology is the science of understanding matter and the control of matter at dimensions of 100 nm scale or less. Otherwise, it is more accepted to talk about micrometre, typically ranging between 1 mm and 1 µm, or sub-micrometre technology, (1 µm to 100 nm). All these technologies from, over the last few decades, part of the most active technical fields in mechanical engineering [1].

One key challenge in very small scale technology (i.e. nano and microtechnology), is very high precision positioning. Significant requirements for these types of device include high accuracy, resolution, range of motion and bandwidth [2]. Despite some mature technologies that are nowadays available, some problems still remain to be solved. One of the most challenging tasks is achieving very accurate positioning (in the order of nm) within a long motion range (of the order of tens of mm). In addition, the difficulty of this task increases when the positioner must operate in cryogenic environments and overcome all the tribological problems associated with these conditions [3], [4]. However, vacuum and cryogenic conditions are mandatory requirements in some applications for optical, aircraft, military and space industries. Some examples of these applications were very precise positioning in a long range is required are in cryogenic environments are, for example: optic alignment in space telescopes, filter wheels and cryogenic optical microscopy [5–7].

An application of particular interest for the device presented in this thesis which represents the main motivation for this research is infrared interferometer spectroscopy. This technique is used in space telescopes with the aim to answer some of the most challenging questions of science such as: how are stars, galaxies and other planetary systems born? What is the chemical composition of the atmosphere on these planets? And possibly one of the most exciting questions ever asked by human beings: can these exoplanets contain life? [8]. The instrumentation for Fourier Transform Infrared Spectrometers requires a mirror to be positioned with extreme precision within a long stroke [9]. In Fig.1.1, a diagram of the SAFARI instrument for the SPICA JAXA-ESA mission is shown, including the positioning mechanism for Fourirer Transform Spectroscopy (*FTS*).

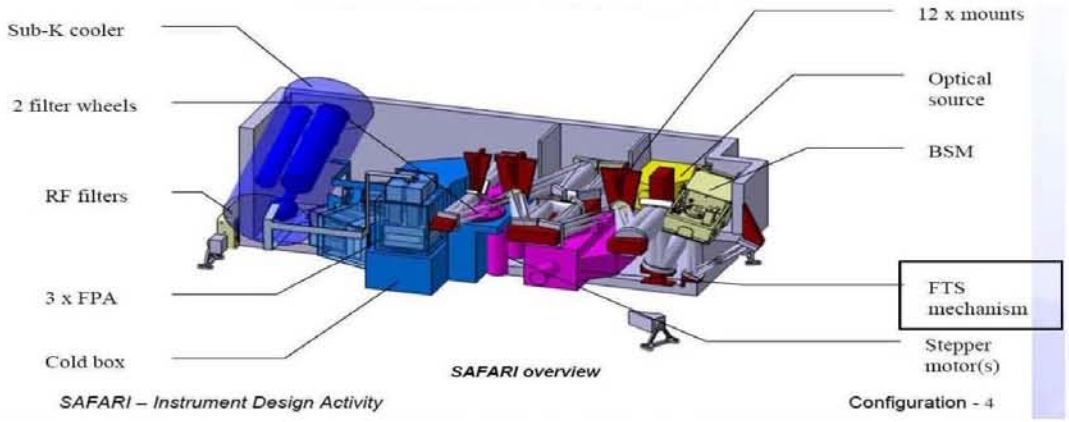

Fig. 1.1 SAFARI instrument (configuration 4) for the JAXA-ESA SPICA mission.

It is noteworthy that the lower the temperature at which the infrared sensor operates, the higher the sensitivity the device will have [8]. Thus, cryogenic conditions are a desirable requirement for these kinds of devices. Moreover, very low energy consumption is also necessary to reduce the cooling power required. In this context of extreme precision positioning in cryogenic environments, there are two main techniques currently used to achieve the extreme precision requirements of the aerospace, manufacturing and medical industries:

Firstly, actuators based on piezoelectric materials. These materials modify their shape due to changes in their crystalline structures when an electric field is applied. Their use is widely extended for "short" range applications of a few hundreds of micrometres, but they are limited for use in long range applications in cryogenic environments. They present strong hysteretic behaviour, have high power requirements and its stroke and resolution are highly temperature dependent.

Another solution available for long range nanopositioning in cryogenic environments is active magnetic levitation. Devices based on this technology use electromagnetic forces to move and stabilise a magnetic source (typically a permanent magnet) with extreme precision. In comparison to piezoelectric and magnetostrictive positioners, they can achieve similar positioning resolution in a larger motion range. However, their high current requirements, their inherent instability and their highly complicated control strategies are some of their disadvantages.

The mechanism presented in this thesis is based on superconducting magnetic levitation. Some previous attempts have been carried out using this technology in precise positioning. However, as far as we know, they are only

able to achieve positioning resolutions in the µm scale in a stroke of just a few millimetres in the best of cases.

Additionally, some other positioning technologies available like diamagnetic levitation, magnetostrictive actuators and acoustic levitation will be introduced, as well as a wide ranging discussion on the state-of-the-art and advantages and disadvantages of all previously mentioned technologies that will be introduced in chapter II of this thesis.

Finally, it is our aim to provide a new perspective on the nanopositioning issue in cryogenic environments and present a novel nanopositioner based on superconducting magnetic levitation with unprecedented performance for superconducting precision positioners. This mechanism is the fruit of a collaborative development between *Universidad Carlos III de Madrid* and the aerospace company *LIDAX Ingeniería S.L. and* has been partially funded by the Comunidad de Madrid (ref 12/09*).*

1.2 Objectives and goals

The main objective of this thesis is to design and demonstrate a mechanism able to position with a very high resolution (nm range) within a long linear stroke (tens of mm) a mirror in a relevant cryogenic environment. This mechanism will be called the *FTS* mechanism from now on and will be based on superconducting magnetic levitation. Below, the objectives of this thesis are introduced:

- To demonstrate that a one DoF positioner based on superconducting magnetic levitation can be used as a high-precision device for long-stroke positioning in cryogenic environments in accordance to technology readiness level (TRL): TRL 6. According to ESA, this requires a "system/subsystem model or prototype demonstration in a relevant environment (ground or space)" [10]. A relevant environment is defined in this thesis as: Temperature ~15 K, High vacuum $< 10^{-4}$ Pa. Moreover, a set of goals were defined in order to place the performance of the device in a real setting of long-stroke high-precision cryogenic positioners. These goals are summarised in Table 1.1.

Table 1.1. Goals for the performance of the mechanism presented in this thesis.

Parameter	Goal
Stroke [mm]	~18
RMS Resolution [nm]	<100
Run out [µm]	<±100
Angular run outs	TBD
Position stability along motion axis	TBD
Current requirement [mA]	≤±500

- To deeply analyse the mechanical behaviour of the mechanism and establish the bases of the design and engineering of these short of mechanisms.

1.3 Structure of this document

This thesis is composed of 8 chapters, a bibliography besides different indexes, two abstracts (one written in English and the other in Spanish) and an essential acknowledgment section.

Furthermore, a short description of each chapter is presented:

Chapter I. **Introduction and objectives:** In this chapter the interest and motivation to start this research are briefly conveyed. Although a general overview of the techniques and applications available are discussed, it should be noticed that a detailed description of the state-of-the-art is presented in chapter II of this document. The objectives and goals of this thesis and a summary of the general structure of this document are also introduced.

Chapter II. ***Superconductivity and nanopositioning. State-of-the-art:*** A short journey through the history and concepts of superconductivity is here presented. Additionally, the state-of-the-art of micro and nanopositioning devices is exposed and the suitability and performance of the most relevant technologies available for long range nanopositioning in cryogenic environments is discussed.

Chapter III. ***Theoretical foundations:*** The theoretical principles and considerations for the design of a non-contact linear slider based on superconducting magnetic levitation for high-precision positioning in a long stroke are presented in this chapter. The special properties of the magnetic interaction between a type II superconductor in the mixed state (stator) and a long permanent magnet (slider) in this invention provide a sliding kinematic pair. Moreover, the system is stable and presents an equilibrium position of the slider. Finally, this initial equilibrium position can be modified (without contact) by controlling the current circulating through a couple of coils.

Chapter IV. **Design and preliminary test of a prototype:** In order to test the working principle of the *FTS* mechanism, a prototype with a ± 9 mm stroke was designed, built and tested. A detailed description of the design of this prototype is given. A simplified model based on FEM calculations supported the design of the actuation system. Once designed and built, a first prototype of the *FTS* mechanism was tested in a bath of liquid nitrogen at ambient pressure and the results of these tests are discussed in this chapter. Lastly, conclusions for the improvement of the device are detailed.

Chapter V. **Engineering of the *FTS* mechanism**: In this chapter, it is demonstrated how the most relevant characteristics of the *FTS* mechanism - such as the stiffness and run outs- can be tuned, mainly by modification to the geometry of the prototype. An experimental study of a real prototype and FEM calculations are in good agreement and support of the design rules given in this chapter.

Chapter VI. ***Test and demonstration in a relevant environment:*** An improved prototype of the FTS mechanism (FTS2) was designed and tested in a relevant environment in a cryostat (T~15 K and a high vacuum <10-6 Pa). The experimental set up and procedure of these tests are presented in this chapter, as well as a discussion of the results and conclusions of the tests. A sub-micrometre resolution of about 230 nm with a symmetric stroke of around 18 mm and a current requirement below ± 450 mA was demonstrated. Finally, the dynamic behaviour of the FTS mechanism was characterised.

Chapter VII. **Long stroke nanopositioning device for cryogenic applications:** A prototype of a long stroke high-precision positioning device for cryogenic applications was designed, built and tested in a relevant

environment as demonstrated in in the previous chapter. In this chapter, additional improvements are made and an improved prototype (FTS3) has been tested in a relevant environment. Results and a discussion of these experiments are conducted in this chapter.

Chapter VIII. **Conclusions and contributions:** This chapter lists the conclusions and main original contributions of this Ph.D thesis. Finally, some items for further research are proposed.

Following these chapters, a bibliography that contains the essential literature references used during development of this thesis is presented.

Chapter II

Superconductivity and nanopositioning. State-of-the-art

A short journey through the history and concepts of superconductivity is here presented. Additionally, the state-of-the-art of micro and nanopositioning devices is exposed and the suitability and performance of the most relevant technologies available for long range nanopositioning in cryogenic environments is discussed.

2.1 Superconductivity

2.1.1 Historical review

Superconductivity is a macroscopically measurable quantum effect. It consists on the loss of all the electric resistivity in the material when it is in the superconducting state; thereby, any electric current can flow through it with no resistance or losses of energy for an infinite time. Superconductors are in the superconducting state only at a temperature lower than that which is called the *transition or critical temperature* T_c. For example, the sudden vanishing of Magnesium Diboride (MgB_2) resistivity at a temperature $T_c =$ 39 K [11] is shown in Fig. 2.1.

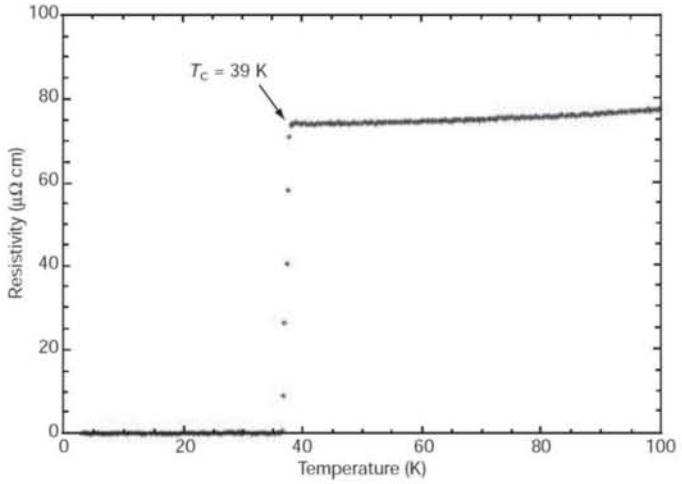

Fig. 2.1. Resistivity of $MgBi_2$ vs. temperature [1].

Superconductivity was discovered in 1911 by a group of scientists commanded by Heike Kamerlingh Onnes; one of the most brilliant students of J.*D.* van der Waals. He found that the resistivity of mercury drops almost to zero (in fact, nowadays we know it was zero) when cooled with liquid helium to below 4 K [12]. Two years later he won the Nobel Prize for his great contributions to the study of matter at low temperature, mainly because he was the first to liquefy helium in 1908. Within two years of the discovery of superconductivity in mercury, Onnes noticed that there was a threshold value of the current density that destroyed superconductivity. In the following years, he also reported on the influence of the magnetic field in the superconductivity of mercury. Nevertheless, it was Silsbee who reported that the [13]:

"threshold value of the critical current is that at which the magnetic field due to the current itself is equal to the critical magnetic field".

The discovery of a subsequent fundamental phenomenon of superconductivity had to wait until 1933. Walter Meissner and Robert Oschenfeld [14] were measuring the magnetic flux distribution outside two cylinders made of lead and tin immersed in an applied magnetic field when they discovered something very revealing to the understanding of superconductivity. They found that the applied magnetic flux was totally expelled from the inside of the sample at the superconducting state; this is known today as the Meissner-Oschenfeld effect or just the Meissner effect.

Superconductivity was first theorised by the London Brothers (Frinz and Heinz London) two years later. A major triumph of the London equations is their ability to explain the Meissner effect [15]. From 1935 to 1950, advances in the superconductivity field were almost limited to the discovery of new superconducting materials with higher transition temperatures. A graphical historical review of this development is shown in Fig. 2.2. During those years, many giant physicists were unsuccessful in postulating a microscopic theory of superconductivity: R. Feimand, N. Bohr, W. Heisenberg and A. Einstein among them [16].

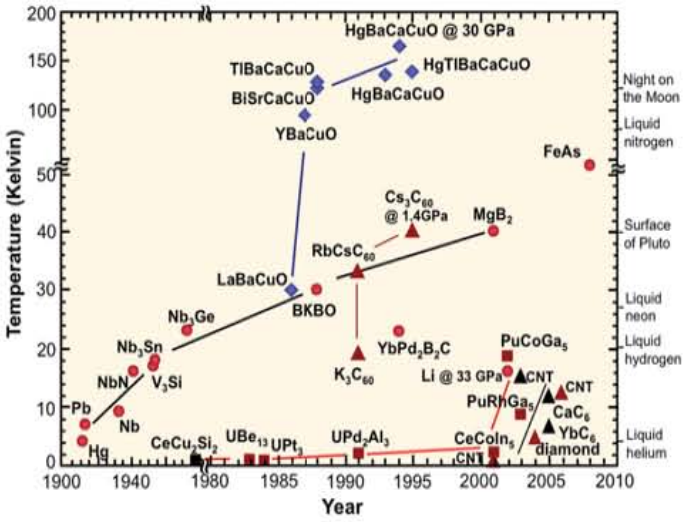

Fig. 2.2. Historical evolution of transition temperature of superconducting materials.

It was in 1950 when Vitaly Ginzburg and Lev Landau generalised the London equations and developed a successful phenomenological theory that explains the macroscopic behaviour of superconductors [17]. Two years later, Alexei A. Abrikosov (based on Landau's theory) explained how the superconducting state and the normal state could coexist in type II superconductors [18].

Abrikosov's hypothesis was simple (but beautiful and correct), as the magnetic flux penetrates the superconducting samples in the shape of magnetic

vortexes generating a mixed state, or as it is also known, the vortex state. Their work was finally recognised in 2003 when the three of them won the Nobel Prize. Thanks to magneto-optical imaging techniques, this vortex can today be observed, as shown in Fig. 2.3.

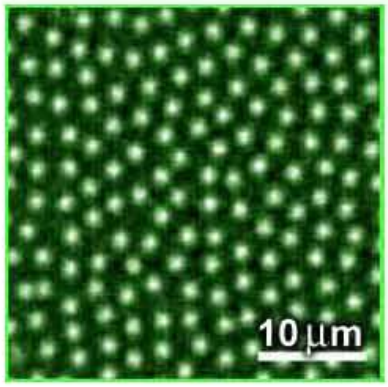

Fig. 2.3. Vortex imaging of NbSe$_2$ at 4 K [19].

However, it was not until 1957 when John Bardeen, Leon Cooper and John Schieffer developed the first theory accepted to explain the superconducting quantum state [20]. The theory was given the not very imaginative name of the BCS theory. They won the Nobel Prize in 1972 for this extraordinary contribution. The theory is based on the fact that the electrons are bound into "*Cooper pairs*". These "*Cooper pairs*" are correlated due to the Pauli Exclusion Principle for the electrons, from which they are composed. Therefore, in order to break a pair, one has to change the energies of all the other pairs. This means that there is an energy gap for single-particle excitation. An example of this energy gap is shown in Fig. 2.4.

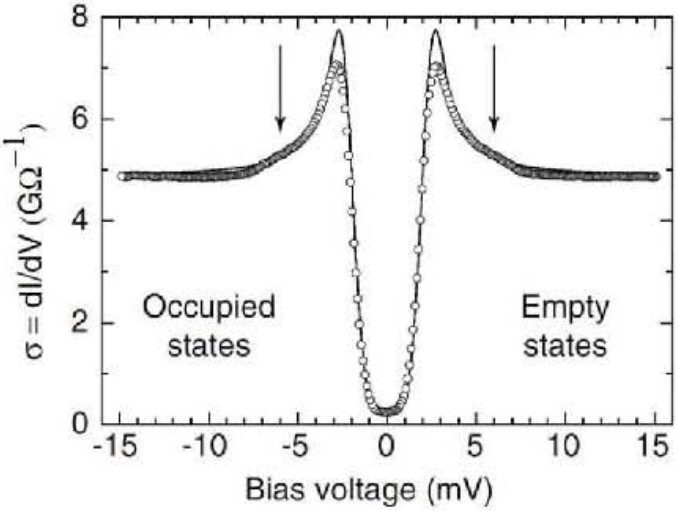

Fig. 2.4. Zero Field superconducting spectrum for MgB2 at 320 mK. No electrons can reside between the coherence peaks of ± 2.9mV [21].

In 1962, Brian *D.* Josephson observed that an electric current appears between two superconductors separated by a potential barrier due to the tunnel effect [22]. This is called the Josephson effect, which is the basic principle of the ultra-sensitive magnetic field detector SQUID [23]. In the same year, the first commercial superconducting wire was developed by scientists from the Westinhouse company.

A great advance in the superconductivity field was made in 1986 when Alex Muller and George Bednorz detected superconductivity in a ceramic material *BaLaCuO* at a temperature of around 30 K [24]. They won the Nobel Prize for this discovery one year later. In 1987, the first superconductor magnet was used in a particle accelerator at the FermiLab. It was also in 1987 when Wu et al. replaced Lanthanum in Muller & Berdnor's compound by Yttrium. This was the birth of *YBaCuO*. This superconducting material presents a transition temperature of 93 K [25] and therefore, it can be cooled using liquid nitrogen (77 K). The importance of this discovery for the technological applications of high temperature superconductors cannot be overemphasised.

Finally, at the present time, the global market and applications of superconductors includes: coil windings and superconducting wires, transformers, magnetic resonance imaging (MRI) and nuclear magnetic resonance (NMR) medical equipment, mass spectrometers in particle accelerators, superconducting magnets, fault-current limiters, flywheels for energy storage, electric motors and generators, railway transportation and superconducting magnetic bearings, etc. [26–29].

2.1.2 Classification of superconductors

There are different criteria used to classify superconductors. They can be differentiated by:

1. Their magnetic behaviour
    a) Type I superconductors: When an external magnetic field is applied on the superconductor, the field is completely expelled from the superconductor. In other words, it is at the Meissner state until the external magnetic field breaks down the superconductivity. Pure metals, such as lead or mercury normally exhibit this behaviour.
    b) Type II superconductors: They present a mixed state where the magnetic field and the superconductivity can coexist

inside the superconductor. They are usually made of metal alloys or oxide ceramics.

c) Type "1.5 superconductors" or semi-Meissner state: In 2005, E. Babaev and M. Speight showed that the classic classification of type I and type II superconductors is insufficient for some multicomponent superconductors, such as MgBr2. More information regarding this superconductor can be found in [30] .

A qualitative comparison of both types of superconductors is shown in Fig. 2.5.

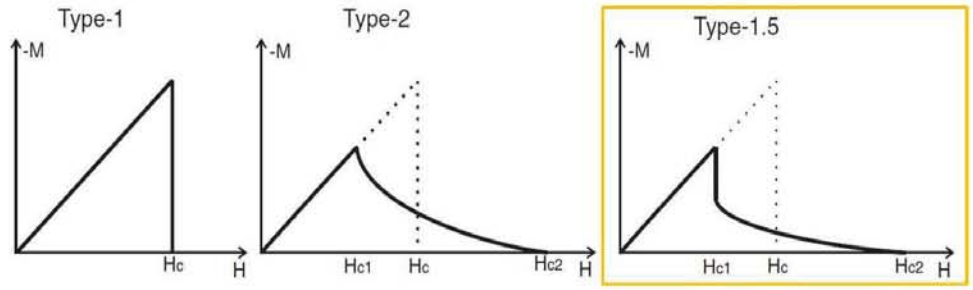

Fig. 2.5. Magnetic behaviour of type I, type II and type 1.5 superconductors [30].

2. Their critical temperature
   a) Low temperature superconductors (LTS): Although there is no common agreement in the use of this term, those superconductors with a transition temperature of less than 30 K are commonly considered low temperature superconductors.
   b) High temperature superconductors (HTS): Those superconductors with a transition temperature of above 30 K. It is also widely accepted to call those superconductors with a transition temperature above the boiling point of liquid nitrogen, 77 K HTS.
3. The theory that explains their behaviour
   a) Conventional superconductors: Their behaviour can be explained by the BCS theory (see section 2.1.1). Type I superconductors usually belong to this group.
   b) Exotic superconductors: Their behaviour cannot be explained by the BCS theory. Phenomenological theories are used to explain their behaviour, such as the Landau theory (see section 2.1.1) and the Beam model [31]. Most type II superconductors belong to this group.

2.1.3 The Meissner effect and superconducting magnetic levitation

The Meissner effect is the total expulsion of an applied magnetic field from a superconductor at the superconducting state (see Fig. 2.6). Therefore, a superconductor at the Meissner state can be considered as a perfectly diamagnetic material (χ=-1).

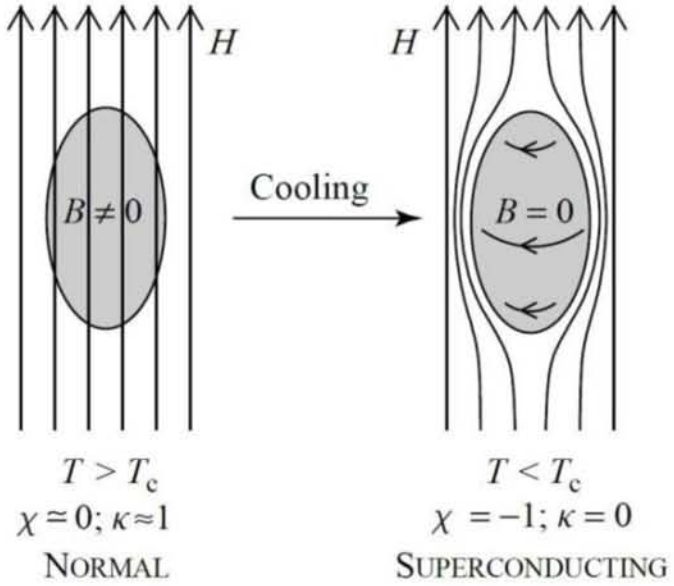

Fig. 2.6. Meissner state. The magnetic field is expelled from inside the superconductor.

The Meissner effect is commonly assumed to be responsible for the apparition of repulsive forces between a magnetic source (e.g., the magnetic flux generated by a permanent magnet) and a superconductor. For type II superconductors, the Meissner state can superpose to a quantum magnetisation of the superconductor in a state known as the mixed state. Superconductors at the mixed state are widely used for stable levitation systems, such as flywheels or superconducting magnetic bearings [27].

The applied magnetic field over which the Meissner state is no longer available in type II superconductors depends not only on the temperature of the superconductor but also on the magnetic field applied. The threshold value of the magnetic field applied is commonly known as the *first penetration field* or *first critical field* (H_p or H_{c1}). If the applied magnetic field is further increased over the so-called *superconducting critical field* or *second critical field* (H_{c2}), superconductivity is totally destroyed. Both, the first and the second critical fields are very temperature dependent, as shown in Fig. 2.7.

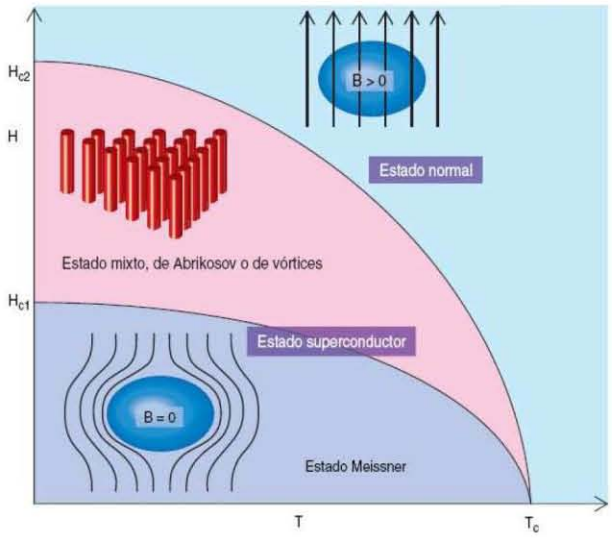

Fig. 2.7. Critical magnetic field vs. critical temperature in type II superconductors.

From the mechanical engineering point of view, a permanent magnet levitating over a superconductor at the Meissner state presents a very different behaviour to the same permanent magnet levitating over a superconductor at the mixed state, as it can be appreciated from Fig. 2.8.

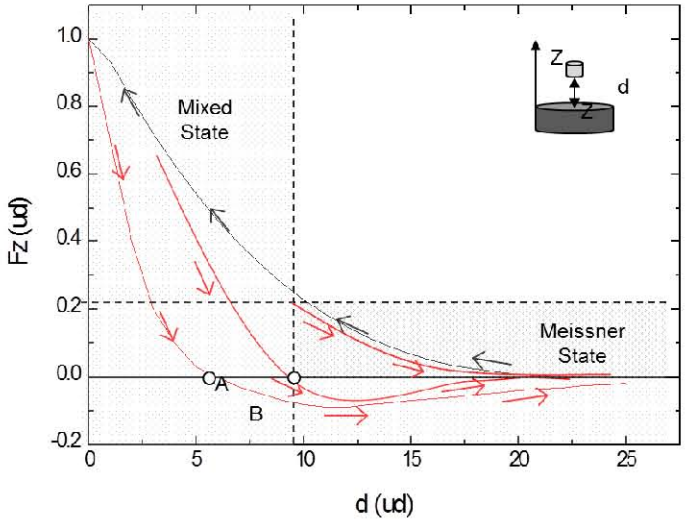

Fig. 2.8. Levitation force (ud) vs. levitation height for a FC at 0 (ud). Both the Meissner state and the mixed state are represented.

It can be seen in Fig. 2.8 that the superconductor in the Meissner state produces completely reversible cycles, whereas a hysteretic behaviour appears when it is at the mixed state. This is thought to be mainly due to the presence of defects in the crystalline structure and chemical impurities in the superconductor that prevent the free mobility of the vortex at the mixed state in the superconductor [32], [33].

In spite of this disadvantage, the mixed state presents several mechanical advantages with respect to the Meissner state. When a superconductor is cooled down in the presence of a magnetic field source (e.g., a permanent magnet) and the *first penetration field* (H_p) of the superconducting material is exceeded (Field Cooled or FC process), the permanent magnet will levitate stably over the superconductor, as was first observed in 1947 by V. Arkadiev [34].

After the cooling process, if the permanent magnet is moved from the initial FC position, drag forces will appear trying to restore the initial equilibrium position of the permanent magnet. This is true provided that the magnetic field seen by the superconductors changes due to the motion of the permanent magnet in any degree of freedom (DoF) [35]. In the case of a superconducting magnetic bearing, where there is an axial rotational symmetry of the magnetic field applied on the superconductor, no drag forces appear for motion in this symmetric DoF of the system (e.g., Z axis rotation in Fig. 2.9). Hence, the permanent magnet is able to spin around the symmetry axis with very little friction [36]. However, drag forces appear if there is a displacement in any other direction [37].

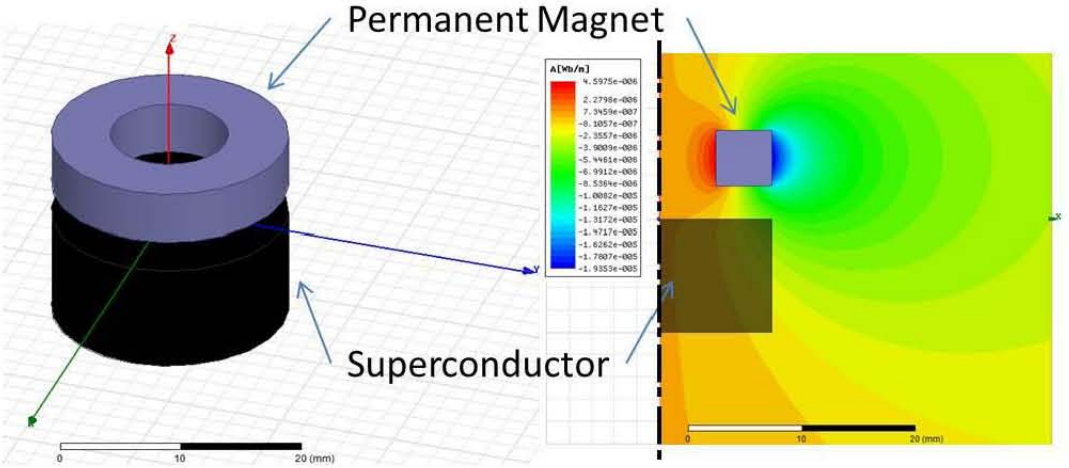

Fig. 2.9. Superconducting magnetic bearing 3D (left) and magnetic flux density in 2D axis-symmetric representation (right).

On the other hand, the magnitude of the levitation forces involved in the mixed state are considered to be significantly higher than those in the Meissner state [38].

2.2 Long range micro and nanopositioning: state-of-the-art

It is usually accepted that nanotechnology is the science of understanding matter and the control of matter at dimensions of 100 nm or less [1]. Otherwise, it is more accepted to talk about micrometre, and sub-micrometre positioning. The last two decades have witnessed the emergence and explosive growth of nanotechnology and nanoscience [1], [39]. The motivation for this has been the increasing demands of microelectronics, optics, biomedical and precision engineering [40]. Given this context, ultra precision positioning with sub-micrometre and nanometre accuracy in a range over a few millimetres has become an important part in the development of precision mechanisms and devices.

Ultra precision manufacturing and inspection systems in micro-automating semiconductor fabrication, copying machines, stepper stages for photolithography, small-scale measuring machines (CMMs) for large area scanning, surface imaging in scanning probe microscopy (SPM), nanopositioning and nanomeasuring machines (NPM-Machine), development of micro-assemblies and micro and nanoelectromechanical systems (MEMS and NEMS) and servo systems of hard-disk drives (HDD), are just a few examples of the wide range of applications where micrometre/nanometre positioning within a long range is required [1], [40–43].

Additionally, in some applications, cryogenic environments are a desirable or mandatory condition. These environments involve very low temperatures (below 120 K, the boiling temperature of Krypton) and typically high or very high vacuums. Under these conditions of very low temperature and high vacuum, conventional mechanisms that are usually based in gears and kinematic chains present severe tribological problems, such as backlash, cold spots, cold welding, fatigue or wearing. In addition, only solid lubrication is available at these temperatures with a reasonably good quality [3], [4], [44]. Consequently, technologies applicable under these conditions are limited to non-conventional mechanisms. The most representative technologies and mechanisms for very precise positioning and their performance and suitability for cryogenic applications will be discussed in the following sections.

As it has been mentioned in chapter I, a field of particular interest for the device presented in this thesis, where high-precision positioning is required in cryogenic environments, is infrared interferometer spectroscopy. This technique

is used in satellites for analysing the Earth's troposphere [45] and the composition of the planets of the solar system [46], [47]. In addition, this technique is used to analyse the formation and evolution of galaxies and stars [48–50]. The instrumentation for far infrared interferometer requires a mirror to be positioned with extreme precision along a large stroke [9]. It is noteworthy that the lower the temperature the infrared sensor operates at, the higher the sensitivity the device will have [8]. Thus, cryogenic conditions are a mandatory requirement for these kinds of devices. Moreover, very low energy consumption is also desirable in these short of devices, not only to reduce the power consumption of the mechanism itself, but also to reduce the heat generated.

Ultimately, it may be noticed that the European Space Agency (ESA) considered the development of long-range positioning devices with extreme accuracy and resolution as a hot research objective in the list of urgent actions of 2009 [9].

2.2.1 Devices based on piezoelectric materials

Piezoelectricity was discovered by brothers Jacques and Pierre Curie in 1880 [51] and is a linear interaction between mechanical and electrical systems in non-centric crystals or similar structures. A material is said to be piezoelectric if the application of an external mechanical stress gives rise to dielectric displacement in this material. Very related is the reciprocal effect whereby a piezoelectric crystal becomes strained (and therefore may suffer deformation) if an external electric field is applied (see Fig. 2.10). Most common piezoelectric materials are: quartz; lithium compounds, such as lithium niobite ($LiNbO_3$), lithium tantale ($LiTaO_3$) or lithium tetraborate ($Li_2B_4O_7$); polymeric materials, such as polyvynilidene fluoride (PVDF) and probably the most extended in piezoelectric actuators, piezoelectric ceramics (PZT) like lead zirconate titanate ($Pb[Zr_xTi_{1-x}]O_3$) [51], [52].

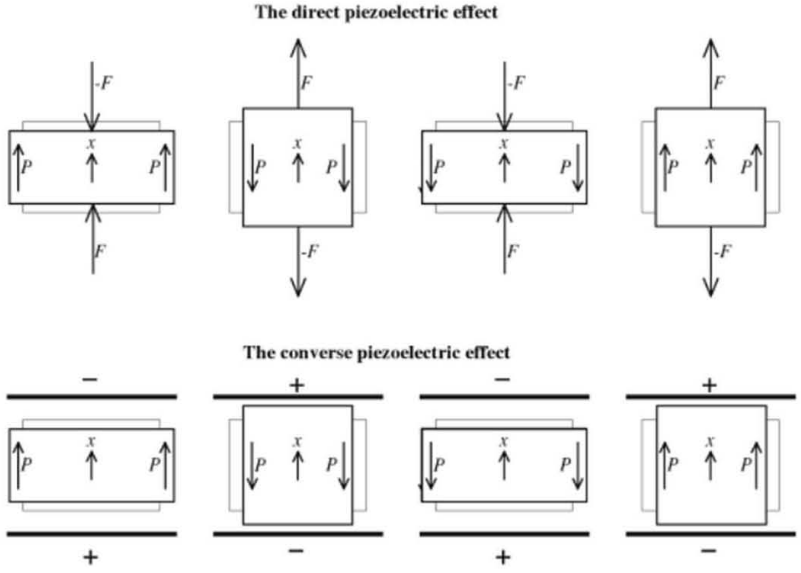

Fig. 2.10. Direct and reverse piezoelectric effect [51].

Piezoelectric actuators are widely used in applications at room temperature where precise positioning is required. They have good characteristics of performance in controlling precise motion, high-frequency response, high efficiency in conversion between electric and mechanical energy and relative small size. In addition, they can achieve outstanding accuracy between 1–10 nm within a short range [39], [53]. As a result, papers and patents related to precise-positioning piezoelectric actuators are numerous [54–56].

Nevertheless, piezoelectric actuators have several limitations for high-precision positioning within a long range. For example, they are sensitive to environmental changes, such as temperature [57] and sometimes they require voltages of the order of hundreds of volts for operation [58]. Furthermore, it is highly probable that one of their principal limitations is that they present hysteresis between the voltage applied to the actuator and the actuator output, nonlinearities and creep [59], [60]. Thus, it is impossible to derive a linear relationship between an input voltage and the actuator output [61]. However, the main disadvantage of piezoelectric actuators remains the very limited motion range, usually no longer than a few hundred micrometres [39], [62].

Despite these limitations, piezoelectric based actuators are now widely used in applications where highly accurate positioning is required within a short range at room temperature. However, relatively few companies are able to provide suitable cryogenic piezoelectric actuators with a stroke in the range of millimetres and a guarantee of a long lifetime, as is required by some industrial and space applications.

2.2.2 Devices based on piezoelectric materials for cryogenic environments

Stepping piezoelectric actuators (SPA) and amplified piezoelectric actuators (APA) (See Fig. 2.12), are used in positioning in aircraft, optical, space and defence applications that include, among others: multi-axis positioning stages, tip-tilt mechanisms, Z rotation devices, refocusing mechanisms or stepper actuators. However, they present some limitations regarding high-precision positioning within a long range in cryogenic conditions:

- The relationship between the input voltage and the induced mechanical strain (and going beyond the induced relative displacement) show a strong temperature dependence in piezoelectric materials and actuators [57], [63]. This dependence can be appreciated from Fig. 2.11. In some cases, the drop of the maximum displacement can be of the order of a 1000% for very low temperatures with regard to reference room-temperature displacement. Position resolution is temperature dependent too [64]. Single crystal piezoelectric actuators exhibit significantly higher performance at both, room and cryogenic temperatures. They can be used for applications requiring stroke < 100 µm at temperatures < 20 K to 300 K [65]. Although single crystal piezoelectric actuators show promise for high-precision positioning applications, the temperature dependence of the strain (i.e., of their stroke) is a very limiting factor that must be taken into account.

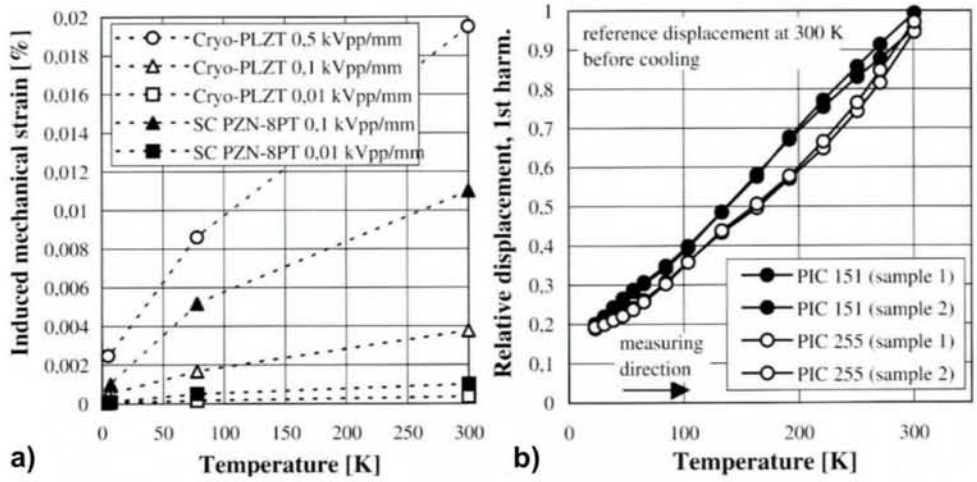

Fig. 2.11. a) Induced mechanical stress vs. temperature in 5 different piezoelectric materials. b) Relative induced displacement (1st Harmonic) vs. temperature for 4 different piezoelectric stacked actuators [63].

- As has been previously mentioned, they require high voltages for operation. This is a big limitation for some applications where low levels of power demands are required.

- Sensitivity of piezoelectric materials to humidity is still a limitation, which must be carefully considered in the lifetime of the application [7].

- Additionally, there are also mechanical issues to solve: multilayer piezoelectric actuators (MLA) can bear high compression forces but they are fragile components when submitted to tensile stress [7].

Fig. 2.12. View of different standard APAs [7].

Even though piezoelectric actuators present several limitations for cryogenic environments, they are (in some cases) a lightweight solution for precise positioning in the short range in cryogenic environments. Examples of applications can be found in the literature and most of them are carefully summarised in [7]:

- *Refocusing mechanisms* to overcome a possible deviation of the laser source in light detection and ranging (LIDAR) instruments, typically for Meteosat and Earth observation. These devices can measure the distance or other properties of a target by illuminating it with light, usually using pulses from a laser that must have a very accurate frequency. Then, the laser oscillator is dynamically refocused with a piezo-actuator with a bandwidth of 10 kHz and a lifetime of 10^{11} cycles. See Fig. 2.13.

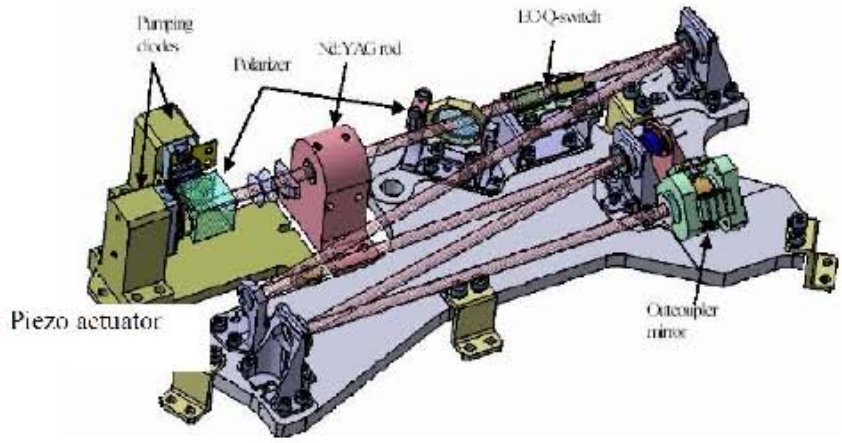

Fig. 2.13. Refocusing mechanism in LIDAR ALADIN on board of AEOLUS spacecraft [7].

- *Optical path difference actuators* (OPDA) used in laser modulation units of the Lisa-Pathfinder interferometer have been developed in order to move a triple prism. It presents a stroke of 60 µm. A maximum deviation of 10 µm for the entire life of the mechanism had to be provided. See Fig. 2.14.

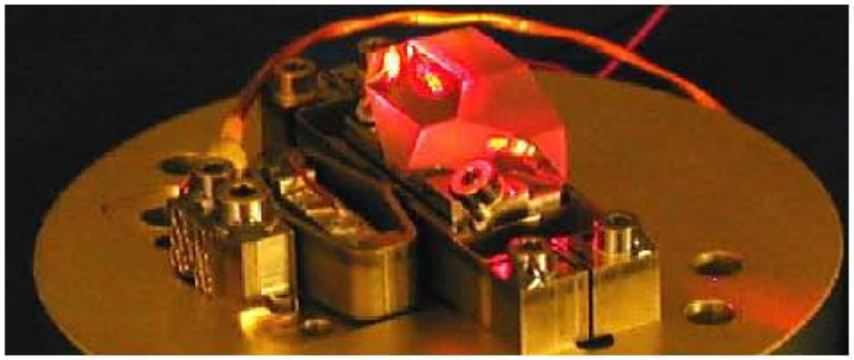

Fig. 2.14. OPDA with its triple prisma [7].

- *New piezo-motors* based on the combination of piezoelectric actuators and mechanical components were developed with some support from the French Space Agency CNES. They can offer long stroke (> 10 mm) and high miniaturisation low power requirements, a nanometre resolution and space compatibility. The long-stroke motion is achieved by step accumulation with an appropriate 0-150 V signal pattern. They operate by accumulation of small steps using inertial mode, impact forces and the stick-slip effect. See Fig. 2.15.

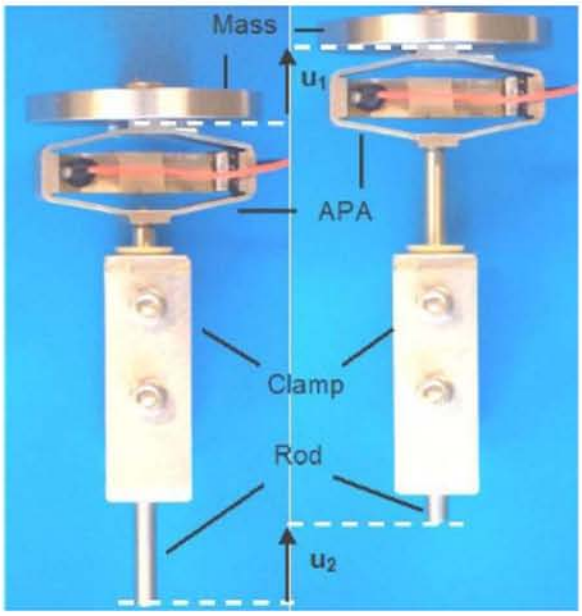

Fig. 2.15. SPA based on the APA60SM before (a) and after (b) motion [7].

In addition:

- In a work founded by NASA, Xiang et al. developed a piezoelectric stack actuator for cryogenic optics applications with a stroke of 35 µm at 77 K (65 µm). They also presented a flextensional actuator with a stroke of 258 µm at room temperature (~50% remaining stroke at 77 K). Nothing is said about the resolution of such devices [65].
- In 2008, Högele et al. proposed a very high-precision XYZ positioning stage for a fibre-based confocal microscope for cryogenic spectroscopy using piezoelectric actuators with a motion range of 7.5 mm, a resolution of 5 nm and suitability for temperatures of 4.2 K [66].
- Some goniometers for cryogenic environments have been developed too. They can typically reach a stroke of around ± 2 mrad with 1% accuracy in a closed loop [67].

2.2.3 Dual stage piezoelectric positioning systems

A special case of piezoelectric actuators are hybrid or dual-stage positioning systems based on piezoelectric actuators. In some applications, they can reach a long stroke with impressive accuracy in a closed loop. Such hybrid devices combine one motion actuator for a coarse step motion and friction piezoelectric actuators to achieve a high level of precision of between three and a few tens of nanometres [68].

In 1998, Awadby et al. used an AC servo motor and a ball screw mechanism to reach a motion range of 300 µm and a position accuracy of ±0.5 µm. A voice coil motor was employed to monitor the nanometre control accuracy. Finally, they solved the issue of how to integrate both stages accurately and obtain the absolute position signal [45].

Two years later, Chen and Dwang presented a dual-stage position mechanism for obtaining single-axis long-range motion control. It had two actuators: one for manipulating the coarse long travel and the other for the final precision monitoring [44].

In 2005, Liu et al. reported a device with a motion range of 450 µm and a position accuracy of 10 nm in a combination of a piezoelectric actuator and a voice coil motor [39]. A diagram of the device is shown in Fig. 2.16.

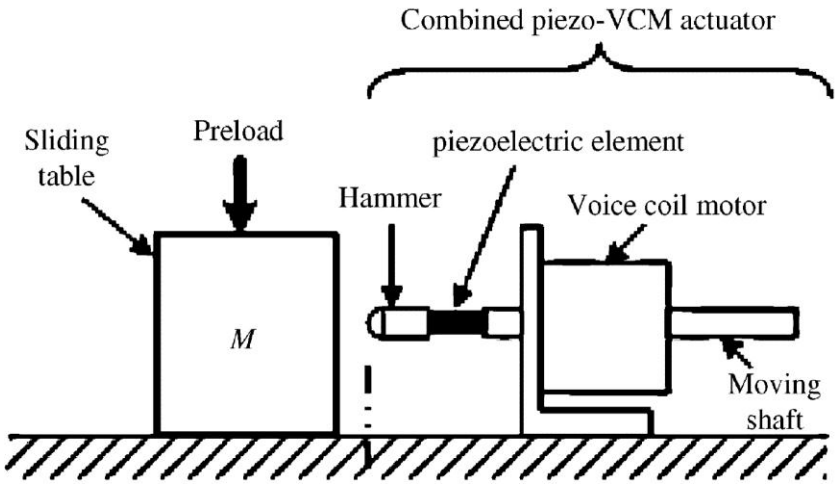

Fig. 2.16. Hybrid positioning device using voice-coil motor and piezoelectric actuator in [39].

Small-scale measuring machines (CMMs) for large area scanning probe microscopy for use on mesoscale objects with nanometre uncertainty is an example of a field where hybrid piezoelectric actuators succeed. Furthermore, there is an increasing demand by microelectronics, optics and precision engineering industries for sensing surfaces or detecting structures. Thus, nanopositioning and nanomeasuring machines (NPM-Machines) are required to fit the requirements of very high-precision measurements in a long range. An example of this sort of machine was developed in the *Technise Universität Imenaul* using a combination of voice coil and piezoelectric actuators. The measuring range of this machine is 25×25×5 mm^3 with nanometre resolution and uncertainty [40].

However, hybrid systems present positioning problems, such as track seek and track follow [1] and although their performance in long-range precise positioning is higher than that of plain piezoelectric actuators, the piezoelectric solution itself is typically three to five times lighter than voice coil solutions for comparable-performance mechanisms [7].

Currently, the friction type piezoelectric stage can be integrated with a linear motor system to achieve a resolution in the nanometre range and a motion stroke over 10 mm. They are available for use in industrial applications too. The most recent advances in cryogenic piezoelectric devices can be followed in companies like *Attocube systems* [69] and *Physic Instrumente* [70], which are owners of US Patent 2010,259,760(A1), US patent 2008,148,589, US Patent 5,424,597, DE Patent 20,2005,020,928 and DE 10 2006 034 162 A1 among others. *Attocube* systems can provide piezoelectric actuators with a motion range over 10 mm and a sub-micrometre/nanometre resolution suitable for cryogenic environments. No published tests on the fatigue and lifetime of these devices were found.

Ultimately, a great summary of hybrid systems that combine piezoelectric materials and friction-inertial actuators is reported in a paper published in 2011 by Zhang et al., which also includes a wide discussion of the present situation and future of these devices [71].

2.2.4 Devices based on giant magnetostrictive materials (GMM)

Magnetostriction was discovered in 1841 by James Joule [72] and his work was published a year later. Magnetostriction is a property of ferromagnetic materials that causes them to change their shape during the process of magnetisation. This effect has been used by many researchers to build high-precision positioners. A very descriptive explanation of this effect is shown in Fig. 2.17, in which the magnetostriction (i.e., the deformation in ppm), is represented as a function of the applied magnetic field (H) in a sample made of *Terfenol-D*. Both, experimental and predicted results are shown.

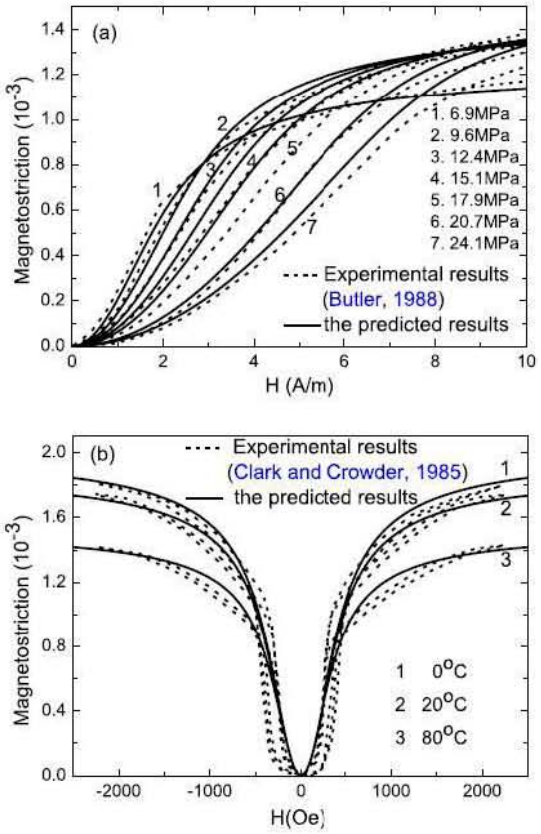

Fig. 2.17. Comparison of the prediction and the experimetal results of the magnetostriction curves for a Terfenol-*D* sample under different: a) pre-stress and b) ambient temperature conditions [73].

In 1992, Wang and Buch-Vishniac reported a position repeatability of 50 nm in an XY stage capable of addressing a 100×100 μm workspace in an open-loop using magnetostrictive actuators. However, the supply current needed around the coils of 800 turns each was of the order of 1.5 A [74].

In 1997, Tsodikov and Rakhovskii published a review on magnetostriction power actuators for super-precision positioning [75], [76]. According to this paper, there are three such instruments: magnetostriction power positioners (MSP), magnetostriction nanoscrews (MN) and magnetostriction actuator-vibrators. The main performance of these devices at that time was reported and is shown in Table 2.1.

Table 2.1. Main technical characteristics of hybrid devices combining PZT motors and magnetostrictive materials reported in magnetostriction power positioners (MSP) and magnetostriction nanoscrew positioners (MN).

Parameter	MSP actuator	MN actuator
Linear stroke coarse (PZT) [mm]	30	30
Linear stroke fine (Magn.) [µm]	15	9.2
Resolution coarse [nm]	5	5
Resolution fine [nm]	0.01	0.01-0.02
Maximum velocity coarse [mm/s]	1	1
Maximum velocity fine [µm/s]	1	1.3
Power consumption [W]	5	5
Mass [kg]	2	
Overall dimensions [mm^3]	120x90x38	

Similar results have been obtained in later works. In 2006, Yang et al. presented a long-stroke positioning device with nanometre resolution over a range of some millimetres, composed of an inchworm controlled by software for coarse positioning and a magnetostrictive actuator made of *Terfelon-D*. The prototype can move with a velocity of up to 97.2 µm/s for a 7 A, 10 Hz current signal with a 15 µm step. Eventually, they demonstrated a fine step resolution of the order of 4 nm (noise ratio around 5 nm) with a current resolution of 0.01 A [77]. In 2007, Ueno and Higuchi, working at the Precision Machinery Engineering Department at The University of Tokyo, published a hybrid contactless positioning device based on a combination of piezoelectric and magnetostrictive materials. They achieved a motion resolution of 1 µm for a few millimetres range using integral control. It is noticeable that they were able to maintain the levitation gap with almost zero-power consumption [78].

2.2.5 Devices based on giant magnetostrictive materials (GMM) for cryogenic environments

The magnetostriction properties of some materials, as for example $Tb_{0.6}Dy_{0.4}Zn_{0.1}$, are increased when working at low temperatures [79], as can be observed in Fig. 2.17. Based on this effect, the use of magnetostrictive actuators for precise positioners in cryogenic applications has already been proposed [6].

In 2000, Voccio working for the American Superconductor Corporation, presented a prototype of cryogenic magnetostrictive actuator designed to operate at temperatures ranging from 20 to 80 K. In this paper, it is clearly explained that there is a strong dependence of the stroke and resolution of the magnetostrictive actuators with regard to the working temperature. They reported a short stroke around a few tens of µm. The excitation system was composed of an HTS coil with 320 A/turn. Maximum currents of 20 A were reached during tests [80]. This high requirement of current makes this sort of mechanism only available using superconducting coils with very low power dissipation. In addition, the required current is a disadvantage for some space applications where the power generation possibilities are very limited. Furthermore, the dependence of the displacement and the applied magnetic field is far from linear, which makes position control more complex.

In the same year, Horner et al. mentioned again the potential of these devices for cryogenic applications and especially for their use in optical applications in the Next Generation Space Telescope (NGST). A new mechanism for precise positioning was proposed, once again using HTS for the excitation system and low temperature magnetostrictive materials. They claimed a resolution of 20 nm in the displacement of the device but no tests or results have been presented [81], [82]. A cross-section diagram of the actuator is show in Fig. 2.18.

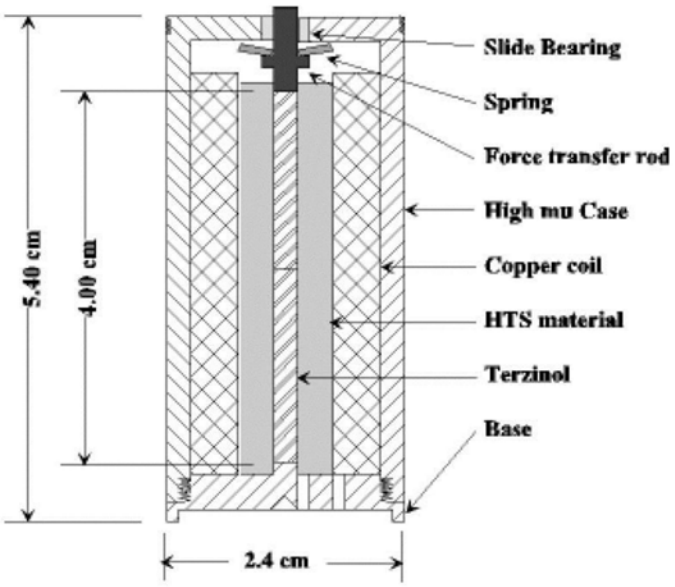

Fig. 2.18. Cross-section diagram of the magnetostrictive acuator in [81], [82].

In summary, actuators based on magnetostrictive materials present some characteristics that make them less than suitable for long-range precise positioning (especially in cryogenic environments). For example, they require high power requirements (sometimes over 10 A), the magnetostriction is very temperature dependent and moreover, the deformation of the magnetostrictive materials is not linear dependent on the applied magnetic field, which makes position control more complex. Finally, magnetostrictive-based actuators themselves are usually only able to reach short strokes. Dual-stage precise positioners, based on magnetostriction materials for the fine step positioning, can reach long strokes with nanometre resolution but they present the same problems and additionally, the disadvantages that may be associated with the coarse step positioner.

2.2.6 Devices based on active magnetic levitation (Maglev)

Magnetic levitation (Maglev) is a very good available solution for long-range nanopositioners, either for room temperature or cryogenic environments. These kinds of devices, being contactless, eliminate the strain, backlash and hysteresis that limit the precision of position control, while also minimising durability and fatigue problems. In comparison with the piezoelectric and magnetostrictive positioners, active magnetic levitation systems can offer the same accuracy for a longer motion range and good performance at very low temperatures. Additionally, they can be used to build multiple DoF nanopositioners.

Many researchers have focused their efforts in developing such devices. In 1998, Kim and Trumper developed and demonstrated a high-precision planar maglev stage with 50 mm planar motion capability, which had a 10 nm resolution and 100 Hz control bandwidth [42]. In 2000, a maglev scanning stage with a 0.6 nm three-sigma horizontal position noise was built and demonstrated [83].

More recently, active maglev stages with greater travel ranges and the same resolution can be found [84]. For example, there are various 6 degrees of freedom active maglev systems that have been improved by Kim et al. between 2004 and 2007, with a travel range of 5 mm in each direction and 3 nm resolution with an accuracy of a few nanometres and a travel range of some millimetres in each DoF [85], [86]. Also a 2×2×2 mm 6-DoF system was developed by Zhang and Menq in 2007 with a 1 nm RMS position resolution for each DoF [87].

In 2009, Van den Dool et. al., working for the Netherlands Organisation for Applied Scientific Research, developed a cryogenic Optical Delay Line (ODL) for use in space interferometry missions, such as ESA's Darwin and NASA's TPF-I. The prototype is shown in Fig. 2.19. They reported a 27 mm stroke (10 mm mechanical) with a resolution of 0.1 nm and an accuracy of 0.5 nm. The total power dissipation of this mechanism was measured to be 20 mW at 40 K. The tilt of the rotor was also measured and was of the order of 40 µrad that could be improved by magnetic compensation to 0.5 µrad [88].

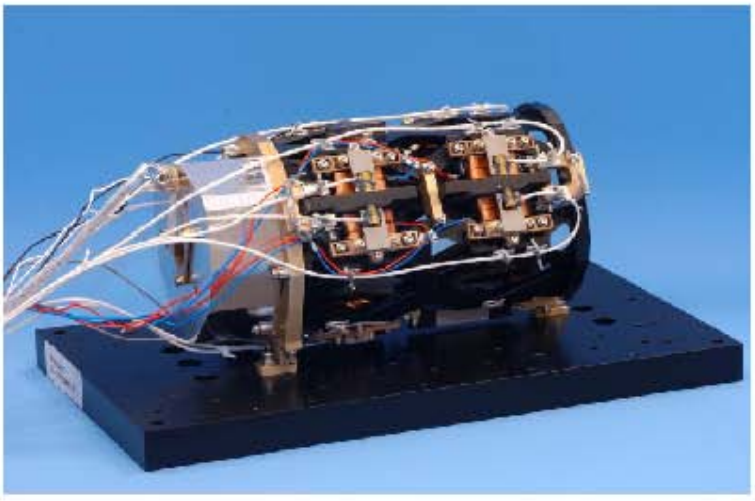

Fig. 2.19. ODL prototype developed by TNO [88].

Both, the requirements of the ODL mechanism and the measured performance of the device by TNO are summarised in Table 2.2. This table also

shows the requirements for the SPICA Far Infrared Instrument, an imaging Fourier transform spectrometer [8].

Table 2.2. Summary of *FTS* requirements for SPICA mission, Optica Dealy Line (ODL) requirements for Darwin and measured performance of ODL prototype [88].

Parameter	ODL requirement	ODL measured
Linear stroke [mm]	>20	20.2
Mirror location accuracy [nm]	<0.5	<0.5(RMS)
Mirror location resolution [nm]		<0.1
Mirror velocity [µm/s]	>250	0-10000
Minimum step [nm]	<0.5	<0.1
Minimum angular run outs [µrad]		<25
Minimum lateral run out [µm]	<50	<1
Lifetime in flight [cycles]		
Operational temperature [K]	40	tested at 25 K
Mass [kg]	<10	<1.7
Dimensions [mm^3]	<100x100x300	<114x116x216

Despite their impressive performance, the main disadvantage of these active magnetic levitation devices is that great effort is required to control them because they are naturally unstable, as was first proposed by *Earnshaw's theorem* [27]. This requires a complex control method and consequently, complex electronics [89]. In addition, greater electrical consumption, even up to a few Watts [89] in a cryogenic environment, causes extra heat and therefore, additional cooling power might be needed.

2.2.7 Devices based on superconducting magnetic levitation (SML)

Neither devices based on piezoelectric or magnetostrictive materials (due mainly to their short motion travels, high power requirements), nor active magnetic levitation devices (due to the complexity of the control systems

required and great energy consumption) seem to be able to fully satisfy the requirements of long-range micro and nanopositioners for cryogenic-environment applications, as needed, for example, in far infrared interferometers on satellites.

In 1939, Braunbek extended Earnshaw's theorem and demonstrated that electromagnetic suspension is possible if materials with relative magnetic permeability $\mu_r < 1$ (as superconducting materials) are introduced [90]. The idea of using superconducting levitation for contactless devices has been widely explored. For example, superconducting linear bearings have been proposed by many researchers. These bearings take advantage of the translational symmetry of a magnetic field in the motion of a superconductor over a railway typically made of permanent magnets and ferromagnetic materials [91], [92]. However, this system is focused on Maglev transportation [93] and therefore, no studies for high-precision positioning in cryogenic or clean environments have been found.

Nevertheless, it is well know that superconductors at the mixed state provide inherent stability [34]. This fact could greatly simplify the control strategy and the power dissipation of the mechanism, as they require very low temperatures to operate and thus, are very suitable for cryogenic environments. In addition the lack of contact solves the disadvantages of contact and lubrication in cryogenic environments.

Despite the obvious advantages that this technology could represent for very precise positioning, only some kinds of conveyors based on superconducting magnetic levitation micro and nanopositioning have been found in the literature. Nevertheless, these devices show reasonable results.

A micro conveyor for X-Y-θ positioning was presented in 1994 by Iizuka et al. They reported a 100 µm stroke for a linear positioner (motion in only one DoF). They reached a speed of 9 mm/s for a driving current of 620 mA working at 77 K. Power consumption over 6 W could be expected. Nothing is specified about the resolution of such a device but based on the results reported, a resolution no better than 10 µm for a two-dimensional motion could be expected [94].

In 1997, Iizuka and Fujita published a dual-stage conveyor with a 2.8 mm stroke and an accuracy of 40 µm in a closed loop [95]. They also reported a "*quick conveyance*" of 280 µm/s. A year later, they published a device with a similar accuracy but with a maximum conveyance speed of 104 $\pm$ 16 mm/s [96]. The setup of the slider and the principle of actuation are shown in Fig. 2.20.

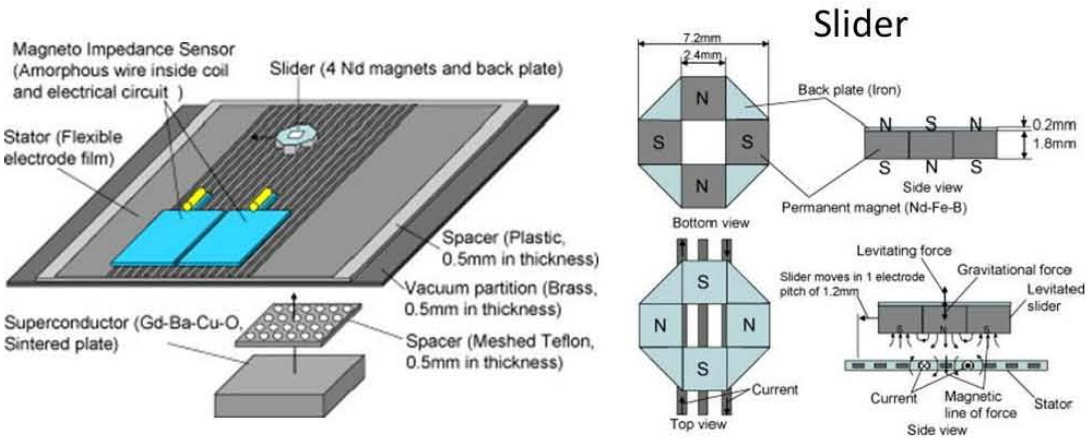

Fig. 2.20. Set up and principle of actuaction of the conveyor in [95].

In 2007, another approach to precise positioning using superconducting magnetic levitation was presented by Lin et al. They modified the height of levitation of a permanent magnet over a field-cooled superconductor bulk by changing the operating current in a properly located Helmholtz coil. Maximum precision obtained by the authors was in the range of μm and the total stroke reached in this experiment was around 140 μm [97].

It was in the same year when Mori, Inoue and Komori published a prototype of superconducting conveyor for use in clean-room applications, as required, for example, in the semiconductor manufacturing industry [98]. Magnetic levitation is especially interesting for these applications because of the lack of contact between parts. This makes it possible to place the stator outside the clean-room and the moving part inside it, as shown in Fig. 2.21. Notice that in this prototype, the motion control was carried out by a conventional positioning stage. In the end, nothing is said regarding the precision of the device but it is clear that superconducting magnetic levitation can be useful not only for cryogenic-environment applications but also for other applications where high-precision positioning is required at a different range of temperatures. The only elements of the system that must be at a very low temperature are the superconductors. Furthermore, high temperature superconductors, such as YBCO, can be cooled using liquid nitrogen, which is not a very expensive coolant.

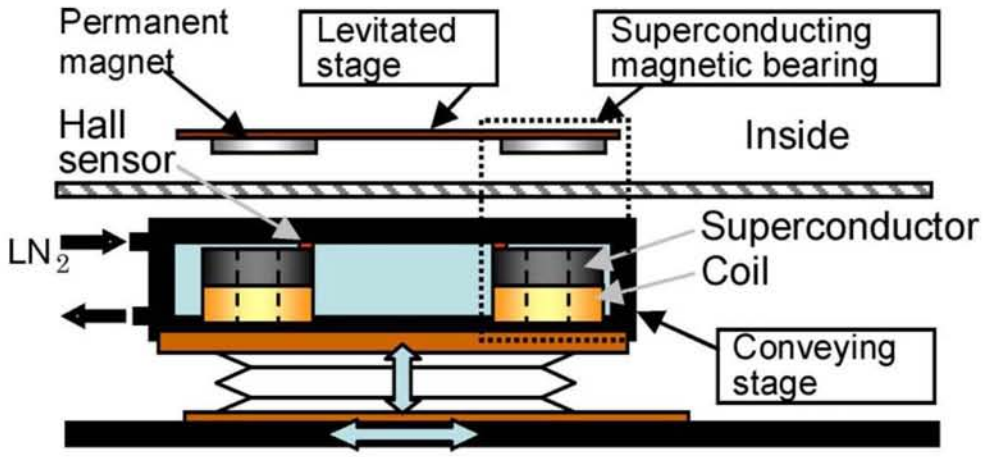

Fig. 2.21. Schematic ilustration of the conveyor in [98].

Some other patent claims have been made in recent decades using a combination of permanent magnets and/or coils and superconducting parts [99–101]. However, the performance of all superconducting devices found in the literature is far inferior to that of active maglev systems and piezoelectric or hybrid devices.

2.2.8 Devices based on other technologies

Even though magnetic levitation (Maglev), piezoelectric actuators (PZT actuators), giant magnetostrictive actuators (GMM actuators) and superconducting magnetic levitation (SML) are the main technologies available for micro and nanopositioning, other scientists have focused their research on new positioning techniques.

Some researchers have focused on magnetic levitation using diamagnetic materials instead of superconducting materials. This idea was explored by Moser and Bleuler in 2002, to build a contactless rotatory motor for precise positioning [102]. Since 2007, a Japanese team from Fukushima National College of Technology, have developed and improved a contact-free micrometre resolution motion XY stage using diamagnetic graphite and Halbach arrays of permanent magnets [103]. However, no deep studies on the motion range and accuracy of such devices have been found. Despite diamagnetic materials not requiring cryogenic environments, the magnitude of the magnetic interaction is various orders of magnitude lower than in superconductors and therefore, the load capacity of these devices can be expected to be lower.

Another interesting approach is based on the use of acoustic levitation. Ultrasound waves can be effectively used to control the positions of various

samples in an atmosphere of inactive gases [104]. Using this technology, a mass of over 10 kg can be suspended. Speeds in the order of 0.5 m/s and positioning resolutions around hundreds of µm can be achieved. In 2000, Ueha et al. presented a 690 mm conveyor using near-field acoustic levitation. However, no intention of precise control of the motion is presented in this paper. In 2007, Ide et al. presented a linear bearing and actuator via ultrasonic levitation but once again, no positioning considerations were presented [105]. Some disadvantages that may be present for these kinds of devices are the high power dissipation, the high vibration induced in the levitating object and the requirement of a gas interface between the stator and the moving object.

Chapter III

Theoretical foundations

The theoretical principles and considerations for the design of a non-contact linear slider based on superconducting magnetic levitation for high-precision positioning in a long stroke are presented in this chapter. The special properties of the magnetic interaction between a type II superconductor in the mixed state (stator) and a long permanent magnet (slider) in this invention provide a sliding kinematic pair. Moreover, the system is stable and presents an equilibrium position of the slider. Finally, this initial equilibrium position can be modified (without contact) by controlling the current circulating through a couple of coils.

3.1 Introduction

The proposed *FTS* mechanism will require a one DoF sliding kinematic pair. Therefore, high stiffness to any other motion or rotation of the slider is required, so that low run outs are present. Run outs of the order of a few microns are usually required for those applications for which this mechanism is intended. Additionally, the mechanism must be able to work in extremely low temperatures and in very high vacuum conditions. Low power consumption is also desirable in order to reduce the power requirement of the cryocooler (see chapter I).

Lubrication options are very limited at cryogenic temperatures. In order to avoid all the tribological problems arising in this sort of environment, the best option is to find a non-contact actuation system for positioning the slider. Therefore, as there is no contact, no lubrication would be necessary. The lack of contact between those parts of the mechanism with relative motion would also improve the lifetime of the mechanism; a key factor for space missions.

As was introduced in chapter II, magnetic active levitation systems achieve non-contact guiding and positioning using a set of controlled closed-loop active coils. Superconducting magnetic levitation, due to its inherent stability could provide a natural guiding system that reduces the issue of control to simply the positioning of the slider.

3.2 Advantages of using superconducting magnetic levitation

The main advantages in the use of superconducting magnetic levitation for the *FTS* mechanism are the following:

1. Inherent stable levitation can be achieved if a type II superconductor in the mixed state is used. This would considerably simplify the control of the position of the levitating part and reduce the power consumption.
2. The symmetry of the magnetic field provides a naturally self-guiding system. Most likely, the best example of this is superconducting magnetic bearings [35]. As has already been explained in chapter II, these mechanical devices take advantage of the revolution symmetry of a magnetic field generated by a permanent magnet to spin. However, high drag forces appear when the permanent magnet is

moved away from the FC position. These forces try to restore the initial equilibrium position, as shown in Fig. 3.1.

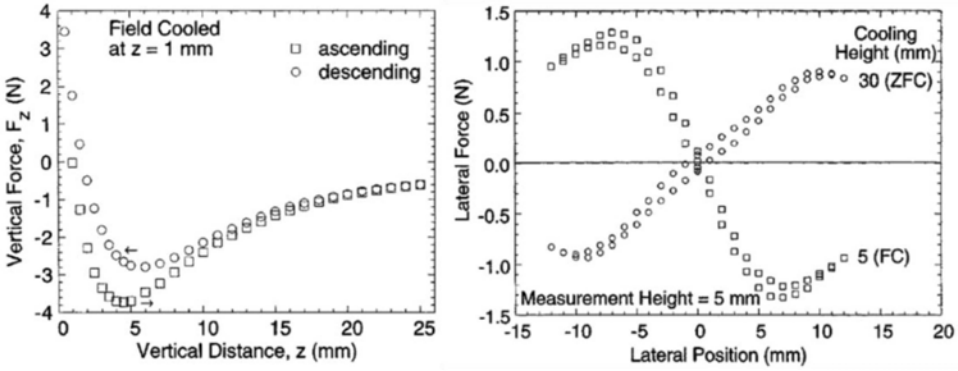

Fig. 3.1. Vertical force for FC at z = 1 mm and lateral force at a levitation height of 5 mm [35].

3. Very low temperatures are required for type II superconductors to operate; therefore, cryogenic environments are very suitable. Moreover, the lower the temperature is, the better the superconducting properties become.
4. Lack of contact provided by superconducting magnetic levitation is a perfect solution for all tribological problems in cryogenic environments, reducing wear and fatigue and improving the lifetime of the mechanism.

3.3 Invention basis

3.3.1 Brief description of the *FTS* mechanism

The basic idea of the *FTS* mechanism proposed here is the following:

1. A stator comprising a set of high temperature superconducting parts (HTS) (1).
2. A slider with a long bar permanent magnet (PM) (2), magnetised parallel to the Z axis in Fig. 3.2. Magnetic interaction between the slider and the stator form a sliding kinematic pair due to the translational symmetry of the magnetic field applied on the superconductors.

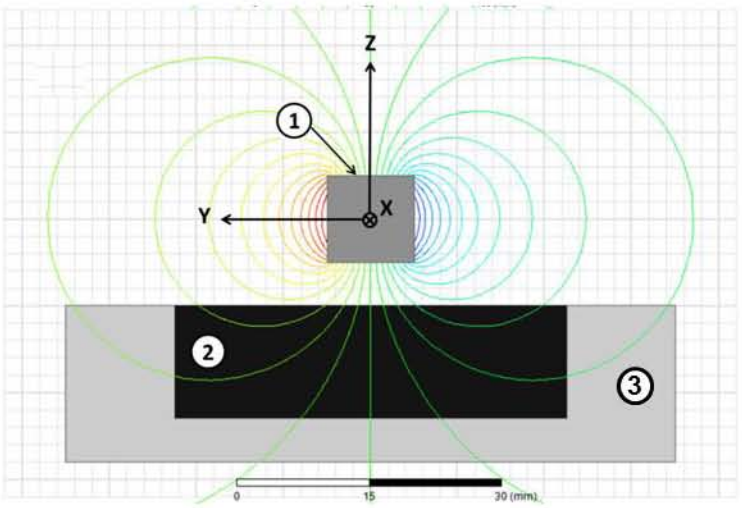

Fig. 3.2. Magnetic flux lines distribution represented in the YZ plane of the *FTS1* prototype. 1) Permanent magnet; 2) superconducting disks; 3) superconductors base. $IFC = 5$ mm.

3. In order to move the slider along its path, two coils (3) are placed at both ends of the stroke. The direction of the magnetic field generated by these coils is also parallel to the Z axis. Further details on the design of the *FTS1* mechanism will be given in the following chapters of this thesis.

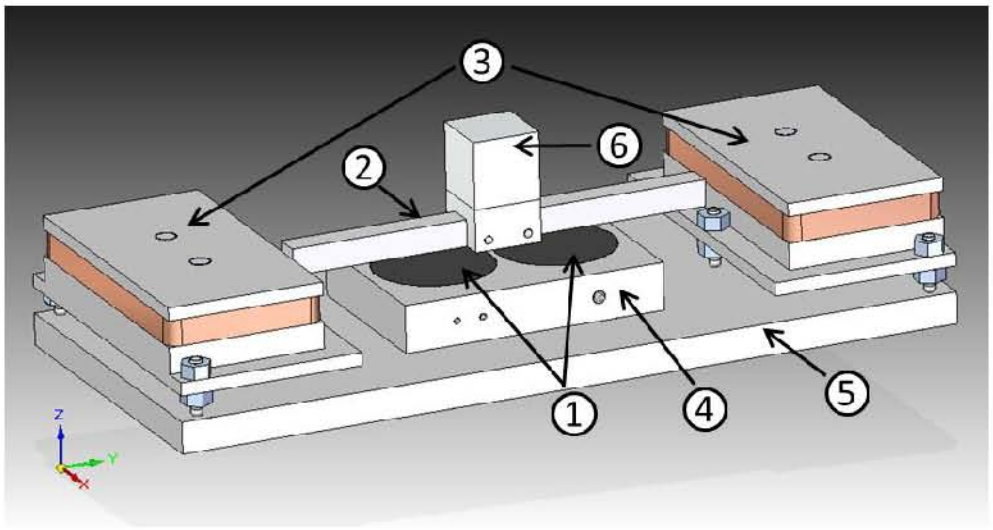

Fig. 3.3. CAD of the first developed *FTS* mechanism prototype (*FTS1*).1) Superconducting disks; 2) long permanent magnet; 3) coils; 4) superconductor's base; 5) base plate and 6) optic mirror cube.

3.3.2 Working principle

This section describes the interaction between the PM and the superconductors. First, the field cooling position (FC position from now on) must be defined. It is the position of the PM when the superconductors are cooled down. In the case of the *FTS* mechanism, a very convenient FC position seems to be the point at which the centre of mass of the PM is located at the intersection of the imaginary line that passes through the centres of both coils and the YZ symmetry plane of the stator. In addition, the axis of the PM must be aligned with the imaginary line that passes through both centres of the coils, as shown in Fig. 3.4.

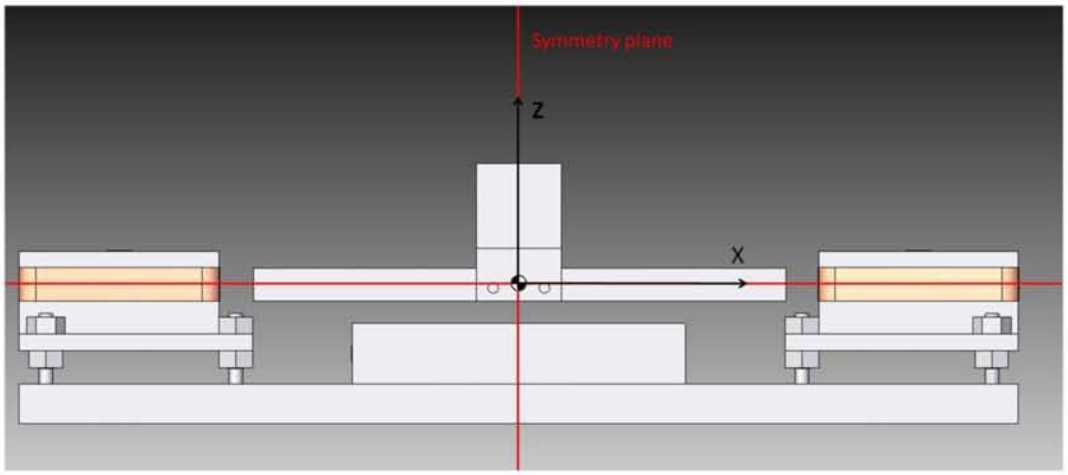

Fig. 3.4. Reference system in the *FTS* mechanism.

The PM must be initially held in the FC position. Once the superconductors are cooled below their critical temperature, the PM and the HTS form a contactless sliding kinematic pair that allows the PM to move in the X direction in Fig. 3.4 with very low resistance [106], [107]. In other words, a sort of "magnetic guideway" is established on the superconductors when they are at a temperature below their critical temperature. An interpretation of this "magnetic guideway" can be derived from Fig. 3.5, where the magnetic flux density on the superconductors at the normal state for different X positions of the PM in its path is plotted.

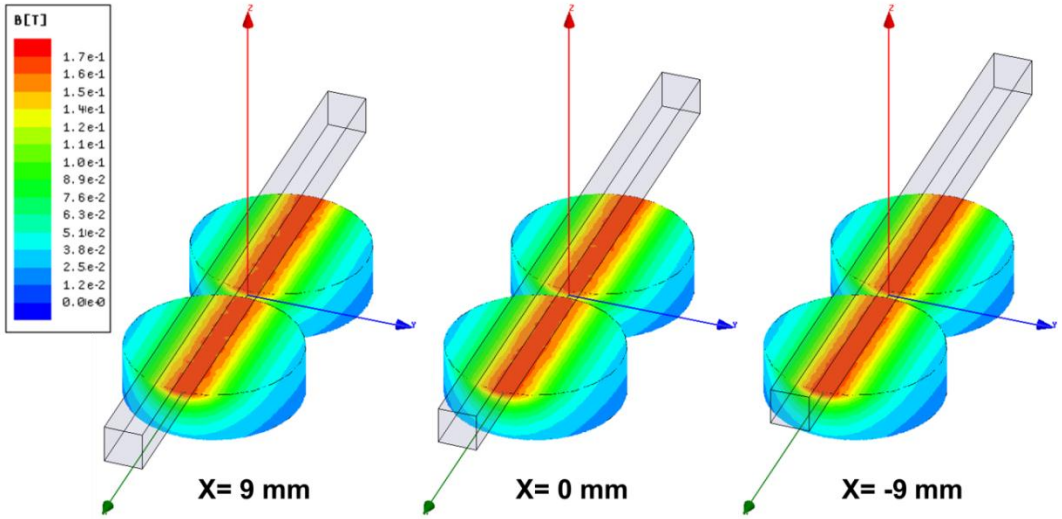

Fig. 3.5. Module of the applied magnetic flux density B in the superconductors for three different positions of the permanent magnet in its path along the X direction for a height of levitation of 3 mm.

The generation of the sliding kinematic pair is only possible if the changes in the magnetic field seen by the superconductors are small for the motion of the permanent magnet. In order to make a qualitative approach to the problem, it can be considered that drag forces exerted on a superconductor can be calculated by the integral over its volume, as shown in eq. 3.1 [108]. Of course, the force acting on the magnet has the same magnitude but is oppositely directed.

$$F_{SC} = \int_{SC} \nabla \cdot (\mathrm{M} \cdot B)\, dV$$

eq. 3.1

where,

$M = \{Mx, My, Mz\}$ is the magnetisation of the superconductor,

$B = \{Bx, By, Bz\}$ is the magnetic flux density,

and V stands for volume of the superconductor.

The magnetisation of the superconductor M is dependent on the history of the magnetic field applied. Therefore, the magnetisation is expected to be heterogeneous inside the superconductor depending on the magnetic field distribution in the superconductor [109].

According to Fig. 3.4 and considering the X direction as the sliding direction of the mechanism, eq. 3.1 now reads:

$$F_{SC\,X} = \int_{SC} \mathrm{M_x} \cdot \left(\frac{\partial B_x}{\partial X} + \frac{\partial B_x}{\partial Y} + \frac{\partial B_x}{\partial Z}\right) + \mathrm{B_x} \cdot \left(\frac{\partial M_x}{\partial X} + \frac{\partial M_x}{\partial Y} + \frac{\partial M_x}{\partial Z}\right) dV$$

eq. 3.2

Even though the magnetisation direction of the PM is mainly in the Z-axis of the reference system, the boundary effects at the ends of the PM have a relevant role. Due to these boundary effects, the X and Y components of the magnetic induction on the superconductors increases when either end of the PM approaches the superconductors. Due to the symmetry of the mechanism in the XZ-plane, for any X position of the mechanism it can be stated:

$$F_{SC\,X} = \int_{SC} M_x \cdot \left(\frac{\partial B_x}{\partial X} + \frac{\partial B_x}{\partial Z}\right) + B_x \cdot \left(\frac{\partial M_x}{\partial X} + \frac{\partial M_x}{\partial Z}\right) dV$$

eq. 3.3

The magnitude of the magnetic induction B_X is represented in Fig. 3.6 for different X positions of the slider in its path. Notice that for the centred FC position, magnetic field gradients are symmetric and therefore, forces are compensated. Due to the high translational symmetry of the magnetic field applied on the superconductors for any X position of the slider in its path, the magnetisation of the superconducting bulk and the X component of the magnetic field applied is not expected to change significantly.

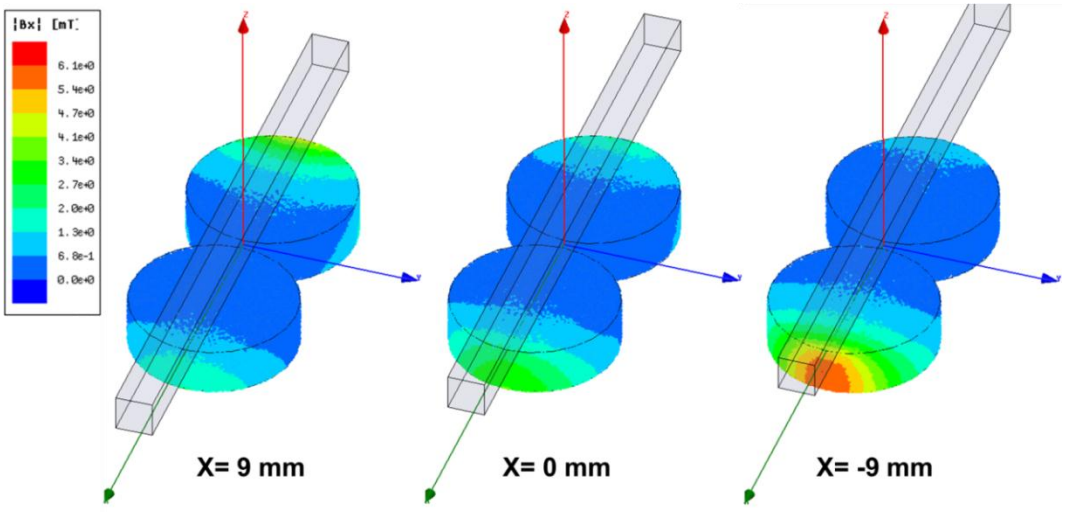

Fig. 3.6. Absolute value of the magnetic flux density BX applied on the superconductors for different X positions of the PM. Height of levitation was 3 mm and the distance between the centres of the superconductors was 47 mm in the X direction.

Thus, the slider would find low resistance to its motion in the X direction, provided that magnetisation changes and magnetic flux gradient variations in the superconductors are small. Even though these magnetic variations due to the motion of the PM are small, they are relevant enough to generate drag forces, which try to restore the initial symmetry of the magnetic field in the superconductors. In summary, it can be said that the FC position is an equilibrium point of the slider. In contrast, the gradient of the magnetic field is considerably higher in the Y and Z direction of the mechanism than it is in the direction of the motion of the slider. Hence, if the permanent magnet is moved in any other direction but the sliding DoF, high magnetic gradients are present and stronger drag forces arise, according to eq. 3.1, guaranteeing good stability of the permanent magnet in its path.

In this invention [110], drag forces that try to re-establish the initial equilibrium position are overcome by magnetic forces exerted on the permanent magnet by two coils placed at either end of the stroke. This makes it possible to modify the equilibrium position of the PM and hence, control the position of the slider just by modifying the current circulating in the electromagnets. The design of these coils will be discussed in depth later.

In summary, it can be said that a contactless sliding kinematic pair is established between the permanent magnet and the superconductors at the mixed state. Lastly, by means of magnetic forces generated by a couple of coils, the permanent magnet can be positioned along the sliding DoF with very low resistance.

3.3.3 The superconductors

One of the fundamental requirements of the *FTS* mechanism is the use of type II superconductors at the mixed state. Thus, a permanent magnet would be able to stably levitate over the superconductors. For the superconducting part, YBaCuO disks were selected. The transition temperature of this material is 93 K and presents a relatively high critical current that provides strong levitation forces and magnetic stiffness [111]. Melt-textured YBCO disks of the required dimensions are found easily in the market.

The basic condition for the superconductors to be at the mixed state is that the applied magnetic field is somewhere in between their first critical field (H_{c1}) and the upper critical field (H_{c2}). Both of these critical fields present high anisotropy with respect to the direction of the applied magnetic field. In other

words, when the magnetic field is applied parallel to the plane *ab* of the crystalline structure of YBCO in Fig. 3.7, the first critical field (H_{c1}) is considered to be a minimum. Because polycrystalline YBaCuO samples were used and consequently, the orientation of the grains in the crystalline structure is not known, the $H_{c1}//ab$ plane is considered the boundary of the Meissner state.

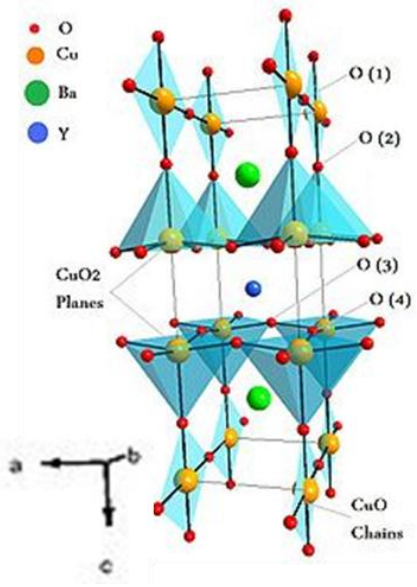

Fig. 3.7. Crystalline structure of YBaCuO. The plane of the CuO2 structures is usually named the ab plane while the normal direction to this plane is usually named the c direction.

The lower critical field has been measured by many researchers. An typical average value of H_{c1} at 77 K found in the literature is $H_{C_1//ab} = 3900 \pm 900\ {}^{A}/_{m}$ [38]. In a vacuum, this corresponds to a magnetic flux density of about $B = 5 \pm 1\ mT$. This value has been classically measured by characterisation of the magnetic properties of the superconducting samples as a function of the magnetic field applied. However, we have recently proposed a new experimental method to measure H_{c1} based on mechanical measurement of the forces between a permanent magnet and a superconductor [112]. The value obtained at 77 K for the *first critical field* was $H_{C_1//ab} = 3200 \pm 200\ {}^{A}/_{m}$, equivalent to about $B = 4.0 \pm 0.2\ mT$ in a vacuum. This value was obtained using similar superconducting disks to those used in the *FTS* mechanism and therefore, it is very convenient to consider the previous value as the *first critical magnetic field* for the purpose of this thesis.

The upper critical field that destroys the superconductivity in YBaCuO has also been measured by other researchers. The difficulty of generating the extremely high magnetic fields needed for this measurement mean that some discrepancies are still present regarding the value of the upper critical field. Typical values of the upper critical field are around $\mu_0 H_{C_2//ab} = 25 \pm 5\ T$ at

77 K [113]. Both, the lower and upper critical fields for each direction of the magnetic field applied, are presented in Table 3.1.

Table 3.1. Lower and upper critical magnetic field of YBCO. Data collected from [38], [113], [114].

T= 77 K	**B[T]**
$\mu_0 H_{C_1//ab}$	$3.9 \cdot 10^{-3}$
$\mu_0 H_{C_1//c}$	$11 \cdot 10^{-3}$
$\mu_0 H_{C_2//ab}$	25
$\mu_0 H_{C_2//c}$	50

As shown in Fig. 3.5, the maximum value of the magnetic field applied on the superconductors is about *0.179 T (for a Height of Field Cooling* of 3 mm). This value is two orders of magnitude higher than the lower critical field H_{c1} but also much lower than the second critical field H_{c2}. Although the critical fields are temperature dependent [115], it can be said that this is also true for the lower operation temperatures between 15 and 77 K. Thus, it can be concluded that the superconductors will be in the mixed state for the range of working temperatures of the *FTS* mechanism.

3.3.4 The actuation system

The slider is mainly composed by a long PM with its magnetisation axis oriented parallel to the Z axis, as shown in Fig. 3.2. In order to move the slider without any contact between the moving parts, a natural solution is to apply magnetic fields. As it is desired to have a reversible movement of the slider in the *FTS* mechanism, it seems very convenient for the actuation system to be symmetric. For this purpose, a couple of coils placed at either of the end of the stroke can be used. Then, the equilibrium position of the slider can be easily modified using magnetic forces. As there is no contact between the slider and the stator, lubrication is not needed, overcoming all tribological problems in cryogenic environments.

According to the Biot-Savart law, the magnetic field (*H)* generated by an electric current distribution along a closed curve, can be calculated by integrating eq. 3.4:

$$\overrightarrow{\delta H} = \frac{\mathrm{i}}{4\pi} \cdot \frac{\overrightarrow{\delta l} \times \vec{r}}{|r|^2}$$

eq. 3.4

where,

i is the current in the conductor,

r is the full displacement vector at which the field is being computed and $\vec{\mathrm{r}}$ is the unit vector of r,

and $\overrightarrow{\delta l}$ is the unit vector of the length of the conductor.

From this equation, it is clear that the magnetic field H is linearly dependent on the current through the coils in the *FTS* mechanism. Now, the force density per unit volume (f) acting in the PM is:

$$f = \mu \cdot \mathrm{M} \cdot \nabla \mathrm{H}$$

eq. 3.5

where,

M is the magnetisation

μ is the magnetic permeability

and H is the magnetic field applied on the PM

Consequently, the force exerted on the PM is linearly dependent on the current thought the coils, *i*. In addition, the coils should have some properties that respect the symmetry of the mechanism. The basic idea is that the gradient of the magnetic field applied to the PM in other directions different from the sliding DoF is minimised. Going beyond, the symmetry of this gradient must be preserved and then, the straightness of the motion and the efficiency of the mechanism will be improved. In this thesis, we propose an actuation system based on a couple of coils with their axes parallel to the magnetisation direction on the PM (see Fig. 3.8) and a height equal to the height of the PM. In addition, the imaginary line that passes through both centres of each coil is coincident with the longitudinal axis of the PM in the slider, as shown in Fig. 3.4 and Fig. 3.8.

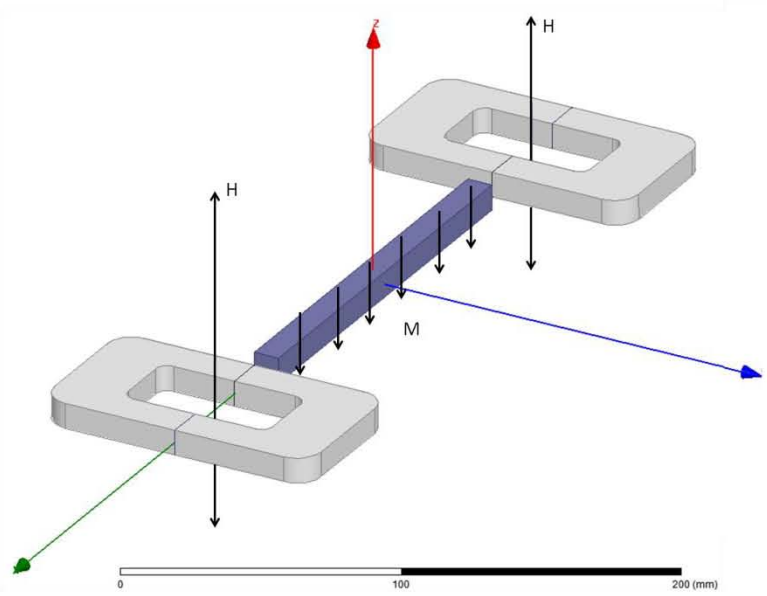

Fig. 3.8. CAD figure of the actuation system and the PM.

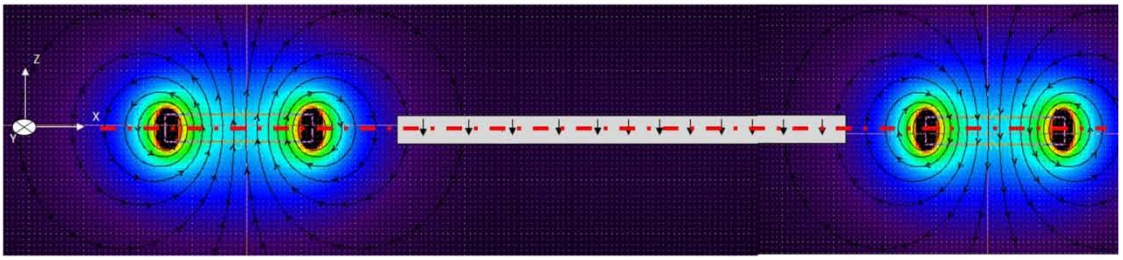

Fig. 3.9. Magnetic field and flux lines in *FTS1* actuation system.

The proposed configuration of the actuation system and the PM presents the following advantages:

- Symmetry variations of the magnetic flux density B in the Z axis can be appreciated in Fig. 3.10 in which the magnetic flux lines and the magnetic flux density are plotted. Therefore, the vertical force exerted on the permanent magnet is null, provided a good alignment between the coils and the PM.

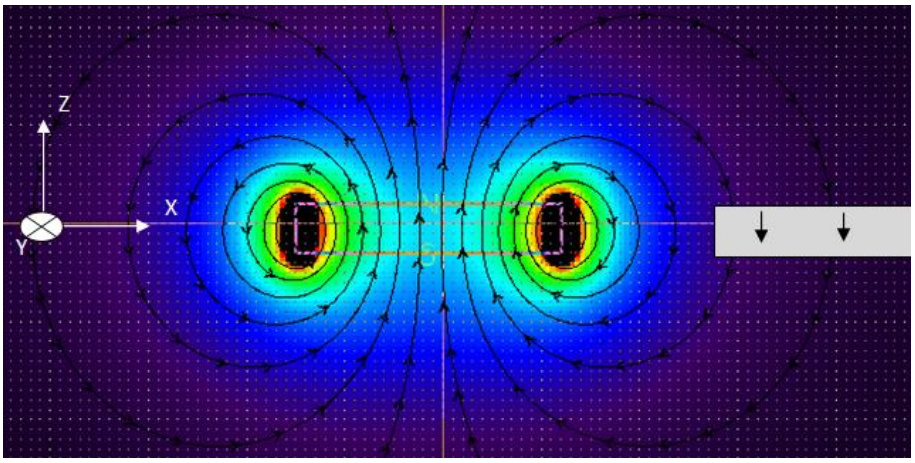

Fig. 3.10. Magnetic field and flux lines in *FTS1* actuation system (closer view).

- Due to the rectangular shape of the coils, the gradient of the magnetic flux density B is also minimised in the Y axis to prevent forces in the case of a misalignment of the PM.
- In addition, it is well known that an alignment torque (τ) appears that tries to align each magnetic dipole of strength m in a magnetic induction B [27] as described by eq. 3.6:

$$\tau = m \times B = |m||B| \sin\theta\vec{n}$$

eq. 3.6

where,

$\vec{n}$ is the unitary orthogonal vector to the m and B vectors,

and θ is the angle between the m and B vectors.

This alignment torque can be added to the torque exerted by the force between the magnet and the magnetic source and, in the case of a 3D magnetic material, the total torque (T) exerted on the permanent magnet can be calculated as in eq. 3.7 [27]:

$$T = \int_V [r \times (M \cdot \nabla)B + M \times B]\ dV$$

eq. 3.7

where r is the vector position.

It can be easily demonstrated that when the permanent magnet is properly aligned, as settled in the design specifications, the contribution of the alignment torque (see eq. 7) is null because the magnetic axis of the coils are aligned with

the magnetisation axis of the permanent magnet for any X position of the slider. Therefore, $M \times B = 0$. In addition, the centres of both coils are aligned with the geometric centre of the permanent magnet and therefore, $r \times (M \cdot \nabla)B = 0$. Thus, the total torque (T) exerted by the coils in the permanent magnet is null when the symmetry of the mechanism is considered. However, there is an alignment or misalignment effect in the PM if it is misaligned with respect to the magnetic axis of the coils. In [116], it has been proposed that angular and lateral run outs could be caused mainly by these misalignments, as is shown in Fig. 3.11. This can be also understood, if good alignment is provided, as the actuation system preventing run outs due to the self-alignment effect of the magnetic fields generated by the coils and the PM.

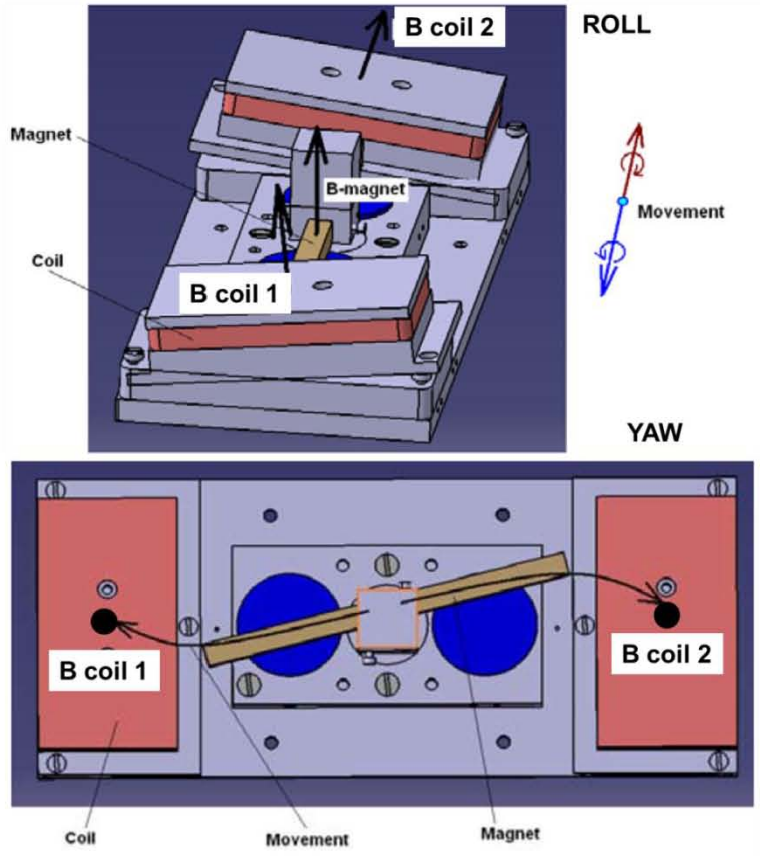

Fig. 3.11. Mechanism generation of yaw, roll and lateral run out due to misalignments (exagerated) between the coils and the PM.

3.4 Conclusions of chapter III

A slider based on superconducting magnetic levitation with a long permanent magnet as the slider and a stator composed of type II superconducting disks in the mixed state theoretically forms a sliding kinematic pair. The sliding kinematic pair is established provided that the magnetic field seen by the superconductors presents a high translational symmetry for the motion of the slider in the sliding DoF. Movement in any other directions but the sliding one present a high stiffness because high gradients of the magnetic field applied on the superconductors are present. In addition, the slider will presumably present an initial equilibrium position at the origin of coordinates. This fact, together with the stable levitation and the guidance provided by the superconductors, considerably simplifies the control of the position of the slider.

A couple of coils symmetrically located at either end of the stroke of the *FTS* mechanism can move the slider without contact. An appropriate design of these coils will provide self-alignment properties to the system, which is very desirable in reducing run outs of the moving part.

*C*hapter IV

Design and preliminary test of a prototype

In order to test the working principle of the FTS mechanism, a prototype with a ± 9 mm stroke was designed, built and tested. A detailed description of the design of this prototype is given. A simplified model based on FEM calculations supported the design of the actuation system. Once designed and built, a first prototype of the FTS mechanism was tested in a bath of liquid nitrogen at ambient pressure and the results of these tests are discussed in this chapter. Lastly, conclusions for the improvement of the device are detailed.

4.1 Description of the *FTS* prototype

According to the theoretical foundations discussed in chapter III, a prototype of the *FTS* mechanism is designed, built and tested. From now on, this first prototype will be called the *FTS1* prototype. In order to make the prototype suitable for use in far infrared interferometer, the following design specifications were considered:

1. A stroke of 18 mm.
2. A maximum circulating current in the coils of about ± 500 mA is required.
3. The slider must carry an optic mirror cube made of polished aluminium with an approximate weight of 40 grams.
4. The prototype will be tested in a bath of LN_2 so that the superconductors will be cooled down to 77 K, i.e., below their critical temperature.

As it was introduced in previous chapters, stable levitation required in the *FTS1* prototype will be provided using type II superconductors and a long permanent magnet. Not only stable levitation will be provided by the superconductors, but also the guidance of the PM in its path. Then, two polycrystalline $YBa_2Cu_3O_{7-x}$ disks (HTS) 45 mm diameter and 13 mm thickness (1) (see Fig. 4.1) will be used as the stator of the device. This material can be cooled using liquid nitrogen, which is very convenient for developing preliminary tests on the prototype without the requirement of a cryostat. In addition, the slider is mainly composed of a rare earth permanent magnet (2) made of $Nd_2Fe_{14}B$. This material presents high magnetic performance with energy products usually higher than Sm-Co permanent magnets [117]. Furthermore, NdFeB permanent magnets are usually less expensive and present better mechanical properties [118]. The permanent magnet in all *FTS* prototypes is a bar 160 mm in length classified as a *N42* magnet (T_{max} = 80 °C; $(BH)_{max}$ = 42 MGOe) with a magnetic remanence B_r = 1.3 T and a coercivity H_c = 900 kA/m. Notice that the magnetisation direction is parallel to the Z axis in Fig. 3.4.

As explained in chapter III, in order to move the slider along its path, two coils (3) are placed at either end of the designed stroke of the mechanism (± 9 mm). These coils are designed following the criteria introduced in the previous chapter. In addition, it was defined that each of the coils would move the permanent magnet in opposite directions (e.g., coil 2 in Fig. 3.11 for +X and coil 1 for –X direction). Ultimately, the coils in the *FTS1* prototype are

composed of a 110×60 mm^2 rectangular solenoid with a thickness of 10 mm and an inner aluminium core of 80×30 mm^2 (negligible magnetic interaction) surrounded by 150 turns of wire. The jacket of the wire is made of Polyvinylidene Fluoride (PVDF) with Polyolefin for greater flexibility and improved heat resistance. The jacket material is also considered vacuum-suitable due to its good outgassing properties [119]. Finally, the resistivity of the wire was measured to be around $1.8x10^{-8}$ Ωm. Other interesting properties of the wire used in the *FTS* prototype are summarised in Table 4.1.

Table 4.1. Some properties of the wire that surrounds the coils in the *FTS1* prototype.

Wire data sheet	
AWG	18
Outer diameter [mm]	1.04
Sheath material	PVFD
Cross section area [mm2]	0.25
Minimum number of conv. passes	5
Conductor material	Tinned copper

The height were the coils are located can be modified with high precision using a set of three M4 screws and nuts. By regulating the height of each pair of nut and screw individually, a plane can be defined for the positioning of the coils.

The material for the construction of the remainder parts of the *FTS1* prototype (e.g., base plate, nuts, screws and so on) was carefully selected. Because of the cryogenic and vacuum conditions, along with the presence of magnetic fields, it is required that the material has good mechanical properties, good thermal conductivity and low magnetic susceptibility at cryogenic temperatures. Aluminium alloy 6061 was selected because it presents the best mechanical strength to mass ratio of the materials used in cryogenic applications [120], has very good machinability [121], the outgassing of aluminium is low when exposed to high vacuum [120] and it presents low magnetic interaction [122]. A picture of the *FTS1* prototype can be seen in Fig. 4.1.

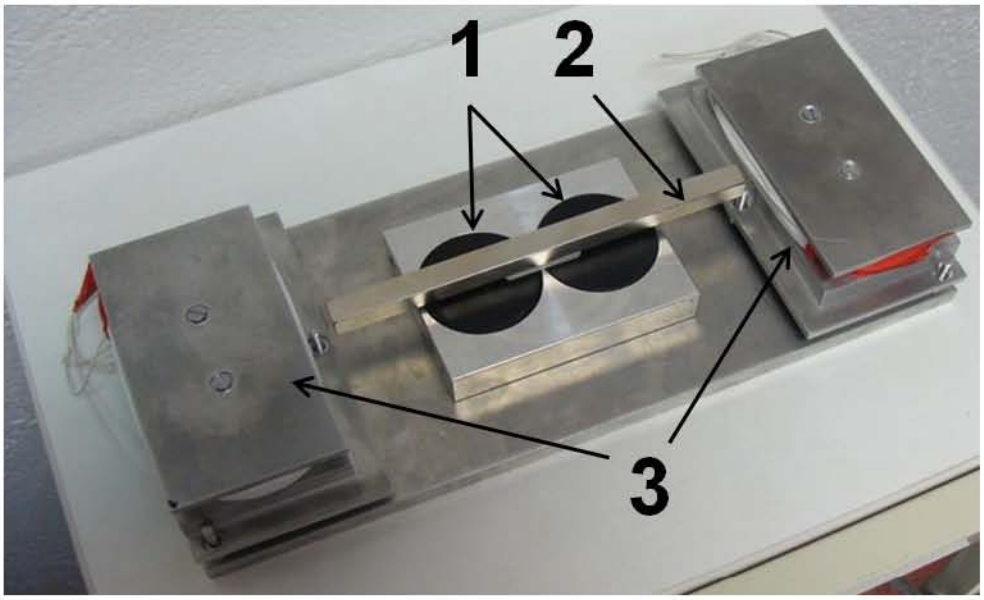

Fig. 4.1. Picture of the *FTS1* prototype. (No mirror)

Finally, an auto-collimator and a laser interferometer were used to measure the rotation deviation and the position of the slider, respectively. Both instruments require a reflecting surface with very low flatness and roughness clearances, of the order of a few nanometres. The required mirror (see Fig. 4.2) was provided by LIDAX S.L. in the shape of an aluminium cube with one-inch side length and approximately 40 grams in weight. It was fixed to the permanent magnet with its centre aligned with the centre of masses of the permanent magnet within a positioning accuracy of 0.05 mm.

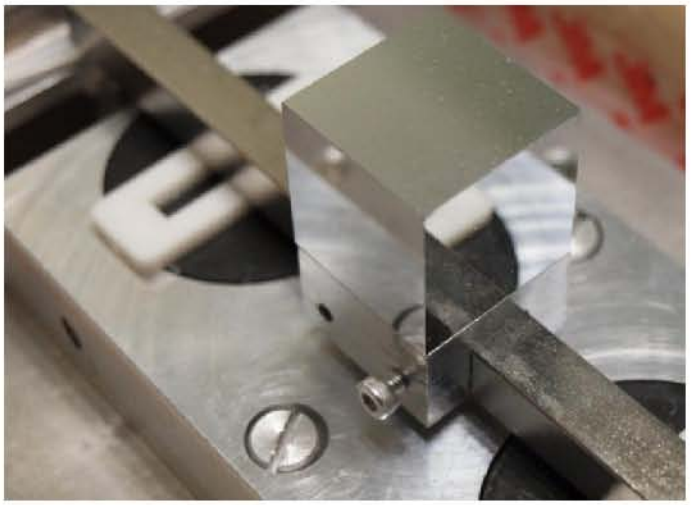

Fig. 4.2. Optic cube used for reflection of beam laser from auto-collimator and interferometer.

4.2 Finite Element Analysis (FEA)

Computer-based calculations with magneto-static analysis using the finite element method (FEM) were carried out in order to determine the dimensions of the actuation system of the *FTS* mechanism. The finite element analysis (FEA) is discussed below.

4.2.1 Decoupled model for the FEA

If the whole *FTS* mechanism is considered for FEA, it must be considered that there are two main problems to be solved. Firstly, the action of the actuation system in the slider (PM) and secondly, its interaction with the superconductors and the simulation of the forces exerted by the superconductors on the slider. This second issue is a very complicated task; no commercial software can be found that considers mixed state in HTS.

On the other hand, if a superconductor in the mixed state is considered as a perfect diamagnetic body ($\mu_r = 0$), the forces exerted on the permanent magnet by the superconductors will be higher than the real ones. A simple way to estimate the forces involved in the mixed state with higher accuracy is to set a value of the relative permeability between 0 and 1, in what is usually called the non-perfect diamagnetic model. At the same time, a very high electric conductivity must be used in the superconducting material [123]. However, the evaluation of the relative permeability is a problem which is frequently solved by comparison of FEM simulations and experimental studies [124] and situations that agree accurately with experimental results are limited. In addition, relative permeability has been demonstrated to be highly dependent on the shape of the superconductor and the permanent magnet and the temperature of the samples [125]. Additionally, simulations are limited by the speed of the motion of the PM [123]. Methods that are more precise, based on the critical state model [126], [127], the frozen field model [128] and the flux-flow-creep model [129] have also been tested in good agreement with experimental results for many different situations.

However, one must consider the time consumption not only in programming the routine to calculate the superconductors at the mixed state but also the computational requirement for such a complicated scenario that contains the PM, the coils and the superconductors at the mixed state. A simplification of the system could make simulations much more efficient if we are only interested

in calculating the force in the sliding direction. With this in mind, a decoupled model is proposed for the FEA.

If we assume that the magnetic interaction between the coils and the superconductors is small compared with the main interaction between the superconductors and the permanent magnet, the presence of the superconductors could be neglected when calculating the force exerted by the actuation system on the slider. This model will considerably reduce the time and computational requirements for the calculations if other models are considered. In order to validate the model and to estimate its accuracy, let us consider the three following scenarios:

1. Scenario I: A first system to be analysed is composed of the permanent magnet and the superconducting disks without the presence of the coils, as shown in Fig. 4.3.

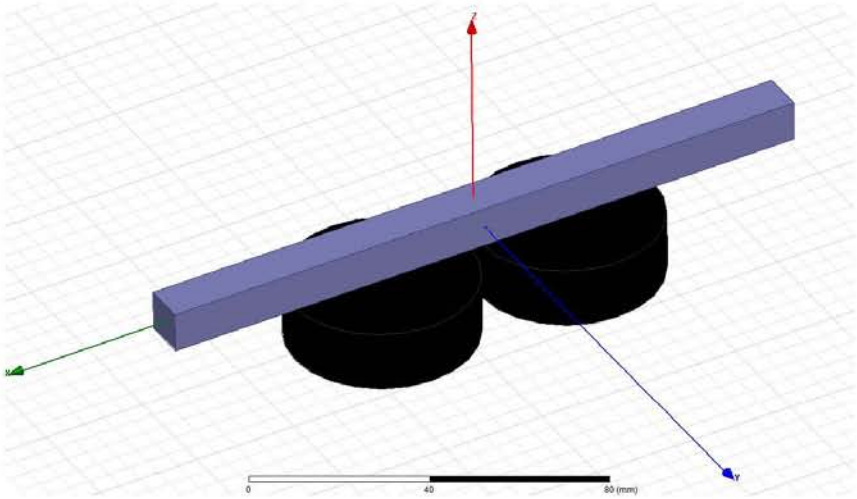

Fig. 4.3. Model for FEA of Scenario I. Only the PM and the superconductors are considered.

2. Scenario II: The second system is composed of the permanent magnet and the coils without superconductors. See Fig. 4.4.

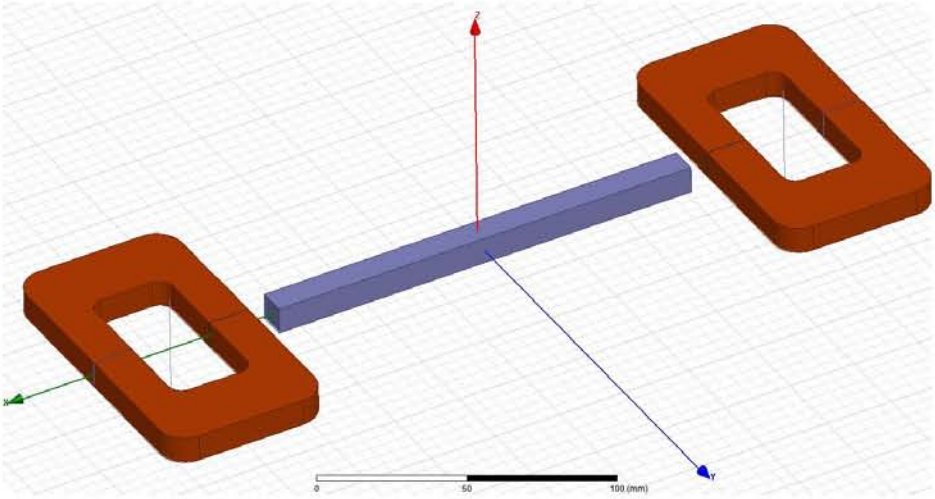

Fig. 4.4. Model for FEA of Scenario II. Only the PM and the coils are considered.

3. Scenario III: A third scenario includes which is a full representation of the mechanism. This system contains all the parts of the mechanism, i.e., the superconductors, the permanent magnet and the coils. See Fig. 4.5.

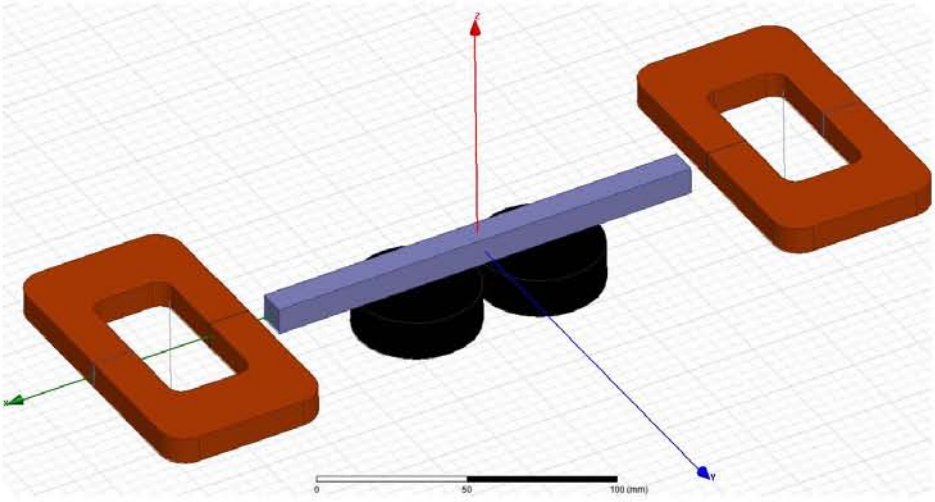

Fig. 4.5. Model for the study of Scenario III with FEM. All elements considered.

If the influence of the superconductors on the force exerted by the coils on the PM is small, it may be a good approximation to say that drag forces in Scenario II are equal but opposite to those acting forces found in Scenario I. Then, equilibrium positions of the PM, for a driven current in the coils, are those where the sum of the forces and moments on the PM are null. In the sliding direction of the mechanism, it can be said that:

$$Fx_{PM}^{I} + Fx_{PM}^{II} \approx 0$$

To validate the model for calculations of the actuation system in the *FTS1* prototype and to estimate its accuracy, a set of simulations including the whole system (scenario III) was developed and the results compared with those in coils in Scenario I and Scenario III. If the interaction between the coils and the superconductors is small, the forces in both scenarios should be very similar. Any difference in these forces would depend on the influence of the superconductors. In next sections, the results of calculations for scenarios I, II and III are introduced and discussed.

4.2.1.1 Scenario I: Superconductors and permanent magnet

It was decided that the perfect diamagnetic model would be used for characterisation of the actuation force exerted by the coils on the PM. As stated in the previous section, forces obtained would be higher than the real ones. However, we considered this excess as a safety margin for the dimensioning of the coils. A similar approach can be done using other models that describe the force between a PM and a superconductor in the Meissner state [130–132]. Force versus the X position of the slider for different magnetic permeability of the superconductors is represented in Fig. 4.6. Some of the relevant FEA parameters involved in these simulations are summarised in Table 4.2.

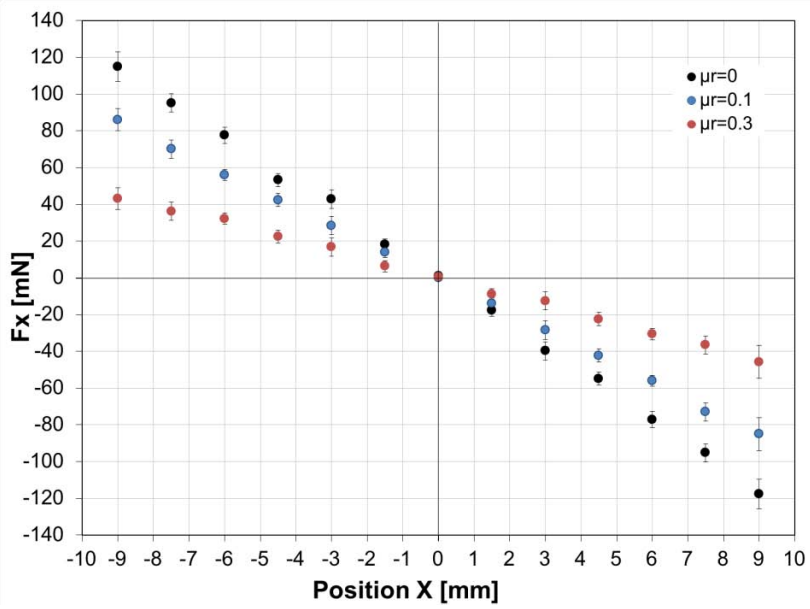

Fig. 4.6. F_X exerted on the PM by the HTS for different magnetic permeability of the HTS.

Table 4.2. FEA characteristics of Scenario I.

FEA parameters	
YBaCuO conductiivity [s/m] [124]	$6.25x10^{10}$
µr YBacuO [-]	$[1x10^{-21},1]$
Minimum number of elements	400000
Energy error assumed	0.05%
Minimum number of convergence passes	7
Estimated convergence error	<3%

The maximum (or minimum) value of the force exerted on the PM is reached at either end of the stroke (X = ±9 mm) and it has a magnitude of around 120 mN for the *FTS1* prototype when a pure Meissner state is considered.

Because, in principle, it is impossible to determine a consequent value of the relative permeability that properly describes the system, we considered forces exerted on the PM when the superconductors are at the Meissner state for dimensioning the coils. Obviously, one can argue that they will be over-dimensioned; however, this will be useful for further studies on the prototype, as will be demonstrated in chapter V.

4.2.1.2 Scenario II: Coils and permanent magnet

Calculations in scenario II were developed for just one acting coil with a driven current of ± 500 mA (see section 4.1). Characteristics of the FEA are summarised in Table 4.3:

Table 4.3. Characteristics of the FEA of Scenario II.

FEA parameters	
PM coercitivity [kA/m]	900
PM remanence [T]	1.3
Number of turns in each coil	150
Maximum energy error	0.05%
Minimum number of elements	400000
Minimum number of conv. passes	5
Refinement per pass	20%
Estimated convergence error	<2%

The refined mesh in the coils and the permanent magnet is shown in Fig. 4.7. The red arrow in coil 1 in Fig. 4.7 represents the direction of the flowing current in the coils and the green arrow indicates the direction of the orientation of the magnetic flux generated in the axis of the coil. On the other hand, the magnetisation of the permanent magnet was set in the direction of the +Z axis, as has already been stated.

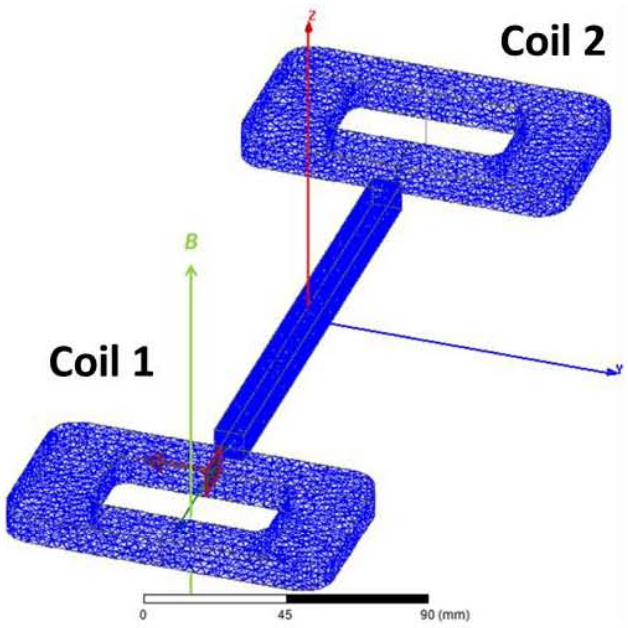

Fig. 4.7. Refined mesh in Scenario II.

The magnetic flux density generated by each of the coils at its centre is $B_z = 3 \pm 0.1 \frac{mT}{A}$.

4.2.2 Convergence and optimization of the FEA

Obviously, the force exerted on the PM by the coils must be equal but opposite to the force exerted in the coils by the PM, as a consequence of Newton's third law applied to scenario I. However, a much faster convergence of the results in forces calculated in the coils was observed, compared with those calculated by the software in the PM. See Fig. 4.8.

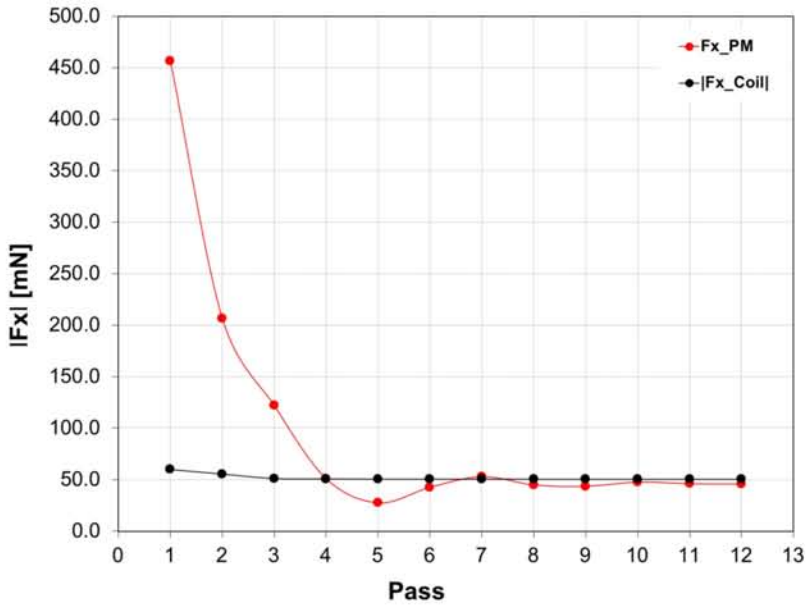

Fig. 4.8. Comparison of convergence of Fx in coil 1 and the PM for X = 0 mm with a circulating current of 500 mA in this coil.

A very similar behaviour was observed for all positions of the PM in its path. Therefore, it is much less computationally demanding to calculate the force on the coils rather than the force on the permanent magnet.

4.2.3 Results of the FEA and discussion

Forces were calculated for different positions of the permanent magnet in its path and different magnitudes of the current circulating in the coil. Errors in these simulations were estimated with the convergence error of the two last passes in the coils and can be considered below 3% in all cases. Forces in the Y and Z directions and the torque exerted on the permanent magnet (or on the coil) are almost zero ($<10^{-5}$), as was expected. Magnitude of F_X on the coil vs. X position of the PM for a driven current of 500 mA is plotted in Fig. 4.9.

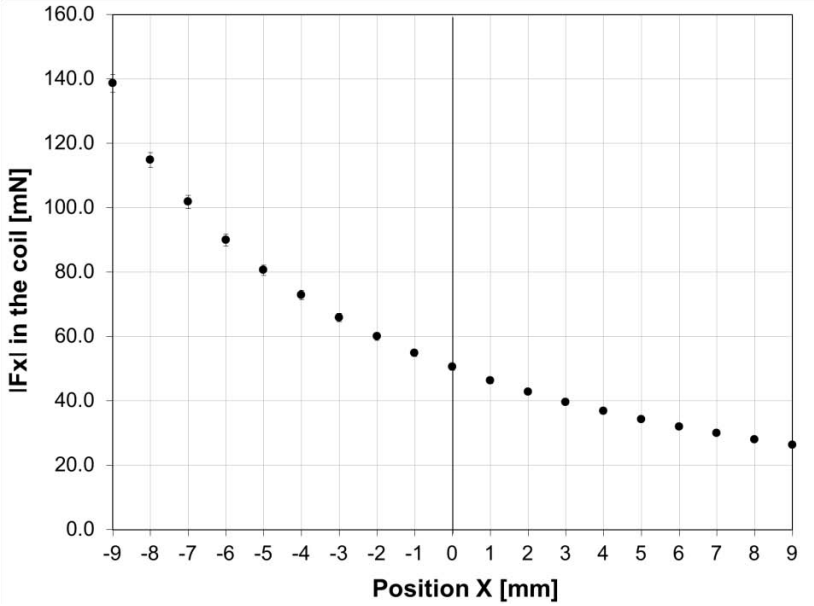

Fig. 4.9. Magnitude of F_X on the coil vs. X position of the PM for a driven current of 500 mA.

It can be observed in Fig. 4.9 how the force decreases rapidly when the permanent magnet moves away from the acting coil. A maximum force of about 140 mN can be achieved when the PM is close to the actuating coil and a current of 500 mA magnitude is supplied. The direction of the applied force can be easily controlled just by changing the polarity in the coils.

In order to dimension them, the force exerted by one coil is compared with the force exerted on the permanent magnet due to its interaction with the superconductors if a pure Meissner state is considered. The maximum force exerted on the permanent magnet by the superconductor is achieved when X is either + 9 or - 9 mm. The magnitude of this force is around 120 mN. On the other hand, the maximum force exerted on the PM by one of the coils under the design specifications described at the beginning of this section, is around 140 mN. Then, the maximum force that the coils can exert is higher than the drag force in the superconductors and, therefore, the actuation system is well designed:

$$Max\{F_{COIL}\} > Max\{F_{HTS}\}_{MEISSNER}$$

4.2.4 Validation of the interpretation of the system

Given the results in scenario I, a set of simulations were developed to check the validity of the "decoupled hypothesis". Forces in the coil in scenario I were compared when the presence of the superconductors are considered in scenario

III. Yet again, the circulating current in the coil is 500 mA for each X position. Relative permeability of the superconductors was also modified between ~0 and 1. Results of these simulations are shown in Fig. 4.10.

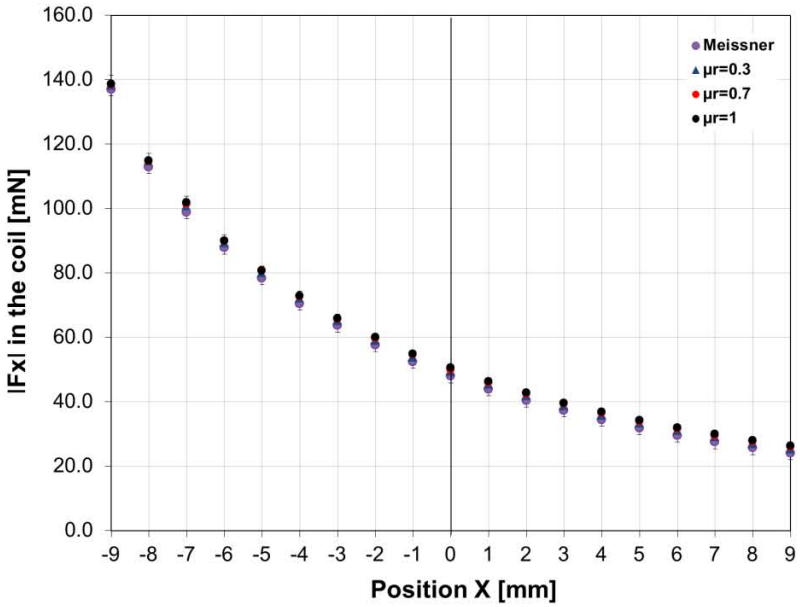

Fig. 4.10. Magnitude of Fx on the coil vs. X position of the PM for different values of relative permeability in Scenario III and for Scenario I.

It must be noticed that the divergence of the results of the calculation of the force exerted on the acting coil increases for higher values of the relative magnetic permeability of the superconductors. In addition, calculations of the difference of both results (scenario I and scenario III) reveal that Fx increases when the permanent magnet is far from the acting coil and the influence of the superconductors is more significant. A deeper analysis shows that the maximum error is always below 8% for any X position of the PM in its path when a Meissner state is considered, as shown in Fig. 4.11.

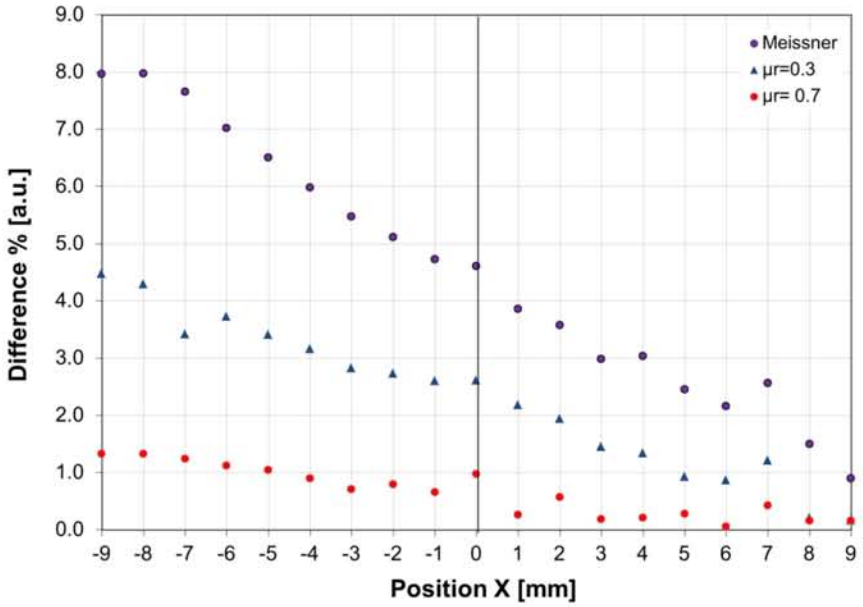

Fig. 4.11. Estimated error of the F_x calculated using Scenario I.

Therefore, a maximum uncertainty of the force calculations in the proposed simplified model for the FEA was estimated to be always lower than 8%. In addition, no programming for the calculation of the superconductors at the mixed state would be required and time and computational requirements will be considerably reduced. Lastly, conclusions obtained from simulations using this decoupled model will be very helpful for the dimensioning of the coils and for the interpretation of some characteristics of the device, as will be demonstrated in the next chapters.

4.3 Technical issues

As explained in a previous section, aluminium alloy 6061 was selected as the material with which to build the structural parts of the prototype (i.e., superconductors housing, base plate, coils, screws, nuts, etc.) not only for its diamagnetic nature but also for its good properties for cryogenic and space applications. Aluminium 6061 also presents good thermal conductivity and low specific heat in the range of temperatures of interest (15–300 K) as shown in Fig. 4.12. This means lower power consumption in the cryostat and a faster cooling process.

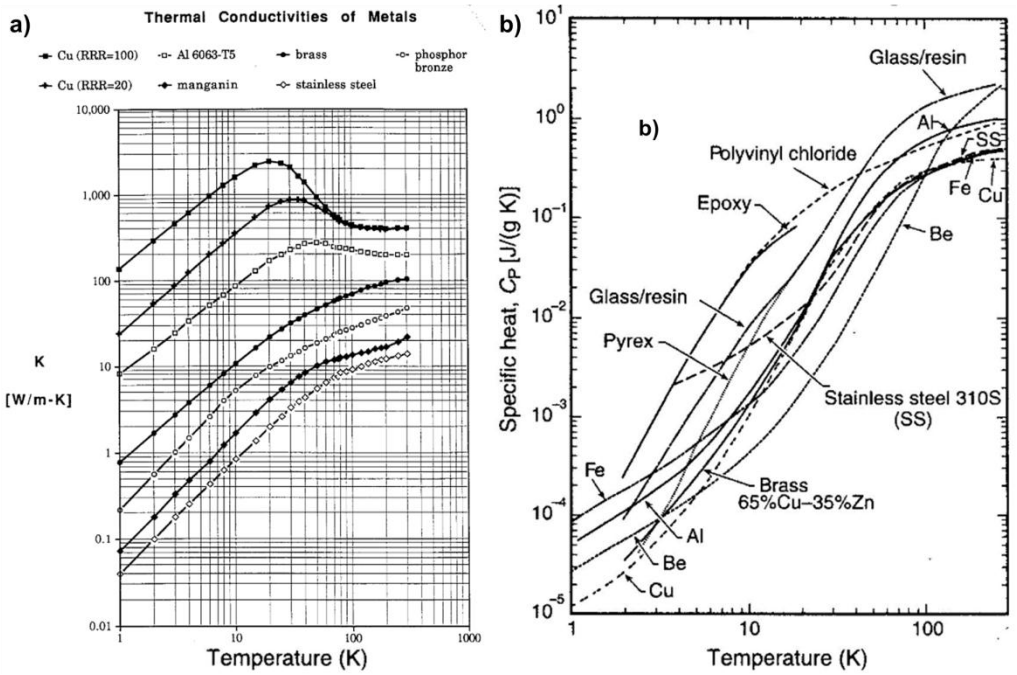

Fig. 4.12. a) Thermal conductivity of metals [133]; b) specific heat of metals [134].

4.3.1 Thermal contraction

It is well known that the size of a solid object changes as its temperature is modified. If the boundary conditions of the material constrain this change, thermal stress appears. This thermal stress can generate very high deformations in other parts of the mechanism and in the worst case, some parts can break down. The superconductors are contained in an aluminium housing with a very different thermal expansion coefficient. Therefore, the design of the prototype must consider this thermal contraction to avoid the superconductors breaking. Therefore, the size of the housing for the superconductors will be calculated next to avoid thermal constraints.

The superconductors are 45 mm diameter disks with a height of 13 mm and they are contained in an aluminium base with two appropriate housings for the superconductors. The *coefficient of linear thermal expansion* of a material is introduced in eq. 4.1.

$$\alpha_L = \frac{1}{\mathrm{L}} \frac{\partial L}{\partial T}$$

eq. 4.1

where,

L is the initial length of the sample (T_{ref}),

and T is the temperature of the sample.

Because at cryogenic temperatures, the coefficient of linear thermal expansion is very temperature dependent, it is quite useful to define a *total thermal linear expansion coefficient* as:

$$\frac{\Delta L}{L} = \frac{L_T - L_{ref}}{L_{ref}}$$

eq. 4.2

where,

L_T is the length at the target temperature,

and L_{ref} is the length at the reference temperature.

The *total thermal linear expansion coefficient* of some materials is shown in Fig. 4.13.

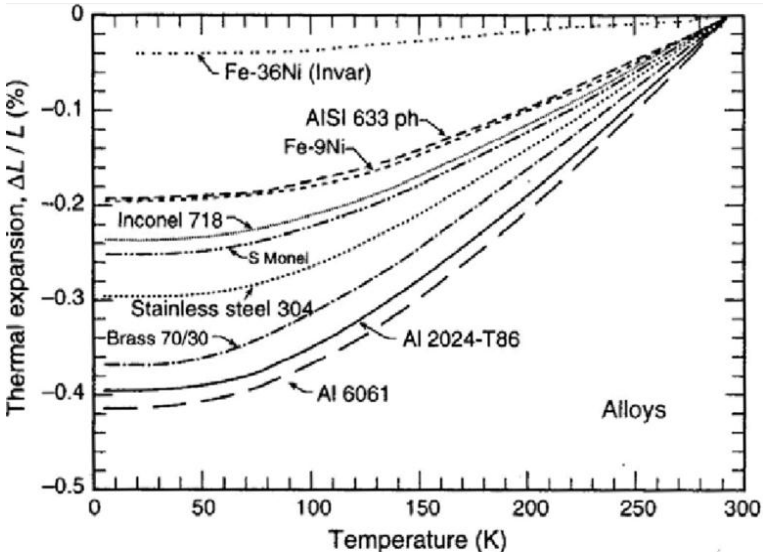

Fig. 4.13. Total thermal linear expansion coefficient of some materials [134].

The coefficient of thermal expansion of melt-textured YBCO was collected from [135] and is represented in Fig. 4.14.

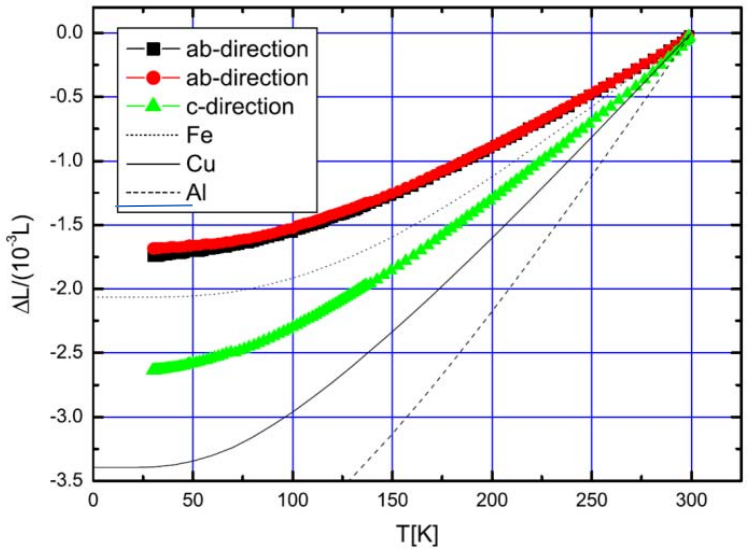

Fig. 4.14. Thermal expansion of melt--textured YBaCuO vs. temperature of the sample.

The total thermal expansion of both aluminium and YBaCuO are summarised in Table 4.4.

Table 4.4. Thermal expansion properties of YBaCuO and aluminium alloy 6061.

Material	**α_l[K^{-1}] at 300 K**	**ΔL/L[%] from 300 to 77 K**
Aluminium	15	-0.4
$YBa_2Cu_3O_{7-x}$ ab plane	5	-0.16
$YBa_2Cu_3O_{7-x}$ c plane	5	-0.25

As a part of the design, it was decided to make the diameters of the YBCO disks and of the holes in the housing coincident at a temperature of 77 K with a clearance of ± 50 µm. For lower temperatures, the *total thermal linear expansion coefficient* for both materials: aluminium and YBCO, is considered to not change significantly. Then, the diameter of both the housing and the superconducting disks at temperature T can be calculated as shown in equation 4.3:

$$\emptyset_T = \left(\frac{\Delta\emptyset}{\emptyset} + 1\right)\emptyset_{300}$$

eq. 4.3

As far as both diameters are meant to match at T = 77 K, the diameter of the aluminium housing can be calculated with eq. 4.4:

$$\emptyset_{Al,77\,K} = \emptyset_{YBCO,77\,K}$$

$$\left\{\left(\frac{\Delta\emptyset}{\emptyset}+1\right)\emptyset_{300}\right\}_{AL} = \left\{\left(\frac{\Delta\emptyset}{\emptyset}+1\right)\emptyset_{300}\right\}_{YBCO}$$

$$\emptyset_{300,Al} = \frac{\left\{\left(\frac{\Delta\emptyset}{\emptyset}+1\right)\emptyset_{300}\right\}_{YBCO}}{\left(\frac{\Delta\emptyset}{\emptyset}+1\right)_{Al}}$$

eq. 4.4

$$\emptyset_{300\,Al} \cong 45.11\,mm$$

Finally, it was decided to define the diameters of the drills in the housing of the superconductors as 45.15 mm with a tolerance specification equivalent to ISO H8.

In order to estimate the contraction of the PM, a coefficient of linear thermal contraction perpendicular to the direction of the magnetisation of $4.8 \cdot 10^{-6}$ °C^{-1} was considered. We assumed a constant coefficient linear expansion, so at a temperature of 15 K (reference temperature 300 K), the total contraction of the PM can be estimated to be about $2 \cdot 10^{-1}$ mm.

It must be mentioned that the prototype is fixed to a 300×131×10 mm^3 aluminium sheet. In the end, the prototype could be contained in a rectangular prism of 300×131×50 mm^3 and has a total weight of around 3 Kg.

4.3.2 Heat exchange and required volume of coolant

The total heat exchange Q, to cool down the prototype can be calculated as shown in equation 4.5:

$$Q = m \cdot \int_{Tf}^{Ti} c\,\partial T$$

eq. 4.5

where,

m is the mass of the prototype,

T is the temperature,

and c is the specific heat of the material.

In the case the prototype is cooled down by immersing it in a bath of liquid nitrogen, one can calculate the volume of liquid nitrogen required for the cooling process as:

$$Q_v = Q$$

eq. 4.6

where Q_v can be calculated as:

$$Q_v = V_{LN_2} \rho_{LN_2} h_v$$

eq. 4.7

where,

V_{LN2} is the required volume of liquid nitrogen,

ρ_{LN2} is the density of liquid nitrogen: 807 kg/m^3,

and h_v is the latent heat of vaporisation of liquid nitrogen, which is around 200 kJ/kg [136].

As a good approximation, the prototype is considered to be fully composed of aluminium 6061 with a total weight of 3 kg. Therefore, the required volume of liquid nitrogen to cool the prototype from 300 to 77 K, if no losses are considered, can be calculated by combining eq. 4.5 and eq. 4.7, which leads to eq. 4.8:

$$V_{LN_2} = \frac{m_{Al}}{\rho_{LN_2} h_v} \cdot \int_{77}^{300} c_{Al}\, \partial T \approx 3.1\ litres$$

eq. 4.8

where,

m_{Al} is the mass of the prototype; 3 kg,

and $\int_{77}^{300} c_{Al}\, \partial T$ has been approximated, as presented in [137].

In summary, around 3 litres of liquid nitrogen (~1 l_{N2}/kgA_l) are needed to cool down the prototype, which is a reasonable volume of liquid nitrogen that can be easily stored and transported in portable commercial Dewar vessels.

4.4 Preliminary Tests: Experimental setup and procedure

Once the *FTS1* prototype was designed and built, some preliminary tests were carried out in order to check both the validity of the working principle of the device and to evaluate its performance. For these preliminary tests, the superconductors were cooled using LN_2 and the whole prototype was placed in an environment at ambient pressure, as has been already introduced in previous sections.

The experimental setup for the *FTS1* preliminary tests is shown in Fig. 4.15. All measurements, except for the X rotation of the slider were performed as shown in Fig. 4.15. (setup A). The measurement of the rotation angle around the X axis (roll) needed a second configuration with the auto-collimator laser beam parallel to the Y axis (setup B).

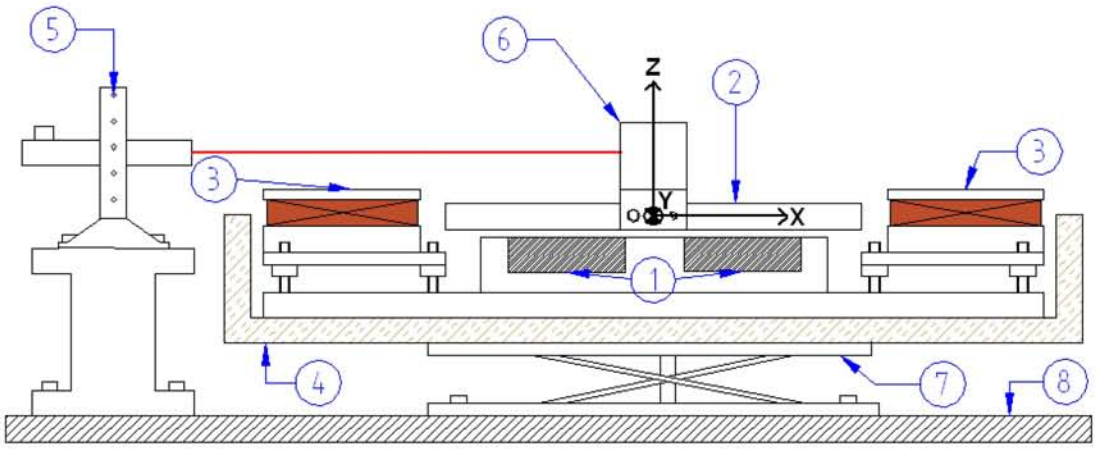

Fig. 4.15. Experimental setup A for the preliminary tests: 1) Superconducting disks; 2) NdFeB permanent magnet; 3) Coils; 4) LN_2 container; 5) Laser auto-collimator; 6) Optic mirror cube; 7) Lab jack stand; 8) Optic table.

First the prototype was placed inside an extruded polyurethane vessel (4) that contained the LN_2 coolant. This vessel is fixed to a lab jack stand (7) that was used to fix the height of the whole prototype with respect to the ground, in order to provide correct alignment with the laser from the auto-collimator (5). The whole system (auto-collimator plus prototype) was fixed to an optic table (8) that provided an adequate flat base and vibration insulation.

4.4.1 Reference system and disposition of the PM

The static reference system used in this thesis is shown in Fig. 4.15. The YZ reference plane is coincident with the Y'Z' symmetry plane of the *FTS* mechanism. In addition, the symmetry axis of the PM was carefully aligned with the X axis in Fig. 4.15 and its centre of mass positioned at the origin of coordinates in the FC initial position. Therefore, if lateral deviations are neglected, the motion of the slider always follows the direction of the X axis of the reference system. Notice that the reference system used in the preliminary tests described here, is coincident with the reference system described in chapter III.

On the other hand, the XY plane of the reference system was set at 10 mm over the top surface of the superconductors using spacers with a low thermal contraction coefficient. This means, the levitation height was +3 mm between the top surface of the superconductors and the bottom surface of the PM with an estimated uncertainty of the order of ± 0.25 mm.

4.4.2 Instrumentation

In order to measure the X and Y position of the slider, scales with 250 µm resolutions were used. The interferometer could not be used due to technical reasons in any of the experiments with LN_2.

Additionally, a *Newport LDS* vector auto-collimator was used for the measurement of the relative angular deviations of the slider. The resolution of the auto-collimator is 0.1 µrad and its accuracy 2% for a measurement field of ± 2000 µrad. The angular deviations measured by the auto-collimator were recorded using a 16-bit acquisition card model NI PCI-6230.

The supply current in the coils was generated by a dual-channel power source and measured with two independent digital multimeters with 10 µA resolution for the measurement field in these tests. Therefore, the supply system is able to provide a different current signal to each of the two coils. A picture of the experimental set up is shown in Fig. 4.16.

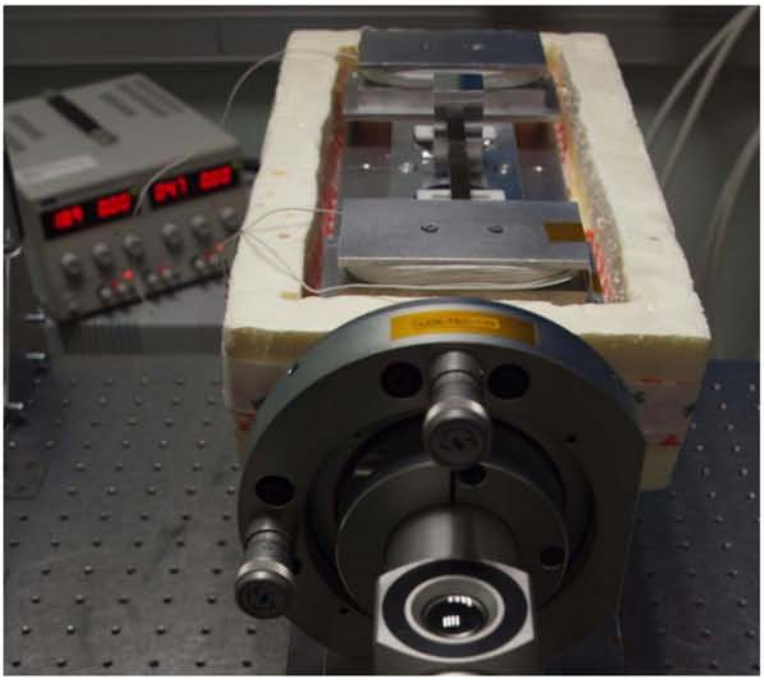

Fig. 4.16. Real picture of the experimental set up.

4.4.3 Experimental procedure

Once the prototype was set up and all the instrumentation was ready, the superconductors were cooled in a bath of LN_2 at ambient pressure to guarantee their temperature below their critical temperature ($T_c \sim 93\ K$). It should be noted that there was no contact between the LN_2 and the PM at any time during the experiments.

As the magnetic field applied on the superconductors is well over the penetration field (H_p) and below the second critical field (H_{c2}), the *Field Cooling* process (FC) will lead to a mixed state in the superconductors. After the FC cooling process, the flux-trapping effect makes the PM levitate stably over the superconductors [35] and the sliding kinematic pair is established.

Following that, the spacers used to fix the levitation height were removed and the position of the PM was smoothly modified using either coil independently. Then, the amplitude of the current in the coils and X, Y and Z positions of the slider were registered. At the same time, the angular deviation in the Y and Z axes of the slider was recorded by the NI PCI-6230 acquisition card in setup A.

After these measurements were recorded, the setup was modified to setup B in order to measure the roll of the slider. A flux diagram of the experimental procedure is shown in Fig. 4.17.

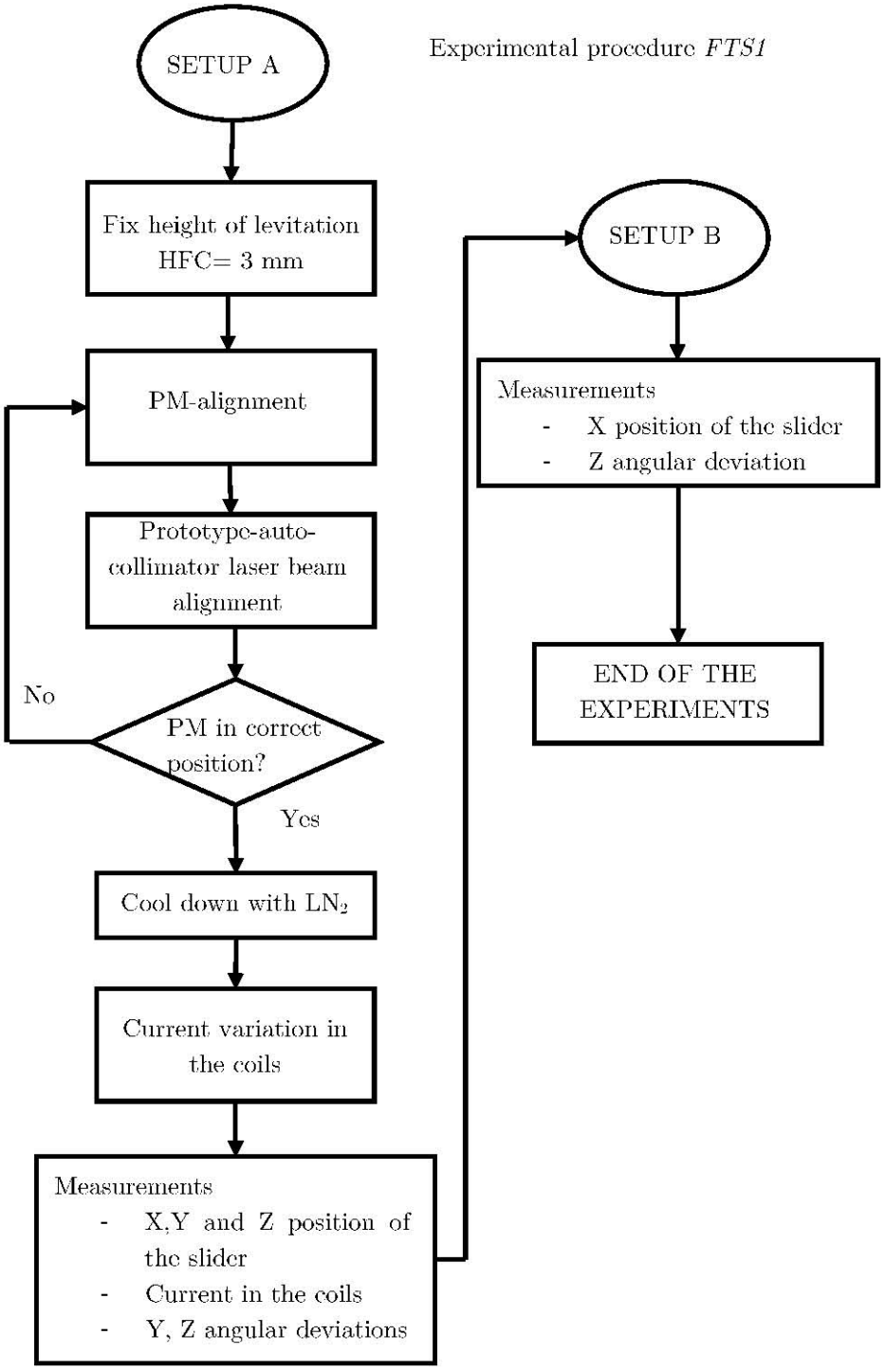

Fig. 4.17. Experimental procedure in the preliminary tests.

Results of these measurements are presented and discussed in the following section.

4.5 Preliminary tests results

Some requirements and conclusions can be derived from the experiments and are summarised in the following sections.

4.5.1 Horizontality requirement

It was observed that the FC position is an equilibrium position of the slider, provided that the inclination of the base of the prototype is lower than 5 minutes of arc. For inclinations higher than 5 minutes of arc the slider becomes unstable in the sliding direction. Therefore, a very fine horizontality must be provided to the base of the prototype to preserve the initial equilibrium position.

4.5.2 Position vs. current in the coils

The X position of the slider along its path versus the current in coil 2 is shown in Fig. 4.18. Only one direction (+X) is represented due to the symmetry of the results.

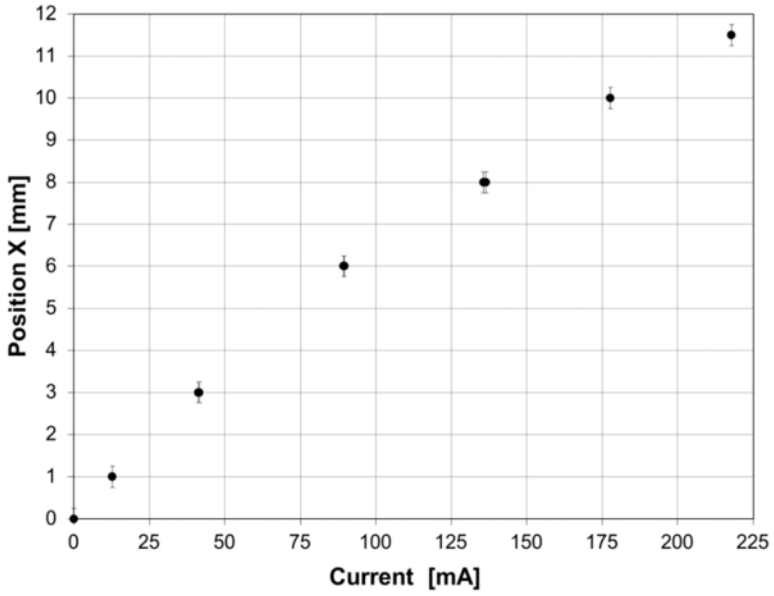

Fig. 4.18. X position of the slider vs. current in the coil.

For the *FTS1* prototype it was noticed that the total stroke measured was about 11.5 mm (± 11.5 mm if considering both directions) and the current required to reach this stroke was below 225 mA. It can also be appreciated that

the relationship between the supplied current and the X position of the slider is highly linear between 0 and 3 mm but that this linearity is reduced for longer displacements. Finally, hysteresis was lower than the resolution of the measurement.

4.5.3 Y and Z position vs. current in the coils

Both the lateral static deviation (Y axis) and the vertical static deviation (Z axis) of the slider were found to be always lower than the resolution of the measurement (250 µm) for any position of the slider.

4.5.4 Angular run outs

Static angular deviations or angular run out were measured with the auto-collimator. From now on, pitch, yaw and roll of the slider will be considered as shown in Fig. 4.19.

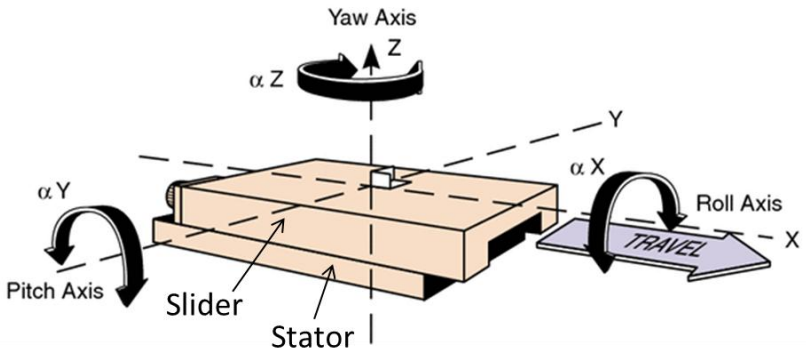

Fig. 4.19. Interpretation of the angular deviations in a linear stage

4.5.4.1 Pitch vs. X position of the slider

Pitch versus the X position of the slider is shown in Fig. 4.20. Pitch was assumed to be related to the effects of gravity and unbalanced lift forces on the permanent magnet when it moved away from the initial equilibrium position (X = 0). A further explanation of this phenomenon is presented in chapter V. A good linearity and hysteretic behaviour can also be observed. Notice that the maximum measured pitch is around 4500 µrad for a full stroke motion.

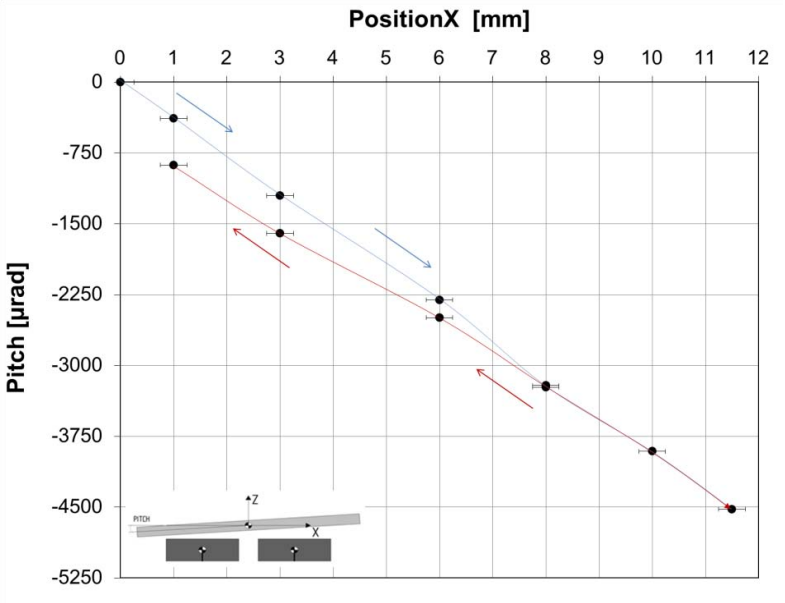

Fig. 4.20. Pitch vs. X position of the slider measured in the *FTS1* prototype at 77 K.

4.5.4.2 Yaw vs. X position of the slider

Yaw versus the X position of the slider is shown in Fig. 4.21. Again, a reasonable linearity is observed but an hysteretic behaviour can also be observed. Yaw was lower than 250 µrad for any X position of the slider.

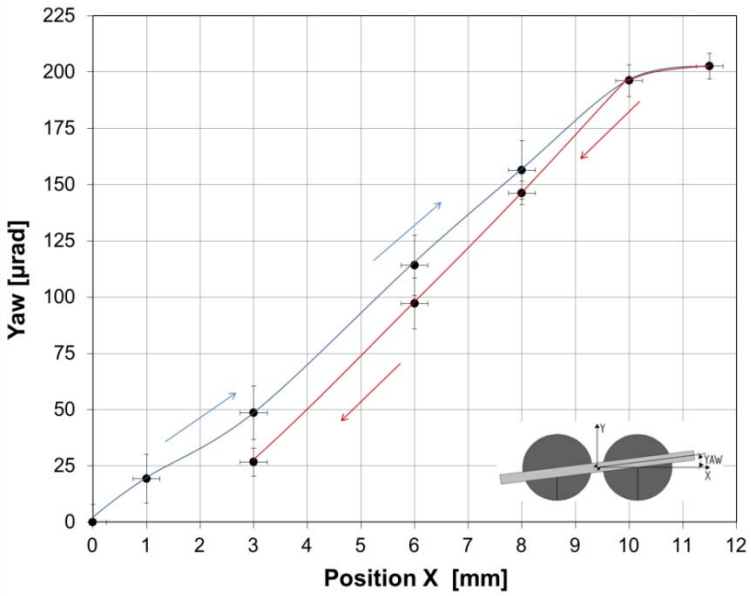

Fig. 4.21. Yaw vs. X position of the slider measured in the *FTS1* prototype at 77 K.

4.5.4.3 Roll vs. X position of the slider

Roll versus the X position of the slider is shown in Fig. 4.22. Due to the finite size of the optic mirror cube (one cubic inch), the maximum field of measurement for roll is reduced to approximately ± 7 mm.

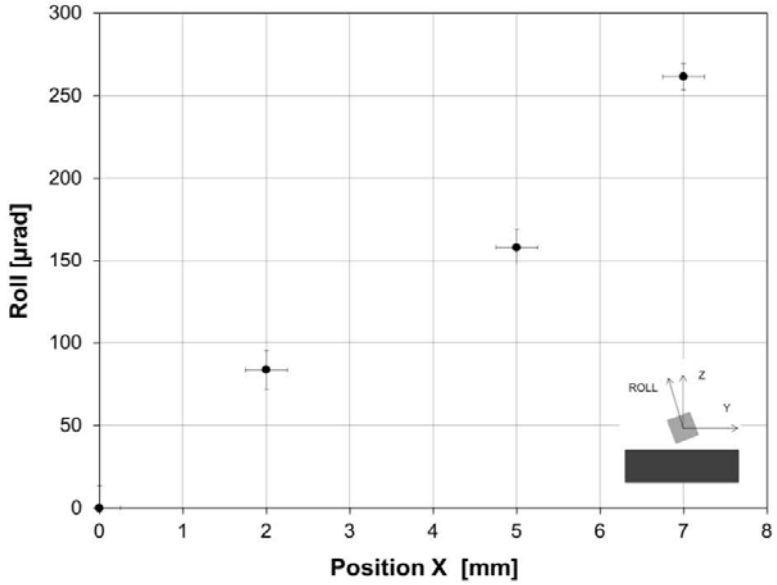

Fig. 4.22. Yaw vs. X position of the slider measured in the *FTS1* prototype at 77 K.

The maximum measured roll was of the order of 250 µrad (around 400 µrad when linearly extrapolated until the measured stroke of 11.5 mm).

4.6 Conclusions of chapter IV

Based on the idea of translational symmetry of the magnetic field generated by a long permanent magnet levitating over two superconductors at the mixed state, a prototype of a magnetic slider for long-stroke nanopositioning was designed, built and tested immersed in a bath of liquid nitrogen (77 K) at ambient pressure.

A decoupled model for actuation and levitation has been proposed and supports the design of the actuation system. The forces exerted by the coil in the PM were calculated by using FEA. In this model, the influence of the superconductors in the calculations of the actuation force on the slider is neglected. A deviation of less than a 8% of the actuation force was estimated for the *FTS1* prototype for any X position of the slider if the presence of the superconductors is neglected. The proposed model considerably reduces the computational time and the resources required for calculations.

The working principle was proved successful in the experiments. Results of the tests reveal that the prototype achieves a stroke over ± 11 mm with a current requirement of ± 225 mA. A summary of the prototype performance is presented in Table 4.5.

Table 4.5. Summary of the *FTS1* prototype performance.

***FTS1* prototype performance**	
Temperature [K]	77
Pressure [atm]	1
Stroke [mm]	11.5
Hysteresis [µm]	<250
Lateral and vertical run our (Y and Z axis) [µm]	<250
Pitch (Y axis) [µrad]	±4500
Yaw (Z axis) [µrad]	±200
Roll* (X axis) [µrad] interpolated to a 11.5 mm stroke	±400

Even though the conceptual idea of the mechanism turned out to be successful, several improvements are still required:

1. Angular run outs should be reduced, especially the pitch of the slider. This makes it very difficult to use the interferometer to measure the position of the slider accurately. These rotation deviations must be also reduced to improve the performance of the mechanism.
2. The equilibrium position is very sensitive to the inclination of the prototype. Even a very small tilt of the mechanism makes the PM move away from the central equilibrium position. An improvement of the equilibrium position stability would be very desirable.
3. An amplifying system must be developed to supply the demanded current in the coils. The available data acquisition and generation card (NI PCI-6230) only provides an output current of $\pm$ 5 mA and the current required through the experiments was up to 200 mA.

In summary, a prototype of a positioner based on superconducting magnetic levitation has been designed, built and tested. The conceptual idea of the linear positioner has been demonstrated and the initial performance has been evaluated. Studies and conclusions of this chapter will be used in the next chapter in order to improve the performance of the mechanism.

Chapter V

Engineering of the *FTS* mechanism

In this chapter, it is demonstrated how the most relevant characteristics of the FTS mechanism - such as the stiffness and run outs- can be tuned, mainly by modification to the geometry of the prototype. An experimental study of a real prototype and FEM calculations are in good agreement and support of the design rules given in this chapter.

5.1 Introduction

Chapters III and IV presented how a prototype of a superconducting magnetic slider (*FTS1*) was designed built and tested. Experimental results on the test developed on the *FTS1* prototype were very successful and the working principle of the *FTS* mechanism was demonstrated. A large stroke over ± 11 mm was proved with a maximum demanded current in the coils of about ± 225 mA. In addition, angular run outs were demonstrated to be always lower than a few mrad. Lateral and vertical run outs were also measured and lower than 250 µm. However, in order to achieve a performance of the *FTS1* prototype closer to the requirements for a cryogenic long-stroke nanopositioner, further investigation is required.

It is the aim of this chapter to establish a set of design rules so the aforementioned parameters of the *FTS* mechanism can be modified Furthermore, an experimental study of different modifications on the *FTS1* prototype and FEM calculations were carried out to prove the suggested design rules.

5.2 Theoretical considerations and design rules

In this section, theoretical considerations for the *FTS* mechanism are considered and a set of design rules introduced. A model for the pitch and theoretical considerations of yaw and roll are presented. In addition, how the sensitivity, stiffness and stability of the FC equilibrium position can be modified is discussed.

5.2.1 A model for the pitch

A mechanical model for the pitch of the PM is proposed. First of all, some hypothesis must be assumed: the pitch is small and the PM is a rigid body; the self-alignment of the PM with the magnetic field generated by the coils is neglected due to the small pitch angles involved; the interaction between the coils and the superconductors is also neglected. Lastly, the displacements of the centre of masses of the PM in the direction of the Z axis (see Fig. 5.1.) are neglected.

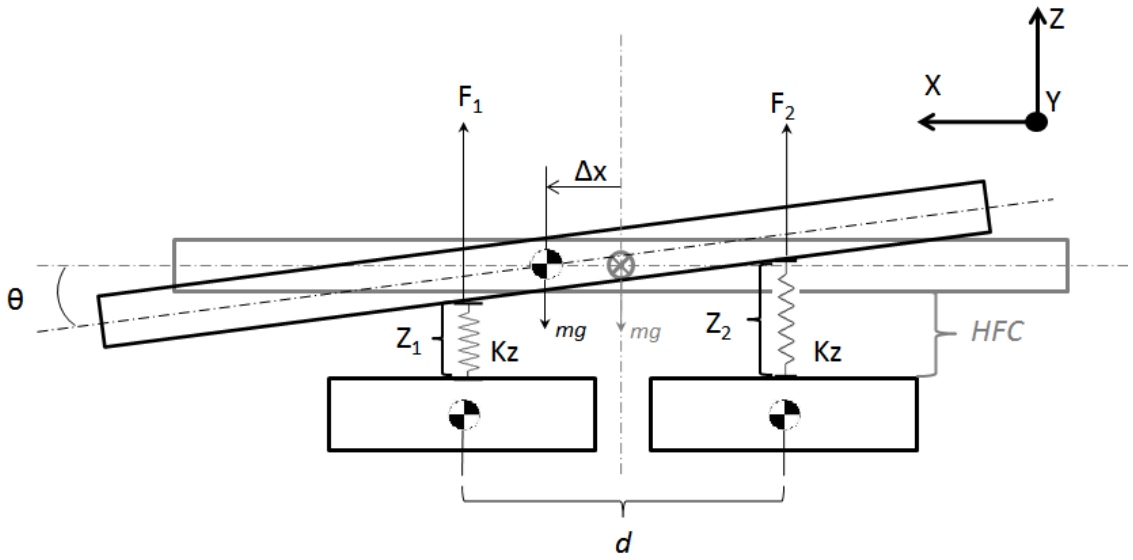

Fig. 5.1. Mechanical model for the pitch.

The forces between the PM and the two superconductors in the mixed state located with a distance d between them, always symmetric with respect to the vertical dashed line, are approximated to the equivalent forces exerted by a couple of springs of constant stiffness K, and initial length Z_0=*HFC* with their axis aligned along the axis of the *HTS* as show in Fig. 5.1.

Then, once there is a displacement in the X direction as presented in Fig. 5.1, and rotation of the PM (θ) occurs at the same time the following can be stated:

Provided the pitch of the PM is very small, some assumptions are valid:

$$tan\,\theta \approx \theta$$

eq. 5.1

$$F \cong F_z$$

eq. 5.2

From the equilibrium of forces and torques on the PM

$$F_1 + F_2 = mg$$

eq. 5.3

Equilibrium of moments lead to eq. 5.4

$$F_1\left(d/2 - X\right) - F_2\left(d/2 + X\right) = 0$$

eq. 5.4

By combination of eq. 5.3 and eq. 5.4, it is easy to demonstrate that:

$$(F_1 - F_2) = \frac{2mgX}{d}$$

eq. 5.5

Insofar as a constant stiffness of the equivalent springs in the model is assumed,

$$\Delta F = -K_Z \cdot \Delta Z$$

eq. 5.6

where

$$\Delta F = F_i - F_i^0 \ and \ \Delta Z = \ Z_i - HFC$$

Obviously, for X=0, the force distribution is symmetric and eq.5.6 means:

$$F_1^0 = F_2^0 = \frac{mg}{2}$$

and consequently

$$\Delta F = \left(F_i - \frac{mg}{2}\right)$$

eq. 5.7

In order to define a relationship between the pitch and the position of the slider, a trigonometric eq. 5.8 can be derived:

$$tan\,\theta \approx \theta = \frac{(Z_2 - Z_1)}{d}$$

eq. 5.8

Eq. 5.8 can also be expressed, in combination with eq. 5.6 as

$$\theta = \frac{(F_1 - F_2)}{K_z d}$$

eq. 5.9

Finally, by combination of eq. 5.9 and eq. 5.5, the following formula describes the pitch of the slider for any X position in its path:

$$\boldsymbol{\theta = \frac{2mg}{K_Z d^2} X}$$

eq. 5.10

From eq. 5.10 some strategies can be deduced to reduce the pitch of the slider:

1. Increase in the vertical magnetic stiffness: It has been demonstrated that the levitation force and the vertical magnetic stiffness of a PM over an FC superconductor is enhanced when the height of field cooling (*HFC*) is reduced [138–141]. Then, the vertical magnetic stiffness can be increased by a reduction in *HFC* and the pitch would also be reduced.
2. Increase in the distance between the superconductors, *d*: According to eq. 5.10. $\theta \sim f\left(\frac{1}{d^2}\right)$. Therefore an increase in *d* would lead to a quadratic reduction in the pitch.
3. Reduction in the mass of the slider would linearly reduce the pitch.

5.2.2 Reduction in the pitch by means of magnetic correction

Pitch was found to be the most critical run out in the tests developed and reported in chapter IV. According to eq. 3.7, an alignment torque is exerted on a PM when it is immersed in a magnetic field. Then, if the elevation of the coils is increased as shown in Fig. 5.2, it can be demonstrated that the total alignment torque on the PM is increased. This correction of the pitch by modifying the elevation of the coils can be interpreted as the magnetic self-alignment of the slider. A huge advantage of this technique would be that it is a completely passive correction of the pitch.

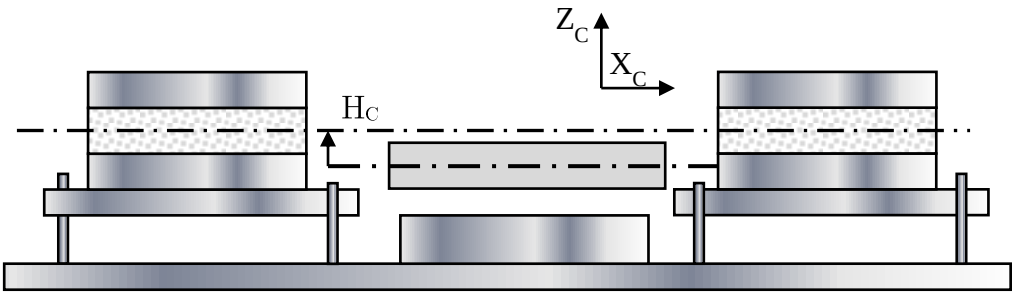

Fig. 5.2. Elevation of the coils is defined as the distance between the imaginary line that passes through the centres of the coils and the axis of the PM.

Another option to reduce the pitch is an active magnetic correction system. By the appropriate application of a magnetic field on the PM, a reduction in the pitch can be obtained. In the case of the *FTS* mechanism, a couple of auxiliary coils were installed in anti-serial configuration as shown in Fig. 5.3.

The magnetic field that they generate is such that pitch can be corrected by modifying the driven current in these auxiliary coils.

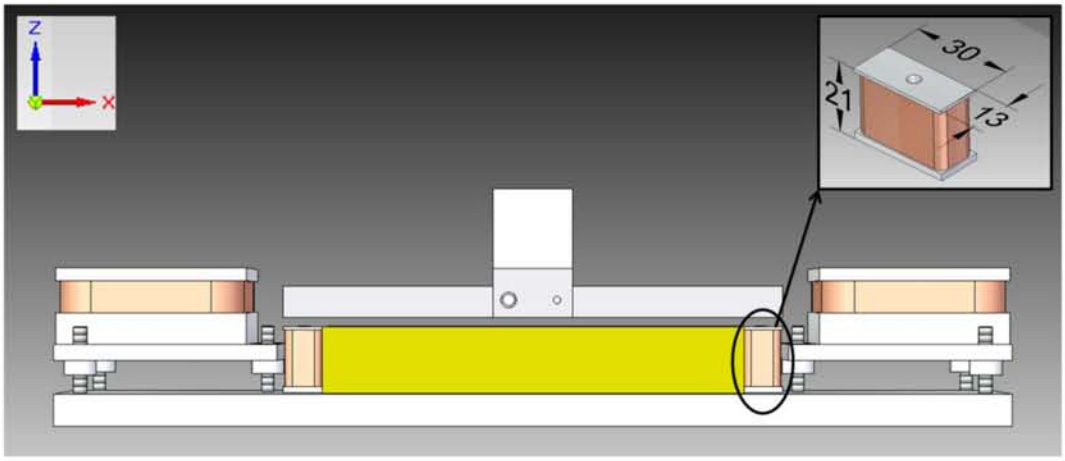

Fig. 5.3. CAD representation of the correction coils installed.

Results of this strategy for the correction of the pitch of the slider can be found in section 5.3.3 of this chapter.

5.2.3 Reduction in the run outs

As has already been suggested, yaw and roll are mainly caused by misalignment between the PM and the coils (more specifically, by the magnetic alignment of the magnetisation direction in the PM and the direction of the magnetic field generated in the coils). In the case in which there is a misalignment, a torque would be exerted in the PM as introduced in eq. 3.7, and an angular run out will appear. The same rules can be applied to the lateral run out of the *FTS* mechanism. In this context, a few considerations can be taken into account in order to reduce both, the yaw and roll of the slider:

1. As introduced in the previous sections, a reduction in the *HFC* leads to an increase in the levitation force and vertical magnetic stiffness. It is also expected that stiffness of the slider in any other DoF are also improved, and therefore, angular run outs are reduced. Obviously, vertical and lateral run outs are also reduced if the vertical stiffness provided by the superconductor is increased. Then, a reduction in the *HFC* will reduce all run outs of the slider.
2. If an improved alignment between the coils and the PM is provided, it is anticipated that the angular run outs and the lateral run out will be reduced.

5.2.4 Sensitivity and stiffness of the slider and stability of the initial equilibrium position

Sensitivity and stiffness to the motion of the slider in the sliding direction are quite related. If the stiffness of the mechanism is increased, then, the sensitivity will be reduced provided the same coils are used. It has been shown that the force exerted on the slider by the superconductors in the *FTS* mechanism is related to the gradient of the magnetic induction and the magnetisation of the superconductors in the sliding direction. The magnetic field in the sliding direction of the *FTS* mechanism is caused by boundary effects, as has been already introduced in chapter III.

As is well known, a magnetic field increases quadratically when the distance to the magnetic source is reduced. In view of this two strategies to increase the stiffness of the mechanism (and consequently reduce the sensitivity of the system) are:

1. Reduce the *HFC*.
2. Increase the distance between the superconductors (d) so that the distance from the superconductors' edges and the PM ends is reduced.

Despite a loss in sensitivity, being considered pernicious in some applications, in this case it may be a benefit. If one wants to locate a slider with nanometric resolution (100 nm) in the range ± 9 mm, a resolution of around 18 bits is required[1]. Therefore, in the case of the *FTS1* prototype, a *"noise-free"* current resolution of about 1 µA with a maximum demanded current of about 225 mA is needed. However, it may be useful to have a less demanding minimum current step even if the maximum current demanded is increased. In summary, it is not necessarily detrimental for the performance of the *FTS* mechanism to reduce its sensitivity due to technical limitations. The stability of the initial equilibrium position will also be highly influenced by the stiffness of the slider to its motion in the sliding direction. Therefore, the same rules can be applied.

[1] 18 bits are equal to 262144 divisions, greater than the 180000 at least required to achieve 100 nm resolution.

5.3 Experimental study

An experimental study was carried out in order to verify the design rules given in the previous sections of this chapter. With regard to the experimental study, different geometric configurations of the *FTS* mechanism were tested. In other words, different variants of the *FTS1* prototype were tested. Some geometric parameters in the *FTS* mechanism modified during these experiments are:

1. The distance between the superconductors (*d),* defined as the total distance between the centres of the superconducting disks *(HTS).*
2. The height of levitation *(HFC),* defined as the distance between the upper surface of the superconductors and the bottom surface of the PM. Both *HFC* and *d* are represented in Fig. 5.4.
3. The elevation of the coils in the Z axis (H_c) defined as the vertical distance between imaginary line that pass though both centres of the coils and the axis of the PM as shown in Fig. 5.9.
4. An active magnetic correction system, based on two auxiliary coils (9) as show in Fig. 5.4 was built with the aim to reduce the pitch of the slider.

In addition, different electric connectivities of the coils were considered and studied.

Regarding the FEM calculations, the decoupled model proposed in chapter IV was used. From the *X position vs. current* function obtained in the experimental study, the forces on the slider were calculated. Then, some parameters like the stiffness of the slider to its motion in the sliding direction of the *FTS* mechanism will be estimated.

5.3.1 Experimental set up and procedure

The experimental set up in these experiments is very similar to the experimental set up described in of chapter IV and is shown in Fig. 5.4.

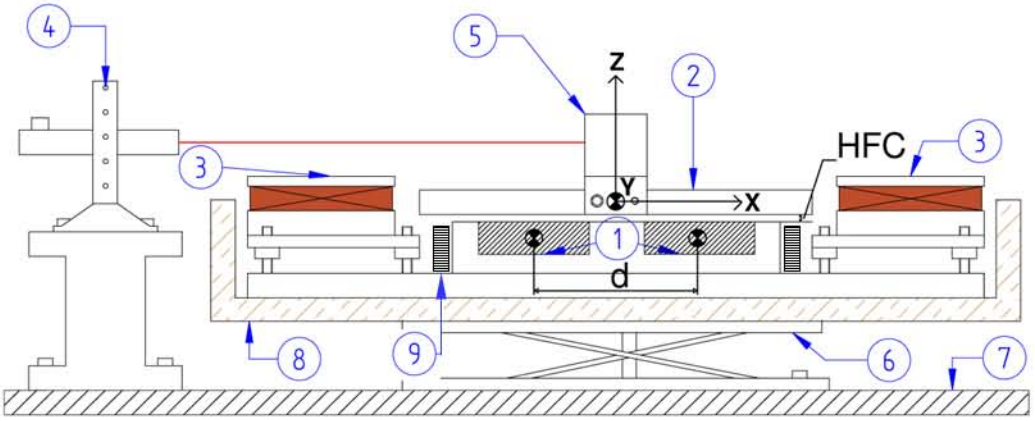

Fig. 5.4. Experimental set up during the tests. 1)HTS; 2) PM; 3) coils; 4) auto-collimator; 5) optic cube; 6) lab-jack stand; 7) optic table; 8) LN_2 vessel and 9) correction coils.

To set multiple distances between the superconductors (d), several boards made of extruded polystyrene were constructed. The superconductors were properly fixed to these boards and they were carefully fixed to the prototype base. In order to set the levitation height (HFC), spacers were again used and retired when the PM was stably levitating over the superconductors.

The elevation of the coils (H_c) with respect to the axis of the PM was fixed using three pairs of screws and nuts on the *FTS1*, already described in chapter IV. Additionally, in order to measure the maximum stroke of the prototype, one of the coils was removed when needed, thus the PM could travel further than the designed stroke of ± 9 mm. Finally, it should be highlighted that uncertain of the position of either HFC, d and H_c, is considered ± 250 µm in all results presented in this chapter. It must be also noted that, for all experiments reported in this chapter, only one geometric parameter was modified at a time.

After a concrete configuration is achieved, the prototype was cooled in a bath of liquid nitrogen at ambient pressure (T= 77 K). Once the superconductors are at a temperature below their critical temperature (T_c=93 K), the PM was able to stably levitate over the superconductors. Then, the position of the slider was modified by variations in the current supplied to the coils, once again generated by a dual-channel power supply. For most data presented in this chapter, only one pushing coil (the force exerted by the coil pushes away the PM) is active, whilst the other is switched off. The current in the coils was measured with independent polymers with a resolution that is dependent on the field of measurement. The position of the slider in each axis (X, Y and Z) was measured using scales with 250 µm resolution.

The Newport auto-collimator used for the preliminary tests was used again to measure the angular run outs of the slider. It also has to be mentioned that

only the pitch and yaw of the slider were measured (set up A in chapter III) to reduce the time needed for the development of all tests presented in this chapter. Therefore, no data regarding the roll of the slider will be found in this chapter.

A diagram of the experimental procedure is shown in Fig. 5.5.

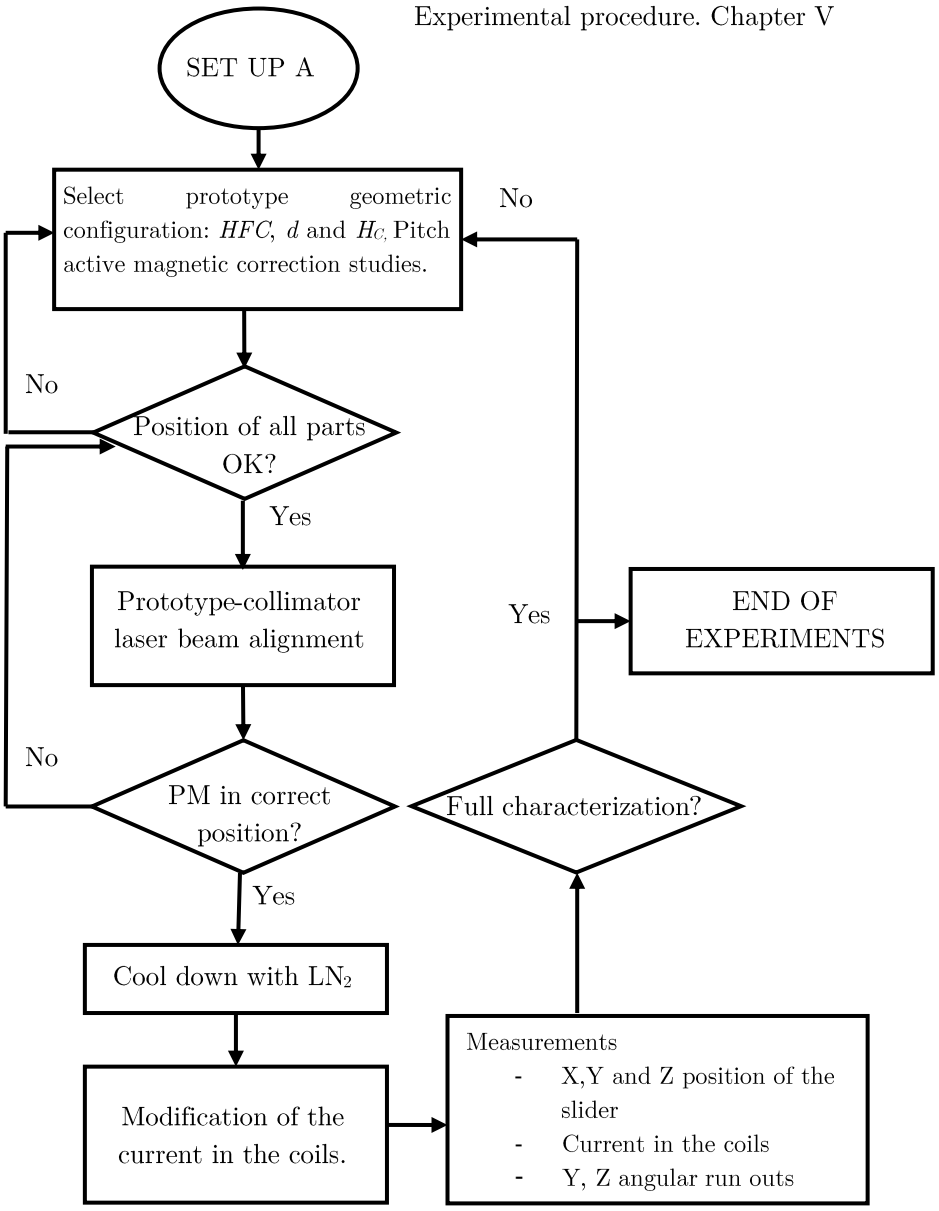

Fig. 5.5. Experimental procedure of the experimental study.

Run outs in Y and Z axis were always lower than 250 µm and therefore, no measurements will be presented in this chapter.

5.4 Test results and discussion

The results of the experimental tests developed and the FEM calculations are discussed in this section. Theoretical considerations proposed at the beginning of this chapter are compared with both, the experimental study and FEA.

5.4.1 Angular run outs

5.4.1.1 Angular run outs versus the distance between the superconductors

According to the proposed model for the pitch, $\theta \sim f\left(\frac{1}{d^2}\right)$, therefore, the higher the value of d, the lower the pitch of the slider. It can be also derived from eq. 5.10 that the relation between the pitch of the slider and the X position of the slider must be linear. Pitch vs. X position of the slider for different values of d is shown in Fig. 5.6. Good linearity of the results can be observed, which are in good agreement with eq. 5.10.

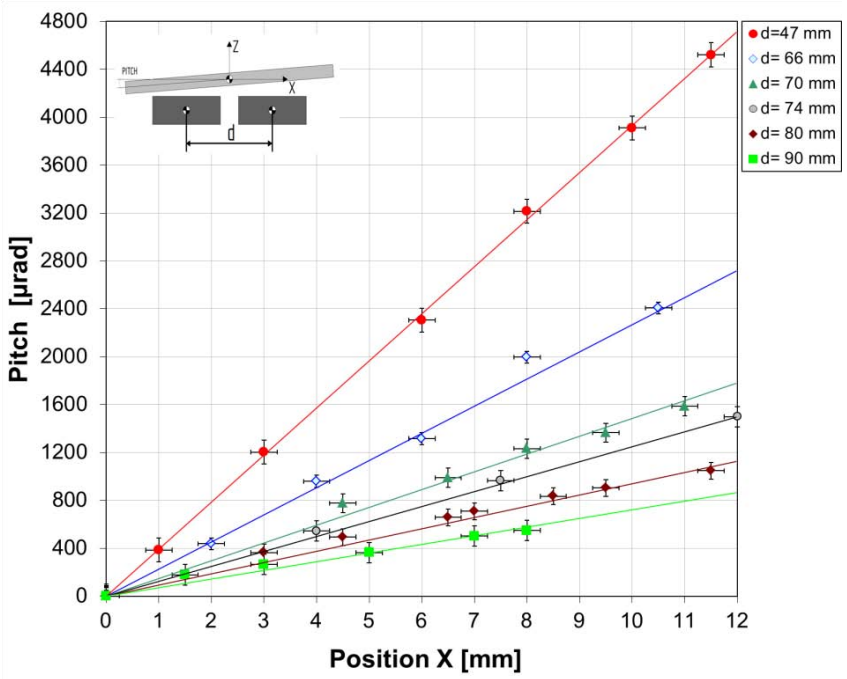

Fig. 5.6. Pitch vs. X position of the slider for different values of *d*. *HFC*= 3 mm and HC=0 mm in all cases. Temperature of the prototype, T= 77 K.

Likewise, pitch sensitivity, (i.e θ/X) presents a behaviour that agrees well with that predicted by eq. 5.10 as it can be seen in Fig. 5.7.

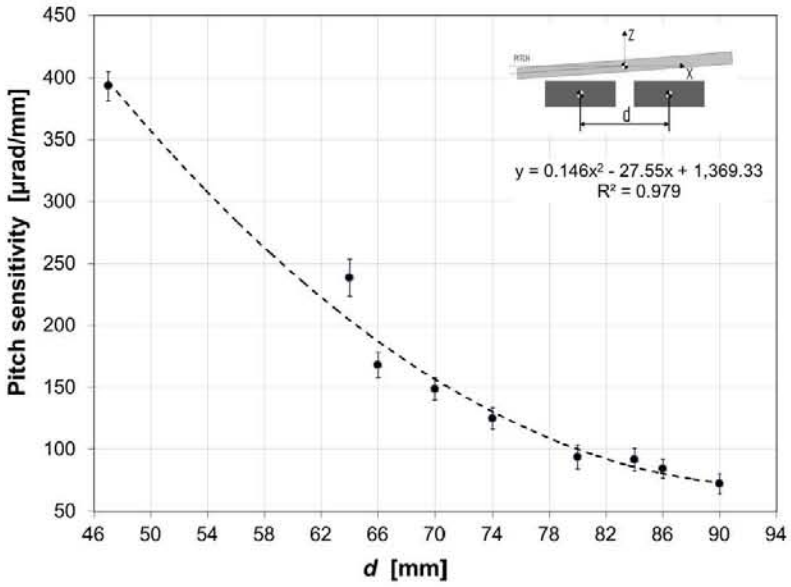

Fig. 5.7. Pitch sensitivity vs. distance between superconductors. *HFC*= 3 mm and HC=0 mm in all cases. Temperature of the prototype, T= 77 K.

Yaw was also analysed for different values of d. The results of these measurements are plotted in Fig. 5.8. Yaw vs. X position shows good linearity for all measurements. In addition, we searched for a relationship between yaw and d but found none. This fact reinforces the idea that this angular run out is due to a misalignment between the magnetisation axis of the PM and the axis of the magnetic field generated by the coils.

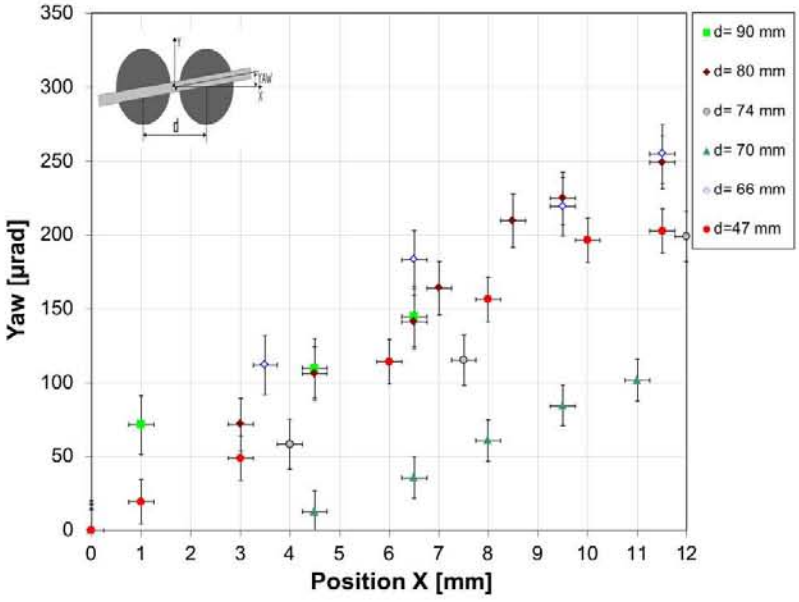

Fig. 5.8. Yaw vs. X position of the slider for different values of d. *HFC*= 3 mm and HC=0 mm in all cases. Temperature of the prototype, T= 77 K.

5.4.1.2 Reduction in pitch by means of magnetic self-alignment

Tests were developed for a configuration of the prototype of *HFC*= 3 mm and *d*= 84 mm. Firstly, an elevation of the coils between 0 and 9 mm has to be considered. Then, the current through the coil was such that the magnetic field generated exerted an attractive magnetic force on the PM. It was observed that the total pitch of the slider was reduced for a higher elevation of the coils. The maximum pitch for a travel length of 9 mm is presented in Fig.5.9.

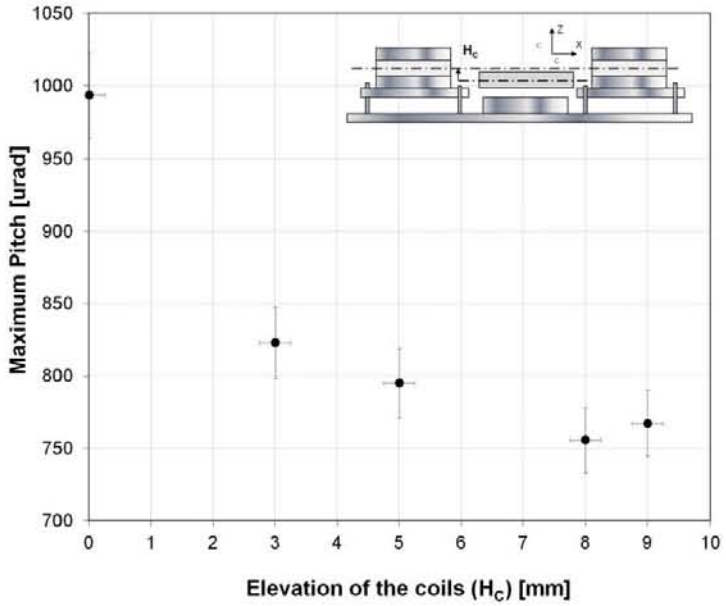

Fig. 5.9. Maximum pitch for a 9 mm stroke vs. elevation of the coils (H_c). *HFC*= 3 mm and *d*= 84 mm. Temperature of the prototype, T= 77 K.

A significant reduction in the pitch can be achieved simply by elevating the coils a few millimetres from the reference position. Nevertheless, the reduction in the pitch becomes much more significant when the PM gets closer to the pulling coil as can be deduced from Fig. 5.10, where pitch vs. relative X position of the slider is plotted for elevations of the coils of 0 and 8 mm.

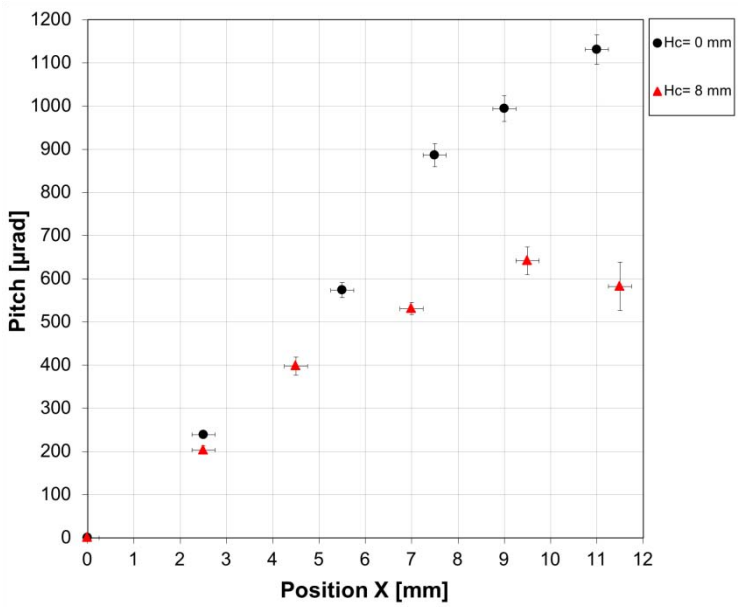

Fig. 5.10. Pitch vs. X position of the slider for different values of Hc. *HFC*= 3 mm and *d*= 84 mm. Temperature of the prototype, T= 77 K

5.4.1.3 Reduction in pitch by means of active magnetic correction

By the selection of *HFC*= 3 mm, *d*= 84 mm and H_C= 5 mm, the pitch could be reduced below ± 800 µrad for a full stroke motion (± 9 mm). However, in order to achieve a lower angular run out of the slider, a couple of auxiliary coils were installed between the superconductors' base and the main coils as show in Fig. 5.4 These correction coils were built with an inner air core with 30 turns each. In order to test the pitch correction using these auxiliary coils, the slider was moved to different X positions in its path and a current was supplied to the correction coils. Upon this, the position, pitch and current in the coils were registered. Pitch vs. current in the correction coil for a *HFC*= 3 mm, *d*= 84 mm and H_C= 5 mm is shown in Fig. 5.11.

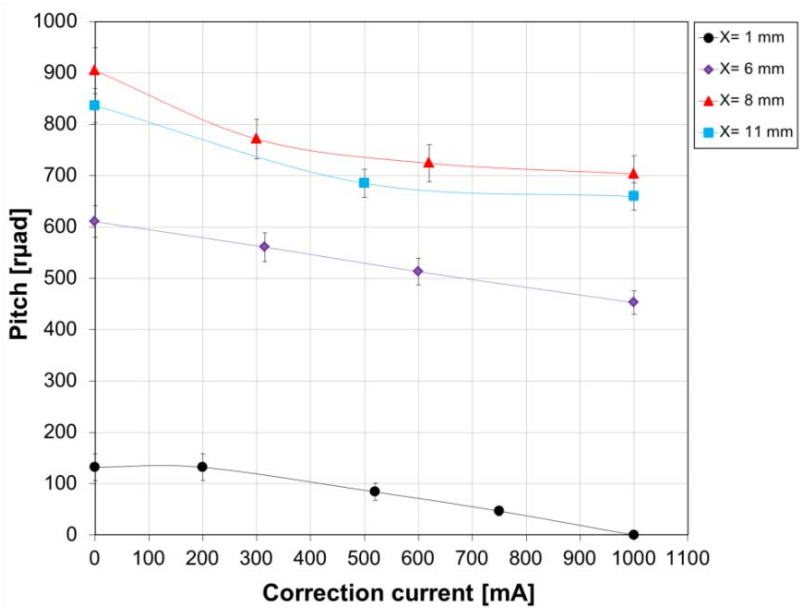

Fig. 5.11. Pitch vs. current in the correction coils for different X position of the slider. *HFC*= 3 mm, *d*= 84 mm and H_C= 0 mm in all cases. Temperature of the prototype, T= 77 K.

Despite the active magnetic correction, turning out to be successful, it has to be mentioned that these correction coils also cause a displacement of the PM in the X direction over a few millimetres in the worst of the cases. This displacement was compensated by circulating an offset current in the main coils. At this point, we decide to discard active magnetic correction in order to simplify the motion control of the slider.

5.4.1.4 Angular run outs versus height of field cooling

Reducing the *HFC* should improve the vertical magnetic stiffness of the PM. Subsequently, a reduction in all angular run outs can be anticipated when reducing the height of levitation. *HFC* was modified between 2 and 6 mm and the performance of the device analysed from the point of view of its angular run outs. Results for pitch of the slider vs. X position for different *HFC* are presented in Fig. 5.12.

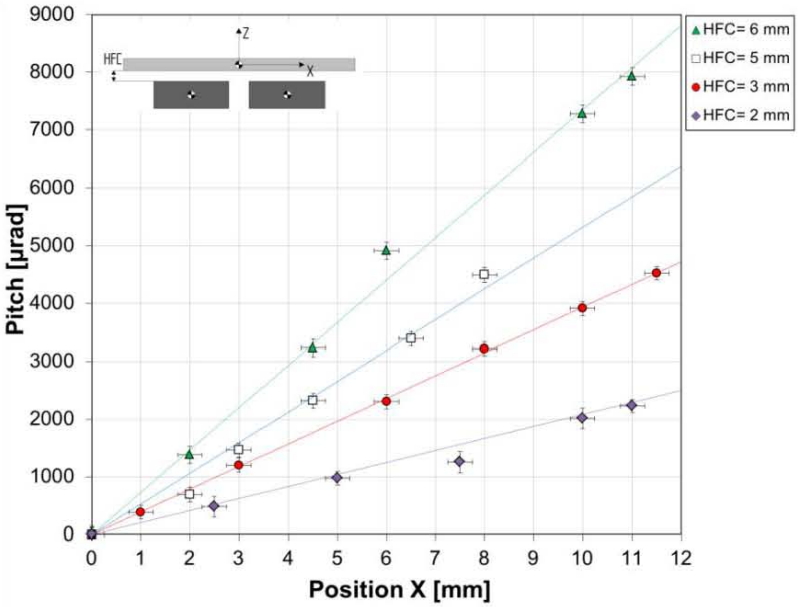

Fig. 5.12. Pitch vs. X position of the slider for different values of *HFC*. *d*= 47 mm and HC=0 mm in all cases. Temperature of the prototype, T= 77 K.

It is clear in Fig. 5.12 that the pitch is reduced by decreasing the height of levitation of the PM. Yaw is also dependent on the *HFC*, as can be deduced from Fig. 5.13. Reduction in the yaw of about a factor of 2 in a stroke of ± 9 mm can be achieved by reducing the *HFC* from 6 mm to 2 mm.

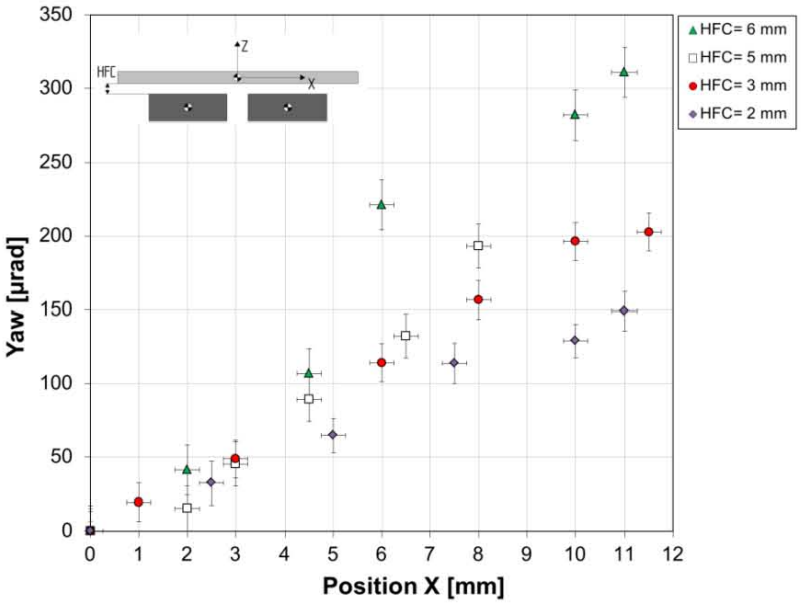

Fig. 5.13. Yaw vs. X position of the slider for different values of *HFC*. *d*= 47 mm and HC=0 mm in all cases. Temperature of the prototype, T= 77 K.

Having seen the results in Fig. 5.12 and Fig. 5.13 it seems clear that the lower the *HFC*, the better the performance of the prototype in terms of angular run outs.

5.4.1.5 Improvement of the proposed model for the pitch

After the set of tests reported in the foregoing sections, the precision of the model can be tested. Some conclusions about the simplified model are:

1. The model explains the linear relationship between pitch and the X position of the slider. Experimental results agree quite well with this conclusion.
2. The model also explains qualitatively the relationship between the pitch and the separation between the superconductors *d*. That relationship was proposed to be of the shape $\theta \sim f\left(\frac{1}{d^2}\right)$ and the experimental results are in good agreement.
3. The stiffness of the equivalent springs in the proposed model was found experimentally to increase for a larger distance between superconductors *d* as shown in Fig. 5.14. In that figure, the experimental normalised stiffness ($K_N = \frac{K_j}{K_{47}}$) where K_i is the stiffness of the equivalent springs in the model at a certain *d* and K_{47} Is the stiffness at *d*= 47 mm is plotted vs. *d*.

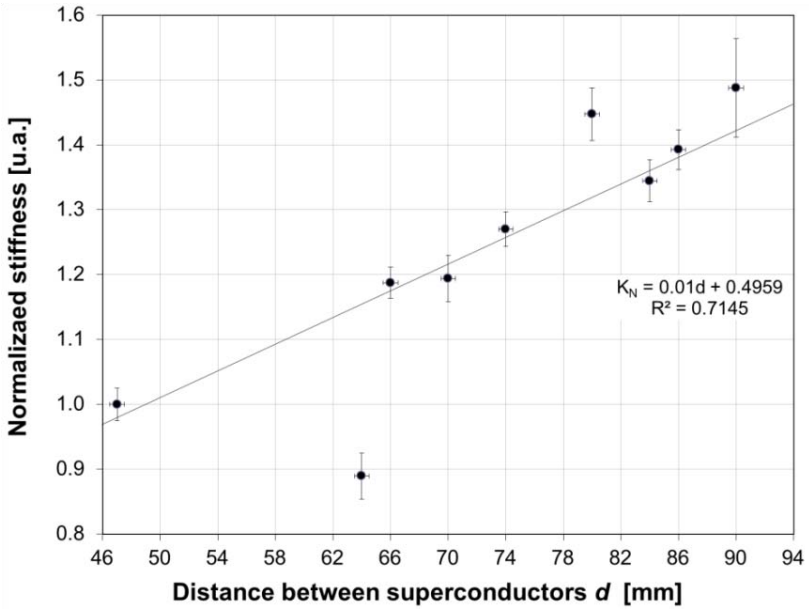

Fig. 5.14. Normalised vertical magnetic stiffness of the slider vs. distance between superconductors. *HFC*= 3 mm and Hc= 0 mm in all cases. Temperature of the prototype, T= 77 K.

A comparison of the two models, i.e. the one with constant stiffness (considering reference stiffness as K for *d*=47 mm) and the other with *K~f(d)* with the experimental data is shown in Fig. 5.15.

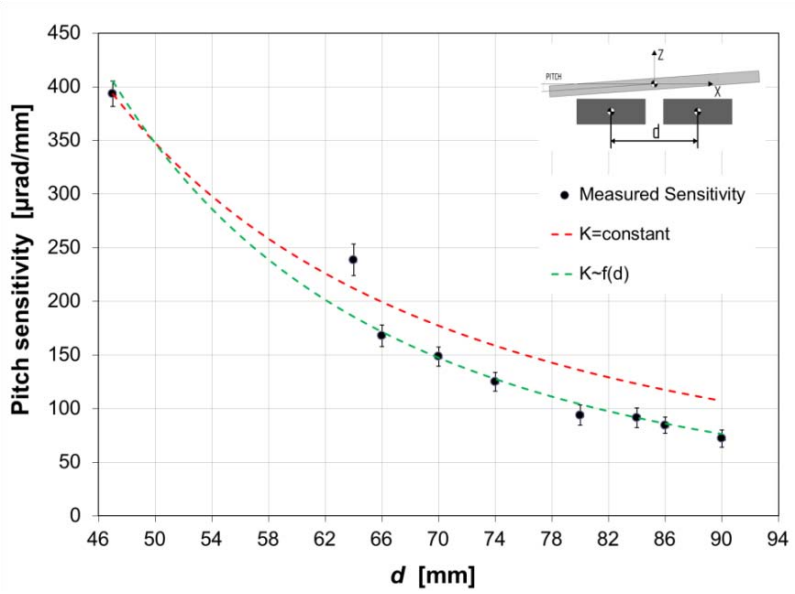

Fig. 5.15. Pitch sensitivity vs. distance between the superconductors. Comparison of the models for the pitch.

In summary, the proposed simplified model for the pitch predicts the behaviour of the pitch of the slider reasonably well. However, an empirically-based correction for the calculation of the vertical stiffness of the superconductors has been proposed, taking into account a linear dependence of K on the distance between the superconductors. Very good agreement between the improved mathematical model for the pitch of the slider and experimental data has been demonstrated.

5.4.2 Sensitivity, stiffness and stability of the equilibrium position

5.4.2.1 Sensitivity versus distance between the superconductors

It was observed in the preliminary tests on the *FTS1* prototype that the stability of the initial equilibrium position was very low due to the action of gravity. Any small misalignment between the Z axis of the PM magnet and the action of gravity makes the slider move away from the initial equilibrium position. It is very desirable to increase the initial stiffness of the slider so that the initial equilibrium position is more stable. Moreover, it has been previously derived that due to the low stiffness of the slider to motion in the X direction, a very low minimum current step (~1 µA) was required for the operation of the *FTS1* prototype. Therefore, an increase in the X motion stiffness of the slider would be desirable.

The first step in order to characterise the magnetic stiffness of the slider to its motion in the sliding DoF to measure the sensitivity to the motion of the PM by using a pushing coil (the coil repeals the PM) for different distances between the superconductors, *d*. See fig. 5.16.

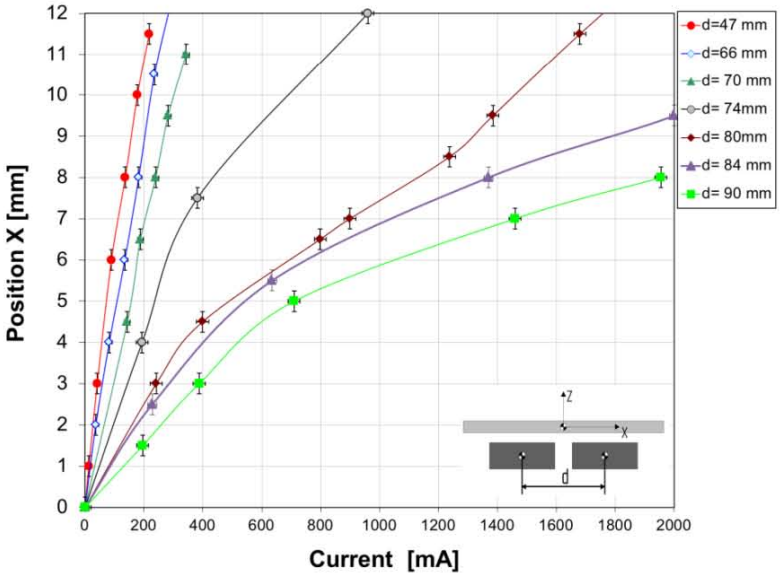

Fig. 5.16. X position of the slider vs. current in the pushing coil. *HFC*= 3 mm and Hc= 0 mm in all cases. Temperature of the prototype, T= 77 K.

Although the sensitivity of the slider to its motion in the sliding direction shows a high dependence on the position of the slider in its path for values of *d* greater than 70 mm, good linearity is observed in all cases for a stroke smaller than ±3mm. Both, the estimated sensitivity and the consequent minimum required current step for a 100 nm resolution are summarised in Table 5.1 for different values of *d*.

Table 5.1. Estimated values of sensitivity (±3 mm stroke) and minimum current step required for nanometre resolution. *HFC*= 3 mm in all cases.

***d* [mm]**	**~S [nm/μA]**	**~Minimum current step [μA]**
47	78.4	1
66	54.9	2
70	31.4	3
74	20.7	5
80	12.4	8
84	10.1	10
90	7.7	13

These results show that the minimum current step to reach nanometre resolution in the position of the slider is increased by about one order of magnitude when the distance between the superconductors, *d*, is increased from 47 to 84 mm. However, the sensitivity of the slider is consequently reduced. This fact must be considered for certain applications.

5.4.2.2 Stiffness, potential energy and stability of the equilibrium position versus distance between superconductors.

Once the dependence of the X position of the slider on the current in the pushing coil has been characterised, the force exerted on the PM by the coils can be calculated using the simplified FEM model introduced in chapter IV. The calculated force in the X direction on the PM exerted by the coil vs. X position reached by the slider is presented in Fig. 5.17.

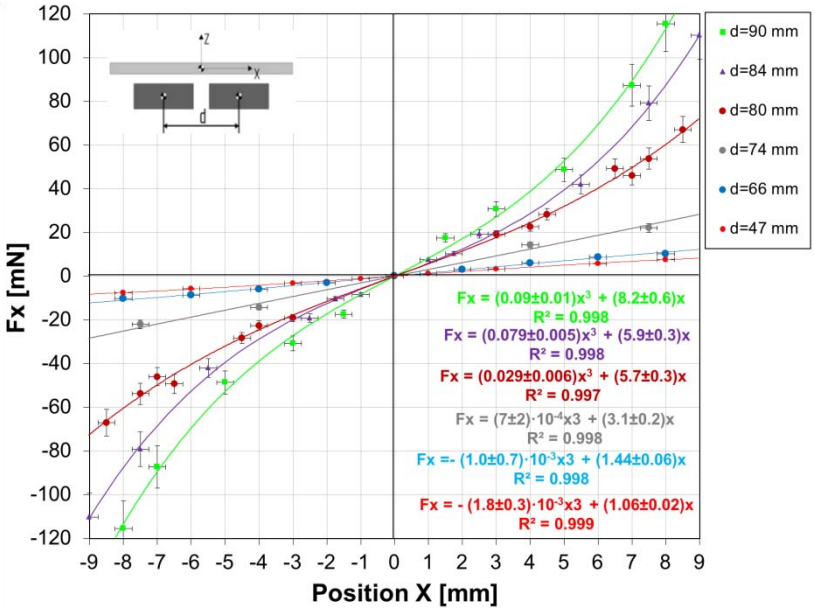

Fig. 5.17. Fx vs. X position of the slider calculated in Maxwell V.15 FEA software from experimental data for different values of *d*. *HFC*= 3 mm and Hc= 0 mm in all cases. Temperature of the prototype, T= 77 K.

As can be seen in Fig. 5.17, the force on the slider in the X direction versus the X position of the slider can be described accurately by a third order polynomial. An estimation of the uncertainty in the force was made by applying the procedure explained in chapter IV and considering the Meissner state as the less favourable situation. The hysteresis of the device was inevitably below 250 µm for all *d* configurations tested. In addition, the stiffness of the mechanism in the X direction K_X, can be expressed by the following formula:

$$K_X = \frac{\partial F_X}{\partial X}$$

eq. 5.11

Calculated stiffness vs. X position of the slider is presented in Fig. 5.18.

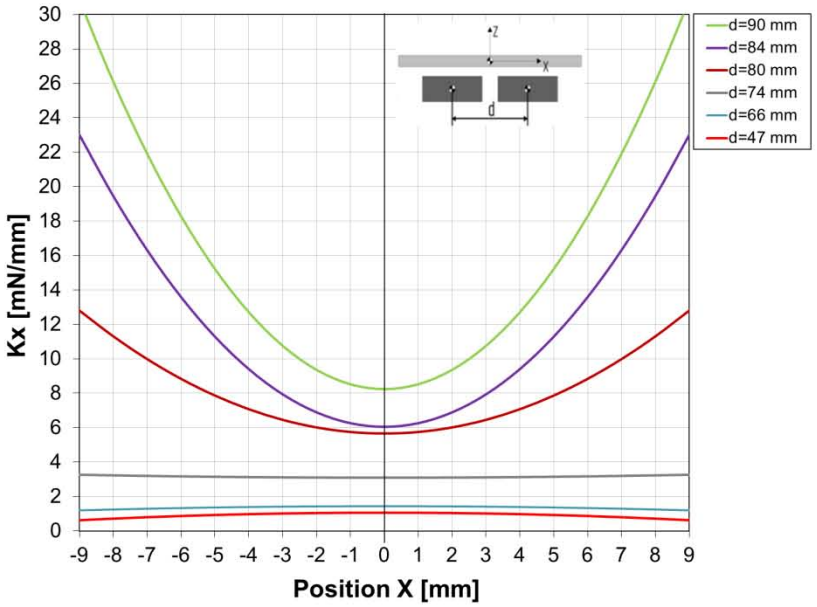

Fig. 5.18. Calculated stiffness vs. X position of the slider for different values of *d*. *HFC*= 3 mm and Hc= 0 mm in all cases. Temperature of the prototype, T= 77 K.

According to Fig. 5.18, two effects can be clearly identified when the distance between the superconductors is increased. First, the initial stiffness of the mechanism is increased (see Table 5.2) from around 1 mN/mm for *d*=47 mm to around 8 mN/mm for *d*=90 mm.

Table 5.2. Stiffness of the *FTS* mechanism at the initial position (X= 0 mm) for different values of *d*. *HFC*= 3 mm in all cases.

K_i [mN/mm]	*d* [mm]
1.06±0.02	47
1.44±0.06	66
3.1±0.2	74
5.7±0.3	80
5.9±0.3	84
8.2±0.6	90

Besides this, the stiffness of the slider becomes less and less linear for increased values of *d*, which will also enhance the stability of the equilibrium point. Due to the low value of the hysteresis in the motion of the slider measured (necessarily below the scale resolution of ±250 μm) the potential energy in the slider when it is moved away from the initial equilibrium position (X=0 mm) is described by eq. 5.12:

$$U_X = \int F_X \partial X$$

eq. 5.12

The potential energy U vs. X position of the slider for different values of d is represented in Fig. 5.19.

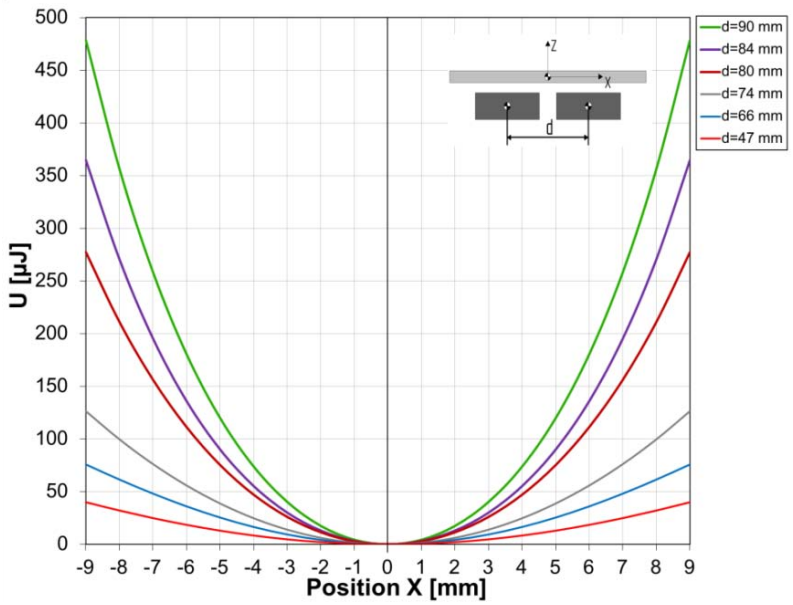

Fig. 5.19. Calculated potential energy vs. X position of the slider for different values of *d*. *HFC*= 3 mm and H_C= 0 mm for all cases. Temperature of the prototype, T= 77 K.

5.4.2.3 Sensitivity versus height of field cooling

The current requirement and stiffness of the system decrease for a higher height of levitation, *HFC*. See Fig. 5.20.

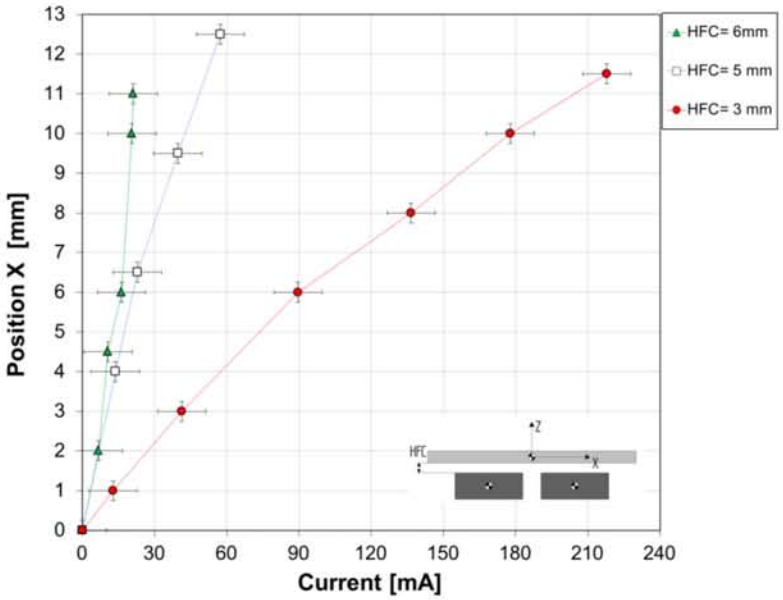

Fig. 5.20. X position of the slider vs. current in the pushing coil for different values of *HFC*. d= 84 mm and H_C= 0 mm in all cases. Temperature of the prototype, T= 77 K.

Sensitivity and the minimum current step needed to reach a position resolution of 100 nm for different values of *HFC* are summarised in Table 5.3.

Table 5.3. Estimated values of sensitivity (± 3mm stroke) and minimum current step required for a 100 nm resolution. d= 47 mm in all cases.

HFC [mm]	**~S [nm/µA]**	**~Minimum current step [µA]**
6	422	0.2
5	293	0.3
3	78	1

It can be also concluded that the stiffness and the stability of the initial equilibrium position decrease for an increasing *HFC*.

5.4.3 Current required in the coils

It is clear, looking at Fig. 5.15 that the current requirement increases for higher values of d. The maximum current needed in the only active coil (pushing coil) for a full stroke motion (±9 mm) vs. d is plotted in Fig. 5.21. There, it is shown that the maximum current required drastically increases for values of d greater than 70 mm.

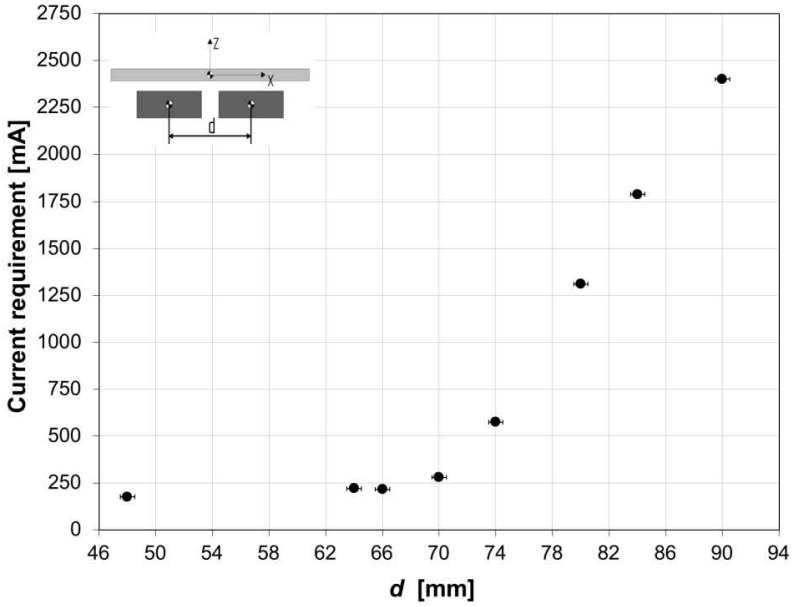

Fig. 5.21. Current requirement vs. distance between the superconductors. *HFC*= 3 mm and *Hc*= 0 mm in all cases. T= 77 K.

In addition, the peak power consumption is also influenced by the *HFC*. Peak current requirement versus HFC to achieve a ± 9 mm is plotted in Fig. 5.22 in a prototype with *d*= 47 mm and H_c=0 mm. It is clear that the current requirement increases exponentially when the *HFC* is reduced.

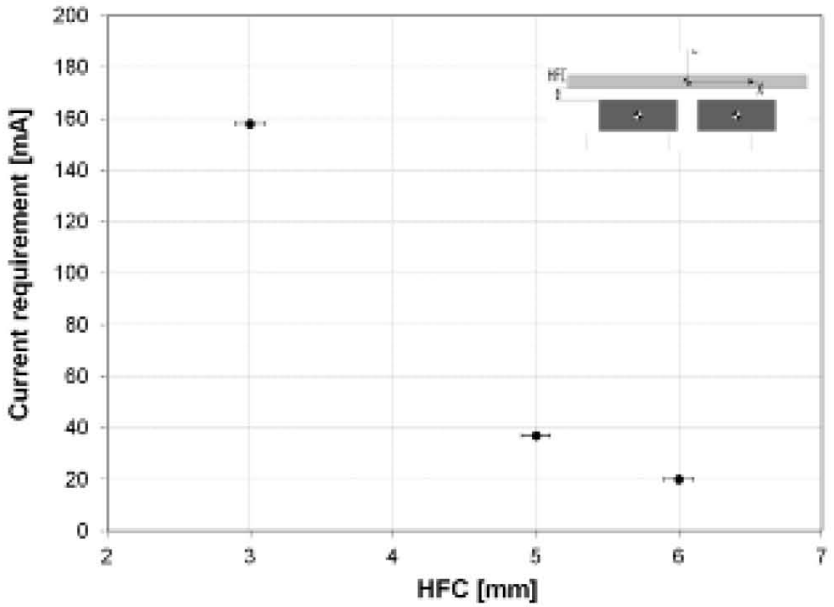

Fig. 5.22.**P**eak current requirement vs. *HFC* in a prototype with *d*= 47 mm and H_c= 0 mm.

In order to design or optimise the prototype a compromise must be made between the different effects of selecting a different value for *d*. On the one hand, the higher the stiffness of the sliding DoF, the more stable the initial

equilibrium position and the higher the minimum current steps. But on the other, the stiffer the slider, the larger the maximum current required and, consequently, the higher the power consumption. Therefore, each of these rules must be considered when making the decision on the optimised prototype.

5.4.4 Optimization of the actuation system

Different electric configurations in the coils were tested. In addition to the characterisation of the force exerted by one coil pushing away the PM, three further configurations were characterised:

1. Intermittent pushing coils: Only one of the coils was switched on at a time. The slider is moved by one of the coils from X= 0 to X= + 9 mm and by the opposite one from X=0 to X= -9 mm. The magnetic field generated by it is what makes the PM move away from the acting coil. Maximum value of force exerted on the PM is reached around the central equilibrium position (X=0 mm) and it is of the order of 50 mN for a circulating current of 500 mA.
2. Intermittent pulling coils: Either of the coils pulls the PM from the initial position. One of them from X= 0 mm to X= -9 mm and the other one from X=0 to X= 9 mm. The maximum current demanded can be drastically reduced by using pulling coils instead of pushing coils as can be observed in Fig. 5.23. In that figure, the magnitude of the demanded current versus X position of the slider for a pushing and a pulling coil configuration is presented. It is estimated that the current demanded can be reduced by about four times and the power consumption of the mechanism can be reduced by around 16 times. The maximum value of force exerted on the PM is now reached at either end of the stroke of the mechanism (X=±9 mm) and is of the order of 140 mN for a circulating current of 500 mA.

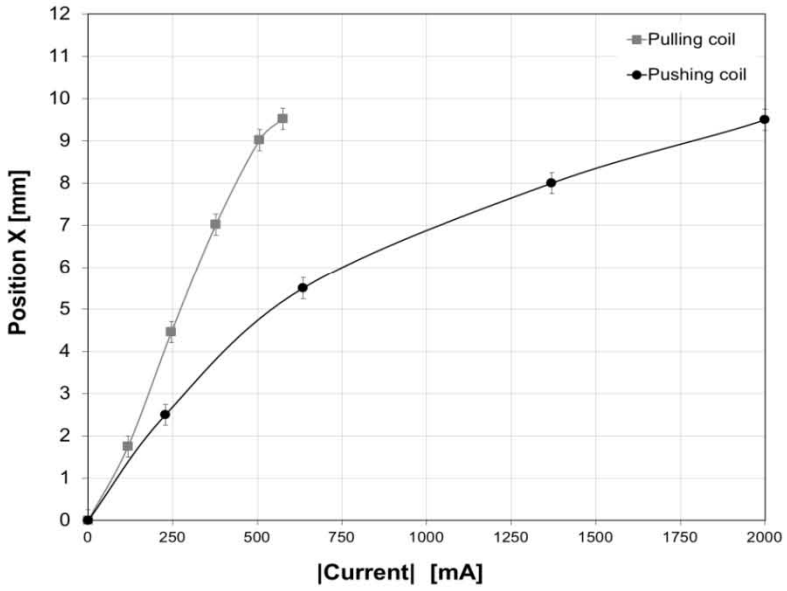

Fig. 5.23. X position of the slider vs. magnitude of the current in a pushing and a pulling coil. *HFC*= 3 mm, *d*= 84 mm and *Hc*= 0 mm in both cases. Pushing coils measured at 77 K, pulling coil at 15 K.

3. Anti-serial pulling-pushing coil: Both coils are connected in an anti-serial configuration, i.e., when one of the coils pulls the PM (attractive force), the other one pushes it away (repulsive force). Then the direction and magnitude of the motion is defined by only one input signal. In addition, the force exerted on the PM is increased with respect to the intermittent pulling coils configuration as shown in Fig. 5.23. It has to be considered that maximum sensitivity of the slider in its path is expected to be increased by about a factor of 2 when using this connectivity between the coils. Finally, a reduction in the demanded current of about a 10-15 % is estimated, and beyond which a reduction in the power consumption of about a 20-30% by using an anti-serial configuration rather than intermittent pulling coils.

The magnitude of the force exerted on the PM for each configuration for a driving current of ±500 mA is presented in Fig. 5.24.

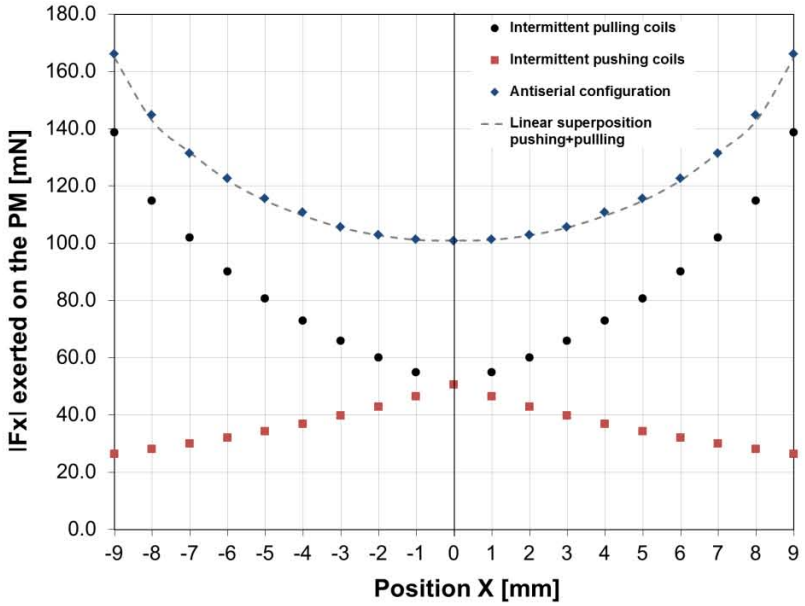

Fig. 5.24. FEM Calculated magnitude of Fx exerted on the PM by the coils for different configurations. Hc= 0 mm in all cases. Maximum error in F_X of about 5% based on convergence analysis of the residuals.

5.5 Conclusions of chapter V

An experimental study and FEM calculations have been carried out in order to prove the theoretical considerations proposed to improve the *FTS* mechanism's performance. A set of prototypes of the *FTS* mechanism were tested, cooling the superconductors with LN_2. FEA was done using the decoupled model proposed in chapter III of this thesis. By comparison of the theoretical predictions and the experimental and FEM results, some design rules for the *FTS* mechanism can be derived and proven. In summary, this design rules are:

- According to the proposed and empirically-improved model for the pitch (see eq. 5.10) pitch of the slider can be reduced by increasing the vertical magnetic stiffness, reducing the mass of the slider or by increasing the distance between the superconductors, *d*. Additionally, the vertical stiffness can be improved by a reduction of the levitation height or *HFC*.

- Magnetic self-alignment of the slider by elevation of the coils can reduce the maximum pitch by about a 25 % for an elevation of H_c= 8 mm (Z axis) from the position where the axis of the PM and the imaginary line that passes through the centres of the coils are aligned.

- Pitch can also be reduced by applying active magnetic force. A couple of auxiliary coils were installed to achieve this reduction. A correction of the pitch that is dependent on the current in the coils and the position of the slider in its path were observed. A correction of the maximum pitch of about a 20% was measured for a driven current in the coils of ±1 A. However, these coils also cause a modification in the position of the slider, needing two variables to control the position of the system.

- Yaw seems to be mainly caused by a misalignment between the PM and the coils. It can be reduced by increasing the magnetic stiffness of the slider, for example, by reducing the *HFC*.

- Lateral and vertical run outs were always below 250 µm for all prototypes tested. Hysteresis is also lower than this value in all cases.

- Force vs. X position of the slider in its path calculated using the decoupled model in FEM described in chapter III, fits a cubic polynomial equation with a R^2 greater than 0.997 in all cases studied. The cubic coefficient results are always about two orders of magnitude, or more, lower than the linear term.

- Sensitivity, stiffness and the stability of the initial equilibrium position can also be modified by geometric modifications to the prototype, such as modification to the *HFC* or the distance between the superconductors, *d*.

- The current requirement and the power consumption of the mechanism are highly dependent on the configuration of the actuation system. A reduction of about a 4 times in the current requirement and 16 times in the peak power consumption can be achieved if an anti-serial connection of the coils is established instead of using only a pushing coil. This connection also is better than a connection of intermittent pulling coils in terms of current and power consumption. The anti-serial configuration also simplifies the control of the position of the slider to just one variable.

Chapter VI

Tests and demonstration in a relevant environment

An improved prototype of the FTS mechanism (FTS2) was designed and tested in a relevant environment in a cryostat (T~15 K and a high vacuum <10^{-6} Pa). The experimental set up and procedure of these tests are presented in this chapter, as well as a discussion of the results and conclusions of the tests. A sub-micrometre resolution of about 230 nm with a symmetric stroke of around 18 mm and a current requirement below ±450 mA was demonstrated. Finally, the dynamic behaviour of the FTS mechanism was characterised.

6.1 Introduction

A prototype (*FTS1*) of a long-stroke and high-precision positioner was designed and built. An experimental study and FEM calculations, introduced in chapter V, supported the definition of reliable design rules for the *FTS* mechanism. A reduction in the angular run outs, the enhanced stiffness of the motion of the slider and a greater stability in the initial equilibrium position were made possible by following these rules.

Therefore, a second prototype (*FTS2* prototype from now on) was designed following these rules, built and tested in a relevant environment according to a TRL 6. This new prototype was tested in a cryostat at an approximate temperature of 15K and in a high vacuum (pressure under 10^{-6} Pa). Results and discussion on these tests are presented in this chapter.

6.2 Description of the *FTS2* prototype

The prototype is essentially composed of a static guideline made of two 45 mm diameter superconducting polycristaline *YBaCuO* disks (1), a slider, mainly composed of a NdFeB vertically-magnetised (Z axis) permanent magnet (2) 160 mm in length carefully aligned on the X reference axis in Fig. 6.1, and two coils (3) placed at either end of the stroke. A CAD representation and a picture of the real *FTS2* prototype are shown in Fig. 6.1.

The superconductors are contained within an aluminium vessel (5), located with their axes separated a distance d away from one another. Based on the design rules presented in chapter V, a reduction in the pitch can be achieved by increasing the distance between the superconductors, d. This will also generate a loss of sensitivity in the sliding of the *FTS2* prototype and a consequent increment of the minimum current step required. Besides, an elevation of the coils H_c has been demonstrated to reduce the pitch of the slider. A value of H_c= 5 mm is selected as the optimum value. An elevation higher than this would cause an excessive reduction in the reflection surface for the laser beam in the optic cube from both, the collimator and the interferometer. A reduction in the *HFC* also reduces the angular run outs. However, the minimum *HFC* achievable was 3 mm due to technical limitations on the operation of the launch & lock system.

At either side of the vessel containing the superconductors, two calibrated class-A PT-100 temperature sensors (4) are placed in order to measure the

temperature of the superconductors throughout the experiments. Indium layers were used in order to assure good thermal contact between the base of the superconductors and the superconductors, and between the base and the PT-100 sensors. In addition, thermal straps were used to enhance the thermal exchange between the cold plate of the cryostat and the prototype, and to make the cooling process faster and more efficient. Ultimately, the temperature registered by the PT-100 sensors was always well below the critical temperature of the superconductors.

Finally, the coils were connected in an anti-serial configuration in order to reduce the power dissipation inside the cryostat and the current demanded for the operation of the *FTS2* prototype. An image and CAD representation of the *FTS2* prototype installed in the cryostat can be seen in Fig. 6.1.

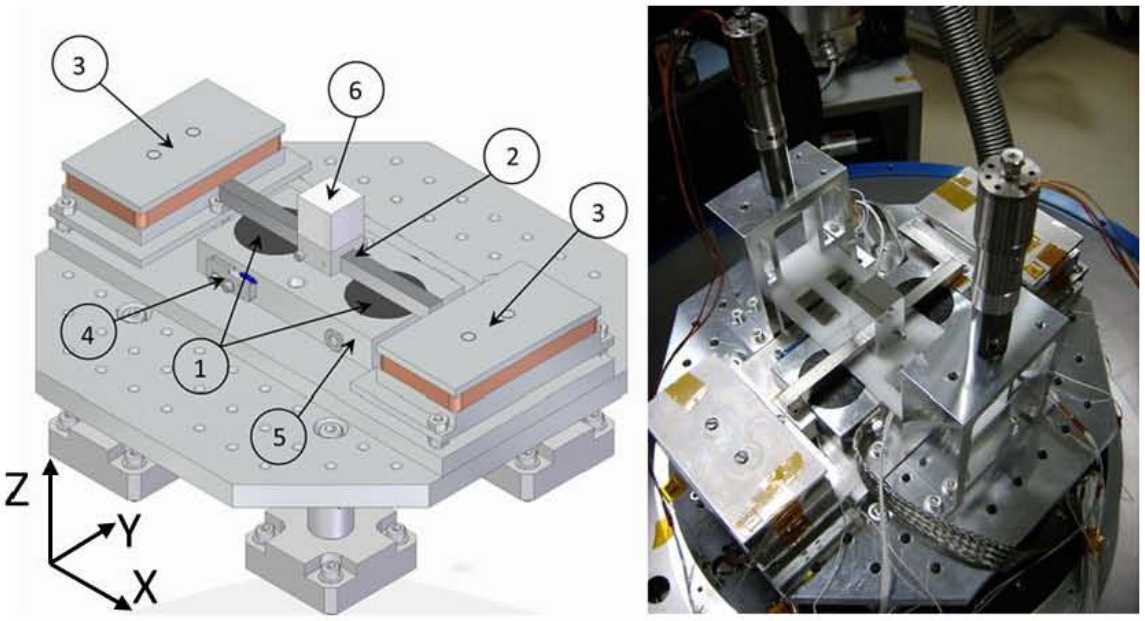

Fig. 6.1. 1) Superconducting disks (*HTS*); 2) PM (PM); 3) Coils, 4) PT-100 sensors, 5) superconductors base and 6) Optic mirror cube. Left: CAD of the *FTS2* prototype. Right: True image of the *FTS2* prototype.

6.3 Experimental set up and procedure

The *FTS2* prototype was installed in the cryostat. In this section, the experimental set up and procedure used are discussed, including the description of any auxiliary system, such as the launch & lock system or the amplifier.

6.3.1 Launch & lock system

Stable levitation can only be obtained when the superconductors are cooled below their critical temperature (T_c=90 K). Therefore, a launch & lock system was designed and built in order to keep the PM in the field cooling (FC) position (X=0 mm, Z= *HFC*) while the superconductors are at a temperature above their T_c. The PM was kept in position by a polyoxymethylene holder (from now on the Delrin holder) that was designed specifically for this purpose.

The Delrin holder stands in two symmetric aluminium structures that also work as the base of the stepper motors. Each of these structures contains a couple of springs (see Fig. 6.2) that provide the required pre-load to maintain the slider in the appropriate *FC* position.

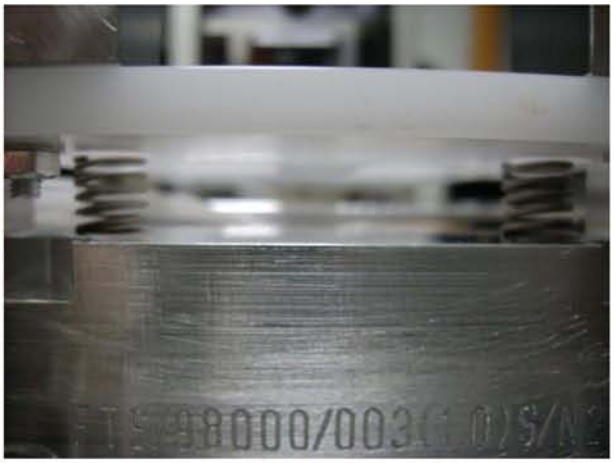

Fig. 6.2. Springs in the launch & lock system.

In addition, the position of the Delrin holder was modified with two cryogenic linear stepper motors from Micos which were symmetrically placed at either side of the prototype. The stepper motors were controlled by SMC Pollux drivers from the same company. By this means, the height of field cooling (*HFC*) was carefully fixed within an uncertain of around ± 100 µm. The whole launch & lock system is shown in Fig. 6.3.

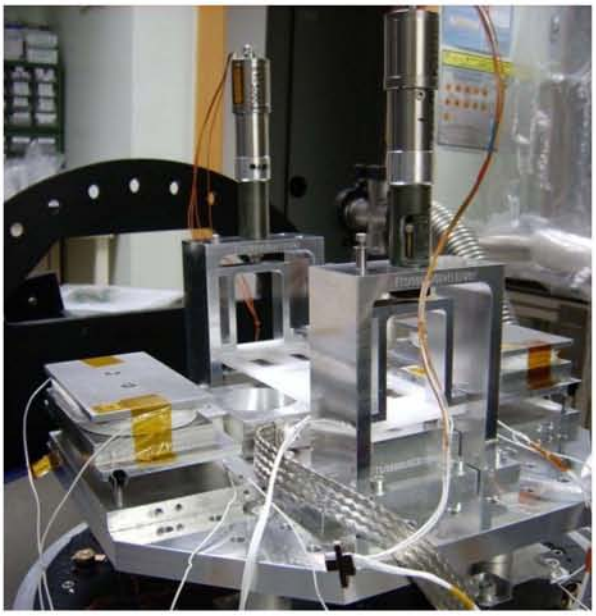

Fig. 6.3. Launch & lock system installed inside the cryo-chamber.

Once the temperature of the cryostat reaches a stable temperature (~15 K) the linear motors push down upon the Delrin holder until the PM is launched and able to levitate stably over the superconductors. Some space is required between the Delrin holder and the superconductor' base to allow the Delrin holder to retreat and launch the PM. The minimum gap required for the operation of the launch & lock system was estimated to be around 3 mm in order to assure there is no interference between the PM and the Delrin holder while the device is in operation. Hence, the *HFC* was set to 3 mm between the *HTS* top surface and the *PM* bottom surface.

6.3.2 Signal generation and data acquisition

In order to generate the input voltage signal, a 16 bit NI 6230 card (1) was used. The minimum voltage resolution of the NI 6230 card is 3.1 mV for a ± 10 V signal field. The generated signal (0-10V) was then amplified (2) and transduced to a current signal (±500 mA) before supplying the coils using a current amplifier described in section 6.3.3 in this chapter.

A second voltage signal for the fine positioning of the slider was provided using an independent output channel in the NI 6230 card. This second parallel voltage signal was not amplified at all, instead having the circulating current controlled by an adjustable precision resistor (3) before supplying the coils. Then, by modifying the equivalent impedance of the electric circuit in the coils, the input current resolution was modified between 100±1 and 15±1 μA. As will

be demonstrated in the following sections: the better the current resolution, the finer and the positioning resolution of the slider.

The current in the coils were measured using two independent NI 4070 FlexDMM multimeters for either the coarse (4.a) or fine step (4.b) motion with 1μA resolution and 100 p.p.m accuracy and 10 nA resolution and 10 p.p.m accuracy respectively.

In order to characterise the behaviour of the slider, it was necessary to synchronise data from the current/voltage signals with data from the interferometer and the auto-collimator (4). The control of all instrumentation and data acquisition, including monitorisation of the temperature inside the cryostat and the control of the stepper motors of the launch & lock system (5), were developed using NI Labview software. Finally a diagram of the electric connectivity of the instrumentation for these tests is shown in Fig. 6.4.

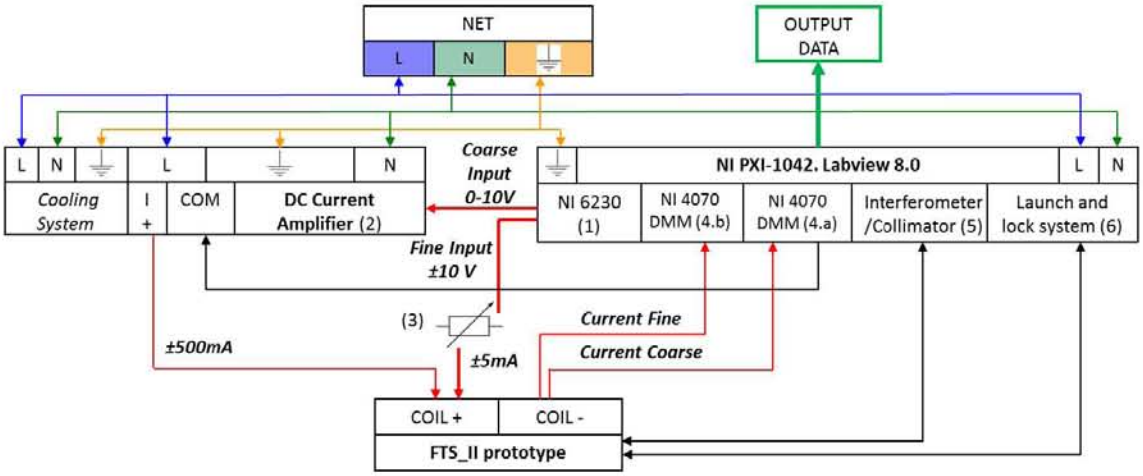

Fig. 6.4. Electric connection diagram of the experimental set up. *FTS2* prototype

6.3.3 Current Amplifier

Due to the low current that the NI 6230 can provide, a current amplifier was designed and built to supply the coils with the required current of ±500 mA. It was necessary to generate a current with the lowest noise to signal ratio possible. An electric diagram of the device is presented in Fig. 6.5.

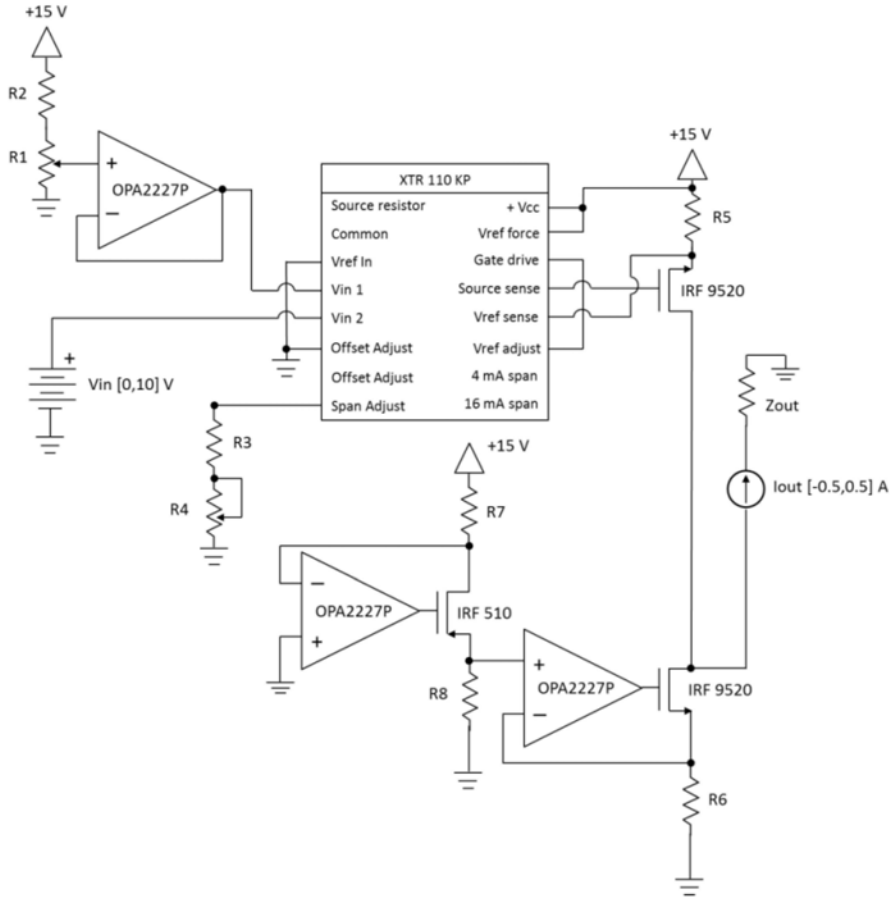

Fig. 6.5. Electric diagram of the current amplifier. R1=2 kΩ, R2=15 kΩ, R3=2.2 kΩ, R4=R7=10 kΩ, R5=100 mΩ, R6=22 kΩ and R8=3.3 kΩ

In a preliminary prototype of the current amplifier (see Fig. 6.6), a noise signal with a magnitude of about 35 mA was measured. In addition, a high thermal drift of the output current signal was registered mainly due to self-heating of the transistors. At this point, it was clear that an improvement in the current amplifier was needed.

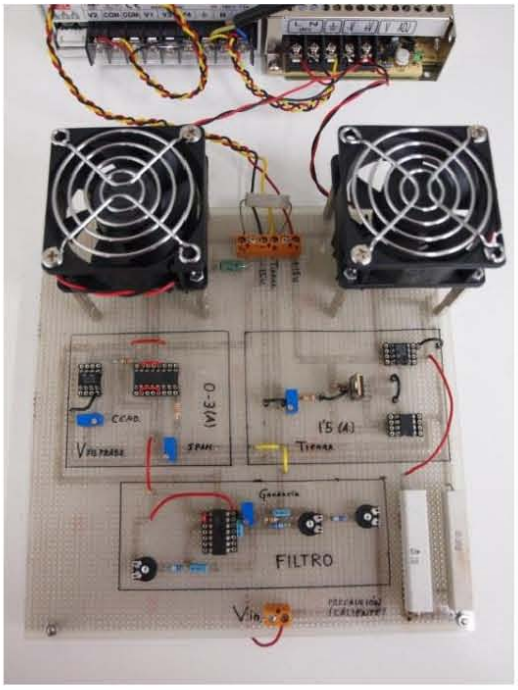

Fig. 6.6. Preliminary prototype of the current amplifier. Courtesy of Juán Sánchez García-Casarrubios

It has long been known that electronic devices like transistors or amplifiers modify their response with their working temperature [142]. Thus, due to the self-heating of the electronic components while in operation, a thermal drift can appear in the output current. We soon realised that forced convention was not enough for heat dissipation, and to consequently avoid the undesired thermal drift in the output current of the current amplifier. In addition, the lower the operation temperature of the amplifier, the lower the noise in the output signal [143].

In order to reduce both, the output current thermal drift and the noise in the current signal, a cooling system based on PID-controlled Peltier cells was designed and developed. This technique has been previously explored for the noise reduction and thermal control of amplifiers [144], [145]. As a result, the temperature of the transistors was controlled within ± 0.1 ^{o}C resolution, and the thermal drift of the output current was minimised. Without regard to other modifications done in the early current amplifier, the use of this cooling system turned out to be very efficient not only in thermal drift reduction but also in reducing the noise ratio of the signal. A picture of the final current amplifier is provided in Fig. 6.7.

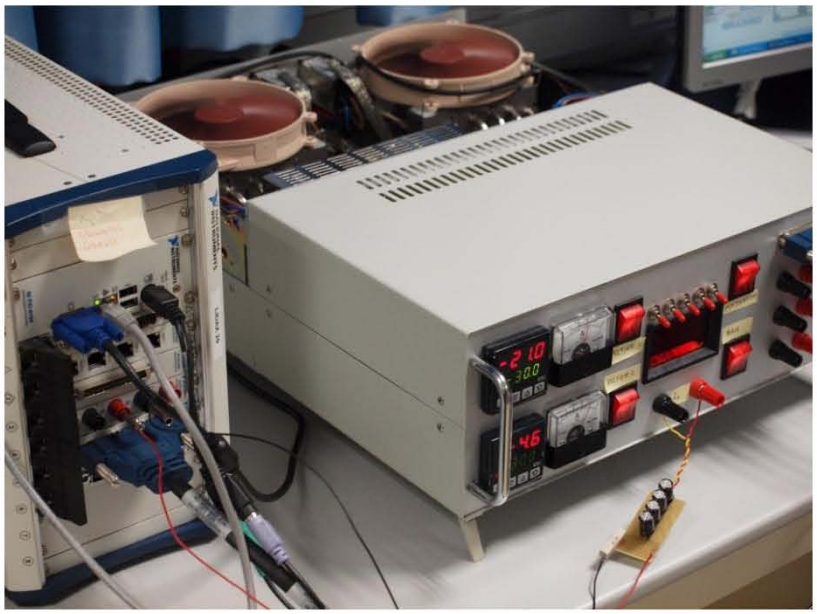

Fig. 6.7. Final prototype of the current amplifier used in *FTS*. Courtesy of Juán Sánchez García-Casarrubios

In addition to the Peltier cooling system, some noise-reduction measures were taken in the final amplifier. For example, installation of decoupling capacitors, an appropriate grounding design, magnetic insulation of the amplifier and optimisation of components distribution inside the amplifier [146], [147]. Due to the previously mentioned measures, the noise in the signal was reduced to a maximum of 50 µA at any working point of the amplifier between ±500 mA. Therefore, it can be said that the noise was reduced by almost three orders of magnitude from around 70000 p.p.m to 100 p.p.m. The noise in the preliminary prototype and in the final current amplifier are shown in Fig. 6.8.

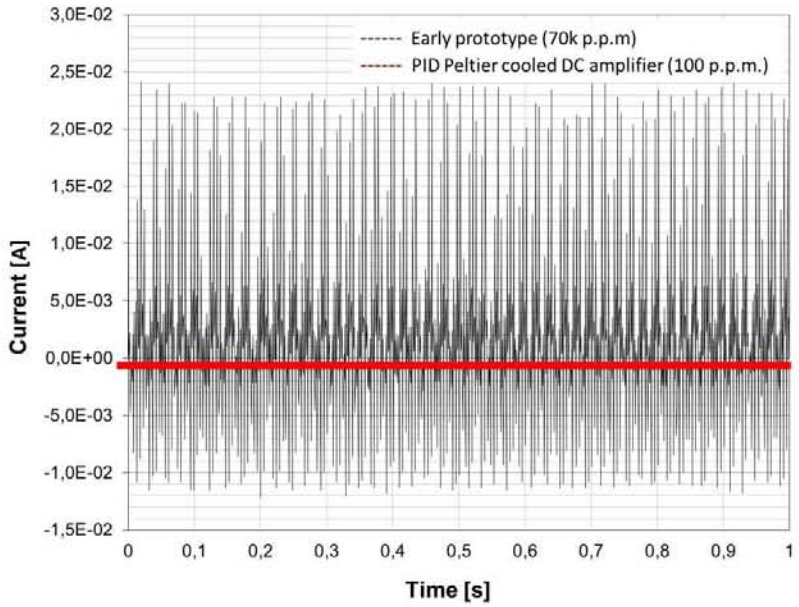

Fig. 6.8. Noise signal measured in both, the preliminary prototype and the PID Peltier cooled amplifier.

Finally, it has to be mentioned that the amplifier was designed so that the relationship between input voltage and output current in the amplifier was linear and almost independent from the output equivalent impedance. In the beginning, it was designed to provide a maximum driving current of around ± 1 A. The output current in the amplifier vs. input voltage from the NI 6230 card is shown in Fig. 6.9.

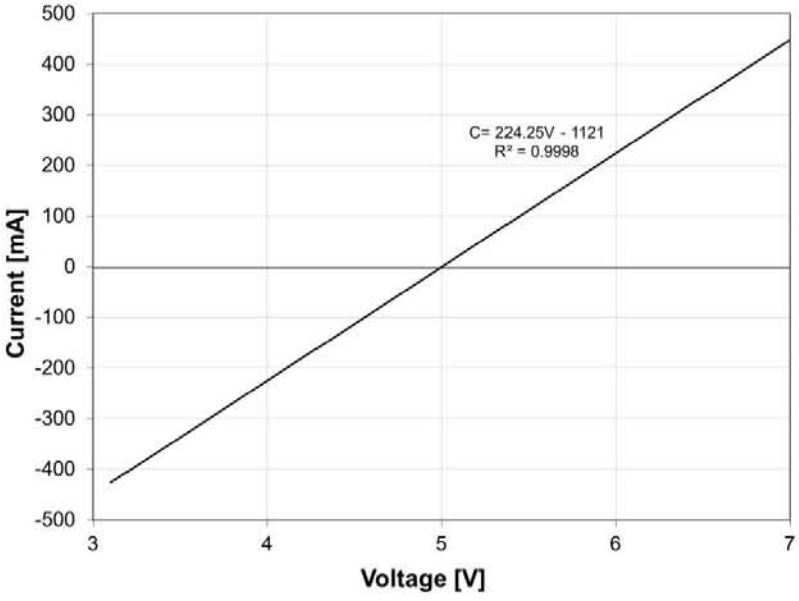

Fig. 6.9. Output current in the current amplifier vs. input voltage from NI 6230.

6.3.4 Position and rotation measurements

The X and Y position of the slider were measured using an Agilent 10706B High Stability Plane Mirror Interferometer with an accuracy of 0.62 nm. The laser from the interferometer passes through an optical window in the cryostat, it is reflected in the mirror cube mounted on the slider, and then returns to the interferometer where the measurement of the position is developed. A picture of the experimental set up is introduced in Fig. 6.10.

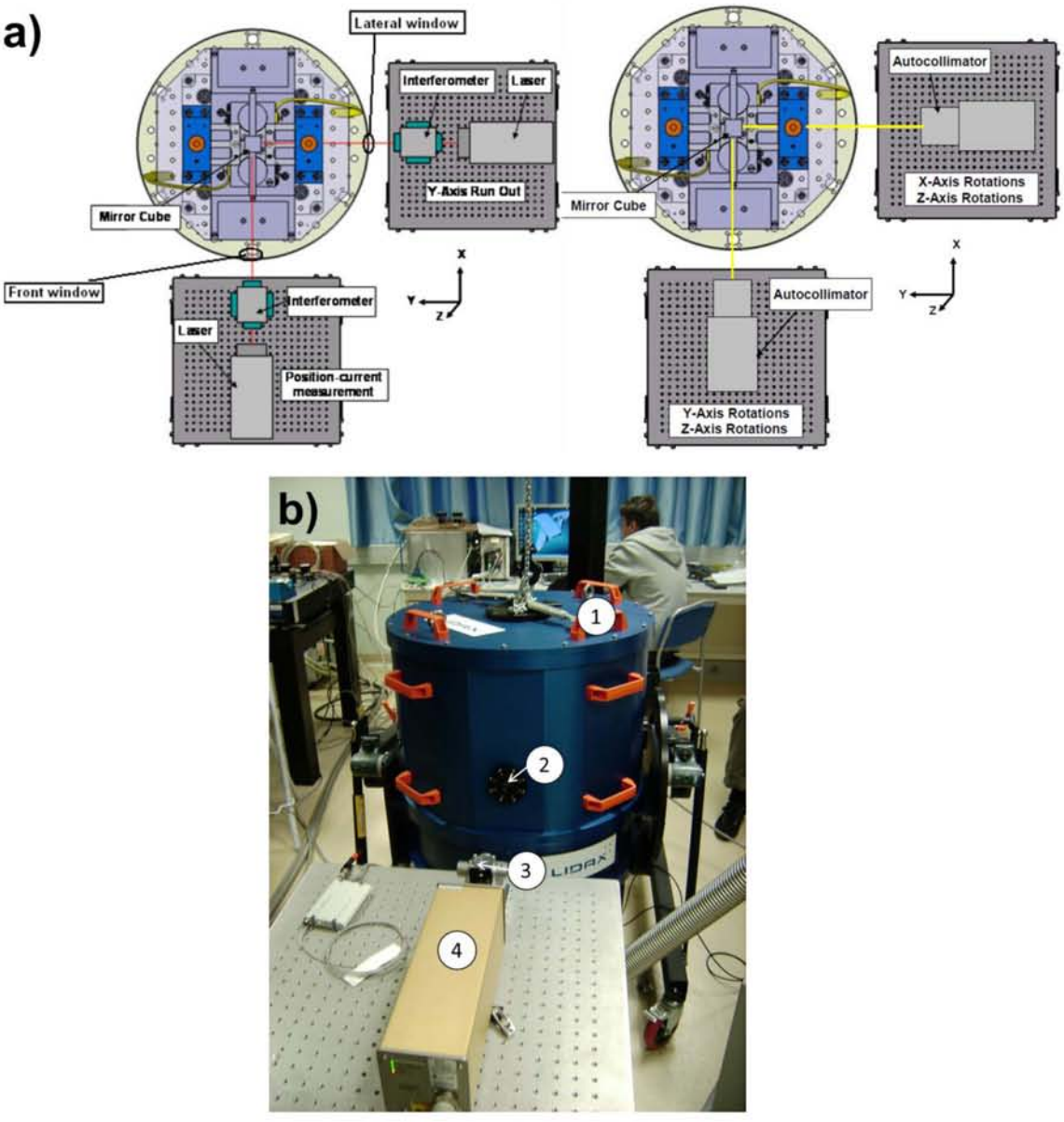

Fig. 6.10. a) Position and angular run outs measurements experimental set up V, picture courtesy of LIDAX, b) Picture of the experimental set up in LIDAX laboratories: 1) cryostat, 2) optic window, 3) interferometer and 4) laser head.

In order to measure the angular run out of the slider, the *Newport LDS Vector auto-collimator* was used. As was previously mentioned in chapter III, the resolution of such an instrument is 0.1 µrad and its accuracy is within 2% of the measurement. Only the interferometer or the auto-collimator, was used at one time. Therefore, for all measurements presented in the following section regarding the run outs of the device, the X position of the slider is obtained by a piecewise polynomial fitting curve of the position X of the slider vs. current in the coils measured with the interferometer. A maximum uncertainty in the X position in all angular run out charts lower than 50 µm was estimated.

Finally, a diagram of the experimental procedure is shown in Fig. 6.11.

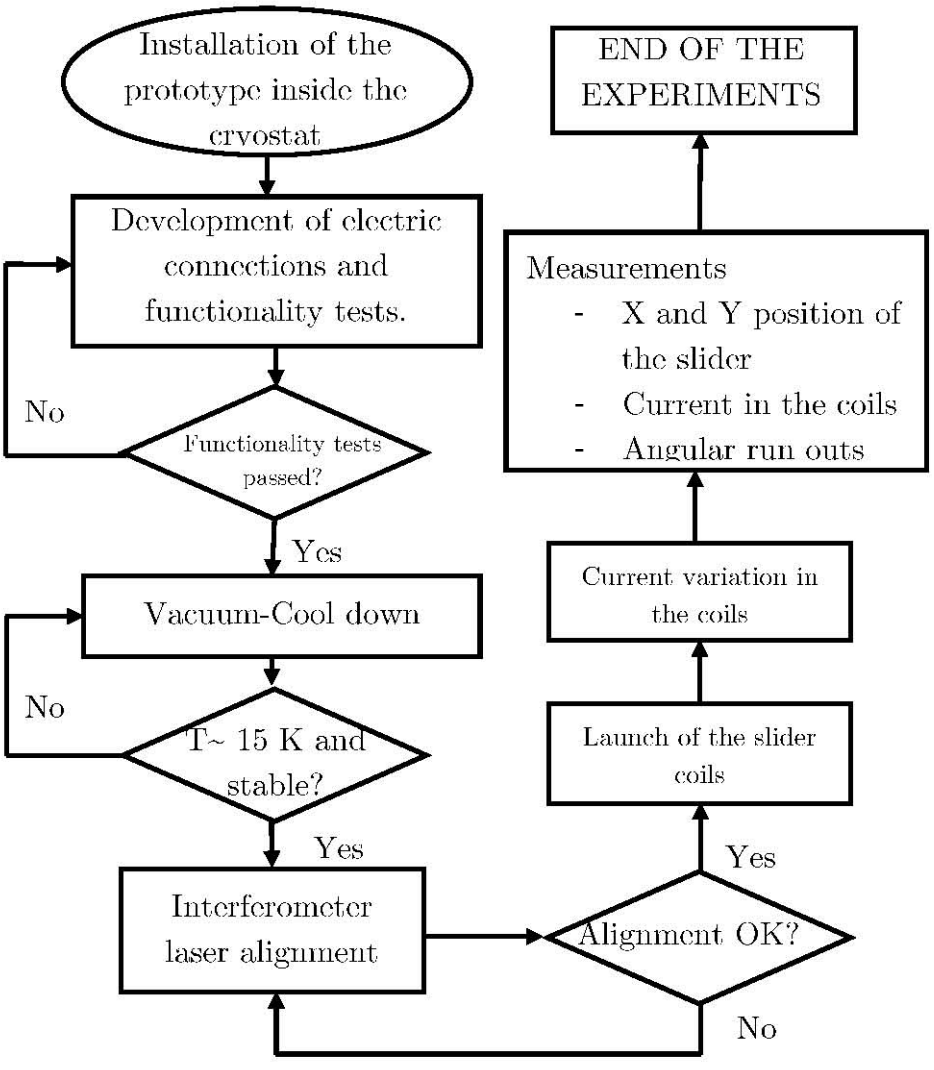

Fig. 6.11. Experimental procedure of the *FTS2* prototype.

6.4 Tests results and discussion

Results of the tests are presented in this section. The position resolution of the mechanism, stability and accuracy, hysteresis, demanded current in operation, and run outs are reported. In addition, the dynamic behaviour of the mechanism was studied and the power consumption of the device determined.

6.4.1 Positioning performance

The main parameters that characterise the positioning performance of the *FTS* mechanism are presented, i.e. the X position vs. input current, position stability and accuracy, position resolution, hysteresis, speed, stiffness and damping of the mechanism. It must be taken into account that the cosine error as a result of an angular misalignment between the measurement laser beam and the axis of motion of the slider has been considered in all results presented in this chapter.

6.4.1.1 X position versus current in the coils

The X position of the slider vs. the current in the coils was measured along the whole stroke of the mechanism. The current in the coils was modified in increments of around 11.20±0.05 mA and multiple full cycles were measured. Results for these measurements are presented in Fig. 6.12.

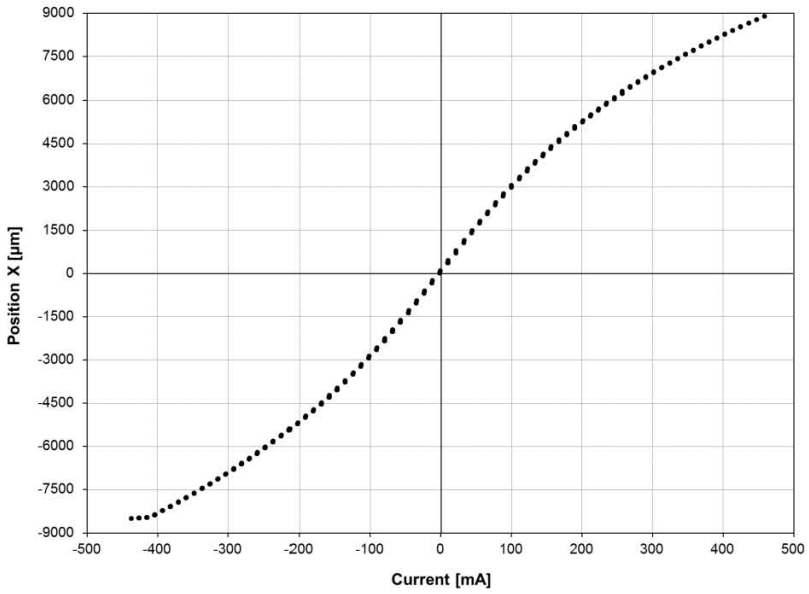

Fig. 6.12. X position of the slider vs. current in the coils. Current increments around 11 mA.

Fig. 6.12 shows that the stroke of the mechanism is about ± 9 mm and the current requirement is lower than ± 450 mA. Although the sensitivity of the motion is not constant along the entire stroke, it can be approximated to be 29±2 µm/mA in a range of ±3 mm around the origin of coordinates. Sensitivity vs. X position of the slider is presented in Fig. 6.13.

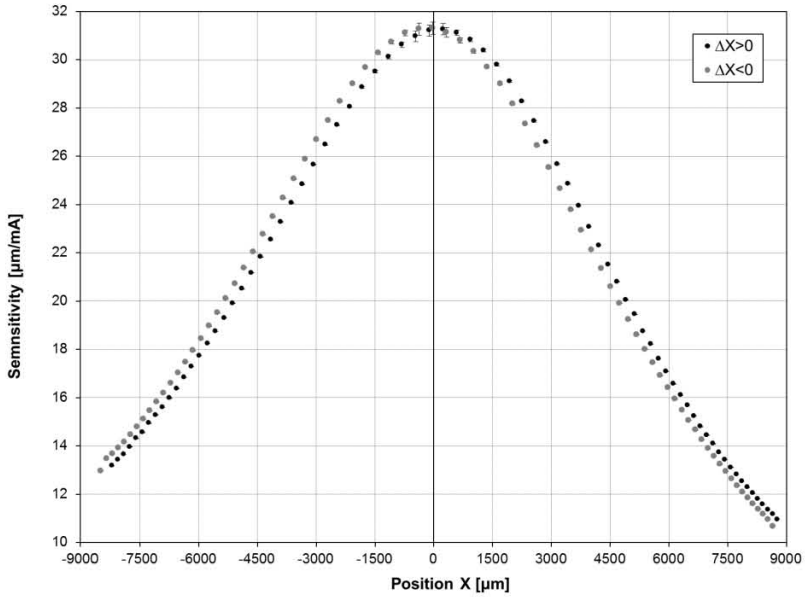

Fig. 6.13. Sensitivity vs. X position of the slider.

6.4.1.2 Position stability and accuracy

The position stability is always an important factor to be considered in magnetic levitation devices. First, vibrations in the *FTS2* prototype were measured with the interferometer with an acquisition frequency of 200 Hz before launching of the slider. The results are plotted in Fig. 6.14. The noise present in the signal is about ±0.15 µm (σx=± 0.07 µm), due to the presence of vibrations.

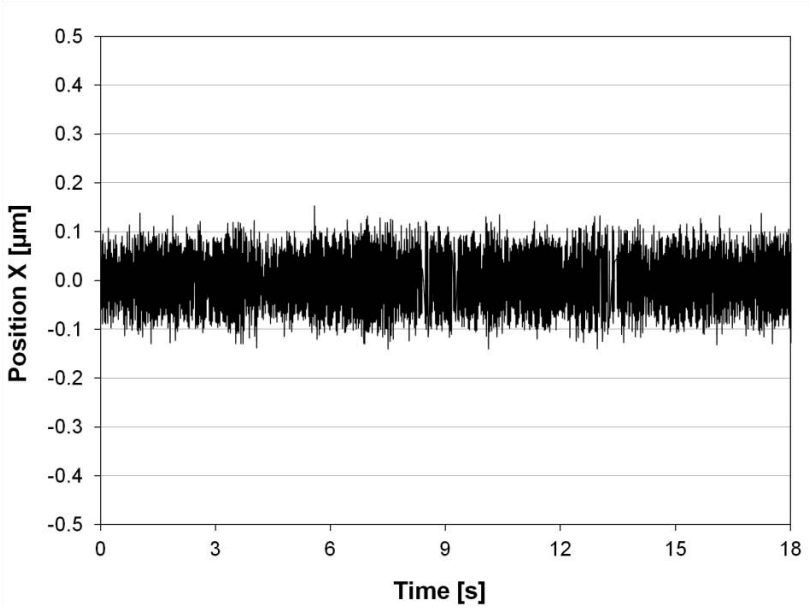

Fig. 6.14. X position vs. time when the slider of the *FTS3* prototype is not already launched. T~ 15 K, acquisition frequency= 200 Hz.

Spectral analysis of the signals was carried out using the Lomb-normalised periodigram. This technique can be extended to situations in which the samples are taken at uneven intervals (as is the case in instance). Lomb-normalised periodigram (spectral power as a function of angular frequency) is defined by eq. 6.1:

$$P_N(\omega) = \frac{1}{2\sigma^2}\left\{\frac{\left[\sum_j (h_j - \bar{h}) cos\ \omega(t_j - \tau)\right]^2}{\sum_j cos^2\omega(t_j - \tau)} + \frac{\left[\sum_j (h_j - \bar{h}) sin\ \omega(t_j - \tau)\right]^2}{\sum_j sin^2\omega(t_j - \tau)}\right\}$$

eq. 6.1

where

$\bar{h}$ is the mean of the data,

σ is the variance of the data (h),

and τ is a frequency dependent time delay (see eq. 6.2), defined to make the periodigram insensitive to time shift [148]. See eq. 6.2.

$$\tau = \frac{1}{2\omega} arctan\left\{\frac{\sum_j sin\ 2\omega t_j}{\sum_j cos\ 2\omega t_j}\right\}$$

eq. 6.2

The Lomb-normalised periodigram on the signal shown in Fig. 6.14 leads to the spectral power density plotted in Fig.6.15:

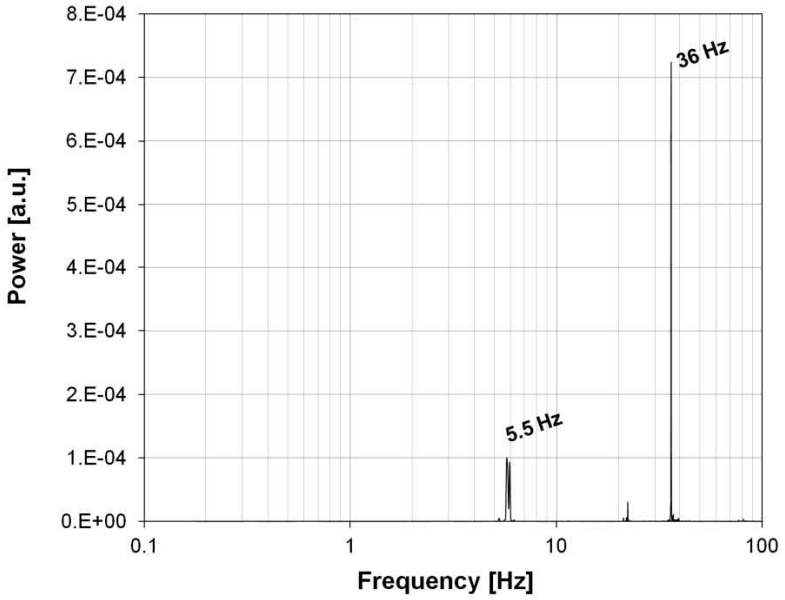

Fig. 6.15. Power spectrum of the position vs. time signal when the slider of the *FTS3* prototype is not yet launched. T~ 15 K, acquisition frequency= 200 Hz.

A major contribution to the spectrum was found at about 36 Hz. A second component can be found at 5.5 Hz.

After this first analysis of the vibrations, the vibration in position was measured with the slider floating at different points along the stroke. The X position of the slider versus time for an acquisition frequency of 1kHz and no current in the coils is shown in Fig. 6.16.

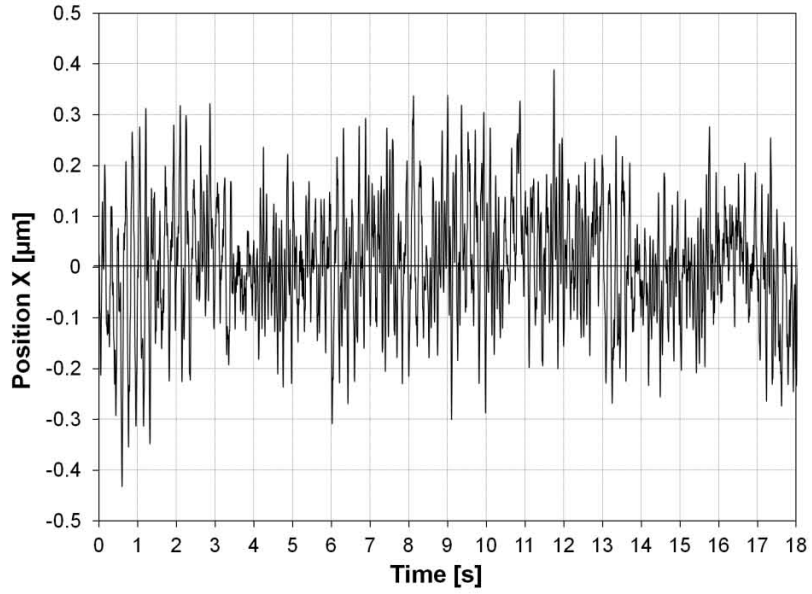

Fig. 6.16. X position of the slider vs. time in the initial equilibrium position. T~ 15 K, acquisition frequency= 200 Hz.

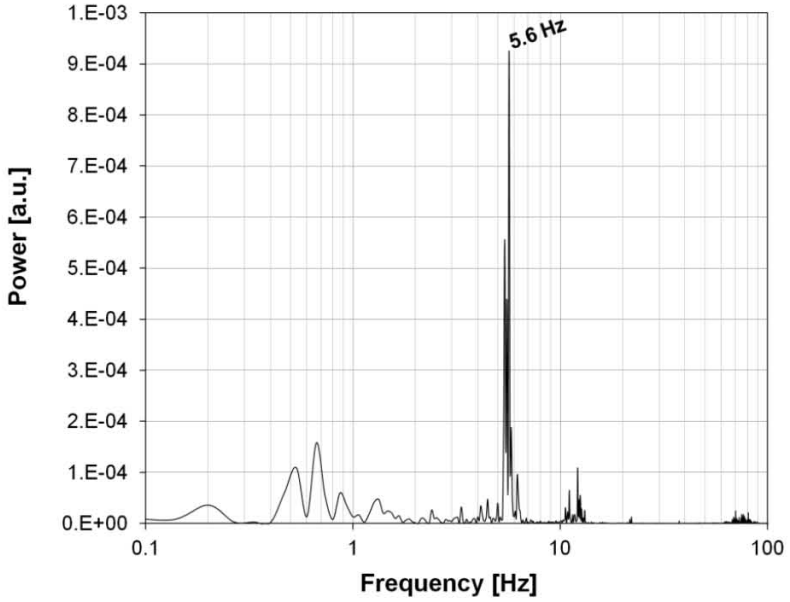

Fig. 6.17. Spectral analysis of the signal in Fig. 6.16.

The main contribution can be located around 5.6 Hz, as shown in Fig. 6.17. Note that when the slider is launched, lower frequencies are amplified and higher frequencies are damped. This suggests that the *FTS2* prototype behaves like a low-pass vibration filter with a cut-off frequency below 10 Hz.

X position stability was also measured along the entire stroke of the mechanism and very similar results were obtained for other positions along the

stroke, as can be seen in Fig. 6.18. Additionally, a very similar frequency spectrum of the signal was found.

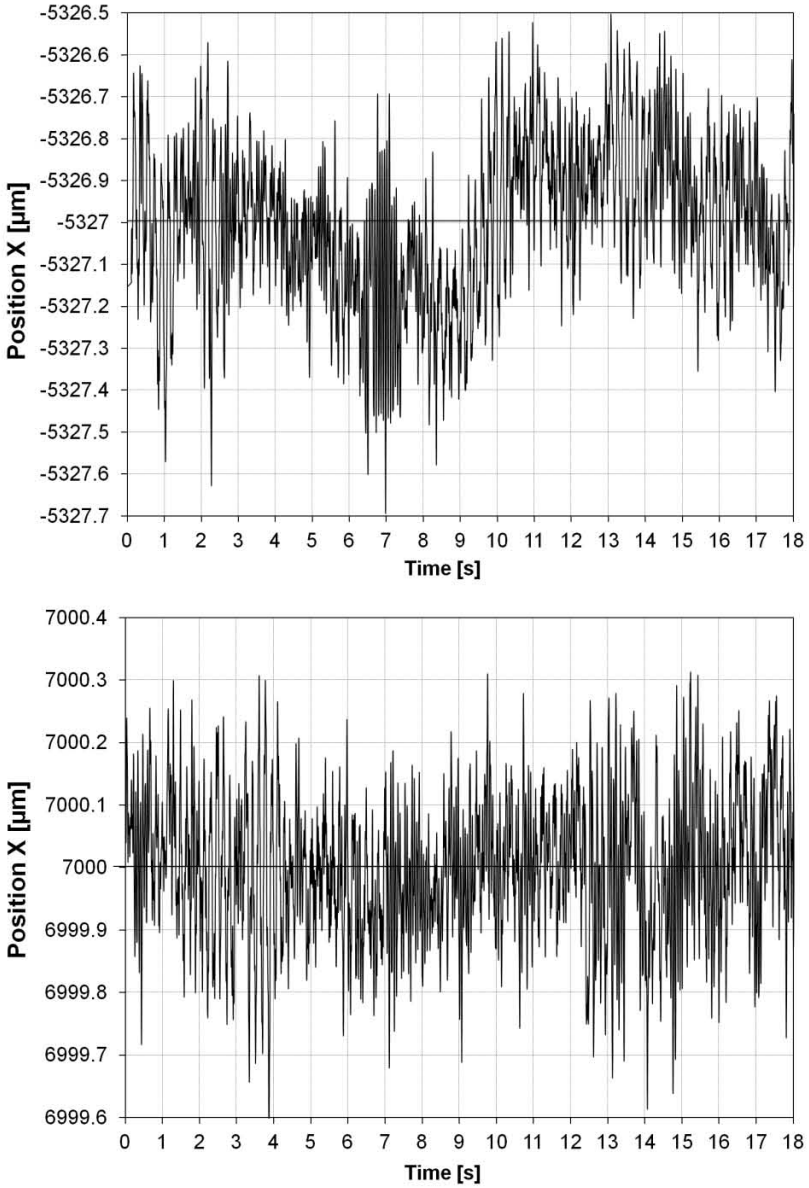

Fig. 6.18. X position of the slider vs. time around different positions in the stroke of the *FTS2* mechanism.

In addition, the Y position stability of the slider was also measured. In this case, the instability of the Y position was also found to be independent of the X position of the slider for the measurement range. The amplitude of the vibration in the Y axis was found to be one order of magnitude higher than in the case of the X stability as shown in Fig. 6.19.

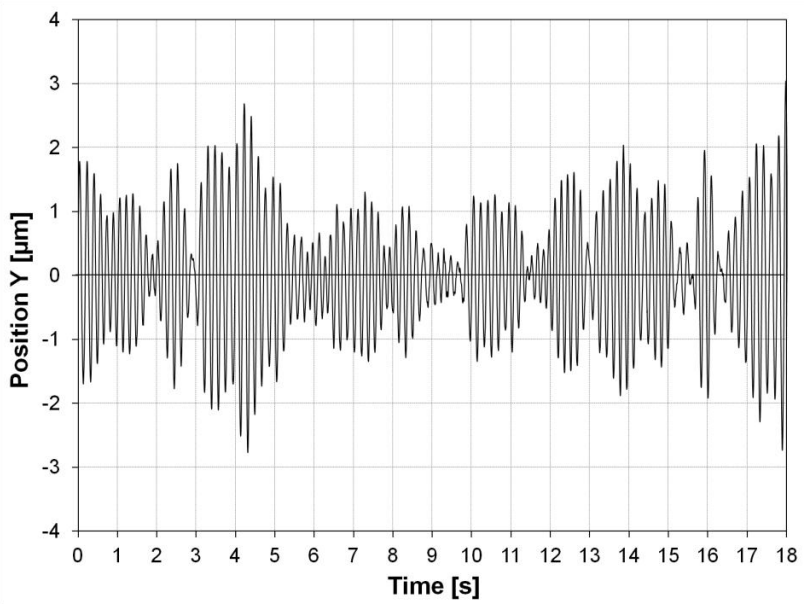

Fig. 6.19. Y position of the slider vs. time in the surroundings of the initial equilibrium position (X=0 mm).

Finally, in view of all results presented in this section, it has been decided to define the accuracy of the X positioning to be around 0.8 µm ($\sigma_X = \pm 0.25$ µm) and around 6 µm ($\sigma_y = \pm 1.2$ µm) in the case of the Y axis.

6.4.1.3 Position resolution

Position resolution was either measured, for the coarse step motion (using the current amplifier) or for the fine step motion with the non-amplified current signal. Despite position resolution at different points along the stroke of the mechanism being measured, only position resolution for the surroundings of the initial position (X=0 mm) are presented. Sensitivity in this position is maximum (31±1 µm/mA), as previously reported. Therefore, it can be expected that the less favourable X positioning resolution is found at this point. Consequently, it is our aim to define the position resolution of the device as the position resolution in the surroundings of the origin of coordinates.

Coarse step motion:

As has already been explained, for coarse step motion, both coils are connected in anti-serial configuration, so when one of the coils pushes the PM, the other pulls it. The position resolution measured around the central equilibrium position shows a position resolution of about 3.3±0.3 µm (see Fig. 6.20). The current resolution of the coarse motion system was about 100±10 µA.

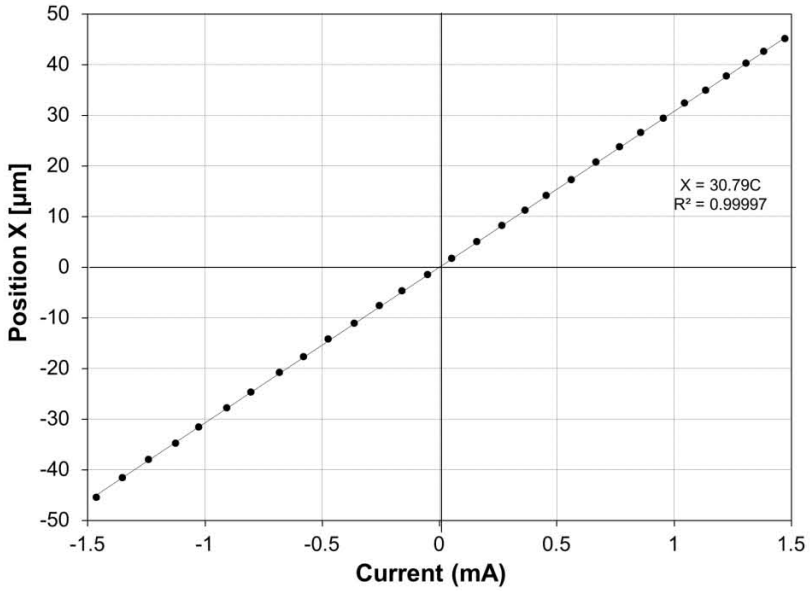

Fig. 6.20. X position of the slider vs. current in the coils ΔC=100±10 µA

Fine step motion:

For the fine step motion in this chapter, only one of the coils was used. The X position of the slider vs. current in the coil is presented in Fig. 6.21. The position resolution under this operating condition was calculated to be about 1.5±0.2 µm. The measured position resolution is just half of the calculated position resolution for the coarse step motion. This is due to the fact that only one pulling coil (attractive force) is acting. Thus, the force exerted on the PM is, approximately, half the force of the coarse step motion.

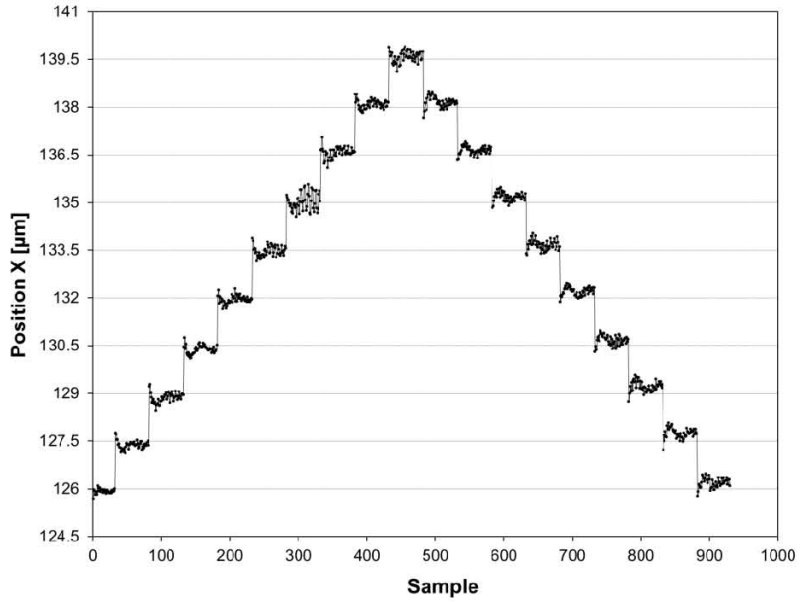

Fig. 6.21. X position of the slider vs. measurement sample. No registered time. ΔC= 100±1 µA.

After this first experiment, the current supplied to the coil was reduced simply by increasing the equivalent impedance of the coils using a precision variable resistor in serial connection with the coils. Fine step motion resolution was calculated to be 230±30 nm around the central position for a current resolution of around 15µA. Very good linearity can be observed in Fig. 6.22. It has to be noted that, yet again, the sensitivity of the motion is half of the coarse step resolution sensitivity because only one coil was used.

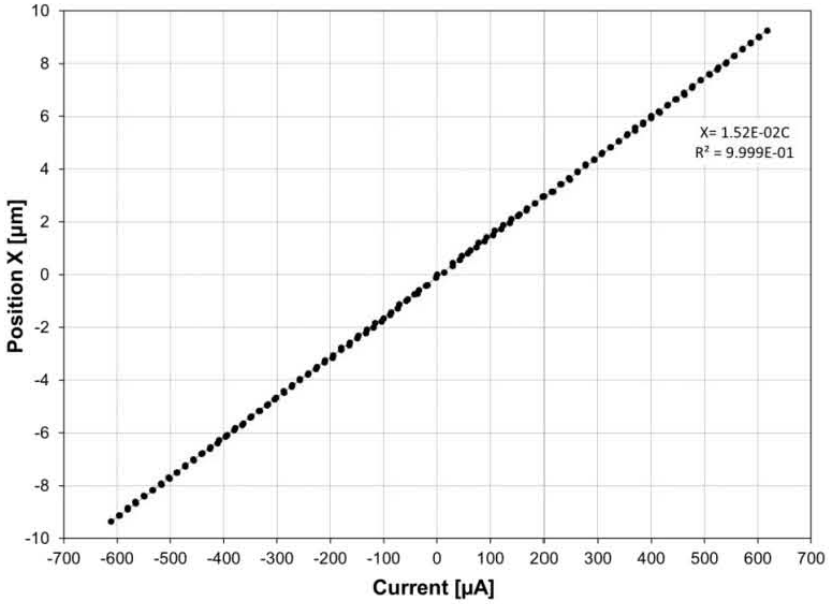

Fig. 6.22. X position of the slider vs. current in the coils. Good linearity for small travel lengths can be observed.

The RMS resolution for the minimum current increment of 15±1µA is plotted in Fig. 6.23. Only RMS values are represented to clarify the figure, because the vibration magnitude is of the order of the measured resolution.

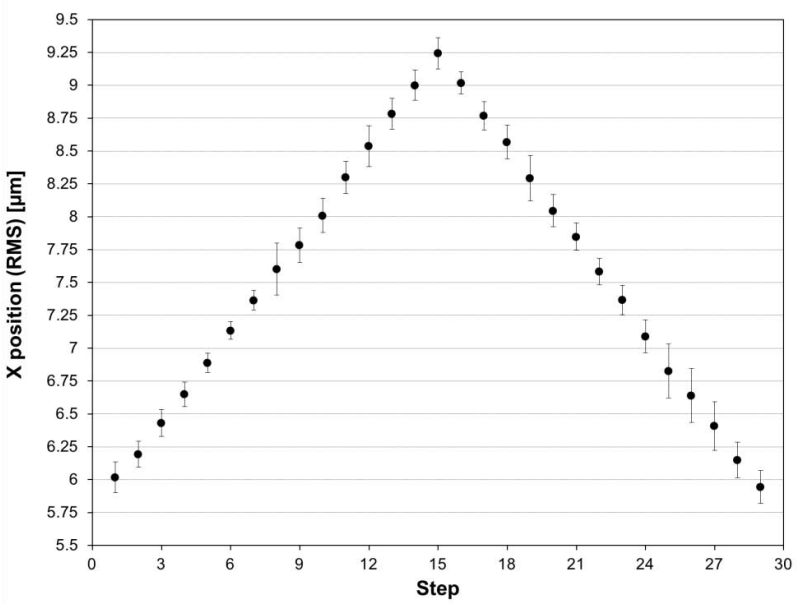

Fig. 6.23. RMS X position resolution vs. current step. No registered time .ΔC= 15±1 µA.

Position resolutions for supplied currents lower than 15 µA were measured. However, the signal to noise ratio was low and no relevant results were obtained.

6.4.1.4 Hysteresis

As has been previously mentioned, a hysteretic behaviour of the slider can be expected due to the presence of impurities in the crystalline structure of the superconductors. This hysteresis was measured along the entire stroke of the mechanism and it was maximum at the central position. The hysteresis of the *FTS2* prototype can be appreciated in Fig. 6.24 which is a zoom of the central position in Fig. 6.12.

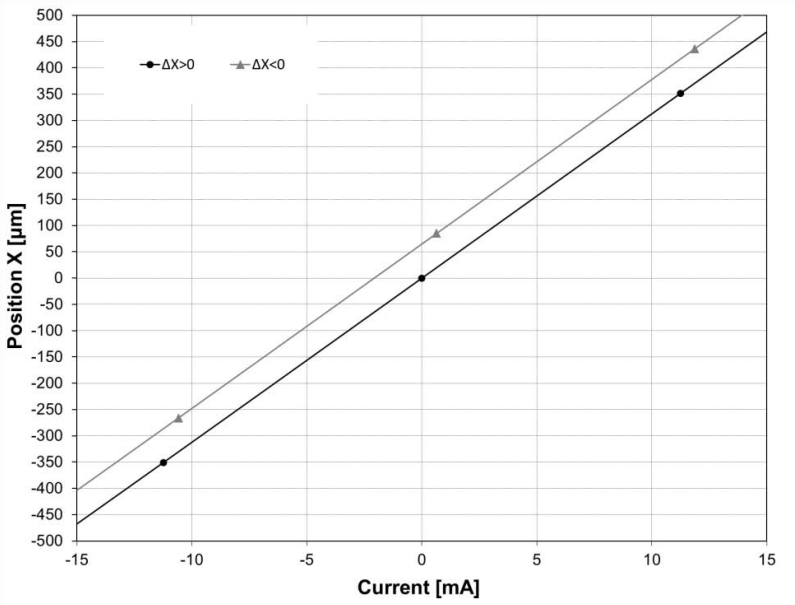

Fig. 6.24. Hysteresis loop of the *FTS2* mechanism focused in the surroundings of the initial equilibrium position, where the hysteresis is the maximum.

The apparent hysteresis was of the order of 60±2 µm for full stroke motion (± 9mm). Ultimately, it was estimated that around 10 µm of the measured hysteresis were caused by expansion of the optic mirror cube due to self-heating while the measurements were developed.

6.4.1.5 Stiffness of the FTS2 prototype

It was demonstrated in chapter IV that the force exerted on the PM by the *HTS* is considerably increased in the *FTS2* prototype with respect to the *FTS1* prototype. FEM analysis of the magnetic field applied on the superconductors reveals that, not only is the magnitude of the flux density on *HTS* in the *FTS2* prototype in the X direction (B_x) higher than the one calculated in the *FTS1* prototype (~6 mT and ~48 mT respectively) but also the magnetic field gradient now seems to be more pronounced. Then, an increased stiffness in the X direction of the slider is expected. The magnetic flux density in the X direction for both, the *FTS1* and the *FTS2* prototype is represented in Fig. 6.25.

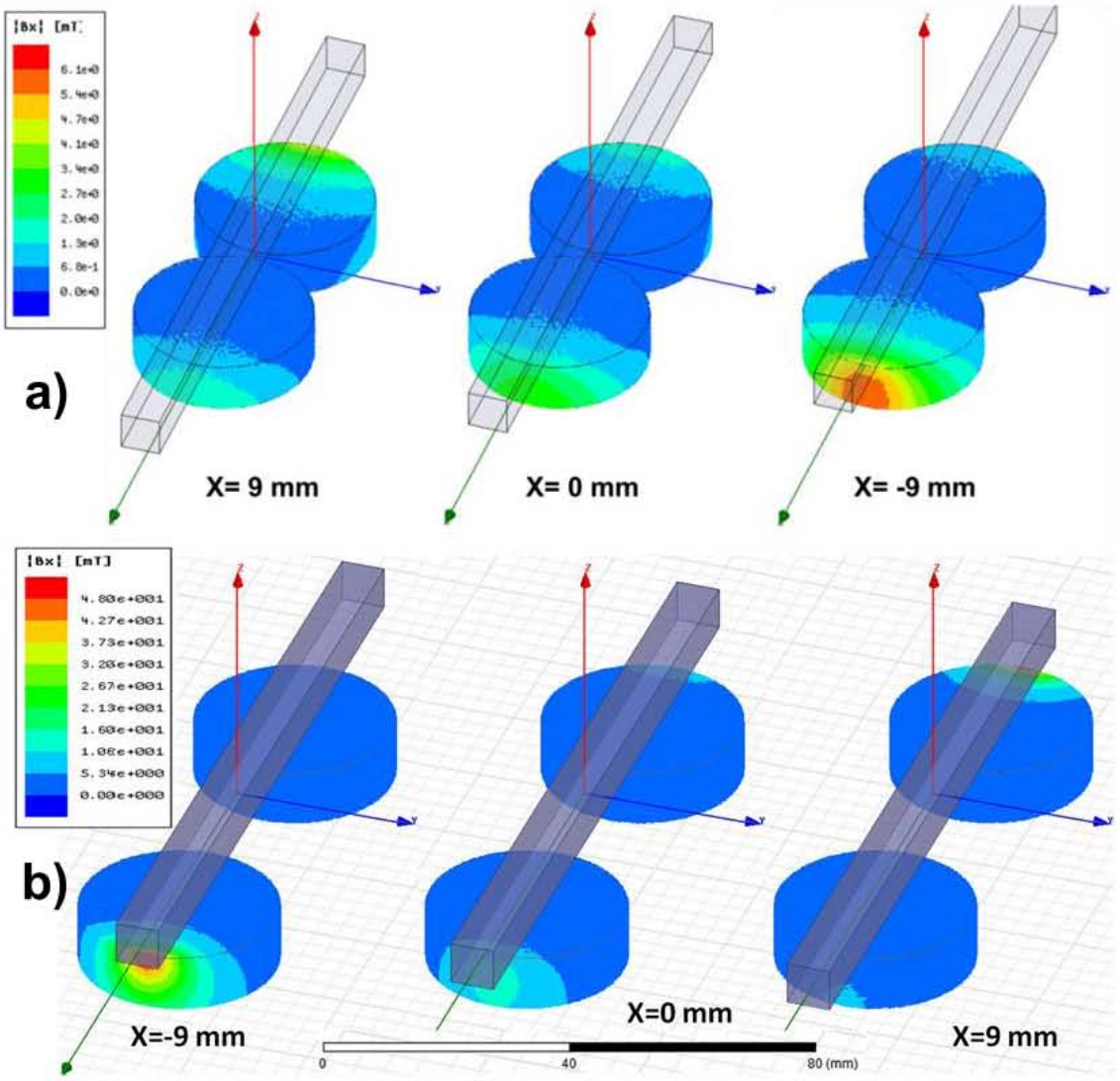

Fig. 6.25. Absolute magnitude of the magnetic flux density in the X direction in the *HTS* in the normal state for a) d= 47 mm (*FTS_1*) and b) d= 84 mm (*FTS2*).

In order to estimate the force in the PM, the same procedure introduced in chapter IV was followed. However, here both coils in an anti-serial configuration were considered in the calculations. Force vs. X position on the slider is presented in Fig. 6.26.

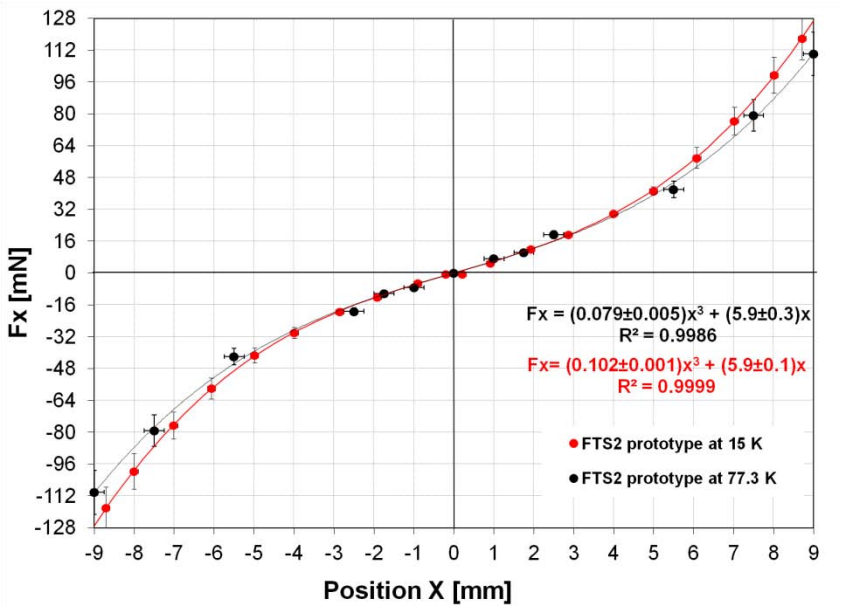

Fig. 6.26. FEM calculated force vs. X position exerted on the slider for *FTS2* prototype at 77 and 15 K.

Forces exerted on the PM are slightly higher for a working temperature of 15 K than for 77 K, especially for higher values of the X position. It is well known that the lower critical field of YBCuO is increased when the temperature of the superconductor is reduced In addition, the strength of the magnetic field generated by NdFeB permanent magnets is typically improved until a temperature about 140 K is reached. From this point, it begans to decay [35]. In the end, a slightly higher force was exerted on the slider of *FTS* mechanism at a working temperature of 15 K.

Fit curve for calculated forces on the slider (T~15 K) now reads:

$$F_x = (1.02 \pm 0.01) \cdot 10^{-1} x^3 + (5.9 \pm 0.1) x$$

eq. 6.3

The potential energy still remains in the same order of magnitude, although a slight increase in the calculated potential energy for the lower temperature test can be observed in Fig. 6.27.

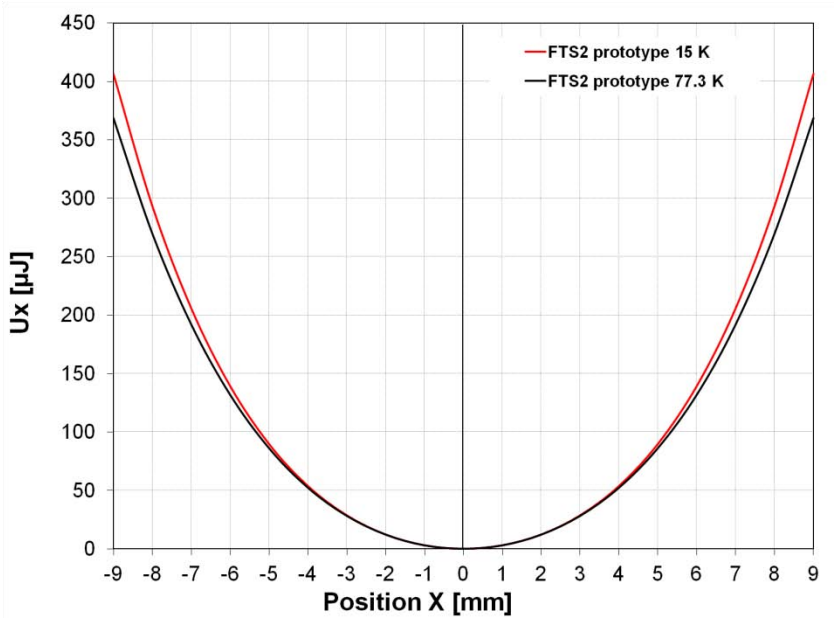

Fig. 6.27. Potential energy vs. X position of the slider in *FTS2* prototypes at 77 and 15 K.

Despite being a dependence between stiffness (and the sensitivity) of the *FTS* mechanism and temperature, the variation in the sensitivity of the mechanism at any point of the stroke is less than a 10% for a variation in the working temperature around 60 K. This dependence of the sensitivity with the temperature of the prototype seems to be less relevant than in piezo-actuators (see chapter II).

6.4.1.6 Dynamics of the FTS mechanism

The elastic force vs. the X position of the slider can be approximated to a nonlinear dependence of shape:

$$F(x) = k_1 x + k_3 x^3$$

eq. 6.4

The energy dissipation of the system is represented by a linear damper with viscous damping coefficient *c*. Let us consider the following mathematical model for the description of the dynamic behaviour of the *FTS* mechanism:

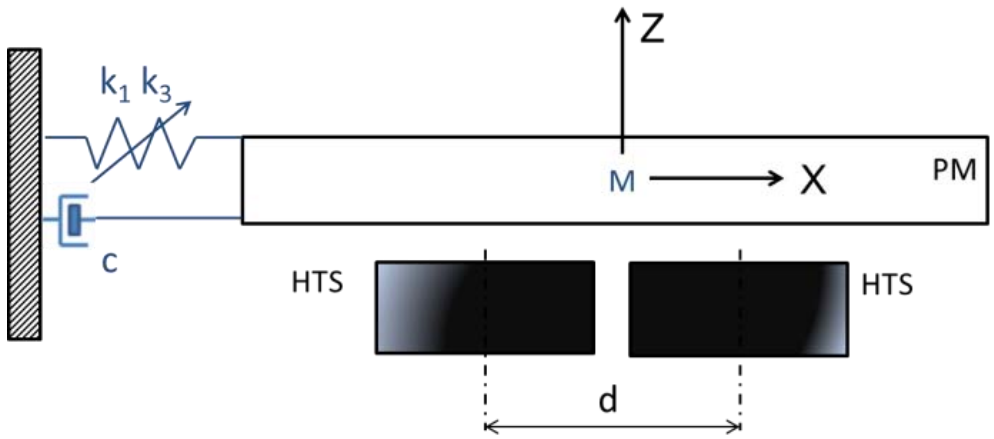

Fig. 6.28. Mechanical model for the motion of the slider.

Then the motion equation of the system can be written as:

$$M\frac{d^2x}{dt^2} + c\frac{dx}{dt} + k_1x + k_3x^3 = 0$$

eq. 6.5

where

M is the levitating mass (170±5 g),
x is the position of the slider,
t is time,
and c the viscous damping coefficient,

Furthermore, the angular frequency of the oscillator will be defined as in [149]:

$$\omega_0{}^* = \sqrt{\frac{k_1 + k_3}{M}}$$

eq. 6.6

The damped angular frequency of the slider, $\omega_d{}^*$ will be:

$$\omega_d{}^* = \omega_0{}^* \cdot \sqrt{1 - \xi^2}$$

eq. 6.7

where

ξ is the damping ratio defined as $\xi = \frac{c}{2\sqrt{M(k_1+k_3)}}$.

Note that, as k_3 is much smaller than k_1, the angular frequency previously defined is quite similar to the natural angular frequency of an harmonic oscillator with linear stiffness k_1. A difference of less than a 1% has been estimated between the natural angular frequency of a harmonic oscillator and the angular frequency. However, if the angular frequency introduced in eq. 6.6 is used, the equation of the motion of the slider can be written as:

$$\frac{d^2x}{dt^2} + 2\xi\omega_0{}^* \frac{dx}{dt} + a_1 x + ax^3 = 0$$

eq. 6.8

where

x is the position of the slider,

t is time,

$a_1 = \frac{k_1}{M}$ and $a_3 = \frac{k_3}{M}$,

and $\omega_0{}^*$ is the angular frequency in eq. 6.6.

These parameters can be measured experimentally as follows: the slider can be moved away from the initial position to different positions along its path and then launched (coils suddenly switched off). Then, the X position of the slider vs. time is recorded for each experiment until the initial equilibrium position is recovered, as shown for example in Fig. 6.29.

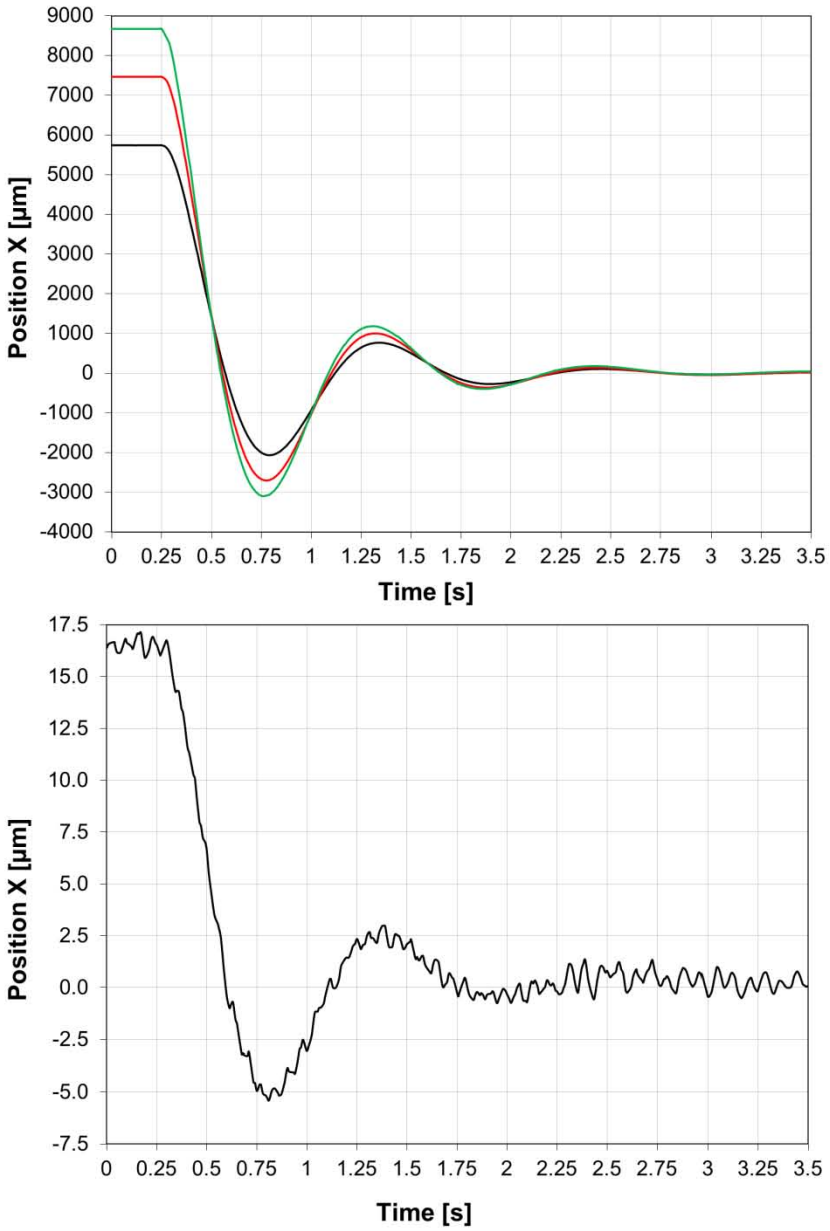

Fig. 6.29. Different signals used for the analysis of the dynamic behaviour of the *FTS* mechanism.

The damping ratio of the system can be determined using the logarithmic decrement method. The damped frequency of the system can be determined using spectral and time analysis.

Spectral analyses based on the Lomb-normalised periodigram is considered a good detector for determining the frequencies of interacting oscillators in a nonlinear system [150]. It was used to find the damped frequency of the mechanism. Power spectrum for records of the same duration (3.5 s) with a frequency acquisition of 100 Hz (remember the time unevenly of acquired datasets) and consequently a frequency resolution around 0.3 Hz. The

normalised spectral power density for displacements of 2.4 µm and 8669 µm are presented in Fig. 6.30.

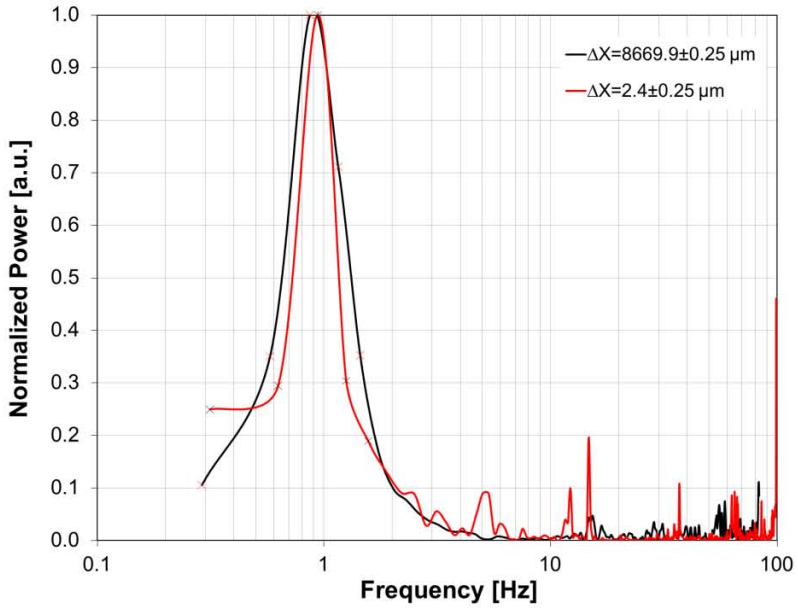

Fig. 6.30. Lomb-normalised periodigram (with normalised spectral power density), for motion of 2.4 µm (red) and 8669.5 µm (black) displacements.

Despite the frequency resolution being relatively low, a clear peak around 1 Hz could be identified. No presence of significant harmonics in the signal was found. Spectral analysis was developed for other displacements of the slider around the central equilibrium position showing very similar behaviour.

In addition, a different approach to calculate the damped frequency was as follows. The period of the signal can be calculated at different relevant points in the motion of the slider in Fig. 6.29. A time-uncertainty in the time of the relevant peaks of 5 ms produces an uncertainty of 10 ms in the period. Results from these analyses of the signal are summarised in Table. 6.1.

Table 6.1. Lomb-normalised periodigram main frequency and initial damped frequency obtained by time analysis for different travel lengths of the slider.

Motion amplitude [µm]	**Lomb-normalised periodigram**	**Time analysis**
	Main damped frequency [Hz]	Average damped frequency [Hz]
2.4±0.25	0.9±0.3	-
16±0.25	1±0.3	0.91±0.02
5739.4±0.25	0.9±0.3	0.91±0.02
7464.9±0.25	0.9±0.3	0.91±0.02
8669.9±0.25	0.9±0.3	0.92±0.02
	Frequency analysis	Time analysis
Average value	0.9±0.3	0.91±0.02

The dependence of the damped frequency of the slider with the amplitude of the displacement is low. The damping ratio of the *FTS2* prototype was calculated as $\xi = 0.32 \pm 0.01$. No relevant dependence of the damping ratio was observed on the amplitude of the displacement. Thus, the viscous damping coefficient c can be calculated to be $c = 0.67 \pm 0.08\ \mathrm{Nsm^{-1}}$ and the critical damping coefficient $c_c = 2.1 \pm 0.1\ \mathrm{Nsm^{-1}}$.

Then, considering an average damped frequency $f_d^* = 0.91 \pm 0.02\ \mathrm{Hz}$, an equivalent angular frequency $\omega_0^* = 6.0 \pm 0.2\ \mathrm{rad/s}$ $\left(f_0^* = 0.96 \pm 0.04\ \mathrm{Hz}\right)$ can be estimated with eq. 6.6. A comparison of the values obtained based on the experiments on the *FTS2* prototype and the values obtained with the theoretical predictions from the FEM calculation of the stiffness of the slider are summarised in Table. 6.2. It can be stated that the theoretical predictions and the values obtained from the experiments agree well within the margin of uncertainty.

Table 6.2. Comparison of the damped and angular frequency obtained from experiments and theoretical predictions based on FEM calculation of the stiffness of the slider of the *FTS2* prototype.

Value obtained from	**Damped frequency f_d^* [Hz]**	**Angular frequency f_0^* [Hz]**
Experiments	0.91±0.02	0.96±0.04
Theoretical predictions ($\xi = 0.32$)	0.90±0.05	0.95±0.02

It is quite relevant that the angular frequency of the oscillator can be theoretically modified just by adjusting the stiffness of the slider. This can be achieved for example, by changing the distance between the superconductors, d or by modifying the *HFC* as demonstrated in chapter V. From the fitting curves in Fig. 5.17, the value of the angular frequency of the slider for different values of d can be calculated using eq. 6.6. See Table 6.3.

Table 6.3. Angular frequencies calculated with eq. 6.6 for different values of the distance between the superconductors d.

d [mm]	**Angular frequency [Hz]**	**Uncertainity [Hz]**
47	0.40	0.01
66	0.46	0.02
74	0.68	0.03
80	0.91	0.04
84	0.94	0.04
90	1.1	0.06

6.4.1.7 Speed of the FTS2 prototype

The phase diagram (Velocity vs. X position) of the slider is shown for different motion steps in Fig. 6.31. The longer the displacement, the higher the velocity reached.

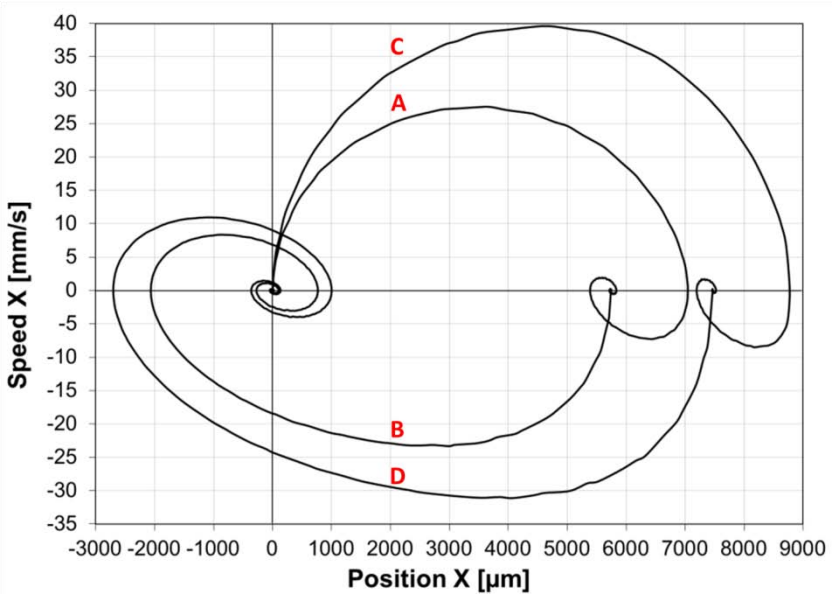

Fig. 6.31. Speed vs. X position for different motion histories of the slider.

However, it may be useful to define an apparent speed as the speed of the mechanism to achieve a stable position after a motion step. We define the final stable position as the position of slider when it is not farther than 1 µm from the target.

Then, the apparent velocity of the mechanism is described by eq. 6.9:

$$V_{ap} = \frac{\Delta X}{\Delta t}$$

eq. 6.9

where,

ΔX is the motion step,

and Δt is the time increment from one stable position to another.

The apparent velocity was calculated for both, motion oscillations from the initial equilibrium position to a certain position in the stroke of the mechanism, and the other way around, from a certain point in the stroke of the device to the equilibrium position. In both cases, the value of the driven current in the coils suddenly changes. Results for the apparent velocity and maximum velocity reached in trajectories A,B,C and *D* in Fig. 6.31 are summarised in Table 6.4.

Table 6.4. Apparent and maximum velocity of the slider for different motion histories.

Trajectory name	**$X_{initial}$ ± 0.25 [µm]**	**X_{final} ± 0.25 [µm]**	**Maximum velocity ± 1 [mm/s]**	**Δt ± 0.1 [s]**	**V_{ap} [mm/s]**
A	0	5731.2	28	1.8	3.2
B	5731.2	0	24	5.8	1.0
C	0	7462.4	40	2.1	3.6
D	7462.4	0	30	6.1	1.2
E	16.0	0	$7\pm1x10^{-2}$	1.9	$8x10^{-3}$

The apparent velocity of the slider could be a useful tool to evaluate the real speed of the modification of the position of the slider. However, because the *FTS2* prototype is an underdamped system, its apparent velocity could be improved by implementing an appropriate PID control or an input shaping strategy.

In summary, the *FTS2* prototype is an underdamped oscillator. The elastic force provided by the spring in the mechanical model in Fig. 6.28 can be represented by a nonlinear function of the X position of the slider, as already demonstrated. In this context, the calculated natural frequency of the system is about 0.90±0.03 Hz and the damping ratio about 0.32±0.01. Apparent velocities over a few mm/s were measured for millimetre travel lengths.

6.4.2 Run out of the *FTS2* prototype

After the characterisation of the motion of the mechanism in the X direction, the experimental set up was modified so that the Y position of the slider could be measured. In order to do so, it was necessary to relocate the interferometer with the laser aligned in the Y direction.

The run out vs. X position of the slider is presented in Fig. 6.32. Clear hysteretic behaviour can be appreciated. In addition, the lateral run out of the slider is of the order of ± 4 µm for a full stroke motion (± 9 mm).

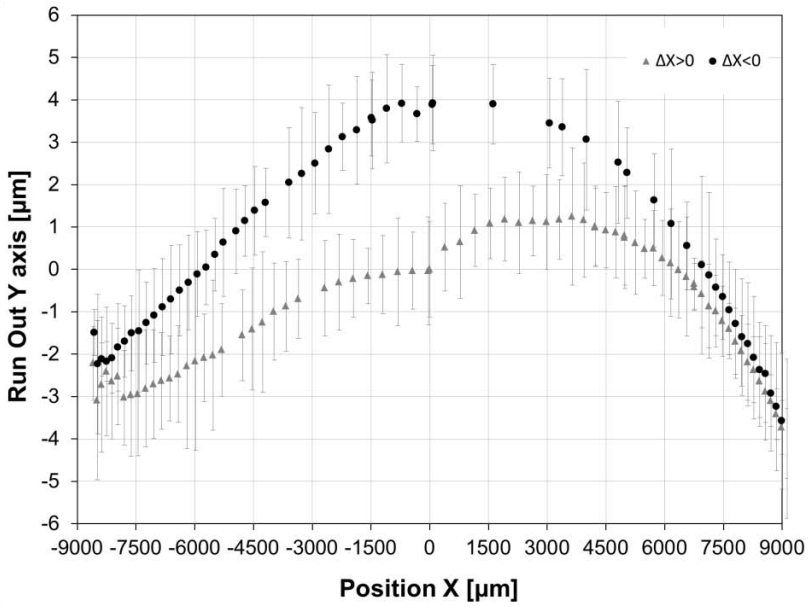

Fig. 6.32. Lateral run out (Y axis) of the slider in the *FTS2* prototype. $\sigma_x < 50$µm.

6.4.3 Angular run outs of the *FTS2* prototype

Yet again, the pitch, yaw and roll of the slider were measured using the Newport auto-collimator.

6.4.3.1 Pitch

Pitch versus X position of the slider is presented in Fig.6. 33. A pitch of about ± 650 µm for a full stroke motion was measured. In addition, the pitch of the slider measured at 15 K was reduced around a 10% with respect to the pitch measured at 77 K for the same prototype.

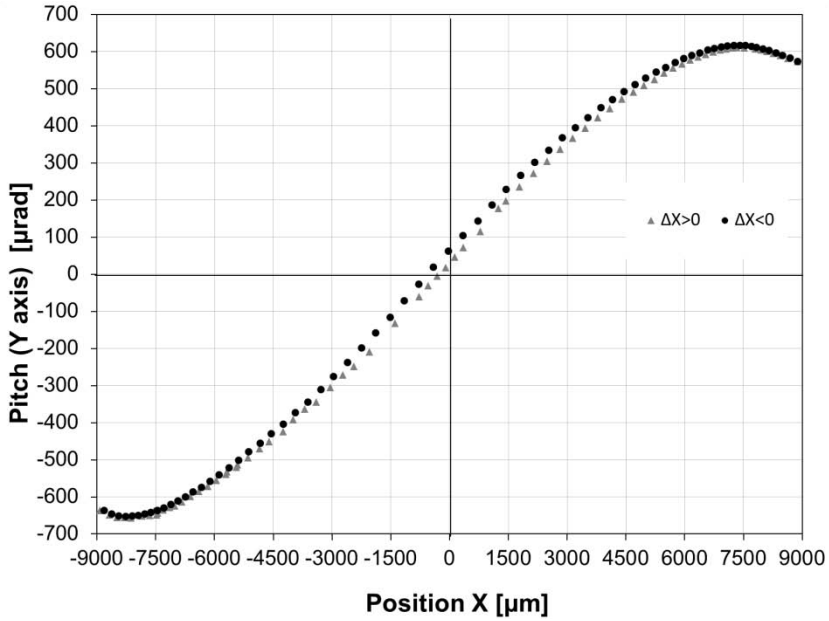

Fig. 6.33. Pitch vs. X position of the slider in the *FTS2* prototype. $\sigma_x < 50\mu m$.

6.4.3.2 Yaw

Yaw versus X position of the slider is plotted in Fig. 6. 34. A clear improvement in the yaw with respect to that measured at 77 K can be seen.

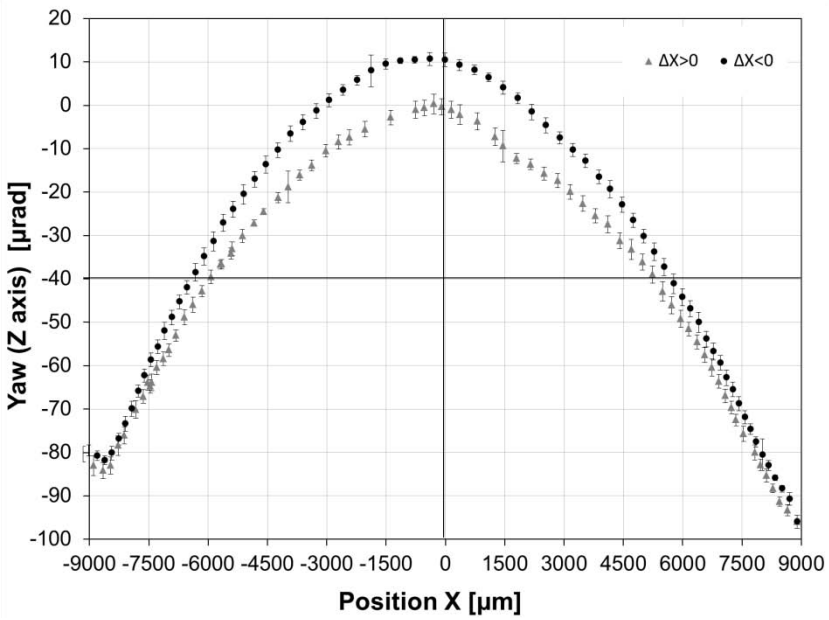

Fig. 6.34. Yaw vs. X position of the slider in the *FTS2* prototype. $\sigma_x < 50\mu m$.

6.4.3.3 Roll

Roll versus X position of the slider is represented in Fig. 6.35. The roll was the higher of the angular run outs measured. After analysing the problem, we concluded that the high value of the roll was mainly caused by a misalignment between the magnetisation of the PM (Z axis) and the magnetic axis of the coils.

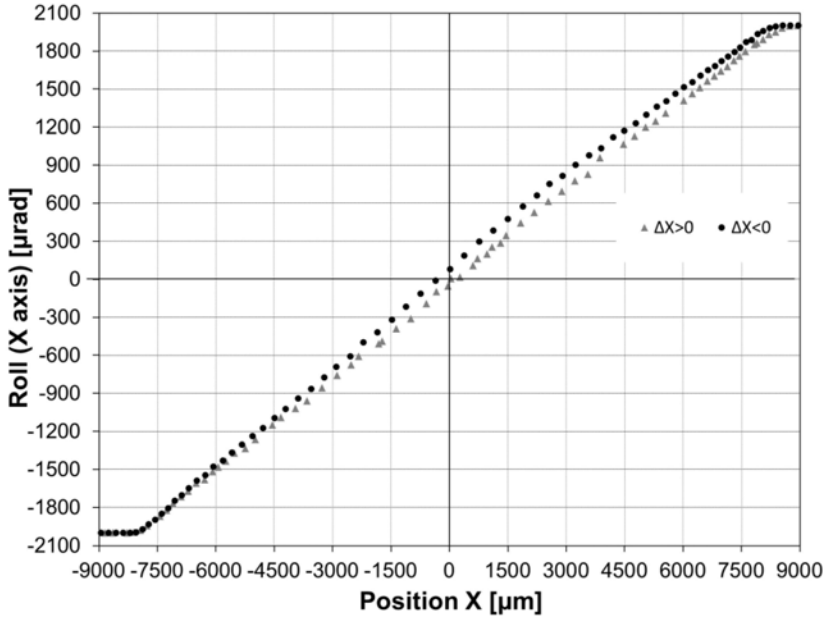

Fig. 6.35. Roll vs. X position of the slider in the *FTS2* prototype. $\sigma_x <$ 50µm.

6.4.4 Power consumption

Resistivity of the wire in the coils was measured to be around 1.8×10^{-8} Ωm and the resistance of each of the coils was 3.1±0.1 Ω at room temperature (300 K). In order to calculate the power consumption of the device, different values of residual resistance ratio (RRR) between 30 and 3000 on the copper wire were considered for calculations. Reduction in copper resistivity as a function of its RRR is shown in Fig. 6.36.

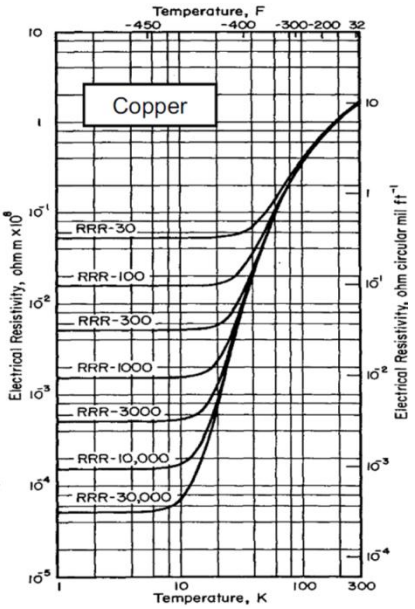

Fig. 6.36. Electric resistivity of different copper materials as a function of the temperature of the sample. [134]

As a good approximation the self-heating of the wire can be neglected and therefore the power consumption of the device itself can be now calculated as:

$$W = 2I^2R(T)$$

eq. 6.10

where

I is the maximum current in the coils,

and R(T) is the resistance of each of the coils at a certain temperature.

Therefore, the peak value of the power consumption can be calculated for a demanded current of 450 mA magnitude. Estimated power consumptions for a working temperature of 15K and the different RRR considered are presented in Table. 6.5:

Table 6.5. Power consumption calculated for different RRR copper wires in the coils.

RRR	Power consumption estimated [mW]
30	40
100	13
300	5
1000	2
3000	0.5

6.5 Conclusions of chapter VI

In this chapter, it has been demonstrated that a device based on superconducting magnetic levitation, designed as described in the previous chapters, can achieve sub-micrometric positioning resolution in a long motion range of ±9 mm. This new technology has been tested in accordance with an ESA TRL 6: A prototype of such a device was successfully tested in a relevant cryogenic environment (~15K and high vacuum < 10-6 Pa). The measured performance of the device is summarised in Table 6.6.

Table 6.6. Summary of the performance of the *FTS2* prototype.

Performance of the *FTS2* prototype	
Device temperature [K]	~15
Cryostat inside pressure [Pa]	~10^{-6}
Stroke [mm]	±9
Sensitivity coarse/fine step motion in the initial equilibrium position (X=0 mm) [µm/mA]	31/15±1 respectively
Resolution coarse [µm]	3.3±0.4
Resolution fine RMS [nm]	230±30
Accuracy [µm]	~1
Power consumption (15K) for RRR=300 [mW]	~5
Hysteresis (X=0) [µm]	60±2
Damping ratio	0.32±0.01
Damped frequency [Hz]	0.91±0.02
Maximum measured velocity [mm/s]	~40
Lateral run our (Y axis) [µm]	±4
Relative pitch (Y axis) [µrad]	±650
Relative yaw (Z axis) [µrad]	<100
Relative roll (X axis) [µrad]	<4000

The performance of the *FTS2* prototype is slightly influenced by the working temperature. Despite some parameters like the sensitivity of the mechanism being affected by temperature, this influence is much lower than the dependence observed in piezo-electric actuators (see chapter II). It is also noticeable that the stroke of the mechanism is not influenced by the working temperature.

Dynamic behaviour was found to be in a very good agreement with that predicted using a nonlinear stiffness obtained with FEM calculations described in previous chapters. The *FTS2* prototype can be properly described as an underdamped harmonic oscillator with very low dependence of its natural frequency with respect to the amplitude of displacements within the length of the designed stroke. The *FTS* mechanism has been demonstrated to behave as an underdamped oscillator with a non-linear stiffness The measured damping ratio was 0.32 for a natural damped frequency of around 0.91±0.02 Hz (not significantly dependent on the amplitude of the displacement). In addition, the angular frequency of the mechanism can be tuned simply by adjusting the stiffness to the motion of the slider, for example, by modifying the distance between the superconductors d.

The measured lateral run out was more than three orders of magnitude lower than the stroke of the mechanism. Angular run outs (pitch, yaw and roll) were also low and below a few milliradians. Therefore, it can be stated that the stability of the contact-less guidance provided by the superconductors is high. A hysteretic loop for full-stroke motion with maximum deviation at the centre of the stroke of 60 µm was measured.

Finally, the *FTS2* prototype showed outstanding performance in comparison with other high-precision positioning instruments based on superconducting magnetic levitation (see chapter II). Despite the motion resolution being well above nanopositioners based on other technologies (such as active magnetic levitation or piezoelectric actuators) it was demonstrated that the performance of the device could be improved by providing better vibration insulation to the device and a better current resolution. In addition, a low power consumption of only a few milliWatts can be achieved using a low RRR winding in the coils.

Chapter VII

Long-stroke nanopositioning slider for cryogenic applications

A prototype of a long stroke high-precision positioning device for cryogenic applications was designed, built and tested in a relevant environment as demonstrated in in the previous chapter. In this chapter, additional improvements are made and an improved prototype (FTS3) has been tested in a relevant environment. Results and a discussion of these experiments are conducted in this chapter.

7.1 Introduction

A sub-micrometre positioning resolution was demonstrated by the FTS2 prototype. This prototype of the *FTS* mechanism was successfully tested in a relevant environment (temperature ~ 15K and pressure $<10^{-6}$ P). Regarding the run outs of the mechanism, roll is the greatest one with a value of around ± 2000 µrad for full stroke motion (± 9 mm).

In order to improve the performance of the *FTS* mechanism, some modifications were carried out to the *FTS3* prototype. The new prototype was tested again in a relevant environment inside a cryostat. The description of the prototype and a discussion of the test results are introduced in the following sections.

7.2 Description of the *FTS3* prototype

The *FTS3* prototype was built following the same design rules in chapter V. A current demanded in the coils lower than ± 500 mA should be achieved. Nanometre resolution must be demonstrated (<100 nm RMS) and angular deviations must be as low as possible. The *FTS3* prototype is mainly composed of three different parts:

A stator, made of two 45 mm diameter and 13 mm thickness polycrystalline *YBaCuO* disks (*HTS*) and a third central disk of 36 mm in diameter and 12 mm thick (1). The *HTS* were contained in an aluminium base (5) with a distance 84±0.1 mm between the centres of larger disks. The smaller one is located with its axis coincident with the Z axis, as shown in Fig. 7.1. Pt-100 sensors were also fixed to the superconductor's base in order to measure the temperature of the superconductor at any moment.

The same $Nd_2Fe_{14}B$ PM (2) described in the previous chapters mainly compose the slider of the mechanism, with its magnetisation direction oriented parallel to the Z axis in Fig. 7.1. In addition, the PM carries an optic mirror cube (6). Now, two levitation heights or Height of Field Cooling (*HFC*) must be defined. The first HFC_1 from the PM to the 45 mm superconducting disks is 2.0±0.1 mm, and the second HFC_2 is 3.0±0.1 mm between the PM and the 36 mm superconducting disk. This difference is required for operation of the launch & lock system as will be introduced later. Finally, the base of the superconductors (5) was re-manufactured including the housing of the central disk and a mechanisation to remove 3 mm of material in the upper surface. This

last operation will be required as well for the operation of the launch & lock system.

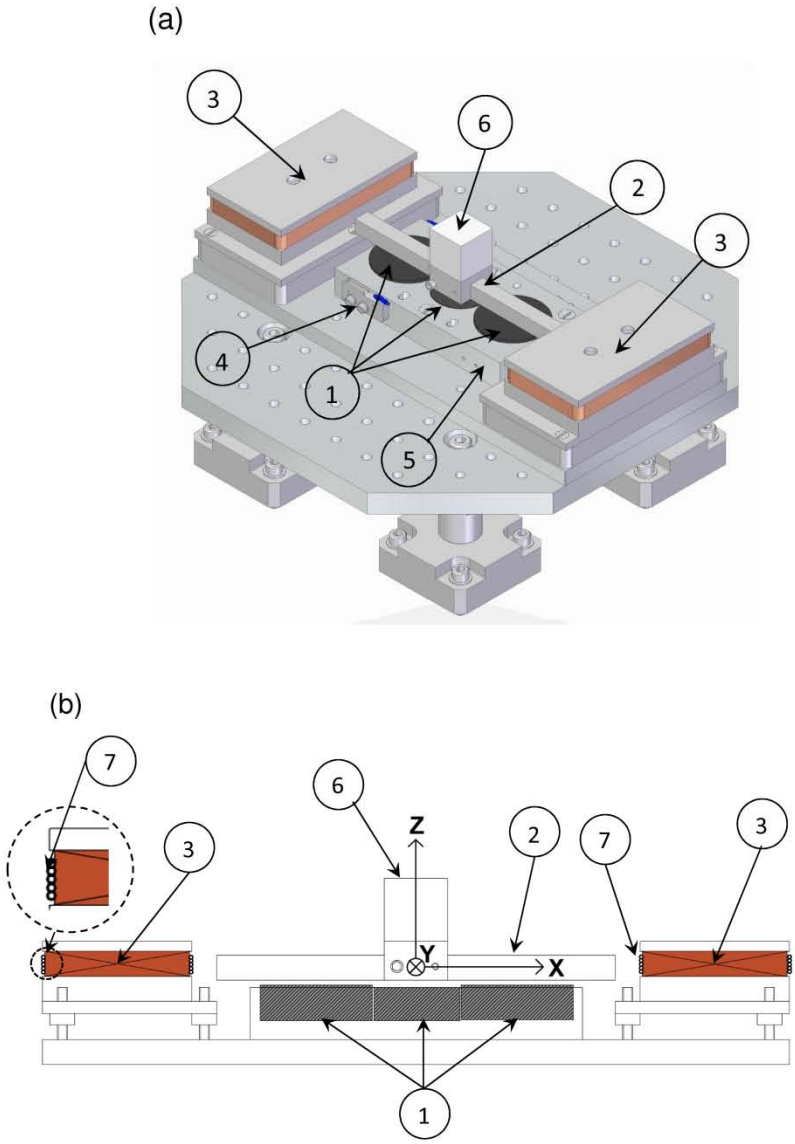

Fig. 7.1. a) 3D CAD representation of the *FTS3* prototype: 1) Superconducting disks (*HTS*); 2) PM (PM); 3) Main coils, 4) PT-100 sensor, 5) superconductors base; 6) Optic mirror cube and 7) Secondary coils. Left: CAD of the *FTS2* prototype. b) Lateral representation of the *FTS3* prototype.

Lastly, the actuation system is again composed of two coils (3) with its axis parallel to the Z axis in Fig. 7.1, placed at either end of the stroke. As has already been demonstrated in chapter V, the current demanded in the coils will be increased due to the reduction in the levitation height because the magnetic field and the magnetic field gradient in the superconductors will be greater due to the reduction in the *HFC*. Increase of the magnetic field and the magnetic field gradient in the sliding direction when the superconducting disks are at the

normal state are shown in Fig. 7.2. Note that the magnitude of the magnetic flux density on *HTS* in the *FTS3* prototype in the X direction (B_x) is higher than the one calculated in the *FTS2* prototype (~48 mT and ~61 mT respectively)

In this figure, it can be also seen that changes in the magnetic field in the X axis are very low in the central disk for any X position of the slider. Therefore, despite this third superconductor contributing to a reduction in the run outs of the *FTS3* prototype, it is considered that its presence does not significantly adjust the current required in the coils.

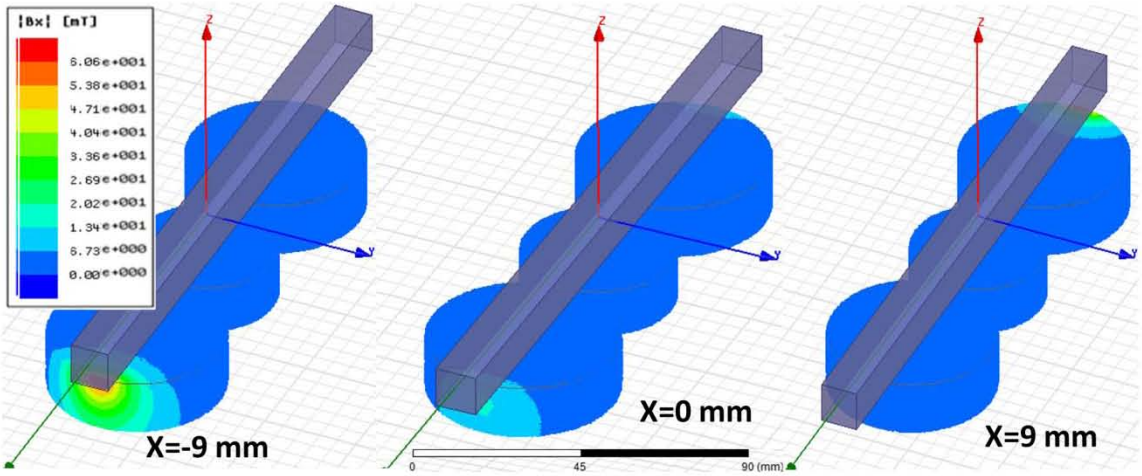

Fig. 7.2. Absolute magnitude of the magnetic flux density in the X direction in the *HTS* at the normal state for a) the *FTS2* prototype and b) the *FTS3* prototype.

In accordance with the estimated increase in the stiffness of the slider, the coils were redesigned in order to provide the extra current required. Electromagnetic calculations demonstrated that the new coils with a rectangular shape 110x60 mm^2 and 10 mm thickness and an inner aluminium core of 68x17 mm^2 surrounded by 190 turns of the wire described in chapter IV could provide enough strength to move the slider in a full stroke motion of ± 9 mm with a demanded current lower than ± 500 mA.

Additionally, two auxiliary coils (7) with 5 turns each were installed surrounding the principal ones in order to provide a fine step motion control of the slider. These coils were also connected in anti-serial configuration. They were fed with a voltage signal between ± 10 V generated in the NI 6230 voltage generation card. In order to fix the current in the coils, an adjustable resistor located outside the cryostat was used.

7.3 Experimental set up and procedure

The *FTS* final prototype was installed inside the cryostat and cooled to a temperature of around 15K. High vacuum ~10^{-6} Pa was also achieved inside the chamber. A real image of the *FTS3* prototype installed inside the cryostat is shown in Fig. 7.3.

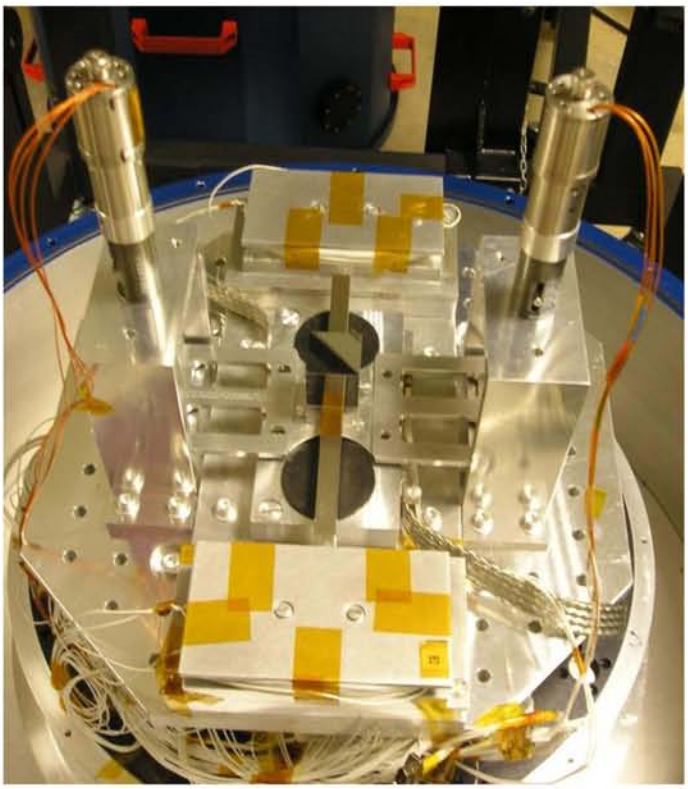

Fig. 7.3. Picture of the *FTS3* prototype inside the cryostat.

Once a stable temperature of around 15K was reached and the sliding kinematic was established, the slider was launched. Experiments developed in this chapter are similar to the experiments introduced in chapter VI. Therefore, the experimental procedure of the experiments in the FST3 prototype are the same as the one described in chapter VI. However, there are some small differences in the experimental set up which are described in the following sections.

7.3.1 Electric diagram

The electric connection diagram was modified in order to provide a second input independent signal to the auxiliary coils for the fine positioning as show in Fig. 7.4.

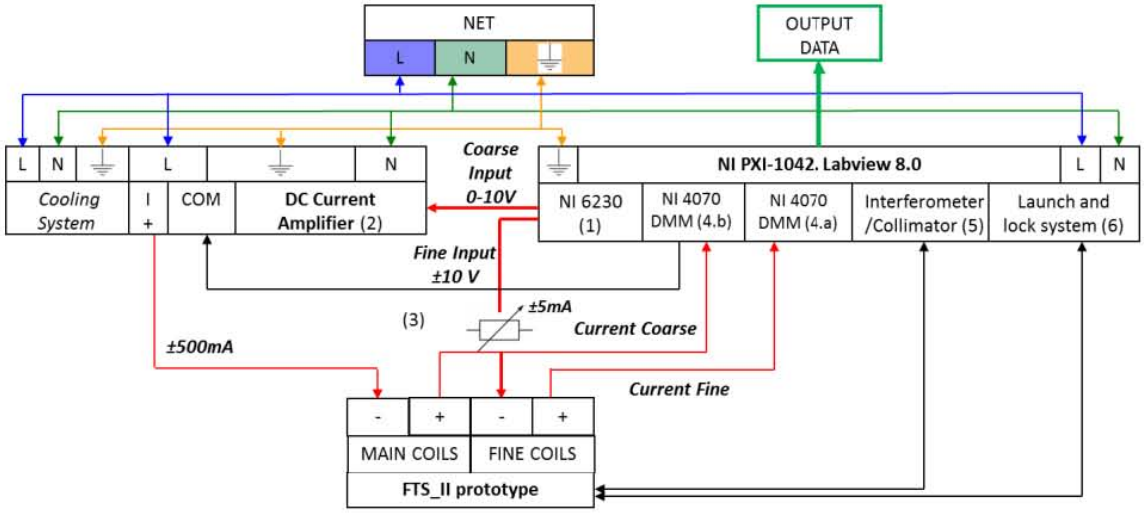

Fig. 7.4. Electric connection diagram of the *FTS3* prototype.

Regarding the amplifier, the prototype was modified so it supplies about ± 500 mA current for an input voltage of 0-10 V. Current vs. input voltage in the amplifier is plotted in Fig. 7.5.

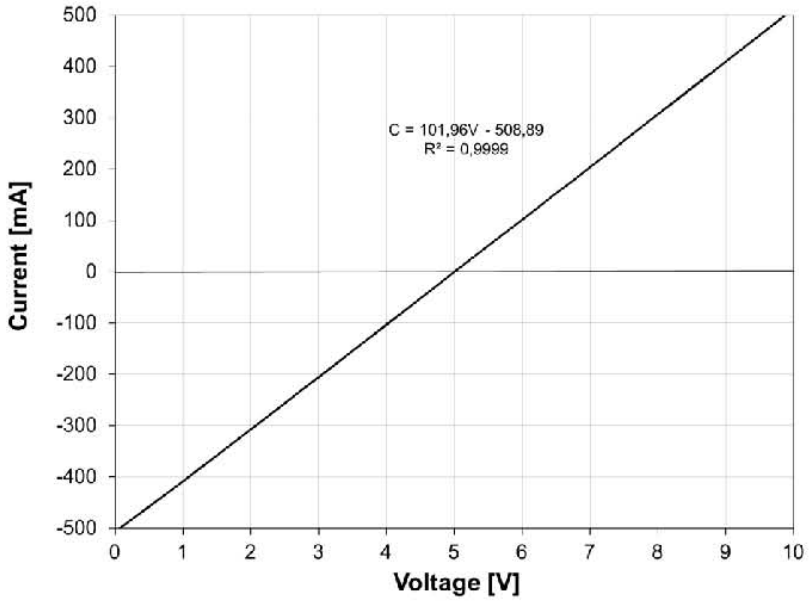

Fig. 7.5. Output current vs. input voltage in the amplifier after modification.

Note that in this chapter, the maximum achievable current resolution in the coarse step motion is around 30 µA in spite of around 100 µA of the current resolution being used for measuring the position resolution in the *FTS2* prototype.

7.3.2 Launch & lock system

The holder of the launch & lock system was modified to reduce the *HFC* of the slider. Together with the modifications to the base of the superconductors, the new holder was manufactured of Al-6061 T6, which provides better rigidity and improves the alignment of the PM and the coils. In addition, two cuts were made in the holder so that it can be dropped and elevated without contact with the 45 mm superconducting disks. Finally, due to the different *HFC* for the 45 mm disks and the 36 mm disks, the *HFC* for the 45 mm disks could be reduced from 3 mm to 2 mm. A sketch of the new holder and a top view of the prototype are shown in Fig. 7.6.

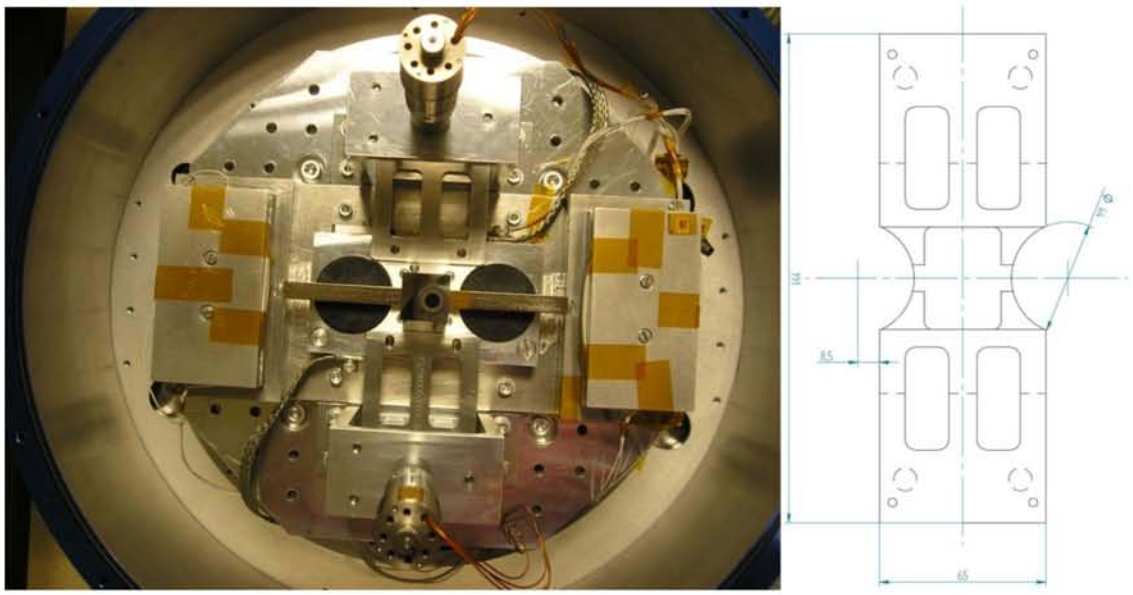

Fig. 7.6. Left: Top view of the prototype inside the cryostat; right: sketch of the holder of the launch & lock system

In addition, some modifications were made in the holder and the *FTS3* prototype in order to provide a better alignment between the PM and the coils. Consequently, run outs were expected to be reduced.

7.4 Tests results and discussion

7.4.1 Positioning performance

The performance of *FTS3* is discussed in this section. The main parameters that characterise the positioner are presented: X position vs. input current, position stability and accuracy, position resolution, hysteresis, stiffness and

damping of the mechanism. Once again, the cosine error as a result of an angular misalignment between the laser beam and the axis of motion of the slider has been corrected in the reported results.

Before introducing the results, it should be mentioned that an initial jump of the slider of ~ 1.5 mm in the -X direction was observed. Upon inspection of the prototype after the warming up process we detected damage to one of the superconducting disks, probably as a consequence of the thermal stress generated by the great number of cooling and warming processes suffered by this point. Small cracks could be seen on the disk. We also determined that if the position of the damaged superconducting disks is changed to the other hole in the housing, the initial offset of the slider occurs in the opposite direction of the prototype.

In order to facilitate the comparison of *FTS2* and *FTS3*, all the charts in this chapter have been offset to the initial equilibrium position. In addition, this is the main reason why the stroke of the mechanism is reduced from ± 9 mm to ± 7.5 mm.

7.4.1.1 X position versus current through the coils

The position of the slider vs. the current in the coils was measured along the whole stroke of the mechanism. The current through the coils was modified by increments of around 10.00±0.05 mA and multiple full cycles were measured. Results for these measurements are presented in Fig. 7.7.

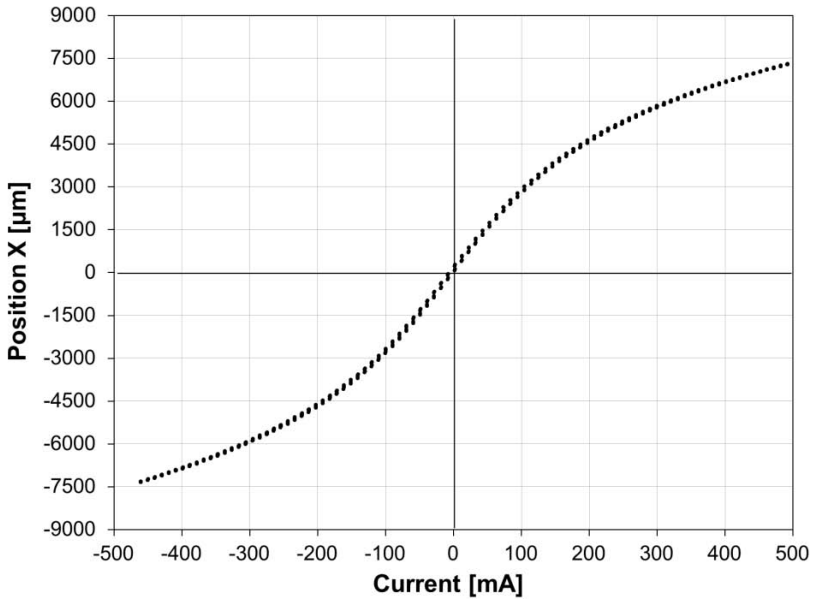

Fig. 7.7. X position vs. current for full stroke motion of the *FTS3* prototype.

It can be observed that the stroke of the mechanism is now around ± 7.500 µm. The power requirement is presently around ± 500 mA. Sensitivity to the motion vs. X position of the slider is presented in Fig. 7.8. Sensitivity in the central position is still in the same order of magnitude, but it decreases with the X position of the slider faster than in the case of the *FTS2* prototype. This is caused by the increased stiffness to the motion of the slider due to the reduction in the *HFC*. Notice that the sensitivity of the mechanism is almost the same for both prototypes and about 31µm/mA in the surroundings of the central position.

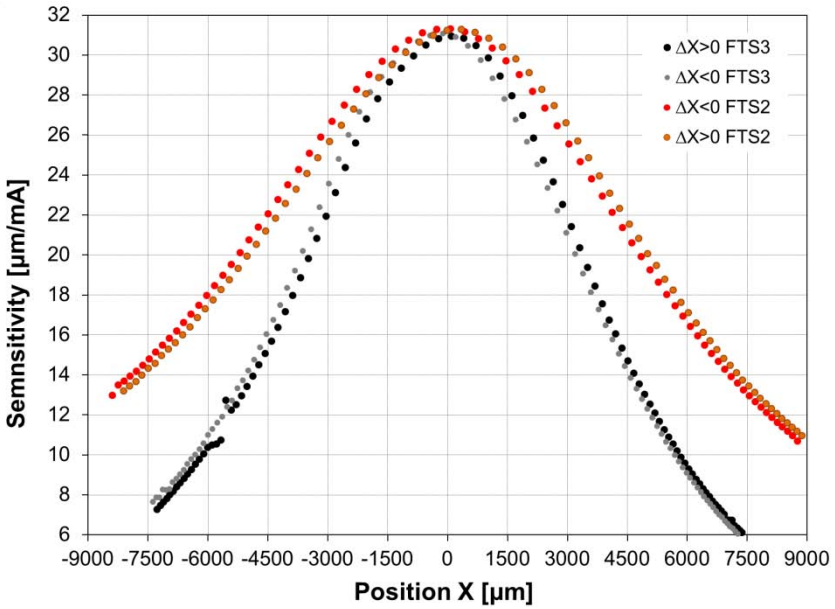

Fig. 7.8. Sensitivity vs. X position of the slider for the *FTS2* and *FTS3* prototypes.

Again, a small divergence in the values of sensitivity for the symmetric position in the stroke can be observed for each of the prototypes. This is assumed to be caused by a small inclination of the cryostat and the resultant force in the X direction of the prototype due to the effects of gravity.

7.4.1.2 Position stability and accuracy

Position stability of the device was measured for different positions in the stroke of the mechanism. Similar results were found and therefore only vibration measurements for the central position of the slider (X= 0 mm) are presented for an acquisition frequency of 1 kHz in Fig. 7.9. A standard deviation of around σ_x= 0.14 µm was obtained for any X position of the slider along its path.

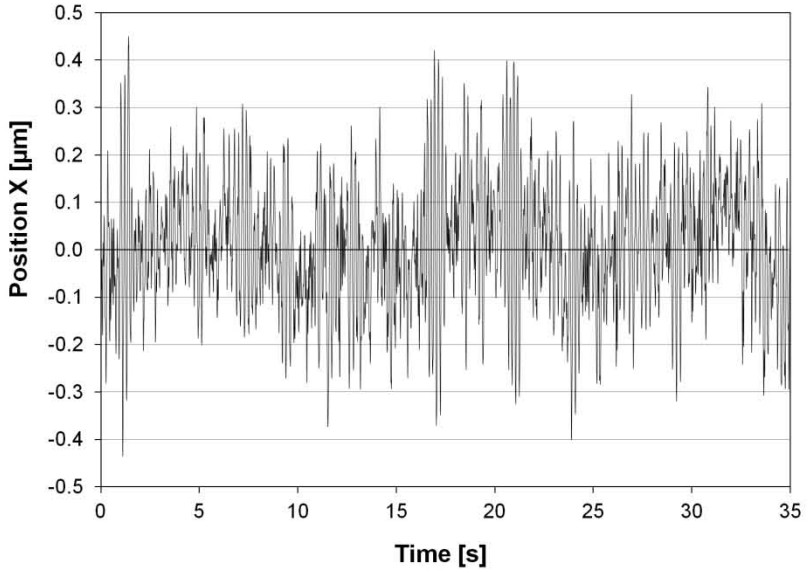

Fig. 7.9. X position vs. time for the surroundings of the central position of the *FTS3* prototype.

In addition, the Y position stability of the slider was also measured. In this case, the oscillation of the Y position was found to be independent of the X position of the slider throughout the measured range. The amplitude of the vibration in the Y axis was found to be one order of magnitude higher than in the case of the X as shown in Fig. 7.10.

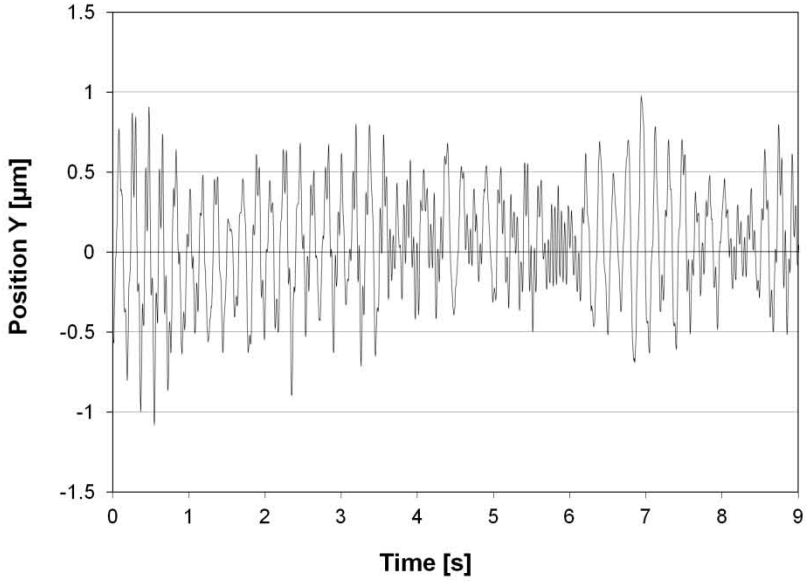

Fig. 7.10. Y position vs. time for the surroundings of the central position of the *FTS3* prototype.

However, the position stability in the Y axis was improved for the *FTS3* prototype with respect that of *FTS2*. This can be interpreted to be caused by the reduction in the *HFC* and the subsequent increase in the stiffness.

Finally, spectral transforms of the X and Y signals using the Lomb-normalised periodigram method are shown in Fig 7.11. The main frequency contribution to the vibration of the slider was found to be 5.5±0.1 Hz.

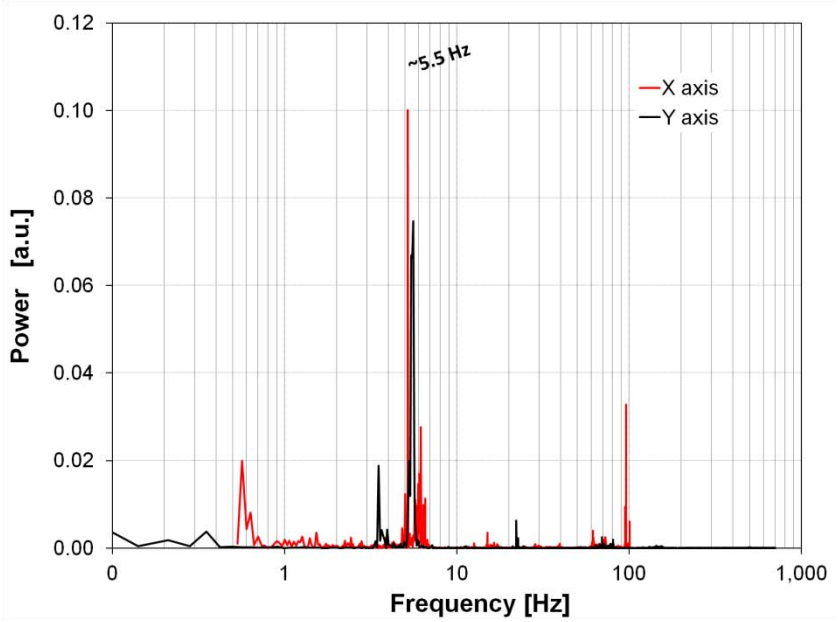

Fig. 7.11. Power density of signals in Fig. 7.9 and Fig. 7.10.

Ultimately, the accuracy of the X positioning can be estimated to be around 0.80 µm (σ_x= ±0.14 µm). Besides, the Y positioning accuracy can be estimated to be 2.0 µm (σ_Y= ±0.4 µm).

7.4.1.3 Position resolution

A significant improvement in the *FTS3* is the use of a double set of motion systems: one for coarse motion (using the main coils) and other for fine motion (using the auxiliary coils).

Coarse step motion:

We defined the coarse step motion resolution of the device as:

"the RMS positioning resolution of the slider when the minimum current step is supplied to the main coils and the slider is in the surroundings of the initial equilibrium position, where sensitivity is maximum"

The resolution in the current signal (∆C) for the coarse current signal measured was of the order of 30±10 µA. The X position of the slider vs. time is presented in Fig. 7.12.

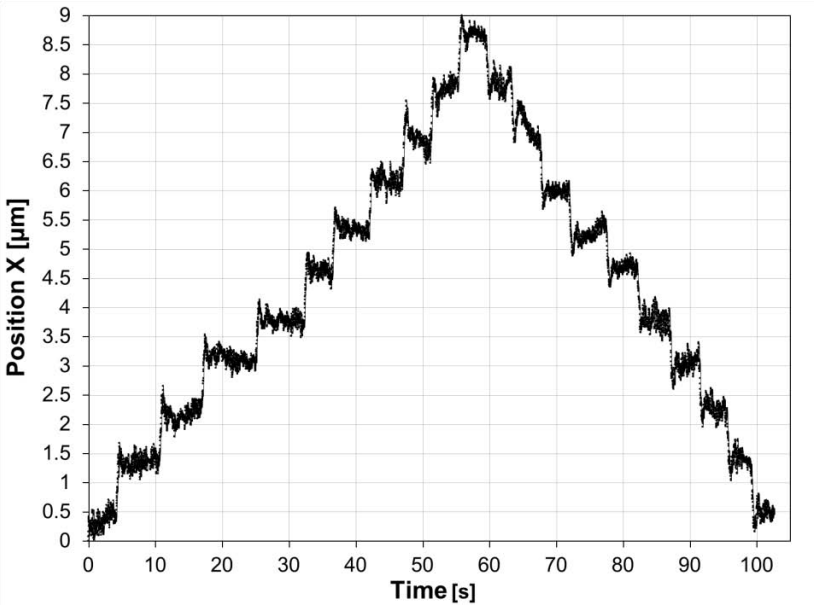

Fig. 7.12. X position of the slider vs. time for current increments of ∆C= 30±10 µA.

It was determined from the data in Fig. 7.12 that the coarse positioning resolution of the *FTS3* prototype was of the order of 0.8±0.2 µm. Note that, the position resolution of the coarse step in the *FTS3* prototype has been improved by around a factor of 4 with respect the *FTS2* prototype due to the better current resolution achieved. Unquestionably, the better the current resolution, the better the coarse motion resolution.

Fine step motion:

Similarly to the experimental procedure described in chapter VI, the current in the coils for fine step motion was set by a variable resistor. Then, starting from a voltage signal generated in the NI 6230 generation card with a resolution of 0.31mV, the current in the fine coils was modified between 100 and 55 µA.

The X position of the slider vs. current increment (∆C=100±10 µA) is presented in Fig. 7.13. In order to make the figure readable, only the RMS X position of the slider is presented. It was calculated that the RMS value of the X position resolution was 120±20 nm.

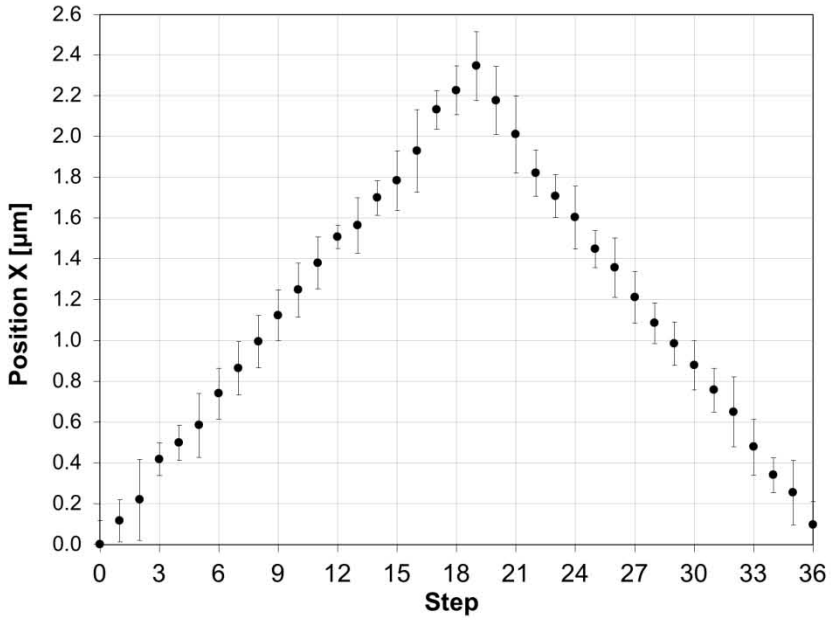

Fig. 7.13. X position (RMS) of the slider vs. current step (ΔC=100±10). Samples measured consecutively with no time registered.

In addition, X position of the slider vs. current in the auxiliary coils for the fine motion was measured. The results are plotted in Fig. 7.14.

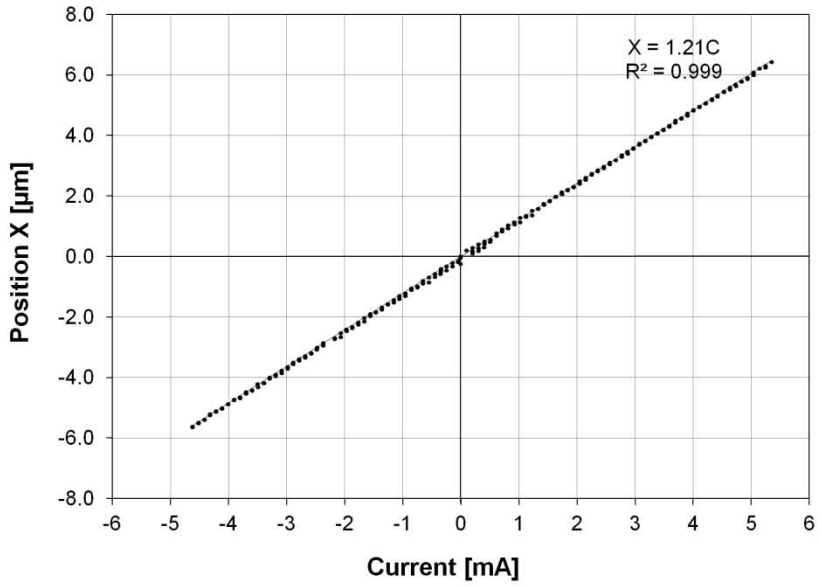

Fig. 7.14. X position of the slider vs. current (ΔC=100±10) in the *FTS3* prototype.

From Fig. 7.14 it can be noted that sensitivity for the fines-step motion using the auxiliary coils is about 1.2 µm/mA, which is almost 30 times lower than the sensitivity in the coarse-step motion. Therefore with a current resolution below 80 µA, a nanometric resolution could be achieved. With a 55±9 µA minimum current step, a nanometre resolution of 70±20 nm in the

surroundings of the central position (X=0 mm) was obtained. Results of these measurements are plotted in Fig. 7.15 and Fig. 7.16.

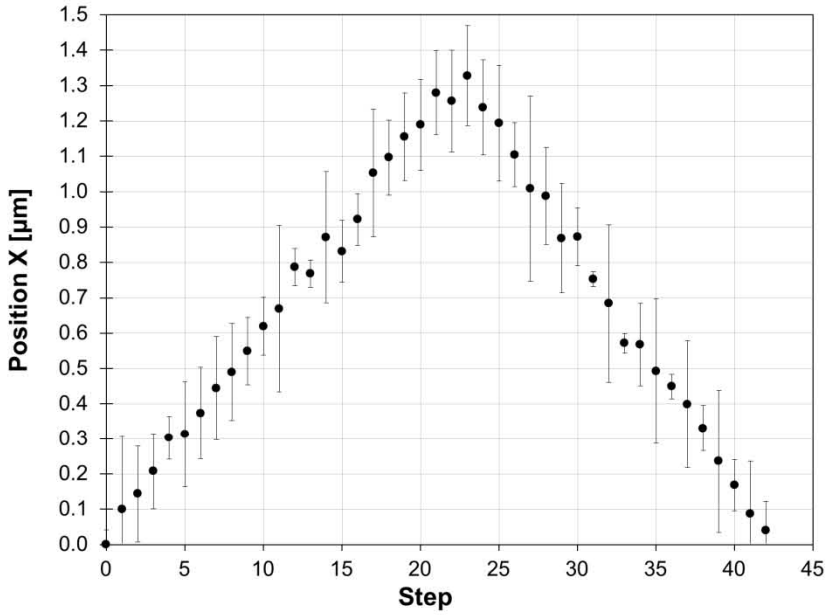

Fig. 7.15. X position (RMS) of the slider vs. current step (ΔC=55±9). Samples measured consecutively with no time registered.

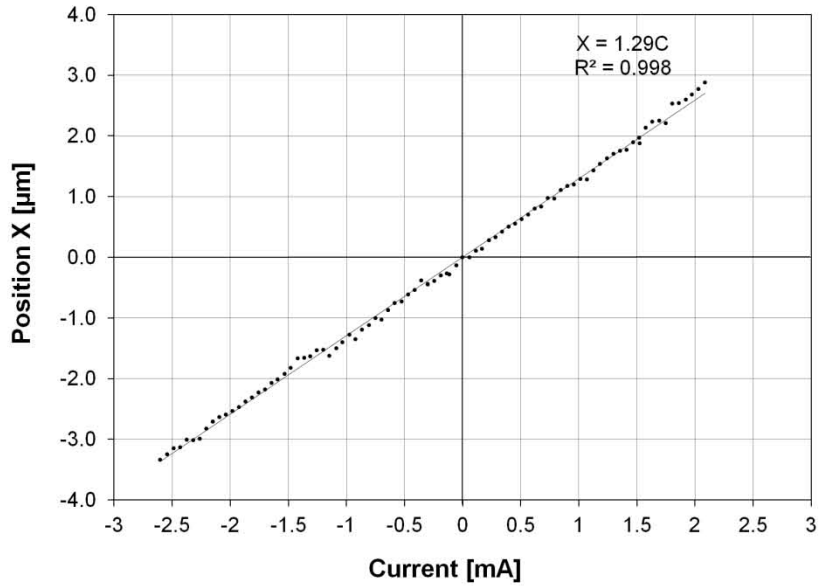

Fig. 7.16. X position of the slider vs. current (ΔC=55±9) in the *FTS3* prototype.

Therefore, if a better current resolution is provided, a better position resolution could be expected.

7.4.1.4 Hysteresis

The hysteresis of the prototype was measured for multiple full stroke motion cycles. Once again, the maximum hysteresis of the loop is in the central position (X= 0 mm). The hysteresis of the *FTS3* prototype can be appreciated in Fig.17 which is a zoom of the central position in Fig. 7.7.

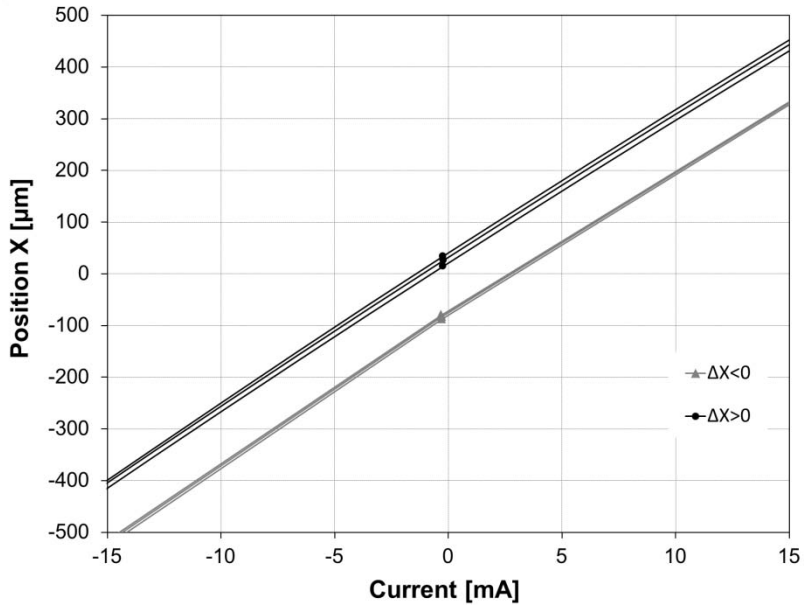

Fig. 7.17. Hysteresis loop of the *FTS3* mechanism focused in the surroundings of the initial equilibrium position, where the hysteresis is maximum.

The apparent hysteresis was now of the order of 100±2 µm for a full stroke motion (± 7.5 mm). That is higher than that measured for the *FTS2* prototype. Ultimately, it was assumed that the increase in the hysteresis of the slider is caused by a reduction in the *HFC* and the consequent increase in the magnetic field trapped in the superconductors. The *HFC* and the magnetic field applied to the superconductor have been already demonstrated to be very relevant for the mechanical properties of Maglev devices [151], [152].

7.4.1.5 Stiffness of the slider

FEA calculations on the *FTS3* prototype show an increase in the resistance to the motion of the slider, especially for the X position closer to the end of the stroke of the mechanism. Calculated forces versus the X position of the slider for the *FTS3* prototype and *FTS2* prototype are plotted in Fig. 7.18.

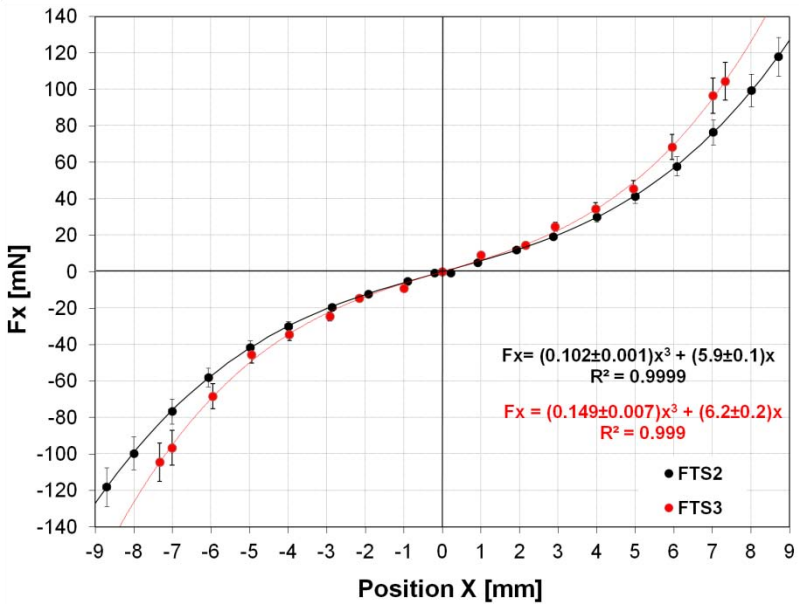

Fig. 7.18. FEM calculated force vs. X position exerted on the slider for the *FTS2* and the *FTS3* prototypes at about 15 K.

The cubic equation for the force now reads:

$$F_x = (1.49 \pm 0.07) \cdot 10^{-1} x^3 + (6.2 \pm 0.2) x \ \ mN$$

eq. 7.1

The stiffness of the mechanism is:

$$K_x = 0.45x^2 + 6.2 \ \ Nm^{-1}$$

eq. 7.2

7.4.1.6 Damping

Once more, the mechanical model proposed in chapter VI is considered to estimate the dynamic behaviour of the *FTS3* prototype. Remember that the mass of the slider is 170±5 grams. According to eq. 6.6 in chapter VI, the natural angular frequency of the slider can now be estimated from the calculated stiffness of the mechanism (see previous sections) to be:

$$\omega_0^* = 6.1 \pm 0.2 \ \frac{rad}{s} \quad or \quad f_0^* = 0.97 \pm 0.03 \ Hz$$

eq. 7.3

Apparently, the natural angular frequency of the mechanism has increased, as was expected according to the results presented in chapter IV. Once again, the slider moved away from the equilibrium position to a new position. Thus,

the current in the coils was suddenly switched off at t=1 s in the measurements presented in Fig. 7.19. X position of the slider vs. time for these displacements was determined.

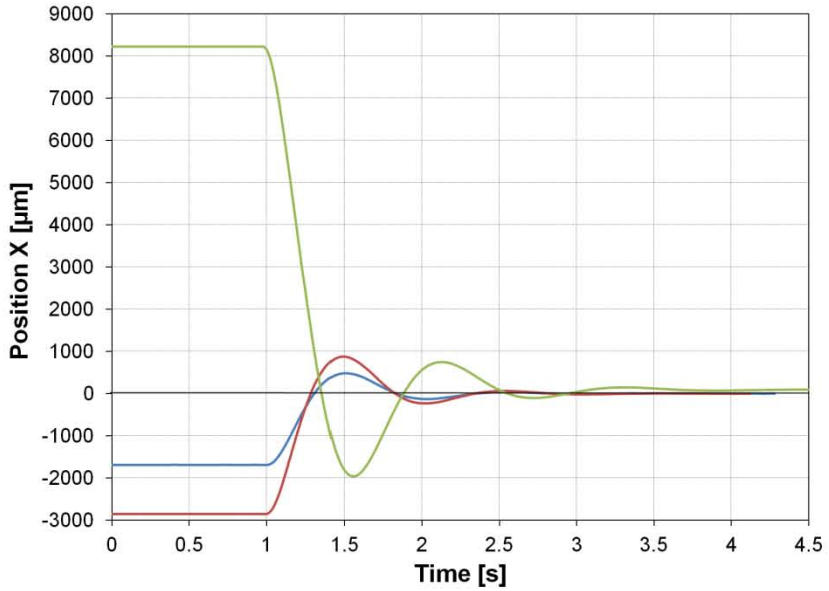

Fig. 7.19. X position vs. time for motion histories on the *FTS3* prototype. Coils are switched off at t= 1 s in all cases.

Spectral analyses of the positions using the Lomb-normalised periodigram method reveal that the main damped frequency is obtained at around 1Hz.

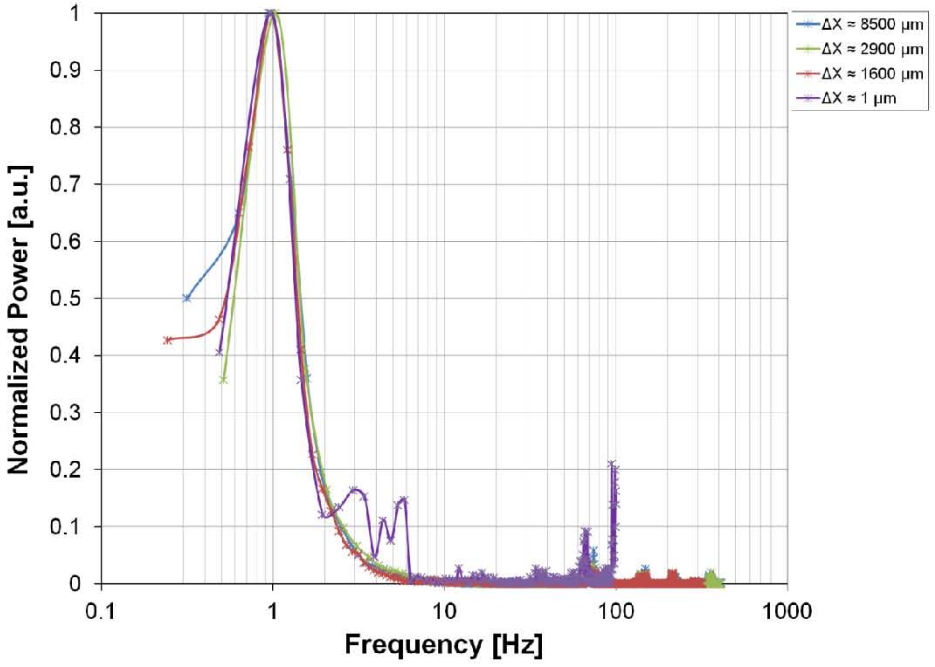

Fig. 7.20. Normalised power spectrum from Lomb-normalised periodigram spectrum analyses of different motion histories on the *FTS3* prototype, including those in Fig.7.19 Frequency resolution: 0.2-0.4 Hz.

More detailed results for the frequency and time analyses of the signal in Fig. 7.20 are summarised in Table 7.1.

Table 7.1. Damped frequency obtained by spectral analysis and time analyses of the signals.

Motion amplitude [µm]	**Lomb-normalised periodigram**	**Time analysis**
	Main damped frequency [Hz]	Average damped frequency [Hz]
0.8±0.2	0.9±0.4	-
162.1±0.2	0.9±0.3	0.90±0.03
(-) 1691.1±0.2	1.0±0.2	0.93±0.02
(-) 2857.4±0.2	0.9±0.2	0.95±0.02
8869.9±0.2	1.0±0.2	0.94±0.02
Average value	Frequency analysis	Time analysis
	0.9±0.4	0.93±0.02

As can be seen in Table 7.1, the measured damped frequency does not strongly depend upon the amplitude of the motion within the stroke of the mechanism.

Additionally, the damping ratio was measured to be 0.37±0.01 for the cases in Table 7.1. Thus, considering an average damped frequency $f_d^* = 0.93 \pm 0.02\ \text{Hz}$, an equivalent angular frequency $\omega_0^* = 6.3 \pm 0.2\ \text{rad/s}$ can be estimated using eq. 6.6. This corresponds to an angular frequency $f_0^* = 1.00 \pm 0.05\ \text{Hz}$. Comparison of the values obtained from the experiments on the FTS3 and the theoretical predictions from FEM calculations of the stiffness of the slider are summarised in Table. 7.2. FEM predictions and the experiments agree within the margin of uncertainty.

Table 7.2. Comparison of the damped and angular frequency obtained from experiments and theoretical predictions based on FEM calculation of the stiffness of the slider of the *FTS3* prototype.

Value obtained from	Damped frequency f_d^* [Hz]	Angular frequency f_0^* [Hz]
Experiments	0.93±0.02	1.00±0.05
Theoretical predictions	0.90±0.05	0.97±0.03

Finally, the damping ratio increased by around 16% with respect to the *FTS2* prototype. Also the natural and the damped angular frequencies slightly increased as a result of the increased stiffness of the mechanism.

7.4.1.7 Speed of the slider

The phase diagram (speed vs. X position) of the slider is shown for different motion steps in Fig. 7.21. Maximum speeds of about 30 mm/s for an 8.8 mm displacement were measured.

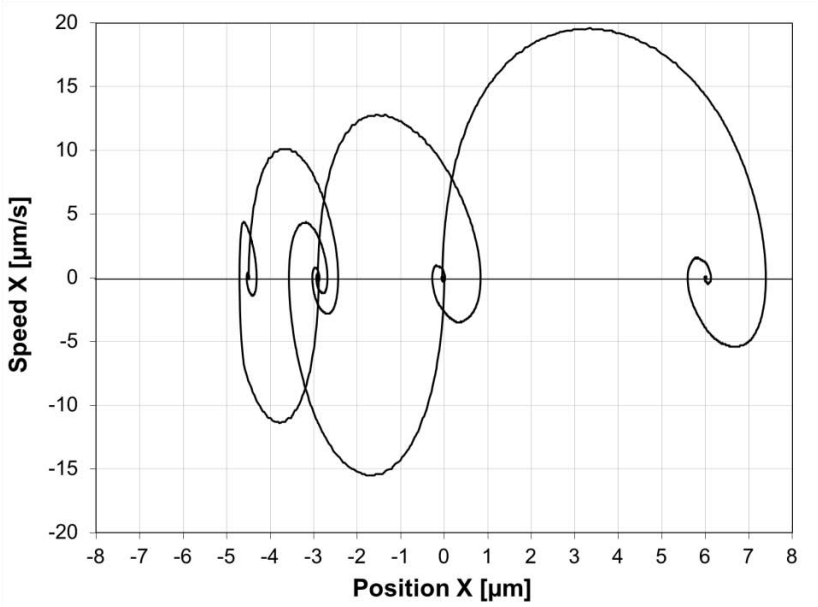

Fig. 7.21. Phase diagram (speed vs. X position) for different motion histories of the slider in the *FTS3* prototype.

The FTS3 maximum speed is twice the maximum speed of *FTS2*. Apparent velocity, as defined chapter VI, was also calculated. Apparent velocities between 0.5 and 2.4 mm/s for a harmonic motion of 1 and 7.5 mm length respectively

were measured. Apparent velocities for the minimum coarse positioning step around the central position were found to be around 1.4 µm/s. See Table 7.3.

Table 7.3. Speeds measured for different motion histories in the *FTS3* prototype.

$X_{initial}$ ±0.2 [µm]	X_{final} ±0.2 [µm]	Maximum velocity ±1 [mm/s]	Δt ± 0.1 [s]	V_{ap} [mm/s]
-8869.9	0	-31	4.5	2.0
0	6040.2	19	3.6	1.7
6040.2	8920.9	16	2.8	1.0
2857.4	0	17	2.6	1.1
1691.1	0	9	2.8	0.8
0	162.1	0.4	2.0	0.08

7.4.2 Run out of the *FTS3* prototype

Lateral run out of the *FTS3* prototype has been reduced to around 3.5 µm with respect the *FTS2* prototype for any X position of the slider. This represents a reduction of a factor of 2 with respect to the *FTS2* prototype. Hysteretic behaviour is still present in Fig. 7.22.

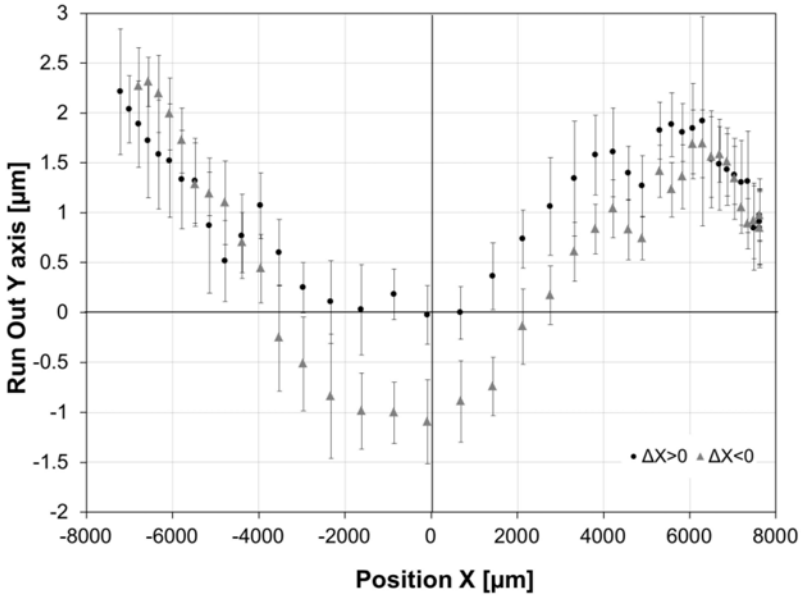

Fig. 7.22. Lateral run out (Y axis) vs. X position of the slider in the *FTS3* prototype.

7.4.3 Angular run outs of the *FTS3* prototype

7.4.3.1 Pitch

Pitch vs. X position of the slider is presented in Fig. 7.23 for a full stroke motion and several cycles. The maximum relative pitch between two points in the stroke of the mechanism is less than 130 µrad. A reduction in one order of magnitude has been achieved in the *FTS3* prototype with respect to the pitch measured in the *FTS2* prototype.

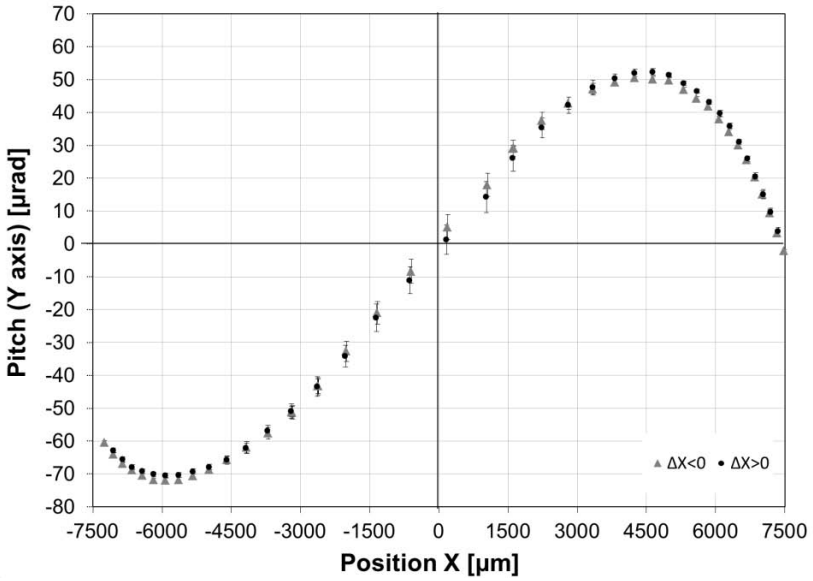

Fig. 7.23. Pitch vs. X position of the slider of the *FTS3* prototype.

7.4.3.2 Yaw

Yaw vs. X position of the slider is presented in Fig. 7.24 for a full stroke motion and several cycles. The maximum relative pitch between two points in the stroke of the mechanism is less than 120 µrad. There is no significant reduction in the angular deviation with respect to the previous prototype, for which 100 µrad was measured.

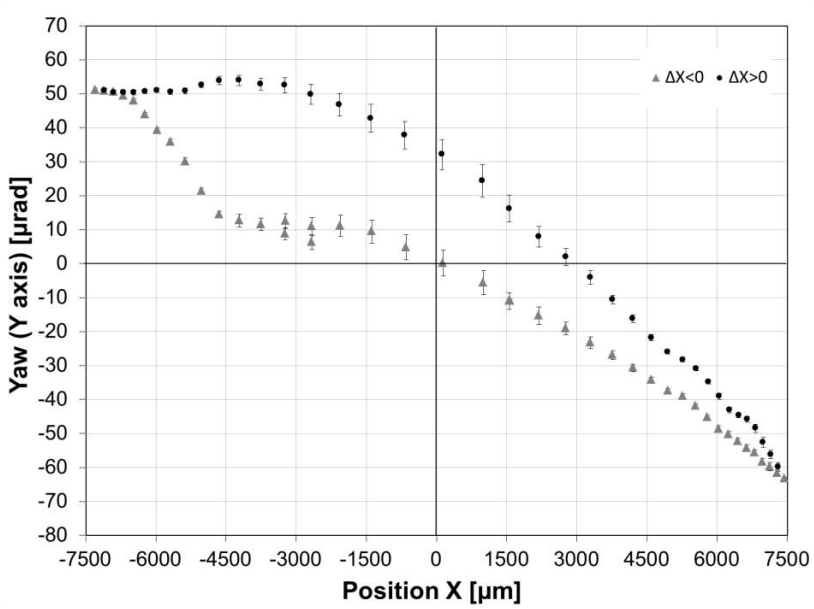

Fig. 7.24. Yaw vs. X position of the slider in the *FTS3* prototype.

7.4.3.3 Roll

Roll vs. X position of the slider is presented in Fig. for a full stroke motion and several cycles. The maximum relative pitch between two points in the stroke of the mechanism is less than 700 µrad. Due to the improvements carried out on the *FTS3* prototype and the better alignment provided between the coils and the permanent magnet in the FC position, the relative roll has been reduced from <4000 µrad in the *FTS2* prototype compared to 700 µrad in the *FTS3* prototype (see Fig. 7.25).

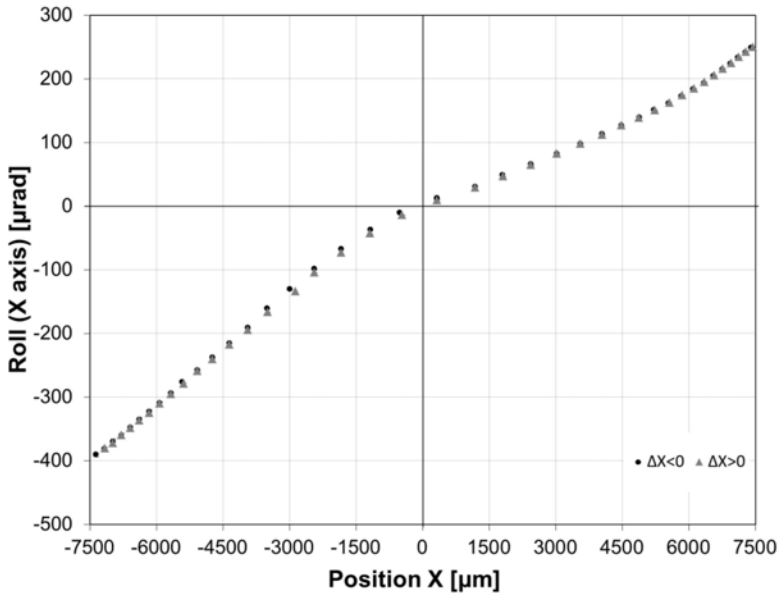

Fig. 7.25. Roll vs. X position of the slider in the *FTS3* prototype.

7.4.4 Power consumption

The measured resistance of the coils at room temperature (300 K) was 3.8 Ω. The increase in the equivalent resistance is due to the greater number of turns in the coils in the *FTS3* prototype compared to the *FTS2* prototype. Therefore, the power consumption of the mechanism at a certain temperature can be estimated using e.q. 6. 10.

Therefore the peak power consumption at 15 K, for a required current of 500 mA and different RRR copper wires [134] is summarised in Table 7.4.

Table 7.4 Estimated power consumption of the *FTS3* prototype for different RRR copper wires in the coils.

RRR [134][134]	**Power consumption estimated [mW]**
30	95
100	19
300	6
1000	2
3000	<1

7.5 Conclusions of chapter VII

The *FTS3* is an improved version of the *FTS2* in which a lower *HFC* is used and an additional piece of superconductor is added. For the *FTS3* a nanometre resolution in a stroke of about ±7.5 mm has been demonstrated. A comparison of *FTS2* and *FTS3* is summarised in Table 7.5.

Table 7.5. Comparison between the *FTS2* and *FTS3* prototypes performance.

Prototype	**FTS2**	**FTS3**
Device Temperature [K]	~15	
Cryostat inside pressure [Pa]	~10^{-6}	
Stroke [mm]	±9	± 7.5
Sensitivity around X=0 mm for the coarse step motion [µm/mA]	31±1	
Sensitivity around X=0 mm for the coarse step motion [µm/mA]	31/15 ±1	1.24±0.04
Resolution coarse [µm]	3.3±0.4	0.8±0.2
Resolution fine RMS [nm]	230±30	70±10
Accuracy [µm]	~1	~1
Power consumption (15K) for RRR=300 [mW]	~5	~6
Hysteresis (X=0) [µm]	60±2	100±2
Damping ratio	0.32±0.01	0.37±0.01
Damped frequency [Hz]	0.91±0.02	0.93±0.02
Maximum measured velocity [mm/s]	~40	~30
Lateral run our (Y axis) [µm]	±4	<3.5
Relative pitch (Y axis) [µrad]	±650	±70
Relative yaw (Z axis) [µrad]	<100	<120
Relative roll (X axis) [µrad]	<4000	<700

The reduction in the stroke of the mechanism was caused by damage to a superconductor, probably due to the thermal stress generated by the large number of cooling and warming processes it had suffered by this point. In spite of the damaged superconductor, the *FTS3* prototype is able to work with good performance, and a nanometre resolution was demonstrated in a stroke of $\pm$ 7.5 mm. This outstanding resolution for a superconducting positioner was possible by using a fine-step system composed of two auxiliary coils with a few turns.

Due to the reduction in the *HFC*, the stiffness of the slider has been increased. This fact not only increases the power consumption of the mechanism, but also increases its angular frequency and its damping ratio and reduces its sensitivity.

Angular deviations and the run out of the mechanism were also reduced due to the reduction in the *HFC*, the addition of a third superconducting disk and the fact that a better alignment between the PM and the coils was provided.

Chapter VIII

Conclusions and contributions

This chapter lists the conclusions and main original contributions of this Ph.D thesis. Finally, some items for further research are proposed.

8.1 Conclusions and contributions

The main conclusions and contributions of this Ph.*D* thesis are listed below:

- A one DoF mechanism able to operate in cryogenic environments based on stably superconducting magnetic levitation has been proposed and demonstrated for high-precision positioning in a long-stroke in cryogenic environments. Different prototypes mainly composed of a long permanent magnet (PM) carrying an optic mirror cube as a slider, a set of high-temperature superconducting disks (*HTS* disks) in the mixed state as the stator and a set of coils as the actuation system were designed, built and tested.

- A set of *HTS* in the mixed state provides stable levitation to a PM. In addition, a self-guiding system is inherent to the *FTS* mechanism. Moreover, displacements in other directions present high stiffness because of the relatively high gradients of the magnetic field. A sliding kinematic pair is established between the PM and the *HTS* disks in the mixed state when the temperature of the superconductors is below their critical temperature. Finally, it is very noticeable that the mechanism presents an initial equilibrium position.

- Due to the symmetry of the magnetic field applied to the superconductors, the position of the PM can be modified with very low resistance and without contact between moving parts. A couple of coils properly designed and placed at either end of the stroke of the mechanism provide the acting force required on the PM to modify its position along the stroke.

- A decoupled model for actuation and levitation has been proposed. The forces of actuation are calculated using FEM calculations. Actuation force versus the X position of the slider can be described by a cubic polynomial (R^2>0.997 in all cases).

- A preliminary prototype of the *FTS* mechanism (prototype *FTS1*) was designed based on the theoretical bases introduced in chapter III. It was also built and tested at ambient pressure with the *YBaCuO* superconductors cooled with liquid nitrogen. A stroke of ±11.5 mm, a pitch of around ±4500 µrad, a yaw about ± 250 µrad, a roll of ±400 µrad (extrapolated to a ±11.5 mm stroke) as well as a hysteresis and lateral and vertical run outs below ± 250 µrad have been determined.

- A set of design rules for the engineering of the *FTS* mechanism has been derived in chapter V and experimentally proven at 77 K (LN_2) and ambient pressure:
    - The lower the *HFC*, the higher the stiffness.
    - The lower the *HFC*, the smaller the angular run outs
    - The lower the *HFC* the higher power consumption.
    - The lower the *HFC*, the lower the sensitivity.
    - Pitch, mostly caused by unbalancing of the lift on the PM and gravity effects when it is moved away from the initial equilibrium position, can be drastically reduced by reducing the mass of the slider, increasing the vertical magnetic stiffness or by increasing the distance between the superconductors *d*.
    - Pitch can also be reduced by means of magnetic self-alignment between the coils and the PM. Then, if the centre of the coils is elevated over the axis of the PM, the pitch can be reduced. A reduction in the maximum pitch of about 25% for an 8 mm elevation of the coils (H_c) was demonstrated for a prototype with *HFC*= 3 mm and *d*= 84 mm.
    - Pitch can also be reduced by applying active magnetic forces. A couple of auxiliary coils were also installed. A correction of the pitch which depends on the current in the coils, and the position of the slider on its path, was observed. Correction of the maximum pitch by about 20% was measured for a driven current tin the coils of ±1A. However, these coils also cause a modification in the position of the slider, making the control process more complicated.
    - Sensitivity, stiffness and stability of the initial equilibrium position can also be modified by geometric modifications on the prototype such as modification of the *HFC* or the distance between the superconductors, *d*.
    - The current requirement and the power consumption of the mechanism are highly dependent upon the configuration of the actuation system. A reduction of about a factor 4 in the current requirement and 16 in the power consumption can be achieved if an anti-serial connection (one coil pushes the PM while the other pulls it) of the coils is set up instead of actuation of the independent pulling coils (repulsive forces).

- An improved prototype (*FTS2*) was designed and built following the design rules previously described and tested in accordance with technology readiness level TRL 6 (ESA). The prototype was tested in a cryostat at a temperature of around 15 K and in a high vacuum of 10^{-6}Pa. The following conclusions were obtained:
    - A sub-micrometre resolution in the fine-step motion of 230±30 nm and a stroke of ± 9 mm was experimentally demonstrated with an open-loop control strategy. The current resolution required was 15±1 µA.
    - A position stability in the sliding direction, independent of the X position of the slider, of about 1 µm (σ= ±0.25 µm) was measured. Spectral analysis of the position vs. time signals show that there was a major contribution located at about 5.5 HZ. Initial vibrations measured before the launch of the slider were σ= ±0.07 µm, with a major contribution at 36 Hz.
    - A hysteretic loop for a full-stroke motion with maximum deviation at the centre of the stroke of 60 µm was measured.
    - Despite a more extended analysis needing to be conducted, it seems that the sensitivity of the slider was only slightly influenced by temperature.
    - The *FTS* mechanism has been demonstrated to behave as an underdamped oscillator with a non-linear stiffness The measured damping ratio was 0.32 for a natural damped frequency of around 0.91±0.02 Hz (not significantly dependent on the amplitude of the displacement).
    - The natural angular frequency of the slider can be easily tuned just by geometry modifications to the *FTS* mechanism, for example, by modifying the distance between the superconductors (*d)* or the *HFC*.
    - There is good agreement of the experimental results with the decoupled model prediction.
    - It was considered that angular run outs and the lateral run out could be highly improved if a better alignment between the PM and the coils is provided.
- A third prototype (*FTS3*) was designed, built and tested in order to demonstrate an improved performance of the *FTS* mechanism. A third superconducting disks was installed in the stator, the *HFC* was reduced thanks to a modification of the launch & lock system and a fine-step motion system was implemented composed of two auxiliary coils with a few turns installed surrounding the main ones. The

prototype was again tested inside a cryostat at a temperature of about 15 K and in a high vacuum of 10^{-6}Pa. The following conclusions were obtained:

- A RMS nanometre resolution (70±10 nm) and a stroke of ± 7.5 mm were experimentally demonstrated with an open-loop control strategy. The current resolution required to achieve this position resolution was 55±9 µA.
- Angular run outs were drastically reduced: pitch from ±650 µrad to ± 70 µrad and roll 4000 µrad to 700 µrad for full stroke motion in the *FTS2* and *FTS3* prototypes respectively.
- A hysteretic loop for full-stroke motion with maximum deviation at the centre of the stroke of 100 µm was measured.
- An increase in the stiffness and the angular frequency and the damping ratio of the *FTS3* prototype was observed in accordance with the theoretical prediction derived in this thesis. However, it is noticeable that the sensitivity of the mechanism remains constant around the initial position.
- The final current requirement and the power consumption will depend upon the RRR of the wires used in the coils, but it can be concluded that is in the order of a few mW.

Finally, the performance of the different prototypes described in this thesis are summarised in Table 8.1.

Table 8.1. Summary of the performance of the three *FTS* prototypes tested. Parameters of lateral run out, relative pitch, relative yaw and relative roll are related to the full-stroke motion of each prototype.

Prototype	***FTS1***	***FTS2***	***FTS3***
Device Temperature [K]	77	~15	
Pressure [Pa]	Ambient pressure	$\sim 10^{-6}$	
Stroke [mm]	±11.5	±9	± 7.5
Sensitivity around X=0 mm for the coarse step motion [µm/mA]	~78	31±1	
Sensitivity around X=0 mm for the fine step motion [µm/mA]	-	15 ±1	1.24±0.04
Resolution coarse [µm]	<250	3.3±0.4	0.8±0.2
Resolution fine RMS [nm]	-	230±30	70±10
Accuracy [µm]	-	~1	~1
Power consumption (15K) for RRR=300 [mW]	~1	~5	~6
Hysteresis (X=0) [µm]	< 250	60±2	100±2
Damping ratio	-	0.32±0.01	0.37±0.01
Damped frequency [Hz]	-	0.91±0.02	0.93±0.02
Maximum measured velocity [mm/s]	-	~40	~30
Lateral run our (Y axis) [µm]	< 250	±4	<3.5
Relative pitch (Y axis) [µrad]	±4500	±650	±70
Relative yaw (Z axis) [µrad]	± 200	<100	<120
Relative roll (X axis) [µrad]	± 400	<4000	<700

8.2 Future developments

Given the results of this thesis, the following are suggestions for possible future developments:

- To develop a mathematical model for the motion and levitation of the mechanism.
- To determine the stiffness to the motion of the slider for all the generalised coordinates.
- Due to the fact that the hysteresis of the mechanism is higher than the position resolution and the position stability is no better than 1 µm, a close loop control strategy would improve the overall performance of the control of the position and will provide enhanced position repeatability. Moreover, due to the low damping of the system, an appropriate closed loop strategy or an input shaping strategy would improve the apparent velocity of the slider.
- To develop a full-Meissner levitation device. Therefore, no hysteresis would be present in the superconductors.

BIBLIOGRAPHY

PUBLICATIONS AND SCIENTIFIC CONTRIBUTIONS DERIVED FROM THIS THESIS

- I. Valiente-Blanco, E. Díez-Jiménez, J.-L. Pérez-Díaz and J.-C. García-Prada, "Mecanismo nanoposicionador sin contacto de carrera larga," Spanish. Patent P2011309102011.

- J.-L. Pérez-Díaz, I. Valiente-Blanco, E. Díez-Jiménez, and J. Sanchez García-Casarrubios, "Superconducting Non-Contact Device for Precision Positioning in Cryogenic Environments," *IEEE/ASME Transaction on Mechatronics* 2013 (accepted 21st Feb 2013)

- J.-L. Pérez-Díaz, J. C. García-Prada, E. Díez-Jiménez, I. Valiente-Blanco, B. Sander, L. Timm, J. Sánchez-García-Casarrubios, J. Serrano, F. Romera, H. Argelaguet-Vilaseca, and D. González-de-María, "Non-contact linear slider for cryogenic environment," *Mechanism and Machine Theory*, vol. 49, pp. 308–314, Oct. 2012.

- J. L. Perez-Diaz, J. C. Garcia-Prada, I. Valiente-Blanco, E. Diez-Jimenez, J. Sanchez-Casarrubios, J. Serrano, F. Romera, D. Gonzalez-de-Maria, and H. Argelaguet-Vilaseca, "Non-contact Linear Mechanism Based on Superconducting Levitation for Cryogenic Environment," *New Trends in Mechanism and Machine Science, Mechanism and Machine Science*, Springer Link, 2013, pp. 671–679.

- J. Serrano-tellez, F. Romera-juarez, D. González-de-maría, M. Lamensans, H. Argelaguet-Vilaseca, J. L. Perez-Diaz, J. Sanchez-Casarrubios, E. Diez-Jimenez, and I. Valiente Blanco, "Experience on a cryogenic linear mechanism based on superconducting levitation," in *Proceedings of SPIE Modern Technologies in Space- and Ground-based Telescopes and Instrumentation II*, vol. 850, 2012.

- I. Valiente-Blanco, E. Díez-Jiménez, J.-L. Pérez-Díaz, E. Diez-Jimenez, and J. L. Perez-Diaz, "Alignment effect between a magnet over a superconductor cylinder in the Meissner state," *Journal of Applied Physics*, vol. 109, no. 7, p. 07E704, 2011.

- E. Diez-Jimenez, I. Valiente-Blanco, and J.-L. Perez-Diaz, "Superconducting Sphere and Finite-Size Permanent Magnet: Force, Torque, and Alignment Effect Calculation," *Journal of Superconductivity and Novel Magnetism*, Jul. 2012.

- J.-L. Perez-Diaz, E. Diez-Jimenez, I. Valiente-Blanco, and J. Herrero-de-Vicente, "Stable thrust on a finite-sized magnet above a Meissner superconducting torus," *Journal of Applied Physics,* vol. 113, no. 6, p. 063907, 2013.

- E. Diez-Jimenez, I. Valiente-Blanco, V. Castro-Feranandez, C. Cristache, J. Sanchez-Garcia-Casarrubios, M.A. Alvarez-Valenzuela and J.L. Perez-Diaz, "Non-hysteretic passive magnetic linear bearing for cryogenic environments," accepted in the *5th World Tribology Congress 2013*, Torino, Italy Sept. 2013.

- I. Valiente-Blanco, E. Diez-Jimenez,J. Sanchez-Garcia-Casarrubios, C.Cristache,M.A. Alvarez-Valenzuela and J.L. Perez-Diaz Contactless "Superconducting Magnetic Instrument for Precise Positioning in Cryogenic Environments," accepted in *ASME 2013 International Mechanical Engineering Congress and Exposition,* San Diego, USA, Nov. 2013

- J. L. Perez-Diaz, J. C. Garcia-Prada, I. Valiente-Blanco, E. Diez-Jimenez, J. Sanchez-Casarrubios, J. Serrano, F. Romera, D. Gonzalez-de-Maria, and H. Argelaguet-Vilaseca, "Non-contact Linear Mechanism Based on Superconducting Levitation for Cryogenic Environment," *in the European Conference on Mechanism and Machine Science, EUCOMES 2012,* Santander, Spain Sept. 2012.

- J. L. Perez-Diaz, E. Diez-Jimenez, I. Valiente-Blanco, and J. C. Garcia-Prada, "Experimental determination of the first penetration field in high-temperature superconductors by mechanical methods," in the *3rd International Workshop on Modelling HTS. Poster session,* Barcelona, Spain 2012.

- I. Valiente-Blanco, E. Díez-Jiménez, J.-L. Pérez-Díaz, E. Diez-Jimenez, and J. L. Perez-Diaz, "Alignment effect between a magnet over a superconductor cylinder in the Meissner state," in *the 55th Annual Magnetism and Magnetic Materials (MMM) conference,* Atlanta, USA, Nov. 2010.

REFERENCES

[1] S. Devasia, E. Eleftheriou, and S. O. Reza Moheimani, "A survey of control issues in nanopositioning," *IEEE Transactions on Control Systems Technology*, vol. 15, no. 5, pp. 802 823, Sep. 2007.

[2] J. Gu, "Development of 6 DOF magnetically levitated instrument with nanometer precision," *Texas A&M University*, May 2003.

[3] Y. Ostrovskaya, T. Yukhno, G. Gamulya, Y. Vvedenskij, and V. Kulcba, "Low temperature tribology at the B. Verkin Institute for Low Temperature Physics & Engineering (historical review)," *Tribology International*, vol. 34, no. 4, pp. 265 276, Apr. 2001.

[4] A. Trautmann, C. R. Siviour, S. M. Walley, and J. E. Field, "Lubrication of polycarbonate at cryogenic temperatures in the split Hopkinson pressure bar," *International Journal of Impact Engineering*, vol. 31, no. 5, pp. 523–544, May 2005.

[5] R. Navarro et al., "Precision Mechanism for Optics in a Vacuum Cryogenic Environment," in *International Conference on Space Optics*, Oct. 2010.

[6] G. N. Weisensel, O. D. McMasters, and R. G. Chave, "Cryogenic magnetostrictive transducers and devices for commercial, military, and space applications," in *Proceedings of SPIE*, vol. 3326, pp. 459–470, June 1998.

[7] T. Maillard, F. Claeyssen, R. LeLetty, O. Sosnicki, A. Pages, and A. Vazquez Carazo, "Piezomechatronic-based systems in aircraft, space, and defense applications," in *Proceedings of SPIE* 2009, vol. 7331, no. 0K, pp. 1–9, May 2009.

[8] ESA/SRE (2009)6, "SPICA: Revealing the origins of planets and galaxies," *Assessment study report*, pp. 110, Dec. 2009.

[9] ESA, "European non-dependence on critical space technologies: EC-ESA-EDA list of urgent actions for 2009." *Joint Task Force final report*, March 2009.

[10] ESA, "ESA technology readiness level definition," 2012. [Online]. Available: http://sci.esa.int/science-e/www/object/index.cfm?fobjectid=37710.

[11] J. Nagamatsu, N. Nakagawa, T. Muranaka, Y. Zenitani, and J. Akimitsu, "Superconductivity at 39 K in magnesium diboride," *Letters to Nature*, vol. 410, pp. 63 64, March 2001.

[12] H. K. Onnes, "Further experiments with liquid helium D - On the change of the electrical resistance of pure metals at very low temperatures, etc V The disappearance of the resistance of mercury," in *Proceedings of the koninklijke akademie Van Wetenschappen TE Amsterdam*, vol. 14 I, pp. 113 115, Amsterdam 1911.

[13] D. Dew-Hughes, "The critical current of superconductors: an historical review," *Low Temperature Physics*, vol. 27, no. 9, p. 713-723, Sep. 2001.

[14] W. Meissner and R. Ochsenfeld, "Short initial announcements.," *Naturwissenschaften*, vol. 21, pp. 787–788, 1933.

[15] F. London and H. London, "The Electromagnetic Equations of the Supraconductor," in *Proceedings of the Royal Society A: Mathematical, Physical and Engineering Sciences*, vol. 149, no. 866, pp. 71–88, Mar. 1935.

[16] J. Schnalian, "Failed theories of superconductivity," *Modern Physiscs Letters B*, vol. 24, no. 27, p. 2679, Aug. 2010.

[17] V. L. Ginzburg and L. D. Landau, "On the theory of superconductivity," *Zhurnal Eksperimental'noi i Teoreticheskoi Fiziki*, vol. 20, p. 1064, 1950.

[18] A. A. Abrikosov, "Vliyanie termicheskoi ionizatsii na raspredelenie chastits v neravnomerno nagretom gaze," *Zhurnal Eksperimentalnoi I Teoreticheskoi Fiziki*, vol. 22, no. 3, pp. 321–330, 1952.

[19] P. Goa, H. Hauglin, and M. Baziljevich, "Real-time magneto-optical imaging of vortices in superconducting NbSe2," *Superconductor Science and Technology*, vol. 14, no. 9, pp. 729 731, Aug. 2001.

[20] J. Bardeen and L. Cooper, "Theory of superconductivity," *Physical Review*, vol. 108, no. 5, pp. 1175–1204, December 1957.

[21] M. Eskildsen, M. Kugler, S. Tanaka, J. Jun, S. Kazakov, J. Karpinski, and Ø. Fischer, "Vortex Imaging in the π Band of Magnesium Diboride," *Physical Review Letters*, vol. 89, no. 18, pp. 1–4, Oct. 2002.

[22] B. D. Josephson, "Possible new effects in superconductive tunnelling," *Physics Letters*, vol. 1, no. 7, pp. 251–253, Jul. 1962.

[23] K. Fossheim and A. Sudbo, Superconductivity: *Physics and Applications*, vol. 58, no. 9. John Wiley Ltd., 2004, pp. 134–136.

[24] J. G. Bednorz and K. A. Muller, "Possible High Tc Superconductivity in the BaLaCuO System," *Physica B: Condensed matter*, vol. 64, pp. 189 193, 1986.

[25] M. Wu, J. Ashburn, C. Torng, P. P. H. Hor, R. Meng, L. Gao, Z. J. Huang, Y. Wang, and C. Chu, "Superconductivity at 93 K in New Mixed-Phase Y-Ba-Cu-O Compound System at Ambient Pressure," *Physical Review Letters*, vol. 58, no. 9, pp. 908–910, March 1987.

[26] K. D. Irwin, "Seeing with superconductors," *Scientific American*, vol. 295, no. 5, pp. 86 94, 2006.

[27] F. C. Moon and P. Z. Chang, Superconducting Levitation. Applications to Bearings and Magnetic Transportation. *Wiley-VCH*, 1994, p. 295.

[28] W. V. Hassenzahl, D. W. Hazelton, B. K. Johnson, P. Komarek, M. Noe, and C. T. Reis, "Electric power applications of superconductivity," in *Proceedings of the IEEE*, vol. 92, no. 10, pp. 1655 1674, Oct. 2004.

[29] Y. Itoh et al., "High-Temperature Superconducting Motor Using YBCO Bulk Materials," *Japanese journal of applied physiscs*, vol. 34, pp. 5574–5578, July 1995.

[30] J. Carlström, E. Babaev, and M. Speight, "Semi-Meissner state and neither type-I nor type-II superconductivity in multicomponent superconductors," *Physical Review B*, vol. 84, no. 13, pp. 1 11, Nov. 2011.

[31] C. P. Bean, "Magnetization of Hard Superconductors," *Physical Review Letters*, vol. 8, no. 6, pp. 250–253, Mar. 1962.

[32] L. F. Magaña-Solis, "Los Superconductores", *Fondo De Cultura Economica USA*, Dec. 2000. ISBN-10: 9681653297.

[33] T. P. Sheahen, "Introduction to High-Temperature Superconductivity", *Kluwer Academic Publishers*, New York 2002, pp. 29–31.

[34] V. Arkadiev, "A Floating Magnet," *Nature*, vol. 160, no. 4062, pp. 330–330, Sep. 1947.

[35] J. R. Hull, "Superconducting bearings," *Superconductor Science and Technology*, vol. 13, no. 2, pp. R1–R15, Jul. 2000.

[36] L. Lynds, B. R. Weinberger, J. R. Hull, and U. Balachandran, "Low friction in high temperature superconductor bearings," *Applied Physics Letters*, vol. 59, no. 9, pp. 1132 1134, Aug. 1991.

[37] A. Cansiz, "Vertical, radial and drag force analysis of superconducting magnetic bearings," *Superconductor Science and Technology*, vol. 22, no. 7, p. 075003, Jul. 2009.

[38] E. Diez-Jimenez, "Fundamentos de ingeniería de mecanismos compuestos por imanes y superconductores en estado Meissner," Universidad Carlos III de Madrid, March 2012.

[39] Y. Liu, R. Fung, and C. Wang, "Precision position control using combined piezo-VCM actuators," *Precision Engineering*, vol. 29, no. 4, pp. 411–422, Oct. 2005.

[40] E. Manske, T. Hausotte, R. Mastylo, T. Machleidt, K.-H. Franke, and G. Jäger, "New applications of the nanopositioning and nanomeasuring machine by using advanced tactile and non-tactile probes," *Measurement Science and Technology*, vol. 18, no. 2, pp. 520 527, Feb. 2007.

[41] I. Busch-Vishniac, "Micro-automating semiconductor fabrication," *IEEE Circuits and Devices Magazine*, vol.7, no. 4, pp. 32–37, July 1991.

[42] W. Kim and D. L. Trumper, "High-precision magnetic levitation stage for photolithography," *Precision Engineering*, vol. 22, no. 2, pp. 66–77, April 1998.

[43] W. R. Lee, J. H. Lee, and K. H. You, "Augmented sliding-mode control of an ultra-precision positioning system," *Precision Engineering*, vol. 35, no. 3, pp. 521 524, July 2011.

[44] N. Fleischer, M. Genut, L. Rapoport, and R. Tenne, "New nanotechnology solid lubricants for superior dry lubrication," in *Proceedings of the 10th European Space Mechanisms and Tribology Symposium*, Sept. 2003, pp. 65 – 66.

[45] G. Bingham, H. Latvakoski, and S. Wellard, "Far-infrared spectroscopy of the troposphere (FIRST): sensor development and performance drivers," in *Proceedings of SPIE Optical Spectroscopic Techniques and Instrumentation for Atmospheric and Space Research V*, 2003, vol. 5157, pp. 143–153, Nov. 2003.

[46] D. Grassi, N. I. Ignatiev, L. V. Zasova, a. Maturilli, V. Formisano, G. a. Bianchini, and M. Giuranna, "Methods for the analysis of data from the Planetary Fourier Spectrometer on the Mars Express Mission," *Planetary and Space Science*, vol. 53, no. 10, pp. 1017–1034, Aug. 2005.

[47] F. M. Flasar et al., "Exploring the Saturn System in the Thermal Infrared: The Composite Infrared Spectrometer," *Space Science Reviews*, vol. 115, pp. 169 297, 2004.

[48] D. T. Jaffe, R. Gusten, and D. Downes, "New H2O Masers Associated with Far-Infrared Sources," *The Astrophysical Journal*, vol. 250, no. 15, pp. 621–630, Nov. 1981.

[49] D. Leisawitz et al., "The space infrared interferometric telescope (SPIRIT): High-resolution imaging and spectroscopy in the far-infrared," *Advances in Space Research*, vol. 40, no. 5, pp. 689–703, Jan. 2007.

[50] C. Telesco and D. Harper, " Galaxies and far-infrared emission," *Astrophysical Journal*, vol. 235, no. 2, pp. 392-404, 1980.

[51] J. Tichý, J. Erhart, KittingerE., and J. Prívratska, "Fuldamentals of Piezoelectric Sensorics", 1st ed. Springer, 2010. ISBN 978-3-540-68427-5

[52] K. Uchino, "Advances in ceramic actuator materials," *Materials Letters*, vol. 22, no. January, pp. 2–5, 1995.

[53] F. Claeyssen, A. Ducamp, F. Barillot, R. Le Letty, T. Porchez, O. Sosnicki, and C. Belly, "Stepping Piezoelectric Actuators Based on APAs," in the *11th International Conference on New Actuators*, Bremen-Germany 9-11, pp. 623–626, 2008, June 2008,.

[54] O. Kenichi and S. Masaki, "Positioning table," U.S. Patent 4,610,442 1984.

[55] R. Gloss and H. Marth, "Adjusting device with piezo drive," U.S. Patent 5,424,597 1994.

[56] J. Kim and S.-R. Nam, "Development of a Micro-Depth Control System for an Ultra-Precision Lathe Using A Piezo-Electric Actuator," *International Journal of Machine Tools and Manufacture*, vol. 37, no. 4, pp. 495–509, 1997.

[57] A. I. Ltd., Piezoelectric Ceramics: Principles and Applications, *APC International Ltd.* USA: , 2002, p. 50.

[58] W. Kim and S. Verma, "Design and precision construction of novel magnetic-levitation-based multi-axis nanoscale positioning systems," *Precision Engineering*, vol. 31, no. 4, pp. 337–350, Oct. 2007.

[59] H. Richter, E. Misawa, D. Lucca, and H. Lu, "Modeling nonlinear behavior in a piezoelectric actuator," *Precision engineering*, vol. 25, no. 2, pp. 128 137, Apr. 2001.

[60] A. A. G. Requicha et al., "Manipulation of nanoscale components with the AFM: Principles and Applications," in *Proceedings of the 2001 1st IEEE Conference on Nanotechnology IEEE-NANO*, vol. 123, no. 112138, pp. 81 86, 2001.

[61] J. Main, E. Garcia, and D. Newton, "Precision position control of piezoelectric actuators using charge feedback," *Journal of Guidance, Control, and Dynamics*, vol. 18, no. 5, pp. 1068–1073, Sept.-Oct.1995.

[62] R. Yang, M. Jouaneh, and R. Schweizer, "Design and characterization of a low-profile micropositioning stage," *Precision Engineering*, vol. 18, no. 1, pp. 20–29, Jan. 1996.

[63] P. Pertsch, H. Marth, P. Anger, and A. Feltz, "Low-Temperature Properties of Piezoelectric Actuators," in *Actuator 2000. 7th International Conference on New Actuators*, Bremen, Germany, June 2000.

[64] G. Martinet, S. Blivet, F. Chatelet, and M. Fouaidy, "Low temperature properties of piezoelectric actuators used in SRF cavities cold tuning systems," in *Proceedings of EPAC06*, pp. 390–392, 2006.

[65] X. Jiang, W. B. Cook, and W. S. Hackenberger, "Cryogenic Piezoelectric Actuator," in *Proceedings SPIE Optical Engineering + Applications*, vol. 7439, no. 74309Z, 2009.

[66] A. Högele, S. Seidl, M. Kroner, K. Karrai, C. Schulhauser, O. Sqalli, J. Scrimgeour, and R. J. Warburton, "Fiber-based confocal microscope for cryogenic spectroscopy," *Review of Scientific Instruments*, vol. 79, no. 2 Pt 1, p. 023709, Feb. 2008.

[67] R. Le Letty, F. Barillot, and H. Fabbro, "Miniature Piezo mechanisms for optical and space applications," in *Proccedings of the 9th Conference on New Actuators*, Bremen Germany, 14-16. June 2004.

[68] Z. M. Zhang, Q. An, J. W. Li, and W. J. Zhang, "Piezoelectric friction–inertia actuator—a critical review and future perspective," The *International Journal of Advanced Manufacturing Technology*, vol. 62, no. 5-8, pp. 669-685, Sept. 2012.

[69] "Attocube nanopositioning systems for cryogenic environments," 2012. [Online]. Available: http://www.attocube.com/nanoPOSITIONING/download/Brochure_nanoPOSITIONING.pdf.

[70] "Physik Instrumente nanopositioners," 2012. [Online]. Available: http://www.physikinstrumente.com/en/products/micropositioning/index.php.

[71] Z. M. Zhang, Q. An, J. W. Li, and W. J. Zhang, "Piezoelectric friction inertia actuator—a critical review and future perspective," *The International Journal of Advanced Manufacturing Technology*, vol. 62, no. 5-8, pp.669-685, Sept. 2012.

[72] M. Gibbs, "Magnetostriction: 150 years from the discovery," *Physica Scripta*, vol. T45, pp. 115 119, 1992.

[73] K. Jin, Y. Kou, and X. Zheng, "The resonance frequency shift characteristic of Terfenol-D rods for magnetostrictive actuators," *Smart Materials and Structures*, vol. 21, no. 4, p. 045020, Apr. 2012.

[74] W. Wang and I. Busch-Vishniac, "A high precision micropositioner based on magnetostriction principle," *Review of Scientific Instruments*, vol. 63, no. 1, pp. 249-254, Jan. 1992.

[75] S. F. Tsodikoc and V. I. Rakhovsky, "Magnetostriction Power Actuators for Superprecision Positioning," *Measurement Techniques*, vol. 40, no. 5, pp. 485-494, May 1997.

[76] S. F. Tsodikov and V. I. Rakhovsky, "Magnetostrictive force actuators for superprecise positioning," in *Proceedings of IEEE 18th International Symposium on Discharges and Electrical Insulation in Vacuum*, vol. 2, pp. 713–719, 1998.

[77] B. T. Yang, M. Bonis, H. Tao, C. Prelle, and F. Lamarque, "A magnetostrictive mini actuator for long-stroke positioning with nanometer resolution," *Journal of Micromechanics and Microengineering*, vol. 16, no. 7, pp. 1227 1232, Jul. 2006.

[78] T. Ueno and T. Higuchi, "Zero-power magnetic levitation using composite of magnetostrictive/piezoelectric materials," *IEEE Transactions on Magnetics*, vol. 43, no. 8, pp. 3477–3482, Aug. 2007.

[79] J. a. Dooley, C. a. Lindensmith, R. G. Chave, N. Good, J. Graetz, and B. Fultz, "Magnetostriction of single crystal and polycrystalline Tb0.60Dy0.40 at cryogenic temperatures," *Journal of Applied Physics*, vol. 85, no. 8, p. 6256-6258, April 1999.

[80] J. P. Voccio, "Design and Testing of a Cryogenic Magnetostrictive Actuator Array," *NGST Science and Technology Exposition. ASP Conference Series*, vol. 207, pp. 532–535, 2000.

[81] G. Horner, L. Bromberg, and J. Teter, "A Cryogenic Magnetostrictive Actuator Using a Persistent High Temperature Superconducting Magnet: Part 1 Concept and Design," in *Proceedings of SPIE* vol. 3674, pp. 499-504, . 1999.

[82] J. P. Teter, G. C. Horner, and L. Bromberg, "Precision cryogenic magnetostrictive actuator using a persistent high TC magnet," *Journal of Applied Physics*, vol. 87, no. 9, pp. 6313-6315, May 2000.

[83] M. Holmes, R. Hocken, and D. Trumper, "The long-range scanning stage: a novel platform for scanned-probe microscopy," *Precision Engineering*, vol. 24, no. 3, pp. 191–209, July 2000.

[84] X. Shan, S. K. Kuo, J. Zhang, and C. Menq, "Ultra precision motion control of a multiple degrees of freedom magnetic suspension stage," *IEEE/ASME Transactions on Mechatronics*, vol. 7, no. 1, pp. 67 78, March 2002.

[85] S. Verma, W. Kim, and J. Gu, "Six-axis nanopositioning device with precision magnetic levitation technology," *IEEE/ASME Transactions on Mechatronics*, vol. 9, no. 2, pp. 384–391, June 2004.

[86] W. Kim and S. Verma, "Multiaxis Maglev Positioner With Nanometer Resolution Over Extended Travel Range," *Journal of Dynamic Systems, Measurement, and Control*, vol. 129, pp. 777–785, Nov. 2007.

[87] Z. Zhang and C. Menq, "Six-axis magnetic levitation and motion control," *IEEE Transactions on Robotics*, vol. 23, no. 2, pp. 196–205, April 2007.

[88] T. C. Van Den Dool, F. Kamphues, W. L. M. Gielesen, and B. C. Braam, "Magnetic Bearing based cryo-mechanisms for future IR missions," in *Astro2010: The Astronomy and Astrophysics Decadal Survey*, 2010.

[89] H. Shakir, "Control Strategies and Motion Plannig for Nanopositioning Applications with Multi-Axis Magnetic-Levitation Instruments," *Texas A&M University*, 2007.

[90] W. Braunbek, "Floating body in the electric and magnetic field," *Zeitschrift for Physik*, vol. 112, no. 11–12, pp. 753–763, Nov. 1939.

[91] D. H. N. Dias, E. S. Motta, G. G. Sotelo, R. de Andrade, R. M. Stephan, L. Kuehn, O. de Haas, and L. Schultz, "Simulations and Tests of Superconducting Linear Bearings for a MAGLEV Prototype," *IEEE Transactions on Applied Superconductivity*, vol. 19, no. 3, pp. 2120–2123, Jun. 2009.

[92] R. de Andrade et al., "Performance of Nd-Fe-B and ferrite magnets in superconducting linear bearings with bulk YBCO," *IEEE Transactions on Appiled Superconductivity*, vol. 13, no. 2, pp. 2271–2274, Jun. 2003.

[93] D. H. N. Dias, G. G. Sotelo, and R. de Andrade, "Study of the Lateral Force Behavior in a Field Cooled Superconducting Linear Bearing," *IEEE Transactions on Applied Superconductivity*, vol. 21, no. 3, pp. 1533–1537, Jun. 2011.

[94] T. Iizuka, Y. Maeda, K. Aihara, and H. Fujita, "A Micro X-Y-thetaθ conveyor by using superconducting magnetic levitation," *IEEE Symposium on Emerging Technologies and Factory Automation*, pp. 62–67, Nov. 1994.

[95] T. Iizuka and H. Fujita, "Precise Positioning of a Micro Conveyor Based on Superconducting Magnetic Levitation," in *International Symposium on micromechanotronics and human science*, 1997, pp. 131–135.

[96] T. Iizuka, N. Sakai, and H. Fujita, "Position feedback control using magneto impedance sensors on conveyor with superconducting magnetic levitation," *Sensors and Actuators A: Physical*, vol. 150, no. 1, pp. 110–115, Mar. 2009.

[97] P.-P. Lin, T.-Y. Yang, S.-Y. Chen, and I.-G. Chen, "Study of Micro/Nano Scale Displacement by Electro-Maglev System Using Bulk Superconductors and Permanent Magnet," *IEEE Transactions on Applied Superconductivity*, vol. 17, no. 2, pp. 2063–2066, Jun. 2007.

[98] T. Mori and A. Inoue, "A prototype magnetically levitated superconducting conveyer," *IEEE Transactions on Applied Superconductivity*, vol. 17, no. 2, pp. 2170 2173, Jun. 2007.

[99] A. Masatake et Al., "Superconducting actuator," Japanese Patent 1,218,370 1989.

[100] R.B. Laibowitz and G.J. Lasher "Controllable levitation device," U.S. Patent 5,298,875 1994.

[101] G. R. Brotz, "Mirror-moving system," U.S. Patent 5,455,706 1991.

[102] R. Moser and H. Bleuler, "Precise positioning using electrostatic glass motor with diamagnetically suspended rotor," *IEEE Transactions on Applied Superconductivity*, vol. 12, no. 1, pp. 937–939, Mar. 2002.

[103] R. Saito, K. Itatsu, M. Kanke, and A. Ito, "Contact-free Two Dimensional Micro-displacement Actuation by Using Diamagnetic Graphite," *IEEE Transactions on Industry Applications*, vol. 130, no. 11, pp. 1221–1225, 2010.

[104] H. Hatano, Y. Kanai, Y. Ikegami, T. Fujii, and K. Saito, "Ultrasonic Levitation and Positioning Samples" *Japane Journal of Applied Physiscs*, vol. 21, no. 21 3, pp. 202 204, 1981.

[105] T. Ide, J. Friend, K. Nakamura, and S. Ueha, "A non-contact linear bearing and actuator via ultrasonic levitation," *Sensors and Actuators A*, vol. 135, pp. 740 747, Apr. 2007.

[106] J.-L. Pérez-Díaz, J. C. García-Prada, E. Díez-Jiménez, I. Valiente-Blanco, B. Sander, L. Timm, J. Sánchez-García-Casarrubios, J. Serrano, F. Romera, H. Argelaguet-Vilaseca, and D. González-de-María, "Non-contact linear slider for cryogenic environment," *Mechanism and Machine Theory*, vol. 49, pp. 308–314, March 2012.

[107] J. L. Perez-Diaz, J. C. Garcia-Prada, I. Valiente-Blanco, E. Diez-Jimenez, J. Sanchez-Casarrubios, J. Serrano, F. Romera, D. Gonzalez-de-Maria, and H. Argelaguet-Vilaseca, "Non-contact Linear Mechanism Based on Superconducting Levitation for Cryogenic Environment," *New Trends in Mechanism and Machine Science, Mechanism and Machine Science, Springer Link*, 2013, pp. 671 679.

[108] F. C. Moon, Magneto-Solid Mechanics. *Wiley*, New York, 1984.

[109] N. Lee, G. E. Jang, C. Kim, T. Sung, Y. Han, and S. Jung, "The effects of artificial holes with different diameters on the surface magnetic properties in YBCO superconductors," *Physica C: Superconductivity*, vol. 463–465, pp. 320–324, Oct. 2007.

[110] J.-L. Pérez-Díaz, E. Díez-Jiménez, I. Valiente-Blanco, and J.-C. García-Prada, "Mecanismo nanoposicionador sin contacto de carrera larga," Spanish. Patent P201130910 2011.

[111] S. Senoussi, "Review of the critical current densities and magnetic irreversibilities in high Tc superconductors," *Journal de Physique III*, vol. 2, no. 7, pp. 1041–1257, July 1992.

[112] J. L. Perez-Diaz, E. Diez-Jimenez, I. Valiente-Blanco, and J. C. Garcia-Prada, "Experimental determination of the first penetration field in high-temperature superconductors by mechanical methods," in *3rd International Workshop on Modelling HTS. Poster session*, 2012.

[113] N. Miura, H. Nakagawa, T. Sekitani, M. Naito, H. Sato, and Y. Enomoto, "High-magnetic-field study of high-Tc cuprates," *Physica B: Condensed Matter*, vol. 319, no. 1–4, pp. 310 320, July 2002.

[114] J. L. Smith et al., "Low-temperature critical field of YBCO," *Journal of Superconductivity*, vol. 7, no. 2, pp. 269–270, April 1994.

[115] L. Krusin-Elbaum and A. Malozemoff, "Temperature dependence of lower critical fields in Y-Ba-Cu-O crystals," *Physical Review B*, vol. 39, no. 4, pp. 2936–2939, Feb. 1989.

[116] J. Serrano-tellez, F. Romera-juarez, D. González-de-maría, M. Lamensans, H. Argelaguet-Vilaseca, J. L. Perez-Diaz, J. Sanchez-Casarrubios, E. Diez-Jimenez, and I. Valiente Blanco, "Experience on a cryogenic linear mechanism based on superconducting levitation," in *Proceedings of SPIE Modern Technologies in Space- and Ground-based Telescopes and Instrumentation II*, vol. 850,article number: 84501Y, 2012.

[117] B. . Ma, J. . Herchenroeder, B. Smith, M. Suda, D. . Brown, and Z. Chen, "Recent development in bonded NdFeB magnets," *Journal of Magnetism and Magnetic Materials*, vol. 239, no. 1 3, pp. 418 423, Feb. 2002.

[118] M. C. Engineering, "Comparison of NdFeB and SmCo permanent magnets," 2013. [Online]. Available: http://www.mceproducts.com/knowledge-base/article/article-dtl.asp?id=32.

[119] ESA, "ESA ESMAT Outgassing database," 2013. [Online]. Available: http://esmat.esa.int/materialframe.html.

[120] J. Polinski, "Materials in cryogenics," in European Course in Cryogenics, 2010. Available online [Feb, 2013]

[121] V. Songmene et al., "Machining and Machinability of Aluminum Alloys," in *INTECH open science.*, 2011. Open access.

[122] Z. Xia, J. Bray-Ali, J. Zhang, and B. Fink, "Magnetization of materials used in cryostats," *Journal of Low Temperature Physiscs*, vol. 126, no.1-2, pp. 655–660, January 2002.

[123] A. Hauser, "Calculation of superconducting magnetic bearings using a commercial FE-program (ANSYS)," *IEEE Transactions on Magnetics*, vol. 33, no. 2, pp. 1572–1575, March 1997.

[124] L. Zheng, J. Jin, Y. Guo, W. Xu, and J. Zhu, "Performance Analysis of an HTS Magnetic Suspension and Propulsion System With a Double-Sided HTS Linear Synchronous Motor," *IEEE Transactions on Magnetics*, vol. 48, no. 2, pp. 655–658, Feb. 2012.

[125] S. Li, H. . Wen, and Z. . Zhao, "Modeling and simulation on the magnetization in field-cooling and zero-field-cooling processes," *Physica C: Superconductivity*, vol. 316, no. 3–4, pp. 293–299, May 1999.

[126] G. G. Sotelo, R. de Andrade, and a. C. Ferreira, "Test and Simulation of Superconducting Magnetic Bearings," *IEEE Transactions on Applied Superconductivity*, vol. 19, no. 3, pp. 2083–2086, Jun. 2009.

[127] E. Bartolomé, X. Granados, T. Puig, X. Obradors, E. S. Reddy, and S. Kracunovska, "Critical State of YBCO Superconductors With Artificially Patterned Holes," *IEEE Transactions on Applied Superconductivity*, vol. 15, no. 2, pp. 2775–2778, June 2005.

[128] M. Tsuchimoto, T. Kojima, and T. Honma, "A stable levitation region of HTSC on a permanent magnet," *CEFC`94. Aix-les-Bains*, 1994.

[129] A. Kamitani, O. Shigetoshi, and T. Yokono, "Magnetic shielding analysis of axisymmetric HTS plate by flux flow creep model," *IEEE Transactions on Applied Superconductivity*, vol. 9, no. 2, pp. 3050–3053, Jun. 1999.

[130] J.-L. Perez-Diaz, E. Diez-Jimenez, I. Valiente-Blanco, and J. Herrero-de-Vicente, "Stable thrust on a finite-sized magnet above a Meissner superconducting torus," *Journal of Applied Physics*, vol. 113, no. 6, article number: 063907, Feb. 2013.

[131] I. Valiente-Blanco, E. Díez-Jiménez, J.-L. Pérez-Díaz, E. Diez-Jimenez, and J. L. Perez-Diaz, "Alignment effect between a magnet over a superconductor cylinder in the Meissner state," *Journal of Applied Physics*, vol. 109, no. 7, article number 07E704, pp.1-3, 2011.

[132] E. Diez-Jimenez, I. Valiente-Blanco, and J.-L. Perez-Diaz, "Superconducting Sphere and Finite-Size Permanent Magnet: Force, Torque, and Alignment Effect Calculation," *Journal of Superconductivity and Novel Magnetism*, vol. 26, no. 1, pp. 71-75, Jan 2013.

[133] J. G. Weisend II, "The Handbook of Cryogenic Engineering". *Taylo r& Francis*, 1998.

[134] J. W. Wkin, "Experimental Techniques for Low Temperature Measurements". *Oxford University Press*, 2006. ASIN:B005NKGFJ2

[135] M. Zeisberger, I. Latka, W. Ecke, T. Habisreuther, D. Litzkendorf, and W. Gawalek, "Measurement of the thermal expansion of melt-textured YBCO using optical fibre grating sensors," *Superconductor Science and Technology*, vol. 18, no. 2, pp. S202–S205, Feb. 2005.

[136] J. S. Shearer, "The heat of vaporization of oxygen, nitrogen and air," *Physical Review*, vol. 17, no. 6, pp. 469–475, Dec. 1903.

[137] N. I. of S. and T. NIST, "Cryogenic Properties of Al 6061," 2012. [Online]. Available: http://cryogenics.nist.gov/MPropsMAY/6061 Aluminum/6061_T6Aluminum_rev.htm.

[138] P. Branco and J. Dente, "Design and experiment of a new Maglev design using zero-field-cooled YBCO superconductors," *IEEE Transactions on Industrial Electronics*, vol. 59, no. 11, pp. 1–8, Nov. 2012.

[139] A. Sanchez and C. Navau, "Vertical force, magnetic stiffness and damping for levitating type-II superconductors," *Physica C: Superconductivity*, vol. 268, no. 1–2, pp. 46–52, Sep. 1996.

[140] R. M. Stephan, R. de Andrade, G. C. dos Santos, M. a. Neves, and R. Nicolsky, "Levitation force and stability of superconducting linear bearings using NdFeB and ferrite magnets," *Physica C: Superconductivity*, vol. 386, pp. 490–494, Apr. 2003.

[141] N. Del Valle, A. Sanchez, E. Pardo, C. Navau, and D.-X. Chen, "Enhanced stability by field cooling in superconducting levitation with translational symmetry," *Applied Physics Letters*, vol. 91, no. 11, p. 112507, Sept. 2007.

[142] R. E. Simpson, "Introductory electronics for scientifics and engineers", Second Ed. *Allyn and Bacon*, 1987, p. 218. ISBN: 0205083773

[143] M. W. Pospieszalski, S. Weinreb, R. Norrod, and R. Harris, "FET's and HEMT's at Cryogenic Temperatures- Their Properties and Use in Low-Noise Amplifiers," *IEEE Transactions on Microwave Theory and Techniques*, vol. 36, no. 3, pp. 552–560, 1988.

[144] M. Iwakuni, "A 20 GHz Peltier-cooled Low Noise HEMT Amplifier," *Microwave Journal*, vol. 28, no. 5, p. 92, 1985

[145] K. Lindstroml and N. Holmerl, "Peltier-cooled J-FET Input Stage for Fast, Low-noise Electrometer Amplifier with Low Leakage Current," *Physica Scripta*, vol. 5, no. 6, pp. 279–284, 1972.

[146] K. Kundert, "Power Supply Noise Reduction," *Designer's Guide Consulting, Inc.*, pp. 1–12, 2004.

[147] P. Brokaw, "An IC Amplifier user's guide to decoupling, grounding, and making things go right for a change," *Application note AN-202, Rev.B Analog Devices Inc.*, pp. 1–8, 2000.

[148] W. . Press, B. P. Flannery, S. A. Teukolsky, and W. T. Vetterling, Numerical recipes in FORTRAN: the art of scientific computing, 2nd ed., vol. 69. *Cambridge University* Press, 1992, pp. 569–577.

[149] N. Stäfnescu and N. Pandrea, "On the stability of the forced damped oscillator with nonlinear cubic stiffness," *in SISOM 2006*, pp. 1 5, 2006

[150] G. MacDonald, "Spectral analysis of time series generated by nonlinear processes," *Reviews of Geophysics*, no. 89, pp. 449–469, Nov. 1989.

[151] W. Liu, S. Y. Wang, H. Jing, J. Zheng, M. Jiang, and J. S. Wang, "Levitation performance of YBCO bulk in different applied magnetic fields," *Physica C: Superconductivity,* vol. 468, no. 13, pp. 974–977, Jul. 2008.

[152] J. Zhou, X.-Y. Zhang, and Y.-H. Zhou, "The Influences of Cooling Height on the Levitation Performance of Single-Domain YBCO Bulk," *Modern Physiscs Letters B*, vol. 23, no. 22, pp. 2615-2624 Aug. 2009.